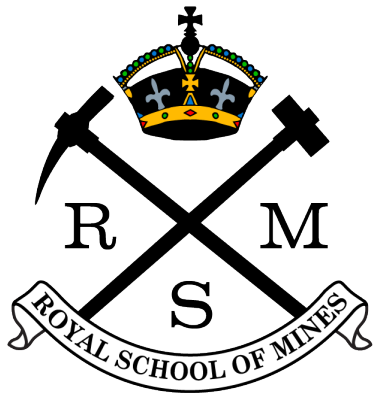


Fire and Ice: Investigating Links Between Mantle Dynamics and Ice Sheet Stability



James A. N. Hazzard

Submitted in part fulfilment of the requirements for the degree of
Doctor of Philosophy
at Imperial College London

Department of Earth Science & Engineering

Imperial College London

May 2024

Abstract

Oceanic and atmospheric warming threaten melting and collapse of Earth’s ice sheets. Global mean sea level rise disrupts coastal ecosystems and communities by increasing destructive potential of coastal inundation events, and disturbing ocean circulation patterns. Therefore, robust projections of spatiotemporal patterns of sea level change are critically important. To construct them, improved understanding of solid Earth structure is required, due to physical couplings between mantle dynamics and ice sheet stability. To date, poor constraint on Earth’s interior structure has obfuscated reliable estimation of future sea level change. Here, a Bayesian inverse framework for self-consistent conversion of seismic velocity into estimates of mantle thermomechanical structure is applied to Antarctica. Low viscosity anomalies are inferred in West Antarctica, such as western Marie Byrd Land, where $\eta = 10^{19.5 \pm 0.3}$ Pa s at 150 km depth. Thick lithosphere, high viscosity, and low geothermal heat flow is inferred in East Antarctica, consistent with cratonic lithosphere. By consideration of time-dependent viscosity perturbations (~ 1 order of magnitude), seemingly disparate inferences of West Antarctic mantle viscosity derived from GPS data are reconciled. Variations in Antarctic geothermal heat flow from 20 to 130 mW m^{-2} are inferred, based on a novel method incorporating crustal composition. Modifying the framework developed for estimating mantle structure, to incorporate use of xenolith-derived palaeogeotherm constraints, Australian lithospheric structure is mapped. It is demonstrated that 97% of metal mass so far mined from Australian base metal deposits is located within 200 km of the 195 km LAB depth contour. Finally, the impact of transient rheology on ice sheet stability is explored, and applied to a simple model of Antarctic glacial isostatic adjustment. For short melting timescales, significantly more near-field deformation is caused by a novel rheological model (exhibiting transient behaviour), as compared to a reference Maxwell model. When melting occurs over 25 years, a 52% increase in Earth surface displacement is observed.

Associated Publications

The following publication is based on the work presented in Chapter 2 and 3. I led the conceptualisation, data curation, methodological development, and analysis of this publication.

Hazzard, J. A. N., Richards, F. D., Goes, S. D. B., & Roberts, G. G. (2023), Probabilistic Assessment of Antarctic Thermomechanical Structure: Impacts on Ice Sheet Stability, *Journal of Geophysical Research: Solid Earth*, 128, e2023JB026653.

The following publication is based on the work presented in Chapter 4. I led the conceptualisation, data curation, methodological development, and analysis of this publication.

Hazzard, J. A. N. and Richards, F. D. (2024), Antarctic Geothermal Heat Flow, Crustal Conductivity and Heat Production Inferred From Seismological Data, *Geophysical Research Letters*, 51, e2023GL106274.

A significant component of the following publication is based on the work presented in Chapter 5. Namely, the construction of Australian palaeogeotherms from xenolith thermobarometry data, and their use within a Bayesian modelling framework to map Australian lithospheric structure. This publication will also include content on xenolith data acquisition and geochemical analysis, and invoke additional information from the geological record to interpret newly generated maps of lithospheric structure in the context of Australia's geological development. Mark Hoggard is leading these aspects of the work, and therefore I am not the lead author of the publication. However, I led the conceptualisation, data curation, methodological development and analysis of all parts of the publication which feature in Chapter 5 of this dissertation.

Hoggard, M. J., Hazzard, J. A. N., Sudholz, Z. J., Richards, F. D., Duvernay, T., Austermann, J., Lynton Jaques, A., Yaxley, G. M. and Czarnota, K. (2024), Thermal Structure of Australian Lithosphere and its Influence on Geological Processes, *Geochemistry, Geophysics, Geosystems*, in preparation.

Statement of Originality

The contents of this dissertation are my original work except where acknowledgement is made in the text.

James A. N. Hazzard

May 2024

Copyright Statement

The copyright of this thesis rests with the author. Unless otherwise indicated, its contents are licensed under a Creative Commons Attribution-Non Commercial 4.0 International Licence (CC BY-NC). Under this licence, you may copy and redistribute the material in any medium or format. You may also create and distribute modified versions of the work. This is on the condition that: you credit the author and do not use it, or any derivative works, for a commercial purpose. When reusing or sharing this work, ensure you make the licence terms clear to others by naming the licence and linking to the licence text. Where a work has been adapted, you should indicate that the work has been changed and describe those changes. Please seek permission from the copyright holder for uses of this work that are not included in this licence or permitted under UK Copyright Law.

Some say the world will end in fire,

Some say in ice.

From what I've tasted of desire

I hold with those who favor fire.

But if it had to perish twice,

I think I know enough of hate

To say that for destruction ice

Is also great

And would suffice.

Fire and Ice

by Robert Frost (1923)

Acknowledgements

I would like to take the opportunity to thank everyone who I have interacted with scientifically over the past four years. The conversations I have had with so many fantastic scientists, whether fleeting or lengthy, online or in-person, have helped shape my experience and development. My deepest gratitude is offered to Fred Richards for his remarkable supervision. From him I have learned more than I could imagine, and I will always be grateful for his guidance and mentorship. Special thanks go to Yasuko Takei, Mark Hoggard and Harriet Lau, with whom I have had the privilege of collaborating. I am indebted to Jerry Mitrovica, who gave his precious time to engage with my research. I am grateful to Saskia Goes and Gareth Roberts, for reviewing my manuscripts and providing invaluable feedback.

To all my family and friends, thank you for your unwavering support. I am grateful to my grandparents Anthony and Marion Hazzard, for stimulating my intellectual curiosity, and revealing to me what I am capable of. I am grateful to my late grandfather Peter Clear for encouraging me to keep going. I thank my parents Joanne and Nick, and my sister Sophie, for their help and guidance whenever called upon. Finally, I would like to thank my girlfriend Rose Jump. She has been there for me from the beginning to the end of my doctoral studies, enduring my stresses and pushing me on. Without the platform given to me by this wonderful network of people, I would never have achieved this work.

Contents

1	Introduction	17
1.1	Estimates of Contemporary Ice Mass Balance	18
1.2	Projections of Future Sea Level Change	21
1.3	Recent Advances	22
1.4	Chapter Overview	23
2	A Bayesian Inverse Method for Calibrating Experimental Parameterisations of Mantle Rock Viscoelasticity	27
2.1	Introduction	27
2.2	Parameterising The Relationship Between V_S and T	29
2.2.1	Empirical Parameterisations	29
2.2.2	Laboratory Parameterisations	31
2.3	Inverse Approach to Conversion Between Upper Mantle V_S and T	36
2.3.1	Independent Geophysical Data Sets	40
2.4	Bayesian Modelling Framework	43
2.4.1	Choice of Sampling Algorithm	47
2.4.2	Synthetic Test	52
2.4.3	Summarising Posterior Outputs	56
2.5	Analysing Posterior Parameter Distributions	58
2.5.1	Parameter Covariance Structure	60

2.6	Conclusions	64
3	Probabilistic Assessment of Antarctic Thermomechanical Structure	65
3.1	Introduction	65
3.2	Predictions of Thermomechanical Structure Beneath Antarctica	69
3.2.1	Viscosity Structure	72
3.2.2	Lithosphere-Asthenosphere Boundary Depth	77
3.2.3	Geothermal Heat Flow	85
3.3	Discussion	88
3.3.1	West and East Antarctic Mantle Structure	90
3.3.2	Comparing Predictions of Geothermal Heat Flow	91
3.3.3	Reconciling Observations and Predictions of Mantle Viscosity	93
3.3.4	Remaining Uncertainties	103
3.4	Conclusions	105
4	Antarctic Geothermal Heat Flow, Crustal Conductivity and Heat Production Inferred From Seismological Data	107
4.1	Introduction	107
4.2	Methods	110
4.2.1	Inferring Thermal Structure from Seismic Data	111
4.2.2	Fitting Geothermal Profiles	113
4.2.3	Parameterising Mantle Structure	113
4.2.4	Parameterising Crustal Structure	114
4.2.5	Sampling Crustal Parameters to Optimise GHF	116
4.3	Results and Discussion	119
4.3.1	Antarctic Upper Crustal Heat Production Estimates	119

4.3.2	Antarctic GHF Estimates	127
4.3.3	Comparison With Previous Studies	130
4.3.4	Comparison With Local Data	132
4.3.5	Methodological Appraisal	136
4.3.6	Outstanding Challenges	137
4.4	Conclusions	139
5	Thermomechanical Structure of Australian Lithosphere and its Influence on Natural Resource Distributions	141
5.1	Introduction	141
5.2	Constructing Australian Palaeogeotherms from Xenolith Thermobarometry Data	143
5.3	Adapting the Bayesian Modelling Framework to Incorporate Palaeogeotherms .	152
5.4	Inversion Performance	155
5.5	Probabilistic Assessment of Australian Lithosphere-Asthenosphere Boundary Depth	161
5.5.1	Results and Discussion	164
5.6	Conclusions	168
6	Relationships Between Transient Rheology, Ice Sheet Stability, and Sea Level	170
6.1	Introduction	170
6.2	Translating Experimental Parameterisations of Mechanical Behaviour Into Generalised Maxwell Form	176
6.2.1	Application to the Master Curve Parameterisation	185
6.2.2	Application to the Pre-Melting Parameterisation	189
6.3	Adapting Pre-Melting Parameterisation For Computational Efficiency	197
6.3.1	Fitting A_P , σ_P and A_η to Experimental Data	202

6.3.2	Influence of Optimised Pre-Melting Parameterisation on Predictions of Antarctic Mantle Structure	210
6.3.3	Co-Inverting For Pre-Melting and Viscoelasticity Parameters With Experimental and Geophysical Data	217
6.4	Implementing Adapted Pre-Melting Parameterisation in a Numerical Simulation of Glacial Isostatic Adjustment	231
6.4.1	Love Number Formulation of the GIA Problem	232
6.4.2	Sea Level Equation	239
6.4.3	Ice Loading and Earth Structure	242
6.4.4	Results	244
6.4.5	Discussion	251
6.5	Conclusions	253
7	Conclusions	257
7.1	Summary	257
7.2	Future Work	262
A	BANCAL22: An Open-Source Algorithm for Bayesian Anelasticity Model Calibration	290
A.1	Installation	291
A.2	Performing Inversions Using BANCAL22	291
A.3	Data, Algorithm and Anelastic Parameterisation Selection	291
A.4	Running an Inversion	293

List of Figures

2.1	Thermal modelling of Antarctic oceanic lithosphere	41
2.2	Flow chart representation of sampling algorithm	49
2.3	Assessing fit of inverted viscoelasticity parameters to Antarctic geophysical data	51
2.4	Assessing fit of inverted viscoelasticity parameters to synthetic data	54
2.5	Difference between synthetic and inverted viscoelasticity parameters reflected in predictions of Antarctic mantle viscosity	55
2.6	Posterior distributions of viscoelasticity parameters	61
3.1	Geophysical and geochemical constraints on Antarctic mantle dynamics and structure	67
3.2	Determining the number of models required to accurately characterise posterior expectation and variance	70
3.3	Diffusion creep viscosity and uncertainty based on forward and inverse modelling	71
3.4	Diffusion creep viscosity beneath Antarctica	73
3.5	Uncertainty in diffusion creep viscosity beneath Antarctica	74
3.6	Lithosphere asthenosphere boundary depth variations beneath Antarctica	76
3.7	Antarctic lithosphere asthenosphere boundary depth dichotomy	77
3.8	Comparison of lithosphere asthenosphere boundary depth variations to contemporary studies	78
3.9	Processing and fitting geothermal profiles	86
3.10	Geothermal heat flow variations across Antarctica	89

3.11 Comparison of upper mantle viscosity estimates based on GPS and seismic tomographic velocity	95
3.12 Inverting an inferred strain history derived from transient rheology for a best-fitting Maxwell model	98
3.13 Assumed stress history, inferred transient strain, and inverted Maxwell strain for each of the remaining geodetic studies	99
4.1 Parameterising Earth structure	112
4.2 Fitting seismically inferred geotherms	115
4.3 Upper crustal heat production	120
4.4 Alexander Island transient geotherms	125
4.5 Amundsen Sea Embayment transient geotherms	126
4.6 Seismically inferred geothermal heat flow	129
4.7 Geothermal heat flow model comparison	131
4.8 Location of geothermal heat flow inferences derived from local data after collection into distinct spatial groups	132
5.1 Australian palaeogeotherms fitted to xenolith P - T data (1 of 2)	150
5.2 Australian palaeogeotherms fitted to xenolith P - T data (2 of 2)	151
5.3 Tomographic shear-wave velocity model FR12	154
5.4 Fit of inverted viscoelasticity parameters to adiabat and Orroroo palaeogeotherm	157
5.5 Fit of inverted viscoelasticity parameters to Australian palaeogeotherms (1 of 2)	159
5.6 Fit of inverted viscoelasticity parameters to Australian palaeogeotherms (2 of 2)	160
5.7 Australian LAB depth inferred from V_S	162
5.8 Investigating the relationship between sediment-hosted base metal deposit location and the transition from thick to thin lithosphere in Australia	163

6.1	Normalised modulus and attenuation as a function of normalised angular frequency, as parameterised by the master curve	183
6.2	Least-squares residual between generalised Maxwell fit and underlying master curve parameterisation, as a function of the number of Maxwell elements (N_M) .	187
6.3	Prony series approximation of $M'_1(\omega')$ and $M'_2(\omega')$, for the master curve parameterisation	188
6.4	Normalised modulus and attenuation as parameterised the pre-melting model .	190
6.5	Contributions towards $\tilde{M}'_1(\omega', \Theta)$ from $\alpha'_i(\Theta)$ as a function of ω'	192
6.6	Prony series approximation of $M'_1(\omega')$ and $M'_2(\omega')$ for the pre-melting parameterisation	195
6.7	Homologous temperature dependence of A_P , σ_P and A_η	200
6.8	Schematic representation of the scaled hyperbolic tangent function	201
6.9	Best-fitting pre-melting functions compared to original functional forms	204
6.10	Fit of pre-melting parameterisations to anelasticity data	206
6.11	Fit of pre-melting parameterisations to viscosity data	208
6.12	Visualising the influence of pre-melting parameter values on $V_S(\omega')$ at fixed temperature	211
6.13	Covariance between posterior distributions of viscoelasticity parameters for the modified pre-melting parameterisation	213
6.14	Assessing fit of inverted viscoelasticity parameters for the modified pre-melting parameterisation	214
6.15	Mean potential temperature difference between original and modified pre-melting parameterisation, $\mu_{\Delta T} = T_{\text{YT16m}}^i - T_{\text{YT16}}^i$	215
6.16	Mean viscosity difference between original and modified pre-melting parameterisation, $\mu_\eta = \eta_{\text{YT16m}}^i - \eta_{\text{YT16}}^i$	216

6.17 Assessing fit of inverted viscoelasticity and pre-melting parameters to geophysical data constraints	222
6.18 Fit of inverted pre-melting parameters constrained via joint inversion approach to anelasticity data	223
6.19 Fit of inverted pre-melting parameters constrained via joint inversion approach to laboratory viscosity data	224
6.20 Best-fitting pre-melting functions compared to original functional forms	225
6.21 Mean potential temperature difference between original and co-inverted pre-melting parameterisation	226
6.22 Mean viscosity difference between original and co-inverted pre-melting parameterisation	227
6.23 Fit of inverted viscoelasticity parameterisation to anelasticity data obtained from experiments on olivine	229
6.24 Love and Shida numbers relevant to Earth surface displacement	246
6.25 GIA induced topography change at the Antarctic Peninsula on a transient Earth	247
6.26 Earth surface displacement and RSL evolution at Marguerite Bay for each ice loading history	248

List of Tables

2.1	Prior and posterior estimates of inverted viscoelasticity parameters	46
2.2	Choice of synthetic model parameters	53
2.3	Comparison of recovered inversion parameters to recent study	59
3.1	Antarctic upper mantle viscosity estimates derived from geodetic observations .	94
4.1	Local-geophysical geothermal heat flow comparison statistics	134
5.1	Localities used to construct Australian palaeogeotherms	145
5.2	Inverted viscoelasticity parameters	157
5.3	Inversion data fit summary statistics	158
6.1	Prior and posterior estimates of the pre-melting parameters	203
6.2	Prior and posterior estimates of the viscoelasticity and pre-melting parameters as constrained via joint inversion	219
6.3	Earth surface displacement and RSL change measures	249

Chapter 1

Introduction

Anthropogenically induced climate change presents society with a myriad of challenges. One such challenge is that oceanic and atmospheric warming threaten melting and collapse of Earth's ice sheets. The Antarctic and Greenland ice sheets contain a volume of ice equivalent to 57.9 ± 0.9 m and 7.42 ± 0.05 m of global mean sea level rise, respectively (Morlighem et al., 2017; Morlighem et al., 2020). Together this corresponds to 99% of global land ice volume, with the rest being made up by glaciers and ice caps (Bamber et al., 2018). While glaciers and ice caps were the dominant land ice contributor to sea level rise during the last century, they have since been overtaken by ice sheet melting (Vaughan et al., 2013).

A climate scenario where global mean surface air temperatures rise to 5°C above preindustrial by 2100, consistent with unchecked greenhouse gas emissions, is expected to cause sea levels to rise in the region of 0.07 m to 1.78 m by the turn of the next century (Bamber et al., 2019). The frequency and intensity of episodic coastal inundation events caused by waves, tides and storm surges are highly sensitive to sea level rise (Oppenheimer et al., 2019b). It has been posited that, without adaptation, global mean sea level rise of 1 m over this period could displace 187 million people living in coastal communities (Nicholls et al., 2011). From an economic perspective, a recent study of coastal flood damage estimates that global gross do-

mestic product could be reduced by as much as 9.3% annually under similar conditions (Hinkel et al., 2014). While significant development of flood protection systems is expected, continued global population growth and limits on adaptive capacity mean that sea level rise represents a significant threat to humanity (Nicholls and Cazenave, 2010). In addition, the loss of ice may disrupt global ocean circulation patterns, marine and coastal ecosystems, and act as a climate feedback via reduced albedo (Vaughan et al., 2013).

Robust prediction of the evolution of the volume and distribution of water over Earth’s surface is thus of vital interest, and requires a reliable assessment of ice sheet stability. To achieve this one requires detailed insight on past ice volumes from the geological record, quantification of present-day ice mass balance, and physically accurate models for the future evolution of the cryosphere (Caron et al., 2018; Debayle et al., 2016; Slanger et al., 2017). Developing an improved understanding of solid Earth structure and dynamics has a key role to play in each of these pursuits. This is because time-dependent lithospheric deflections caused by evolving surface loads and mantle flow alter the elevation of palaeo sea level indicators, the shape of the oceans and gravity field, and the stability of grounded ice (Austermann et al., 2015; Gomez et al., 2018; Mitrovica et al., 2020). Therefore, poor constraints on Earth’s interior structure, and the interaction of Earth’s interior with polar ice sheets, are major impediments to accurate forecasting of future ice volume change for several reasons, which are outlined in Section 1.1 and 1.2. In this thesis, these issues are addressed by leveraging recent observational, theoretical and computational advances to construct state-of-the-art models of Earth’s mantle rheology, and interpret these models in the context of ice sheet stability and sea level change.

1.1 Estimates of Contemporary Ice Mass Balance

Grounded ice sheets acquire mass via snow accumulation, and lose mass via meltwater run off and ice discharge. The balance between these phenomena ultimately determines their time-

dependent ice mass balance (Shepherd et al., 2018a). Estimates of contemporary ice mass balance are therefore crucial to understanding the real-time response of the Antarctic and Greenland ice sheets to ongoing climate forcing, and the corresponding effect on sea level. Such estimates typically rely on satellite missions recording either altimetric or gravimetric data (Shepherd et al., 2018b, 2020; Zwally and Giovinetto, 2011). For example, the Gravity Recovery and Climate Experiment (GRACE) and its successor GRACE Follow-On (GRACE-FO), in principle, offer indirect regional scale insight into ice mass balance via the tracking of temporal changes in Earth’s gravitational field strength (King et al., 2012). However, glacial isostatic adjustment (GIA) also influences the gravity field significantly on decadal timescales. Therefore, the contaminating GIA signal must be removed to accurately estimate ice mass balance.

GIA refers to the viscoelastic response of the solid Earth to changes in the distribution of ice and water over its surface. The spatiotemporally evolving GIA signal is responsible for perturbations to the shape of the solid Earth, the geoid, and Earth’s pole of rotation and rotation rate (Mitrovica and Milne, 2002). For example, consider the melting of an ice sheet. In the near field, a fall in relative sea level (RSL; i.e., the depth of the water column) is observed. This occurs for two reasons. First, Earth’s surface deforms outwards (postglacial rebound), in response to the stress release associated with deglaciation. Second, local ice mass loss reduces the gravitational attraction between nearby seawater and the ice sheet, causing a redistribution of seawater away from the site of melting. In addition, subsidence of the glacial forebulge around the circumference of the former ice sheet draws water away from the far field, in a process known as ocean syphoning (Mitrovica and Milne, 2002). This redistribution, combined with the overall increase in global oceanic water volumes due to melting, causes additional ocean basin subsidence and upwarping of the continent; a process known as continental levering (Mitrovica and Milne, 2002). These transfers of mass over Earth’s surface cause its rotational

state to be perturbed, in turn altering the geoid and exciting further solid Earth deformation (Whitehouse, 2018). Therefore, GIA induces spatial variability in sea level away from the global average upon the addition of meltwater. Since Earth’s mantle behaves viscoelastically, the crustal deformation response contains instantaneous and time-dependent components, such that sea level changes are not only spatially dependent, but evolving in time. Since RSL exerts a significant influence on ice sheet stability, the rate of further melting is GIA-dependent, meaning ice sheet and solid Earth evolution are fundamentally coupled (Gomez et al., 2010).

The Earth is still responding today to deglaciation following the Last Glacial Maximum (ca. 21 ka). For example, in Antarctica, elastically adjusted GPS uplift rates range from -5 mm a^{-1} to 5 mm a^{-1} (Thomas et al., 2011). Therefore, determination of ice mass loss from modern satellite gravity measurements requires accurate knowledge of the present-day amplitude and spatial pattern of this long-term adjustment. However, calculation of the GIA signal requires two main inputs that are weakly constrained; the first being a reconstruction of ice sheet history, and the second a viscoelastic Earth model. Due to the sparsity of ice sheet extent and thickness data, numerical models are used to reconstruct ice sheet histories (Whitehouse, 2018). Such ice models typically assume a one-dimensional solid Earth structure, local sea levels tracking the global average, and limited to no coupling between the solid Earth and ice dynamics. From a viscoelastic Earth model perspective, most GIA models assume a one-dimensional, or a poorly constrained laterally variable, mantle rheology. Each of these limitations introduces significant uncertainty into assessment of present-day ice mass loss.

For example, Caron et al. (2018) used a probabilistic approach to quantify GIA uncertainty introduced into gravity data estimates for Antarctic Ice Sheet mass balance using approximately 10^5 combinations of ice sheet and one-dimensional viscosity models. The authors concluded that the amplitude of the GIA uncertainty was 44% of the total GRACE gravity signal. This is likely to be an underestimate of the true GIA uncertainty, since the aforementioned study does

not account for significant lateral heterogeneity in upper mantle viscosity (e.g., see Barletta et al., 2018), and only accounts for coupling between GIA and ice dynamics via the perturbation to Earth’s rotation axis caused by melt. Therefore, GRACE-derived estimates of ice mass balance are likely even more uncertain than currently assumed.

1.2 Projections of Future Sea Level Change

The quality of projections of future sea level change is heavily reliant on the ability to model GIA as accurately and precisely as possible. Due to the presence of physical couplings between solid Earth and ice dynamics, GIA tells us not only how sea level is affected by ongoing melting of the Greenland and Antarctic ice sheets, but also the reverse. Treatments that ignore such solid Earth feedbacks in their estimation of future sea level are therefore limited (e.g., DeConto and Pollard, 2016). GIA models that do incorporate solid Earth feedbacks will be particularly sensitive to the underlying mantle rheology, which acts as a direct control on viscoelastic deformation rates (Whitehouse, 2018). For example, the presence of low viscosity mantle beneath melting marine-based sectors of the Antarctic Ice Sheet, such as the Amundsen Sea Embayment, may help to delay or even prevent unstable grounding line retreat (Barletta and Bordoni, 2013). This enhanced dependence on knowledge of mantle rheological structure points to the requirement for coupled ice sheet-sea level modelling, incorporating accurate estimates of three-dimensional mantle thermomechanical structure (Gomez et al., 2018). The use of laterally variable mantle structure is important even without consideration of solid Earth-ice sheet coupling. Recent tests show that the difference in RSL predictions for 2100 CE between best-fitting one-dimensional and three-dimensional Earth models is as large in amplitude as the one-dimensional RSL signal itself (Milne et al., 2021). Therefore, accurate quantification of Earth’s thermomechanical structure is critical for the construction of reliable sea level projections.

1.3 Recent Advances

In this thesis, four recent advances are used to address the outstanding challenges in understanding solid Earth-cryosphere interactions outlined above. First, a huge increase in the availability and quality of seismic data has been enabled by expanded seismic array deployment. Concurrently, sophisticated tomographic inversion methods have been developed, allowing images of Earth's three-dimensional seismic structure to be determined. These developments enable shear-wave velocity (V_S) structure to be mapped globally at sub- 1° resolution (Schaeffer and Lebedev, 2013). On a regional scale, even higher resolutions are possible, e.g. allowing ~ 100 km features beneath Antarctica to be constrained (Lloyd et al., 2020). In addition, the presence of polar geophysical and geochemical data, such as GPS-derived viscosity inferences and xenolith-derived palaeogeothermal profiles, allows reliable benchmarking of predictions made from seismic data (Barletta et al., 2018; Hoggard et al., 2020; Klöcking et al., 2020).

Second, development of experimental parameterisations of mantle rock viscoelasticity enables self-consistent conversion between seismic velocity and thermodynamic parameters including temperature, density and viscosity (Takei, 2017; Yamauchi and Takei, 2016). These are key inputs for geodynamic simulations. Third, advances in inverse theory including key developments in algorithmic implementation enable robust exploration of the parameter spaces needed to constrain geophysical problems (Andrieu and Thoms, 2008; Eilon et al., 2018; Fukuda and Johnson, 2010; Gelman et al., 1997; Haario et al., 2001; Roy, 2020). In particular, taking a probabilistic approach toward parameter inversion allows formal uncertainty quantification. These advances allow laboratory derived parameterisations of mantle rock viscoelasticity to be reliably calibrated against independent geophysical data. Finally, improved understanding of the interaction between solid Earth deformation and ice sheet dynamics is reflected in the development of advanced numerical modelling techniques for GIA (Whitehouse, 2018). For example, dynamic ice sheet reconstructions interacting with a three-dimensional solid Earth are

under development for use in GIA studies (Gomez et al., 2018). In addition, time-dependent variations in apparent mantle viscosity are implied by the latest parameterisations of mantle rock viscoelasticity (Qu et al., 2021; Yamauchi and Takei, 2016). Such variations influence the timescale and character of Earth’s viscoelastic deformation response to surface loading changes. Theoretical frameworks for incorporating this so-called transient rheology into GIA models have recently been developed, and serve as the basis for investigating relationships between transient rheology, ice sheet stability and sea level change (Lau, 2024).

1.4 Chapter Overview

Chapter 2 concerns the exploitation of seismic data as a geophysical proxy for mantle thermomechanical structure. Earthquake-generated shear waves, detected at Earth’s surface, are sensitive to the thermal state of the mantle material they are transmitted through, via measurable properties such as wave speed and attenuation. Previously, empirical parameterisations with a number of limitations have been used to relate V_S anomalies to changes in mantle temperature (T). By replacing empirical parameterisations with experimental parameterisations of mantle rock viscoelasticity, accurate V_S-T conversions are facilitated (Richards et al., 2020a; Yamauchi and Takei, 2016). Such laboratory-derived parameterisations incorporate polycrystalline anelasticity, a form of time-dependent but fully recoverable deformation, which causes a significant reduction in V_S at near-solidus temperatures. In this chapter, a Bayesian inversion approach is adopted, enabling the use of independent geophysical data constraints to calibrate the V_S-T relationship. The use of a Bayesian framework for tackling the problem allows for rigorous uncertainty quantification. A posterior ensemble of models can be used to convert V_S into estimates of mantle thermomechanical structure, with associated uncertainties.

In Chapter 3, the inverse framework developed in Chapter 2 is applied to Antarctica. The recently developed high-resolution Antarctic tomographic velocity model **ANT-20** of Lloyd et al.

(2020) is exploited, alongside four geophysical constraints pertaining to mantle structure within the spatial footprint of the seismic data. The main constraint is a regionally optimised model of age-dependent oceanic lithospheric thermal evolution. In this model, mantle potential temperature, plate thickness and zero-age ridge depth are treated as free parameters to be fitted against regional age-depth and age-heat flow data. The resultant best-fitting structure is used to constrain the relationship between V_S and T between 50 km and 125 km depth. This constraint is complemented by an adiabatic profile used to estimate mean asthenospheric temperatures, a radial profile of seismic shear-wave attenuation, and an estimate of average asthenospheric shear viscosity. Application of the inversion approach enables estimation of Antarctic thermomechanical structure, including mantle diffusion creep viscosity, lithosphere-asthenosphere boundary (LAB) depth, and geothermal heat flow (GHF). Viscosity and lithospheric thickness are first order controls on GIA and resulting inferences of ice sheet stability. Meanwhile, ice sheet model predictions also depend on accurate maps of heat flow. Therefore, the estimates provided can be used to improve understanding of past, present and future sea level. Furthermore, the issue of time-dependent apparent viscosity is applied, in order to reconcile seemingly discrepant predictions of Antarctic mantle viscosity derived from GPS observations of GIA-related deformation. It is shown that anomalously low viscosity inferences from West Antarctica (e.g., 4×10^{18} Pas in Amundsen Sea Embayment, see Barletta et al., 2018), are biased low by up to ~ 1 order of magnitude due to the assumption of Maxwell rheology.

Chapter 4 tackles the issue of GHF in more depth. This parameter quantifies the supply of thermal energy from the solid Earth into the base of an ice sheet. Geothermal heat flow is a key component of the thermal boundary conditions of an ice sheet, influencing melt rates and ultimately ice sheet stability. In Antarctica, heat flow varies from values as low as $\sim 20 \text{ mW m}^{-2}$, to as high as $\sim 130 \text{ mW m}^{-2}$. In order to model future ice sheet evolution, an accurate model of the spatial pattern of such heat flow variations is required. In Chapter 4,

shear- and compressional-wave velocities are combined to provide sensitivity to the thermal and compositional structure of Antarctic lithosphere. Crustal conductivity, radiogenic heat production, and GHF are co-constrained as part of a novel modelling framework. The resulting heat flow estimates are compared to previous studies, and local borehole data. Incorporating lateral variations in crustal composition is shown to improve agreement with available heat flow measurements.

In Chapter 5, attention is turned to Australia, where robust quantification of lithospheric and asthenospheric thermal structure is pertinent to a range of human-related issues, including the sea level focus maintained in Chapters 2–4. Completed as part of Geoscience Australia’s Exploring for the Future research program, the probabilistic framework developed for mapping mantle structure in Chapter 2 is extended to allow the use of pressure-temperature constraints derived from xenolith thermobarometry. Hyperparameters built into the Bayesian inversion are used to objectively weight individual xenolith-derived palaeogeotherms based on their reliability. An updated inventory of xenolith constraints is used to construct high-resolution models of Australian mantle temperature structure and LAB depth, with rigorously quantified uncertainty. Such models are important inputs for reconstructions of past sea level based on palaeoshoreline indicators, whose elevation requires correction for topographic changes due to GIA and dynamic topography (Richards et al., 2023). The LAB depth maps are of significant economic value, since the transition between thick and thin lithosphere on the edge of cratons was recently shown to be strongly correlated with base metal prospectivity (Hoggard et al., 2020). Base metals and subsidiary metals they co-occur with, such as cobalt and indium, are key ingredients of many technologies that are required for an economy based on renewable energy, making a sustainable supply of such metals integral to the green transition. Correlations between previously identified deposit locations and estimated LAB depth are used to constrain the 195 km LAB depth contour as the most powerful indicator of deposit location.

Finally, Chapter 6 returns to Antarctica, and an exploration of the relationship between time-dependent rheology, ice sheet stability, and sea level. A blueprint for the implementation of experimental parameterisations of mantle rock viscoelasticity into continuum mechanics models is developed. This provides the basis for incorporating spatial and temporal variations in mantle viscosity into future GIA models. Designed to accompany such models, a revised parameterisation of mantle rock viscoelasticity is developed. This parameterisation is fitted to the laboratory data of Yamauchi and Takei (2016), and includes a set of functions which are computationally efficient to calculate. These steps ensure that any such GIA implementation is faithful to the most recent data pertaining to mantle rock deformation behaviour, and is computationally feasible. In order to estimate the importance of time-dependent viscosity in affecting ice sheet stability and sea level, the revised parameterisation is applied to a simple model of Antarctic GIA. It is demonstrated that, for short ice melting timescales, up to 52% more near-field deformation is induced by the time-dependent rheological model, as compared to a reference Maxwell viscoelastic model. The results have important implications for studies seeking to invert deformation observations (e.g., sea level and GPS records) for estimates of mantle structure, as well as those seeking to model future sea level in response to possible deglaciation scenarios.

Chapter 2

A Bayesian Inverse Method for Calibrating Experimental Parameterisations of Mantle Rock Viscoelasticity

2.1 Introduction

Earth's interior thermomechanical structure controls spatial and temporal patterns of deformation on its surface. For example, three-dimensional variations in mantle temperature dictate the location of density anomalies, driving viscous mantle convection behaviour over timescales of millions of years. Variations in lithospheric thickness, mantle viscosity and elastic modulus govern viscoelastic deformation in response to events altering surface loading, such as glacial collapse, over timescales spanning 10 to 10,000 years. Therefore, accurate models of Earth's mantle structure are critical for a variety of geodynamic modelling applications. Since it is not possible to directly access and observe Earth's interior, its structure must be inferred via

geophysical proxy. In this context, a geophysical proxy is a class of information produced by some geophysical phenomenon, and detectable from Earth’s exterior, which contains sensitivity to its interior structure. A range of useful proxies can be extracted from seismic data, including phase velocity, attenuation, and anisotropy.

Images of how seismic shear-wave velocity (V_S) varies from location to location within Earth’s interior, obtained by seismic tomography, are a powerful tool for estimating mantle thermal structure due to the strong sensitivity of V_S to temperature (Faul and Jackson, 2005). Laboratory experiments show sub-solidus temperature changes can induce up to 20% variations in V_S (Priestley and McKenzie, 2013, and references therein). Although volatiles and composition may also influence V_S (Karato and Jung, 1998; Lee, 2003), recent studies show close agreement between xenolith-derived temperature profiles and those inferred from tomographic models using parameterisations that ignore the potential impact of compositional heterogeneity in the asthenosphere and lower lithosphere, indicating that temperature is indeed the dominant control on shallow mantle V_S variation (Hoggard et al., 2020; Klöcking et al., 2020). Temperature- and pressure-dependent parameterisations of mantle density and viscosity can be applied to estimate how spatial variations in temperature translate into mechanical properties. Therefore, maps of three-dimensional V_S structure can be used to infer mantle structure given a suitable modelling framework, which the purpose of this chapter is to introduce.

Firstly, theoretical relationships between V_S and output parameters such as temperature, T , and viscosity, η , are discussed. It is shown why relationships grounded in laboratory observations are needed to accurately relate seismic observations to mantle structure. Secondly, a set of unknown parameters required for conversion between V_S and T is introduced. The presence of these unknown parameters motivate the use of an inverse modelling framework, incorporating additional geophysical constraints, in order to produce a self-consistent set of output predictions. Thirdly, a probabilistic implementation of the inverse theory is presented,

which allows uncertainty in the output predictions to be estimated via a robust characterisation of free parameter covariances.

2.2 Parameterising The Relationship Between V_S and T

The sensitivity of V_S to temperature derives from the effect temperature has on the mechanical properties of mantle rock, which in turn control the characteristics of shear-wave propagation. Therefore, in order to make use of V_S information and gain insight into upper mantle structure, a model capturing this sensitivity must be employed.

2.2.1 Empirical Parameterisations

In the past, most studies took advantage of an empirical approach for converting between V_S and temperature, viscosity and density (e.g., Austermann et al., 2013; Davies et al., 2019; Milne et al., 2018; Steinberger et al., 2019). For example, the following prescription was used by Austermann et al. (2013):

$$\delta \ln \rho(r, \theta, \varphi) = \Delta_{V_S}^\rho(r) \delta \ln V_S(r, \theta, \varphi), \quad (2.1)$$

$$\delta T(r, \theta, \varphi) = -\frac{1}{\alpha(r)} \delta \ln \rho(r, \theta, \varphi), \quad (2.2)$$

$$\eta(r, \theta, \varphi) = \eta_r(r) e^{-\epsilon \delta T(r, \theta, \varphi)}. \quad (2.3)$$

In these equations, the vector (r, θ, φ) represents a location within Earth's interior, specified in terms of radius, latitude and longitude, respectively. V_S is the shear-wave velocity, and ρ , T and η are the density, temperature and viscosity, respectively. $\alpha(r)$ is the coefficient of thermal

expansion. $\Delta_{V_S}^\rho(r)$ is a temperature-independent scaling factor connecting relative changes in V_S to relative changes in density, and ϵ is a free parameter controlling the sensitivity of viscosity to changes in temperature. Combining Equations 2.1 and 2.2, a direct mapping between V_S and temperature is obtained.

$$\delta T(r, \theta, \varphi) = -\frac{\Delta_{V_S}^\rho(r)}{\alpha(r)} \delta \ln V_S(r, \theta, \varphi). \quad (2.4)$$

Given that V_S and T within Earth's interior are inversely proportional, it can be inferred from Equation 2.4 that the scaling factor $\Delta_{V_S}^\rho(r)$ is a positive quantity. The sign of $\Delta_{V_S}^\rho(r)$ appears innocuous until the mechanics of wave propagation in a viscoelastic medium are considered, in which transverse wave velocity and density are inversely proportional, $V_S \propto \rho^{-\frac{1}{2}}$. Therefore, if $\Delta_{V_S}^\rho(r)$ is representative of the expression

$$\frac{\partial \rho}{\partial V_S} \propto -\rho^{\frac{3}{2}}, \quad (2.5)$$

and indeed $\frac{\partial \rho}{\partial V_S}$ is often used as the symbolic reference to the scaling factor, it appears that $\Delta_{V_S}^\rho(r)$ should be a negative quantity. To resolve this apparent disagreement, it must be understood that temperature-induced changes in shear-wave velocity do not occur at constant shear modulus, M_U . The quantity $\Delta_{V_S}^\rho(r)$ implicitly captures variation in V_S due to changes in both ρ and M_U , for a given temperature-induced change in density.

Although such empirical scalings obscure the mechanics underlying V_S-T sensitivity, this does not necessarily mean that they are unable to relate velocities obtained from seismic tomography to mantle thermal structure. However, $\Delta_{V_S}^\rho(r)$ inherently assumes that at a given depth, a percentage change in V_S corresponds to a constant percentage change in ρ and T , irrespective of the initial V_S prior to perturbation. In fact, significant viscosity reductions observed near the solidus temperature in laboratory experiments on mantle rock and associated analogues (Faul

et al., 2007; McCarthy and Takei, 2011; Takei, 2017; Yabe and Hiraga, 2020), and corroborated by geophysical observations (Richards et al., 2020a), indicate that the relationship between V_S and T is highly non-linear. Empirical scalings such as that presented above fail to appropriately capture this relationship, and therefore inaccurately relate V_S to mantle structure.

2.2.2 Laboratory Parameterisations

In order to accurately relate V_S to T , empirical scalings are avoided, and instead the physical parameterisation of Yamauchi and Takei (2016) is employed, which captures the underlying temperature-dependent viscoelastic behaviour of mantle rock based on a series of forced oscillation experiments. Such experiments were conducted using a polycrystal analogue of the olivine-basalt system called borneol-diphenylamine. The fundamental assumption of Yamauchi and Takei (2016) is that, to within a set of material-specific scalars, the phenomenological behaviour of mantle rock and the synthesised rock analogue under mechanical testing is the same. This is likely to be a valid assumption because borneol and diphenylamine form a binary eutectic system with an equilibrium microstructure similar to that of olivine and basalt, and borneol is known to deform via the same types of diffusion and dislocation creep processes as minerals (Yamauchi and Takei, 2016). Since borneol has a much smaller melting temperature than mantle rock, experiments conducted by Yamauchi and Takei (2016) at room temperature tap into the same normalised frequency range as seismic waves at the near-solidus temperature conditions relevant to the upper mantle. Crucially, this makes their findings relevant to studies of the upper mantle as imaged by seismic waves. Yamauchi and Takei (2016) were able to attribute significant non-linearity in the $V_S(T)$ relationship at homologous temperatures $0.92 \leq T/T_S \leq 1$ to the effect of pre-melting, a process which enhances diffusionaly accommodated grain boundary sliding and high-frequency seismic attenuation.

Forced oscillation experiments involve applying a sinusoidal-in-time stress $\sigma(t) = \text{Re} [\sigma^*(t)]$

to the material in the form of

$$\sigma^*(t) = \sigma_0 \exp(-i\omega t), \quad (2.6)$$

and measuring the associated strain response $\varepsilon(t) = \text{Re} [\varepsilon^*(t)]$, where

$$\varepsilon^*(t) = J^*(\omega)\sigma^*(t). \quad (2.7)$$

In Equation 2.6, σ_0 is the magnitude of the applied stress, $i = \sqrt{-1}$, ω is the angular frequency of the applied oscillatory stress, and t refers to elapsed time. In Equation 2.7, $J^*(\omega) = J_1 + iJ_2$ is known as the complex compliance. $J^*(\omega)$ encodes the frequency- and thermal state-dependent viscoelastic properties of the material under testing, which determine its time-dependent response to loading. Expanding the right-hand-side of Equation 2.7 in terms of real and imaginary components of $J^*(\omega)$, the strain response can be expressed as

$$\varepsilon(t) = \text{Re} [(J_1 + iJ_2)\sigma_0 \exp(-i\omega t)], \quad (2.8)$$

$$\Rightarrow \varepsilon(t) = J_1\sigma_0 \cos(\omega t) + J_2\sigma_0 \sin(\omega t). \quad (2.9)$$

An equivalent representation of Equation 2.9 can be found using a compound-angle trigonometric expansion as follows

$$\varepsilon(t) = \varepsilon_0 \cos(\omega t + \phi), \quad (2.10)$$

$$\Rightarrow \varepsilon(t) = \varepsilon_0 \cos(\phi) \cos(\omega t) - \varepsilon_0 \sin(\phi) \sin(\omega t). \quad (2.11)$$

Therefore, the strain response is sinusoidal-in-time, like the applied stress, but with a modified amplitude and phase. By comparison with Equation 2.9, some useful relations between the

complex compliance terms and the form of the strain response can be established:

$$J_1 = \frac{\varepsilon_0}{\sigma_0} \cos(\phi), \quad (2.12)$$

$$J_2 = -\frac{\varepsilon_0}{\sigma_0} \sin(\phi). \quad (2.13)$$

These equations show that by measuring the relative amplitude of the strain response, ε_0/σ_0 , and its phase delay with respect to the applied stress, ϕ , J_1 and J_2 at a temperature and frequency of interest can be calculated, and indeed these principles are applied by Yamauchi and Takei (2016) in their experiments.

To build further intuition for the components of $J^*(\omega)$, consider again Equation 2.9. The real component of the complex compliance, $J_1 = \text{Re}[J^*]$, is a multiplicative prefactor of the cosine component of the strain response, which is in-phase with the applied stress. The imaginary component of the complex compliance, $J_2 = \text{Im}[J^*]$, is a prefactor of the sine component of the response, which is out-of-phase with the applied stress. Calculating the work done during each oscillatory cycle of applied stress,

$$E_d = \oint \sigma d\varepsilon = \int_0^{2\pi/\omega} \sigma \frac{d\varepsilon}{dt} dt, \quad (2.14)$$

it can be found that

$$E_d = \int_0^{2\pi/\omega} \sigma_0 \cos(\omega t) \frac{d}{dt} (J_1 \sigma_0 \cos(\omega t) - J_2 \sigma_0 \sin(\omega t)) dt, \quad (2.15)$$

$$\Rightarrow E_d = \omega \sigma_0^2 \int_0^{2\pi/\omega} (-J_1 \cos(\omega t) \sin(\omega t) - J_2 \cos(\omega t) \cos(\omega t)) dt, \quad (2.16)$$

$$\Rightarrow E_d = \pi\sigma_0^2(0 \cdot J_1 + 1 \cdot J_2) = \pi\sigma_0^2 J_2. \quad (2.17)$$

Therefore the out-of-phase compliance term, J_2 , is responsible for energy dissipation. It can be shown that the maximum energy stored within each cycle is given by $E_S = \frac{1}{2}\sigma_0^2 J_1$, and thus that the in-phase compliance term, J_1 , is responsible for energy storage (Nowick and Berry, 1972). These two components of the complex compliance are referred to as the loss compliance and storage compliance, respectively. Conveniently, both shear-wave velocity, V_S , and attenuation, Q^{-1} , can be expressed directly in terms of the loss and storage compliance,

$$V_S = \frac{1}{\sqrt{\rho J_1}} \left[\frac{1 + \sqrt{1 + (J_2/J_1)^2}}{2} \right]^{-\frac{1}{2}} \approx \frac{1}{\sqrt{\rho J_1}}, \quad (2.18)$$

$$Q^{-1} = \frac{J_2}{J_1} \left[\frac{1 + \sqrt{1 + (J_2/J_1)^2}}{2} \right]^{-\frac{1}{2}} \approx \frac{J_2}{J_1}, \quad (2.19)$$

where ρ is the density of the medium (McCarthy and Takei, 2011). A parameterisation of complex compliance in terms of temperature, pressure and forcing frequency was constructed by Yamauchi and Takei (2016) on the basis of their laboratory data as follows

$$J_1 = J_U \left(1 + \frac{A_B \tau_S^{\alpha_B}}{\alpha_B} + \frac{\sqrt{2\pi}}{2} A_P \sigma_P \left(1 - \text{erf} \left[\frac{\ln(\tau_P/\tau_S)}{\sqrt{2}\sigma_P} \right] \right) \right), \quad (2.20)$$

$$J_2 = J_U \left(\tau_S + \frac{\pi A_B \tau_S^{\alpha_B}}{2\alpha_B} + \frac{\pi}{2} A_P \exp \left[\frac{-\ln^2(\tau_P/\tau_S)}{\sqrt{2}\sigma_P} \right] \right), \quad (2.21)$$

where J_U is the unrelaxed compliance, which serves as the infinite-frequency (elastic) limit of the complex compliance and is inversely related to the unrelaxed shear modulus by $J_U = 1/M_U$. $A_B = 0.664$ and $\alpha_B = 0.38$ are the amplitude and slope of the high-temperature background relaxation, and A_P and σ_P are the temperature-dependent amplitude and width of a high-

frequency relaxation peak, defined by

$$A_P(\Theta) = \begin{cases} 0.01 & \text{if } \Theta < 0.91, \\ 0.01 + 0.4(\Theta - 0.91) & \text{if } 0.91 \leq \Theta < 0.96, \\ 0.03 & \text{if } 0.96 \leq \Theta < 1, \\ 0.03 + \beta(\phi) & \text{if } \Theta \geq 1, \end{cases} \quad (2.22)$$

and

$$\sigma_P(\Theta) = \begin{cases} 4 & \text{if } \Theta < 0.92, \\ 4 + 37.5(\Theta - 0.92) & \text{if } 0.92 \leq \Theta < 1, \\ 7 & \text{if } \Theta \geq 1, \end{cases} \quad (2.23)$$

where $\Theta = T/T_S$ is the homologous temperature, T is the temperature, T_S is the solidus temperature, ϕ is the melt fraction and $\beta(\phi)$ is the direct poroelastic effect of melt. The factor $\beta(\phi)$ can be ignored for upper mantle applications in which melt retention is expected to be low enough that $\beta(\phi)$ has negligible impact (McKenzie, 2000; Richards et al., 2020a).

In Equations 2.20 and 2.21, $\tau_P = 6 \times 10^{-5}$ is a constant, representative of the experimentally determined centroid timescale of the high-frequency relaxation peak. τ_S represents the seismic wave period, normalised by $2\pi\tau_M$, in which $\tau_M = \eta J_U$ is the Maxwell relaxation timescale, and η is the shear viscosity given by

$$\eta = \eta_r \left(\frac{d}{d_r} \right)^m A_\eta(\Theta) \exp \left[\frac{E_A}{R} \left(\frac{1}{T} - \frac{1}{T_r} \right) \right] \exp \left[\frac{V_A}{R} \left(\frac{P}{T} - \frac{P_r}{T_r} \right) \right], \quad (2.24)$$

where $\eta_r = \eta(d = d_r, T = T_r, P = P_r)$ is the reference viscosity at reference temperature (T_r), pressure (P_r) and grain size (d_r), m is the grain size exponent, E_A activation energy, V_A activation volume, and $R = 8.3145 \text{ J K}^{-1} \text{ mol}^{-1}$ is the molar gas constant. A_η is a homologous-

temperature dependent factor, similar to A_P and σ_P , incorporating the extra reduction in viscosity just below the solidus temperature caused by pre-melting, defined as

$$A_\eta(\Theta) = \begin{cases} 1 & \text{if } \Theta < \Theta^\eta, \\ \exp\left[-\frac{\Theta-\Theta^\eta}{\Theta-\Theta^\eta} \ln \gamma\right] & \text{if } \Theta^\eta \leq \Theta < 1, \\ \gamma^{-1} \exp(-\gamma\phi) & \text{if } \Theta \geq 1, \end{cases} \quad (2.25)$$

where $\gamma (\geq 1)$ represents the factor of additional viscosity reduction and Θ^η is the normalised temperature above which pre-melting enhances the activation energy E_A by ΔE_A . As with A_P and σ_P , the influence of melt is ignored and therefore $A_\eta = \gamma^{-1}$ at super-solidus temperatures, $\Theta \geq 1$.

2.3 Inverse Approach to Conversion Between Upper Mantle V_S and T

Application of the complex compliance parameterisation of Yamauchi and Takei (2016) in principle allows for conversion from temperature to V_S and Q^{-1} via J^* , as well as vice versa, using Equations 2.18 and 2.19, but is dependent on four additional assumptions. Firstly, a parameterisation of upper mantle density must be selected, $\rho = \rho(P, T)$, for which the approach of Grose and Afonso (2013) is followed. Temperature-dependent expansivity is incorporated using the linear relationship

$$\alpha(T) = \alpha_0 + \alpha_1 T, \quad (2.26)$$

where $\alpha_0 = 2.832 \times 10^{-5} \text{ K}^{-1}$ and $\alpha_1 = 0.758 \times 10^{-8} \text{ K}^{-2}$. The effect of pressure on thermal expansivity is incorporated using the following form

$$\frac{\alpha(P, T)}{\alpha(T)} = \left(\frac{V_0}{V} \right)_T \exp \left[(\delta_T + 1) \left(\left(\frac{V_0}{V} \right)_T^{-1} - 1 \right) \right], \quad (2.27)$$

where $\delta_T = 6$ is the Anderson-Grüneisen parameter. The direct effect of pressure on density is incorporated by calculating the isothermal volume change, $(V_0/V)_T$, associated with a given pressure using the third-order Birch-Murnaghan equation of state

$$P = \frac{3}{2} K_0 \left[\left(\frac{V_0}{V} \right)_T^{7/3} - \left(\frac{V_0}{V} \right)_T^{5/3} \right] \left[1 + \frac{3}{4} \left(\frac{\partial K}{\partial P} \right)_T \left(\left(\frac{V_0}{V} \right)_T^{2/3} - 1 \right) \right], \quad (2.28)$$

where $K_0 = 130 \text{ GPa}$ is the bulk modulus at zero pressure and $(\partial K / \partial P)_T = 4.8$ is the pressure derivative of the bulk modulus at constant temperature. The isothermal density change associated with $(V_0/V)_T$ is then

$$\rho(P) = \rho_0 \left(\frac{V_0}{V} \right)_T. \quad (2.29)$$

Combining both temperature and pressure dependencies, the complete parameterisation is given by

$$\rho(P, T) = \rho(P) \left[1 - \frac{\alpha(P, T)}{\alpha(T)} \left(\alpha_0(T - T_0) + \frac{\alpha_1}{2}(T^2 - T_0^2) \right) \right], \quad (2.30)$$

where surface temperature $T_0 = 273 \text{ K}$.

Secondly, the unrelaxed shear modulus must be parameterised, for which the following linear relationship is assumed

$$M_U(P, T) = \mu_0 + \frac{\partial \mu}{\partial T}(T - T_0) + \frac{\partial \mu}{\partial P}(P - P_0), \quad (2.31)$$

where μ_0 is referenced to surface temperature $T_0 = 273\text{ K}$ and pressure $P_0 = 101\text{ kPa}$, and all three of μ_0 , $\partial\mu/\partial T$ and $\partial\mu/\partial P$ are constants.

Thirdly, the depth-dependent solidus temperature within the upper mantle must be parameterised, in order to be able to relate homologous temperatures provided in the compliance parameterisation of Yamauchi and Takei (2016) to absolute temperatures. To do so, the linear relationship

$$T_S(z) = T_S(z_0) + \frac{\partial T_S}{\partial z}(z - z_0) \quad (2.32)$$

is employed, where $T_S(z_0)$ represents the reference solidus temperature at $z_0 = 50\text{ km}$ depth. Finally, suitable values for the free parameters contained within the complex compliance framework must be selected. These free parameters are sevenfold: μ_0 , $\partial\mu/\partial T$, $\partial\mu/\partial P$ regulate the instantaneous, elastic component of the deformation response, meanwhile η_r , E_A , V_A and $\frac{\partial T_S}{\partial z}$, control the time-dependent anelastic (fully recoverable) and viscous contribution. Together, these parameters are referred to as “viscoelasticity parameters”.

The viscoelasticity parameters cannot be constrained directly from the laboratory data of Yamauchi and Takei (2016), since the former apply specifically to the upper mantle. A forward-modelling approach is typically taken to estimate them, by combining an assumed mantle composition with a computational Gibbs free energy minimisation technique to estimate μ_0 , $\partial\mu/\partial T$, and $\partial\mu/\partial P$, and using these values to calculate the elastic component of $V_S(P, T)$. A correction for anelasticity is then applied using values of η_r , E_A , V_A , $T_S(z_0)$ and $\frac{\partial T_S}{\partial z}$ compiled from laboratory-based experiments on mantle minerals. There are two key drawbacks to this method. The first is that applying experimentally determined parameter values to mantle conditions requires extrapolation of grain size-dependent behaviour across several orders of magnitude, the validity of which remains unclear. The second is that discrepancies between tomographic velocity models are introduced by subjective choices such as regularisation, model parameterisation and choice of reference model (Richards et al., 2020a). The

forward approach then becomes problematic as, for a constant choice of viscoelasticity parameters, highly discrepant physical predictions are generated depending on the chosen velocity model, as modelling choices particular to a given tomographic model are propagated.

To tackle these issues and ensure a conversion consistent with geophysical data pertaining to the region of interest, the viscoelasticity parameter space is instead calibrated against a suite of regional temperature, attenuation and viscosity constraints (Priestley and McKenzie, 2006, 2013; Richards et al., 2020a). A regional calibration is preferred to using viscoelasticity parameters obtained from a global study, since the former approach ensures consistency with the chosen tomographic velocity model. Calibration can be achieved within the framework of a Bayesian inversion, incorporating stochastic sampling to characterise the model space. The set of samples obtained can then be used to propagate uncertainties in the viscoelasticity parameters into formally quantified uncertainties in the resulting rheological model. Two additional sources of uncertainty are not directly modelled in this process. The first is tomographic uncertainty, which is ignored when converting velocities into thermomechanical parameter estimates. This uncertainty is partially mitigated by the calibration procedure, which ensures that V_S values from the chosen velocity model are consistent with independent geophysical constraints on upper mantle structure. The second is a phenomenological source of uncertainty, deriving from the assumption that the parameterisation of Yamauchi and Takei (2016) is an accurate representation of upper mantle viscoelasticity. This assumption is investigated in more detail in Chapter 6. It should be noted that the inverse modelling framework developed herein is designed to be equally applicable to any choice of parameterisation. Readers interested in the extent to which different rheological parameterisations agree within the context of Antarctic upper mantle structure are invited to view the work of Ivins et al. (2021).

2.3.1 Independent Geophysical Data Sets

For the purposes of demonstrating the viscoelasticity parameter calibration procedure, Antarctica will be used as the region of interest. The tomographic velocity model **ANT-20** (Lloyd et al., 2020) will be employed, which provides estimates of $V_S = V_S(r, \theta, \varphi)$ with regional-scale resolution (~ 100 km), and thus serves as a suitable starting point for mapping upper mantle temperature and viscosity. Further detail on Antarctica as a choice of setting, as well as the tomographic velocity model **ANT-20**, is provided in Chapter 3. Independent constraints on mantle properties are collated and used as data sets in a joint inversion of the viscoelasticity parameters. These data are complementary in that they are collected over a range of depths (0 km to 400 km) and temperatures (0 °C to 1500 °C), and help to tackle the issue of non-uniqueness via their different sensitivities to a given change in the parameter space.

The first constraint used is the observed $V_S(T)$ relationship in conductively cooling oceanic lithosphere. V_S data from a tomographic model may be compared to thermal structure obtained via numerical modelling when binned by age and depth (Richards et al., 2020a). The 15 km maximum vertical resolution of **ANT-20** informs the decision to sample V_S and T data points in 25 km bins over the range 50 to 125 km. This depth range is chosen to avoid non-negligible compositional effects at shallow depths due to mantle melting and the potential incorporation of spurious low velocity structure resulting from the bleeding of crustal velocities down into deeper depth ranges.

To construct a suitable thermal model for Antarctica, a Crank-Nicholson finite difference scheme with a predictor-corrector step is used to numerically integrate the heat diffusion equation. The implementation set out by Richards et al. (2018) and Richards et al. (2020b) is followed, in which the heat capacity, C_P , mantle density, ρ , and thermal conductivity, k , vary as a function of temperature, T , and composition, X . The latter two variables are also dependent on pressure, P .

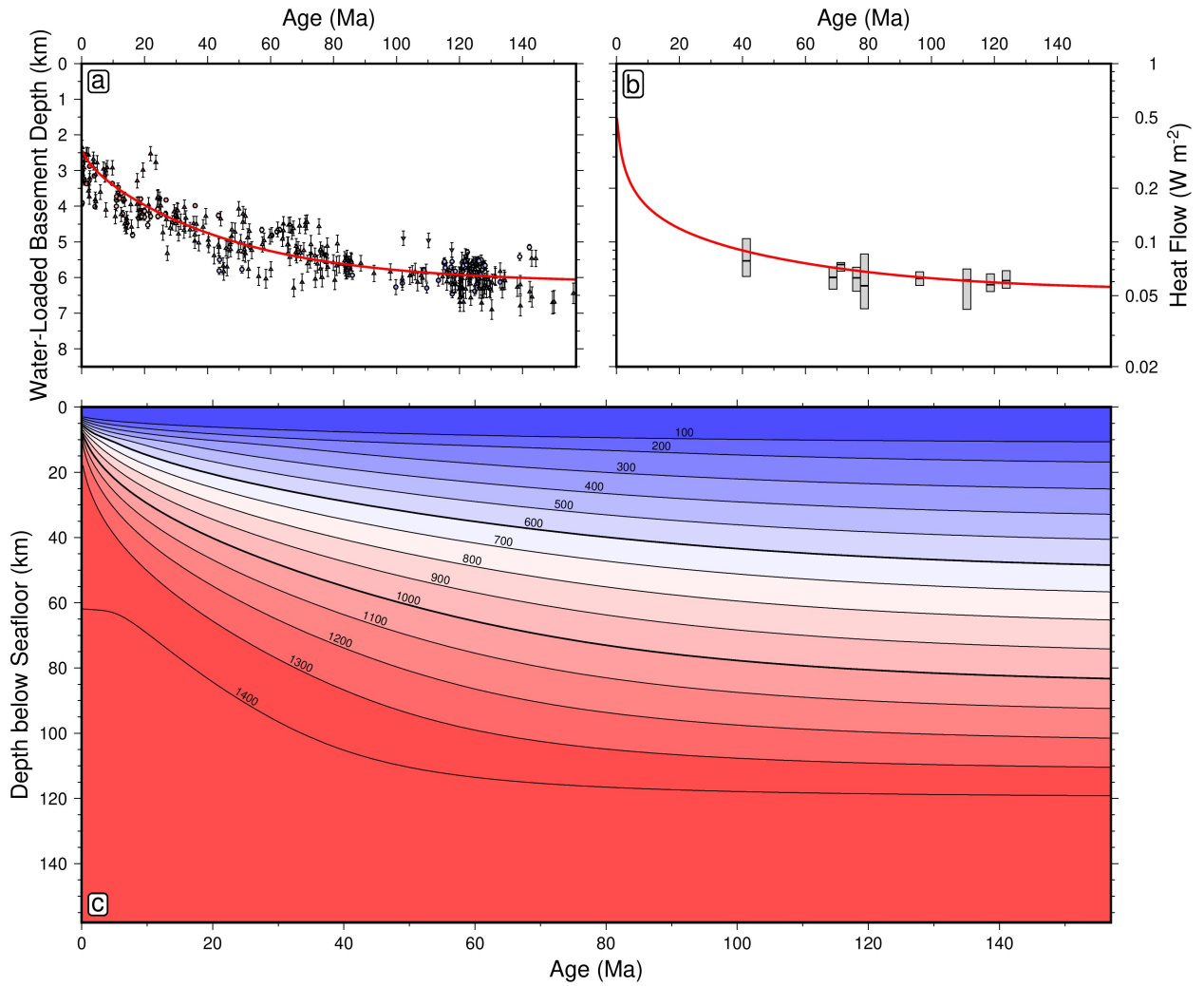


Figure 2.1: Thermal modelling of Antarctic oceanic lithosphere. (a) Thermal model fit to oceanic age-depth data from the Antarctic oceanic region placed into 2.5 Ma bins (Richards et al., 2018). (b) Same as (a) for age-heat flow data (Richards et al., 2018). (c) Plate cooling model solution constructed using a Crank-Nicholson finite-difference scheme to numerically solve the 1-D heat-diffusion equation (Richards et al., 2018; Richards et al., 2020b). Antarctica-specific regional data are used to capture any local deviation from the globally averaged thermal trend. Model isotherms ($^{\circ}\text{C}$) given by black curves in panel (c).

Mantle potential temperature, plate thickness and zero-age ridge depth are optimised by assessing the misfit to heat flux and subsidence data located within the footprint of the **ANT-20** seismic tomographic model. The result is a best-fitting model describing the thermal structure beneath the oceans surrounding Antarctica (see Figure 2.1), suitable for comparison with V_S measurements over the same age-depth bins, such that the regional oceanic $V_S(T)$ relationship can be obtained for the lithosphere. A mantle potential temperature of $T_P = 1420 \pm 50$ °C is estimated, approximately 5% hotter than the geochemically constrained global average $T_P = 1333$ °C (Richards et al., 2018). The regional best-fitting value of $T_P = 1420$ °C is consistent with regional geochemical estimates of mantle potential temperature, which span the range 1314-1550 °C, with an average 1385 ± 40 °C (Figure 3.1). Although these constraints are only available along the circum-Antarctic ridge system, they are nevertheless indicative of anomalously hot mantle beneath the Southern Ocean. In the inversion, V_S measurements are compared to inferences of V_S from temperature at each age-depth bin (Figure 2.3a).

Since the lithospheric thermal model is only applicable at depths of $z \leq 125$ km, a $T_P = 1420$ °C (1693 K) isentrope is used to characterise temperatures in the convective portion of the mantle, over the depth range $z = 225$ to 400 km. Here, temperature is calculated according to

$$T = T_P \exp \left(\frac{\alpha g z}{C_P} \right), \quad (2.33)$$

where α is thermal expansivity, g , acceleration due to gravity, and z , depth. This serves as the second constraint in the inversion, whereby V_S measurements are compared to inferences of V_S from temperature at each depth bin (Figure 2.3b). The third constraint is the **QRFSI12** attenuation model of Dalton et al. (2008), which provides an average radial profile of seismic attenuation at depths $z = 150$ to 400 km beneath Antarctic ocean floor of age ≥ 100 Ma. Both the isentropic temperature and attenuation profiles are sampled at 25 km intervals to match

the chosen V_S binning resolution (Figure 2.3c). To assess the misfit between data and model for these two constraints, tomographic V_S measurements are compared to V_S inferred from isentropic temperature, and attenuation measurements are compared to attenuation inferred from tomographic V_S , respectively. The final constraint used is a single estimate for the average steady state shear viscosity between 225 to 400 km depth, $\eta = 10^{20 \pm 1}$ Pa s (Lau et al., 2016, based on GIA modelling of relative sea level and geodetic data assuming a Maxwell rheology, i.e. diffusion creep). Here, the viscosity constraint is compared to the corresponding depth-averaged viscosity inferred from V_S (Figure 2.3d).

2.4 Bayesian Modelling Framework

Formulating the inverse problem in a Bayesian framework entails treating each of the model parameters as random variables. There are several reasons why this is favourable to taking a deterministic approach. By incorporating hyperparameters, the reported uncertainties on each data set are scaled to more appropriately capture the misfit between data and model (see Eilon et al., 2018). This approach allows for integration of multiple constraints into a joint inversion without the need to use subjective weightings on each data set (Fukuda and Johnson, 2010). Secondly, prior information on the nature of the parameter space can be incorporated. Thirdly, the use of statistical sampling enables much more informative and rigorous treatment of uncertainty, and a natural way to propagate this into uncertainty in physical parameters of interest.

The objective of the inversion is to numerically characterise the *a posteriori* probability density function $p(\mathbf{\mathcal{X}}|\mathbf{\mathcal{D}})$. This function describes how the probability of an infinitesimal volume, $d\mathbf{\mathcal{X}}$, of the model space, $\mathbf{\mathcal{X}}$, varies as it is traversed through, given the observed data. In the following, a particular choice of model will be referred to using the superscript notation, $\mathbf{\mathcal{X}}^i$. A particular component of the model will be referred to using the subscript notation, \mathcal{X}_i .

The model space $\mathcal{X} = \mathcal{X}(\mathbf{m}, \boldsymbol{\sigma})$ contains seven viscoelasticity parameters

$$\mathbf{m} = [\mu_0, \partial\mu/\partial T, \partial\mu/\partial P, \eta_r, E_A, V_A, \partial T_S/\partial z]^T, \quad (2.34)$$

as well as three hyperparameters

$$\boldsymbol{\sigma} = [\sigma_1, \sigma_2, \sigma_3]^T. \quad (2.35)$$

An individual hyperparameter is used to tune the uncertainties for each data set. A fourth hyperparameter associated with the viscosity constraint is omitted, due to the instability of this parameter when used to constrain a data set containing only a single data point. The posterior density, $p(\mathcal{X}|\mathcal{D})$, is dependent on the outcome of the experiments undertaken, via the data, \mathcal{D} . Since it is usually not possible to access $p(\mathcal{X}|\mathcal{D})$ analytically, stochastic methods are used instead.

Bayes' theorem states that the *a posteriori* density, $p(\mathcal{X}|\mathcal{D})$, is linked to the *a priori* information that is known about the model space, as well as the likelihood of obtaining the observed data given a particular model, which are described by the density functions, $p(\mathcal{X})$ and $p(\mathcal{D}|\mathcal{X})$, respectively. The relationship is expressed mathematically as

$$p(\mathcal{X}|\mathcal{D}) = \frac{p(\mathcal{X})p(\mathcal{D}|\mathcal{X})}{p(\mathcal{D})}. \quad (2.36)$$

The *a priori* probability density on the data, $p(\mathcal{D})$, takes on a fixed value for a given set of observations and is thus treated as a normalisation. This allows us to compare probability densities between two different models \mathcal{X}^1 and \mathcal{X}^2 by evaluating the ratio

$$\frac{p(\mathcal{X} = \mathcal{X}^1|\mathcal{D})}{p(\mathcal{X} = \mathcal{X}^2|\mathcal{D})} = \frac{p(\mathcal{X} = \mathcal{X}^1)p(\mathcal{D}|\mathcal{X} = \mathcal{X}^1)}{p(\mathcal{X} = \mathcal{X}^2)p(\mathcal{D}|\mathcal{X} = \mathcal{X}^2)}. \quad (2.37)$$

Therefore, to estimate the variation in posterior density one needs a suitable method for

calculating the prior and likelihood functions. The prior should be selected as a function which agnostically summarises the knowledge one has about the model space before performing the inversion, usually in the form of a uniform or Gaussian distribution. Here a Gaussian distribution is used to summarise prior knowledge of each parameter \mathcal{X}_i ,

$$p(\mathcal{X}_i) = \frac{1}{\sqrt{2\pi}s_i} \exp\left(-\frac{(\mathcal{X}_i - \mu_i)^2}{2s_i^2}\right), \quad (2.38)$$

where μ_i and s_i represent the prior estimate and its uncertainty respectively. This distribution is useful as it enforces a non-zero probability density for any choice of model, \mathcal{X}^i , and enables us to use conservative uncertainty estimates for model parameters based on experimental studies (Table 2.1). The priors on the elastic sector of the parameter space, $\mathcal{X}_{\text{elastic}} = \{\mu_0, \partial\mu/\partial T, \partial\mu/\partial P\}$, were calculated by sampling a range of thermochemical states, $\mathbf{S} = \{X, P, T\}$, where X is pyrolitic composition defined in terms of the proportion of harzburgite to basalt. A database containing the dependence of elastic shear modulus on \mathbf{S} was utilised to build a prior picture of $\mathcal{X}_{\text{elastic}}$. This database was constructed using the software **Perple_X** according to the method laid out by Cobden et al. (2008), using the compilation of thermodynamic parameters of Stixrude and Lithgow-Bertelloni (2011). Activation energy (E_A), activation volume (V_A) and the solidus gradient ($\partial T_S/\partial z$) were estimated by summarising literature reported values (Hirth and Kohlstedt, 2004; Jain et al., 2019). Reference viscosity (η_r) was estimated using the following equation,

$$\eta_r = \frac{d_r^p}{A} \exp\left(\frac{E_A + P_r V_A}{R T_r}\right), \quad (2.39)$$

where the reference thermodynamic state is given by $P_r = 1.5$ GPa and $T_r = 1200$ °C, $d_r = 1$ mm is the reference grain size, p its exponent, and A is a scaling coefficient. By sampling A , p , E_A and V_A over suitable ranges retrieved from the literature (Hirth and Kohlstedt, 2004; Jain et al., 2019), a summary of η_r could be established. The assumption that each model

Model parameter i	Prior μ_i	Prior s_i	Posterior μ_i	Posterior s_i	MAP
μ_0 (GPa)	81	8	74.8	0.4	74.8
$\partial\mu/\partial T$ (GPa K $^{-1}$)	-0.014	0.003	-0.0129	0.0005	-0.0131
$\partial\mu/\partial P$ (unitless)	1.6	0.2	2.04	0.06	2.09
$\log_{10} \eta_r$ (Pas)	22	3	23.2	0.7	22.9
E_A (kJ mol $^{-1}$)	400	200	542	146	476
V_A (cm 3 mol $^{-1}$)	6	4	5.35	0.32	5.02
$\partial T_S/\partial z$ (K km $^{-1}$)	2.25	2.25	1.63	0.14	1.65
$\log_{10} \sigma_1$ (unitless)	0	1	-0.317	0.024	-0.328
$\log_{10} \sigma_2$ (unitless)	0	1	0.093	0.148	0.136
$\log_{10} \sigma_3$ (unitless)	0	1	0.588	0.105	0.514

Table 2.1: **Prior and posterior estimates of the inversion parameters.** The inversion parameters are made up of the seven material-dependent components of YT16, denoted by \mathbf{m} , as well as the three hyperparameters, denoted by $\boldsymbol{\sigma}$. Prior μ_i and s_i represent the mean and standard deviation of the Gaussian prior distribution for each parameter. Posterior μ_i and s_i are estimates of the mean and standard deviation of the posterior distribution for each parameter. MAP represents the maximum *a posteriori* model.

parameter is conditionally independent is taken, allowing the multiplication of the prior on each parameter to form an overall prior density given by

$$p(\mathbf{\mathcal{X}}) = \prod_{i=1}^{N_p} \frac{1}{\sqrt{2\pi}s_i} \exp\left(-\frac{(\mathcal{X}_i - \mu_i)^2}{2s_i^2}\right), \quad (2.40)$$

where N_p is the number of parameters within the model.

The data points within each data set are assumed to be independent, allowing use of a Gaussian distribution to describe the likelihood function for each data set,

$$p(\mathbf{d}_k | \mathbf{\mathcal{X}}(\mathbf{m}, \boldsymbol{\sigma})) = \frac{1}{(2\pi\sigma_k^2)^{N_k/2} |\boldsymbol{\Sigma}_k|^{1/2}} \exp\left(-\frac{1}{2\sigma_k^2} (\mathbf{d}_k - \hat{\mathbf{d}}_k)^T \boldsymbol{\Sigma}_k^{-1} (\mathbf{d}_k - \hat{\mathbf{d}}_k)\right). \quad (2.41)$$

In this equation, \mathbf{d}_k represents the k^{th} data set containing N_k data points, $\hat{\mathbf{d}}_k = \hat{\mathbf{d}}_k(\mathbf{\mathcal{X}})$ the corresponding model prediction, $\boldsymbol{\Sigma}_k$ the data covariance matrix containing the uncertainty on each data point, and σ_k the hyperparameter weighting applied to the data set.

If the data sets are independent of each other, the overall likelihood function can be con-

structed by simply multiplying together the likelihood function for each of the N_d data sets:

$$p(\mathcal{D}|\mathcal{X}(\mathbf{m}, \boldsymbol{\sigma})) = \prod_{k=1}^{k=N_d} \frac{1}{(2\pi\sigma_k^2)^{N_k/2} |\Sigma_k|^{1/2}} \exp \left(-\frac{1}{2\sigma_k^2} (\mathbf{d}_k - \hat{\mathbf{d}}_k)^T \Sigma_k^{-1} (\mathbf{d}_k - \hat{\mathbf{d}}_k) \right). \quad (2.42)$$

2.4.1 Choice of Sampling Algorithm

Once a set of mathematical expressions for the prior and likelihood densities has been established as above, a suitable algorithm must be selected to characterise the posterior space. The Metropolis-Hastings algorithm is one of the most common methods for doing so and involves generating a chain of models with associated posterior density values (Metropolis et al., 1953).

Given a current model \mathcal{X}^n , a proposal model \mathcal{Y}^{n+1} is constructed according to the relationship

$$\mathcal{Y}^{n+1} = \mathcal{X}^n + \mathcal{P}, \quad (2.43)$$

where $\mathcal{P} \sim \mathcal{N}(\mathbf{0}, \Sigma^{\text{proposal}})$ and Σ^{proposal} is a suitable $N_p \times N_p$ proposal sampling covariance matrix. For simplicity, this matrix is typically chosen to be diagonal. The proposal model is accepted with probability

$$a^n = \min \left(1, \frac{p(\mathcal{Y}^{n+1} | \mathcal{D})}{p(\mathcal{X}^n | \mathcal{D})} \right), \quad (2.44)$$

where a^n is known as the acceptance ratio and is calculated using Equation (2.37). If the proposal model is accepted one sets $\mathcal{X}^{n+1} = \mathcal{Y}^{n+1}$. Otherwise the current model remains and one sets $\mathcal{X}^{n+1} = \mathcal{X}^n$. This process is repeated until the parameter space is suitably explored. Since the probability of a model being accepted is proportional to its posterior density, convergence towards optimal regions of the parameter space occurs. However, less probable models still have a finite acceptance probability, meaning the procedure is also capable of escaping local maxima (analogous to local minima observed in deterministic formulations). To circumvent the issue that the evolution of samples is, at first, correlated with the initial

starting point, the first 50% of trials are discarded as a so-called “burn-in” period. Only the post burn-in set of samples are used in the analysis.

While powerful, the Metropolis-Hastings algorithm in its original form is not sophisticated enough to perform the inversion efficiently, since strong trade-offs between model parameters invalidate the use of a diagonal proposal covariance matrix. The precise form of Σ^{proposal} has a strong impact on the average model acceptance rate a , which is optimised when $a \approx a^*$, where $a^* = 0.234$ (Gelman et al., 1997). When Σ^{proposal} is too small, a large proportion of models are accepted but only small steps around the model space are taken. When Σ^{proposal} is too large, only a small proportion of models are accepted and so the inversion algorithm tends to sample the same area of the model space for a prohibitively large number of trials, before wildly jumping elsewhere. This applies when any region of the multi-dimensional proposal covariance space is poorly estimated. Both situations lead to inefficient convergence towards the posterior distribution and so, for a finite number of trials, inhibit achievement of ergodicity: full exploration of the parameter space such that the discrete set of posterior samples converges onto the underlying continuous posterior distribution. Therefore, the use of adaptive Metropolis algorithms was investigated further, which are intended to improve the efficiency of the sampling procedure.

Haario et al. (2001) serves as a good reference point for the implementation of such an algorithm. It utilises the condition found by Gelman et al. (1997) that for a Metropolis algorithm on \mathbb{R}^d , the proposal is optimally scaled when the proposal state is generated according to

$$\mathbf{y}^{n+1} \sim \mathcal{N}(\mathbf{x}^n, \Sigma^{\text{proposal}}), \quad (2.45)$$

$$\Sigma^{\text{proposal}} = \gamma \Sigma^{\mathbf{x}}, \quad (2.46)$$

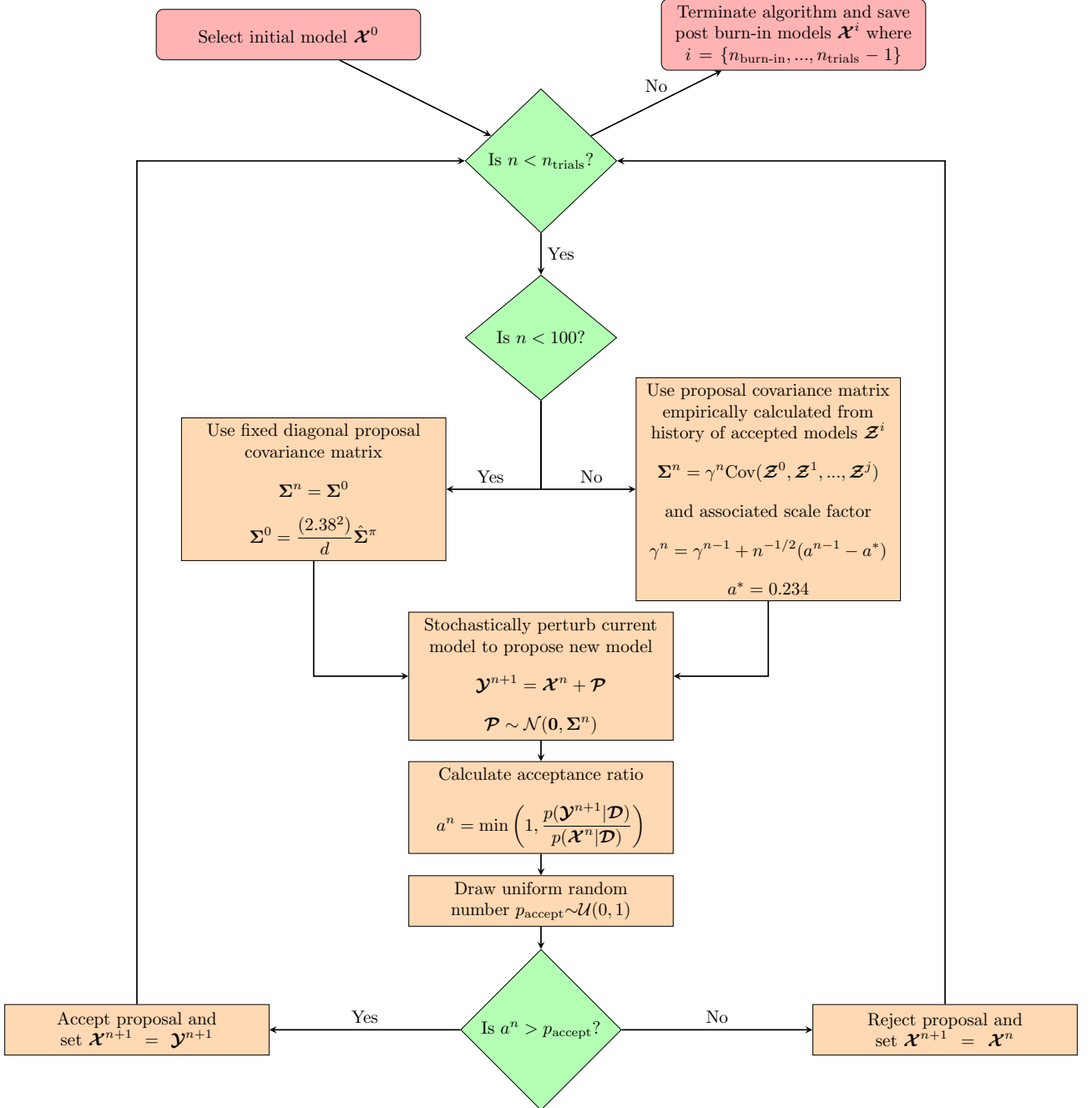


Figure 2.2: Flow chart representation of the Globally Adaptive Scaling Within Adaptive Metropolis (GASWAM) adaptation (Andrieu and Thoms, 2008) of the Metropolis-Hastings algorithm (Metropolis et al., 1953). Optimal acceptance ratio, $a^* = 0.234$, from Gelman et al. (1997). Initial proposal sampling covariance matrix based on the proposition of Haario et al. (2001). Algebraic superscripts refer to a particular choice of model.

where $\Sigma^{\mathcal{X}}$ is the posterior covariance matrix, and $\gamma = \frac{2.38^2}{d}$ is the scaling coefficient. The condition implies that the ideal proposal covariance matrix is a scalar multiple of the target posterior covariance. Since the posterior is the object to be accessed and characterised via the sampling procedure, and therefore an unknown quantity, employing a suitable proposal is challenging. To address this issue, Haario et al. (2001) use an unbiased estimate of the target posterior covariance, which can be calculated empirically based on the evolving chain of generated samples. On the n^{th} trial, where $n - 1$ samples have been generated so far, the unbiased estimate of the posterior covariance is

$$\bar{\Sigma}^{\mathcal{X}} = \frac{1}{n-2} \sum_{i=1}^{n-1} (\mathcal{X}^i - \bar{\mathcal{X}}) (\mathcal{X}^i - \bar{\mathcal{X}})^T, \quad (2.47)$$

where $\bar{\mathcal{X}} = \frac{1}{n-1} \sum_{i=1}^{n-1} \mathcal{X}_i$. The prefix “adaptive” therefore comes from the iterative adaptation of the proposal covariance matrix. For multi-dimensional parameter spaces ($d > 1$), $\bar{\Sigma}^{\mathcal{X}}$ may take a considerable number of trials to resemble the true posterior covariance, $\Sigma^{\mathcal{X}}$, however, it should provide better performance than a fixed proposal setup. Substituting \mathcal{X} in Equation (2.47) for only the subset of trial models that were accepted, \mathcal{Z} , may offer more efficient convergence towards the posterior covariance. This approach is known as the “greedy start” procedure, and is made use of in this study (Figure 2.2). It should also be noted that since Equation (2.47) relies on the history of all preceding trials, the chain of samples is no longer Markovian. However, it has been proven that ergodicity still holds for adaptive algorithms given some loose assumptions on the posterior (see Haario et al., 2001 for details).

Implementation of the Adaptive Metropolis algorithm shown above is theoretically easy, however the optimal scaling factor, $\gamma = \frac{2.38^3}{d}$, does not work in practice if there are significant correlations between the parameters in the model. In this case, the solution is to also update γ adaptively. The Global Adaptive Scaling Within Adaptive Metropolis (GASWAM) scheme employs this technique to estimate a suitable proposal covariance matrix

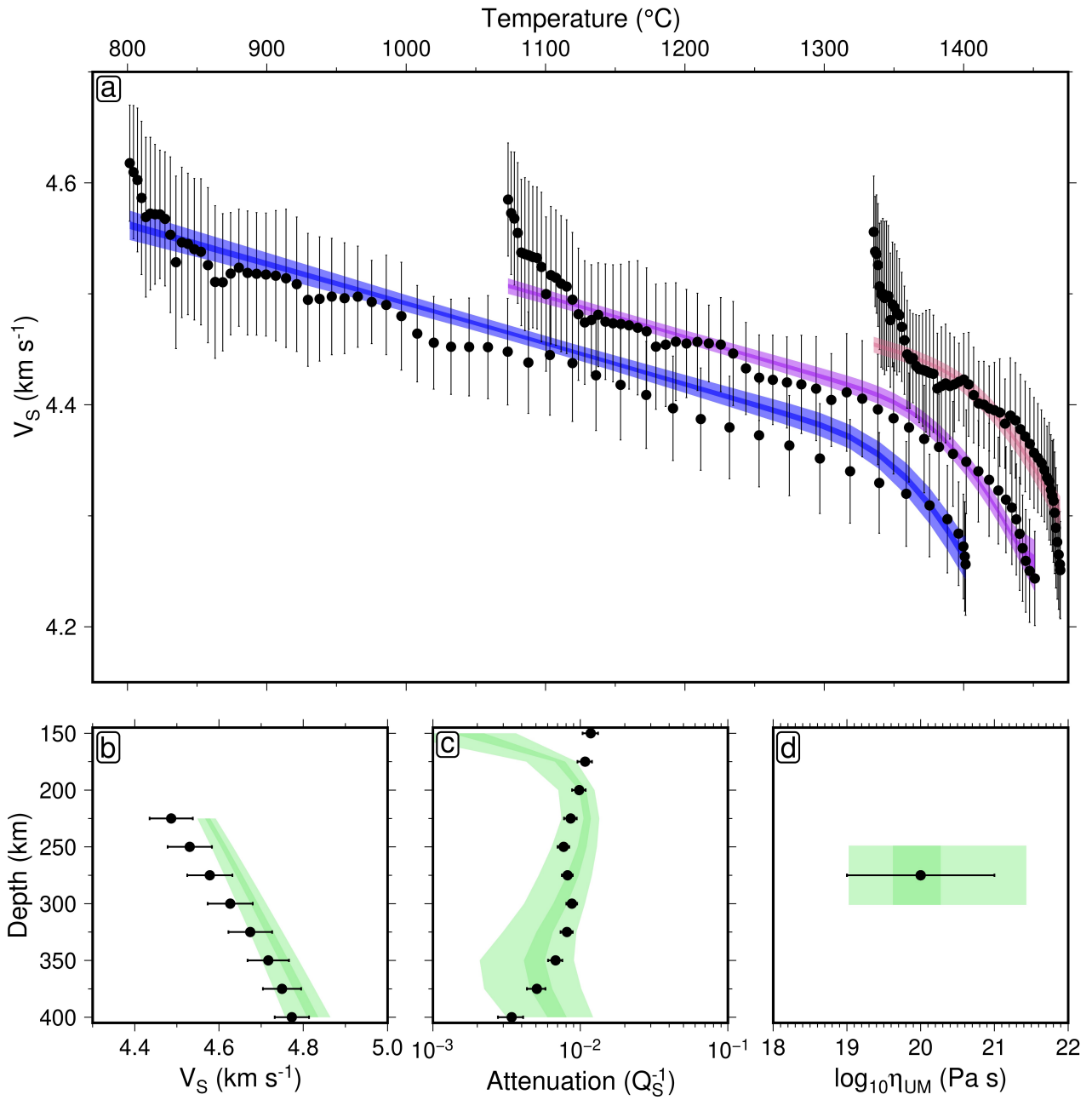


Figure 2.3: **Assessing fit of inverted viscoelasticity parameters to Antarctic geophysical data.** Fit of post burn-in models to the four geophysical data sets used to constrain the inversion procedure (circles/error bars; see Section 2.3.1). Pale shaded regions represent the 99% credible interval, and dark shaded regions represent the 50% credible interval. (a) Plate cooling model fit for depth ranges 50 to 75 km (blue), 75 to 100 km (purple) and 100 to 125 km (red). (b) Adiabatic model fit for depth range 225 to 400 km. (c) QRFSI12 seismic attenuation model fit at depths 150 to 400 km beneath ocean floor for ages ≥ 100 Ma. (d) Average viscosity between 225 to 400 km compared to $\eta = 10^{20 \pm 1}$ Pa s estimate.

$$\Sigma^{\text{proposal}} = \gamma^n (\bar{\Sigma}^{\mathcal{X}} + \epsilon \mathbf{1}), \quad (2.48)$$

$$\gamma^n = \gamma^{n-1} + \eta^n (a^{n-1} - a^*). \quad (2.49)$$

Here, the scaling factor to be used for the n^{th} trial, γ^n , is updated by a factor proportional to the difference between the current and ideal acceptance ratios, a^{n-1} and a^* , respectively. The function, $\eta^n = n^{-1/2}$, is used to ensure adaptation decays in size as the simulation progresses. The presence of the constant $\epsilon > 0$ ensures ergodicity, and is chosen to be negligibly small compared to the size of the proposal covariance matrix. This algorithm can be employed after some fixed number of trials – long enough to provide a suitable first estimate of Σ^{proposal} – and initiated with the traditional Adaptive Metropolis scaling factor $\gamma^0 = 2.38^2/d$.

By using GASWAM to simultaneously update the shape and size of the proposal covariance matrix, stabilisation of the inversion procedure can be achieved by enforcing the optimal acceptance ratio, such that $a \approx 0.234$. This stability is ensured by looking at a suite of convergence diagnostics including the running mean of each parameter as the trial proceeds, frequency density plots of each parameter, the potential scale reduction factor (Gelman et al., 1997; Roy, 2020), and the fit of the models to the data (Figure 2.3). The performance of the inversion algorithm was also tested against synthetic data, verifying that it behaved as expected.

2.4.2 Synthetic Test

The first step in generating a synthetic data set is to specify a choice of model. This was selected to lie reasonably close to the centre of the prior distribution, and the resulting model, $\mathcal{X}^{\text{synthetic}}$, is shown in Table 2.2.

To generate a synthetic oceanic plate V_S data set, the “true” plate temperatures described in

Model parameter i	Synthetic value	MAP
μ_0 (GPa)	75.0	74.9
$\partial\mu/\partial T$ (GPa K $^{-1}$)	-0.0130	-0.0129
$\partial\mu/\partial P$ (unitless)	2.00	1.98
$\log_{10} \eta_r$ (Pas)	22.5	22.7
E_A (kJ mol $^{-1}$)	400	454
V_A (cm 3 mol $^{-1}$)	4.00	4.91
$\partial T_S/\partial z$ (K km $^{-1}$)	1.7	1.69
$\log_{10} \sigma_1$ (unitless)	-1.00	-1.03
$\log_{10} \sigma_2$ (unitless)	-1.04	-0.95
$\log_{10} \sigma_3$ (unitless)	0.24	0.19

Table 2.2: **Choice of synthetic model parameters, $\mathcal{X}^{\text{synthetic}}$, and the corresponding maximum *a posteriori* (MAP) inversion output.**

Section 2.1 were converted into V_S using the parameters of $\mathcal{X}^{\text{synthetic}}$. An analogous approach was taken to generate a synthetic adiabatic V_S data set, by converting the “true” adiabat temperatures into V_S , using the choice of synthetic viscoelasticity parameters $\mathcal{X}^{\text{synthetic}}$. The attenuation data set was generated by converting the “true” ANT-20 V_S into Q^{-1} using the chosen synthetic model. The same method was applied to generate a set of viscosities, which were then averaged to form a synthetic bulk viscosity data point. Random noise was added to each data set by sampling from a Gaussian distribution, scaled to match the fractional uncertainty on the respective real data sets.

Since each data set contains a finite number of data points, the true uncertainty on each data set after the addition of random noise deviates from the width of the Gaussian distribution used to generate it. Therefore instead of specifying the synthetic hyperparameters, their values have been intrinsically created as a by-product of performing the noise addition procedure, and should be calculated. To do this, the root-mean-squared (RMS) misfit between the synthetic data prior to, and after, the addition of random noise was calculated. The hyperparameter was then calculated as the ratio of this RMS misfit to the reported uncertainty.

The inversion is then completed as previously specified. The posterior set of samples fit the synthetic data very well, giving us confidence that the underlying synthetic model space

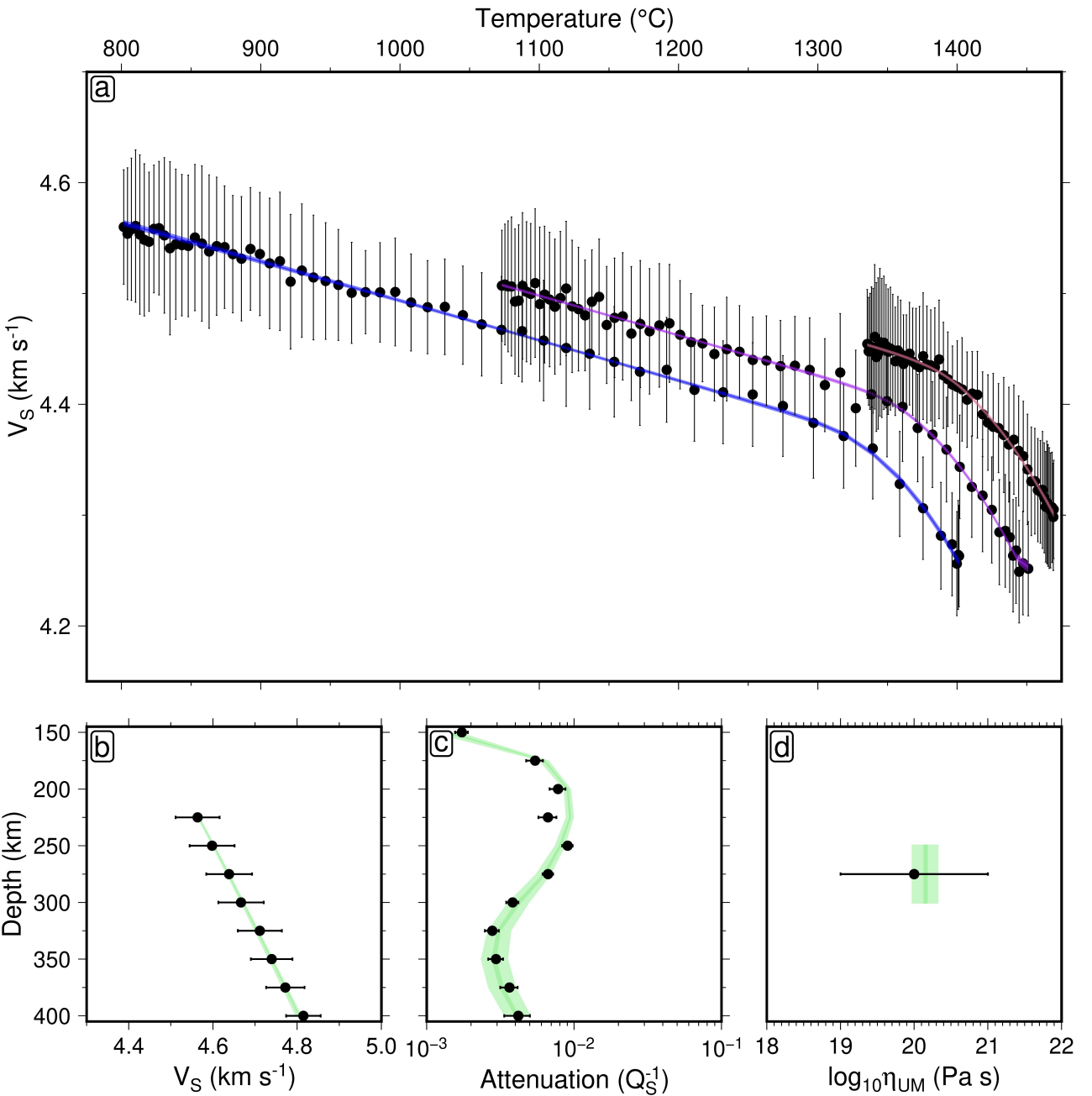


Figure 2.4: **Assessing fit of inverted viscoelasticity parameters to synthetic data.** Fit of post burn-in models to the four synthetic data sets used to constrain the inversion procedure (circles/error bars). Pale shaded regions represent the 99% credible interval, and dark shaded regions represent the 50% credible interval. (a) Plate cooling model fit for depth ranges 50 to 75 km (blue), 75 to 100 km (purple) and 100 to 125 km (red). (b) Adiabatic model fit for depth range 225 to 400 km. (c) Seismic attenuation model fit at 150 to 400 km depth. (d) Average viscosity between 225 to 400 km depth compared to $\eta = 10^{20 \pm 1} \text{ Pa s}$ estimate.

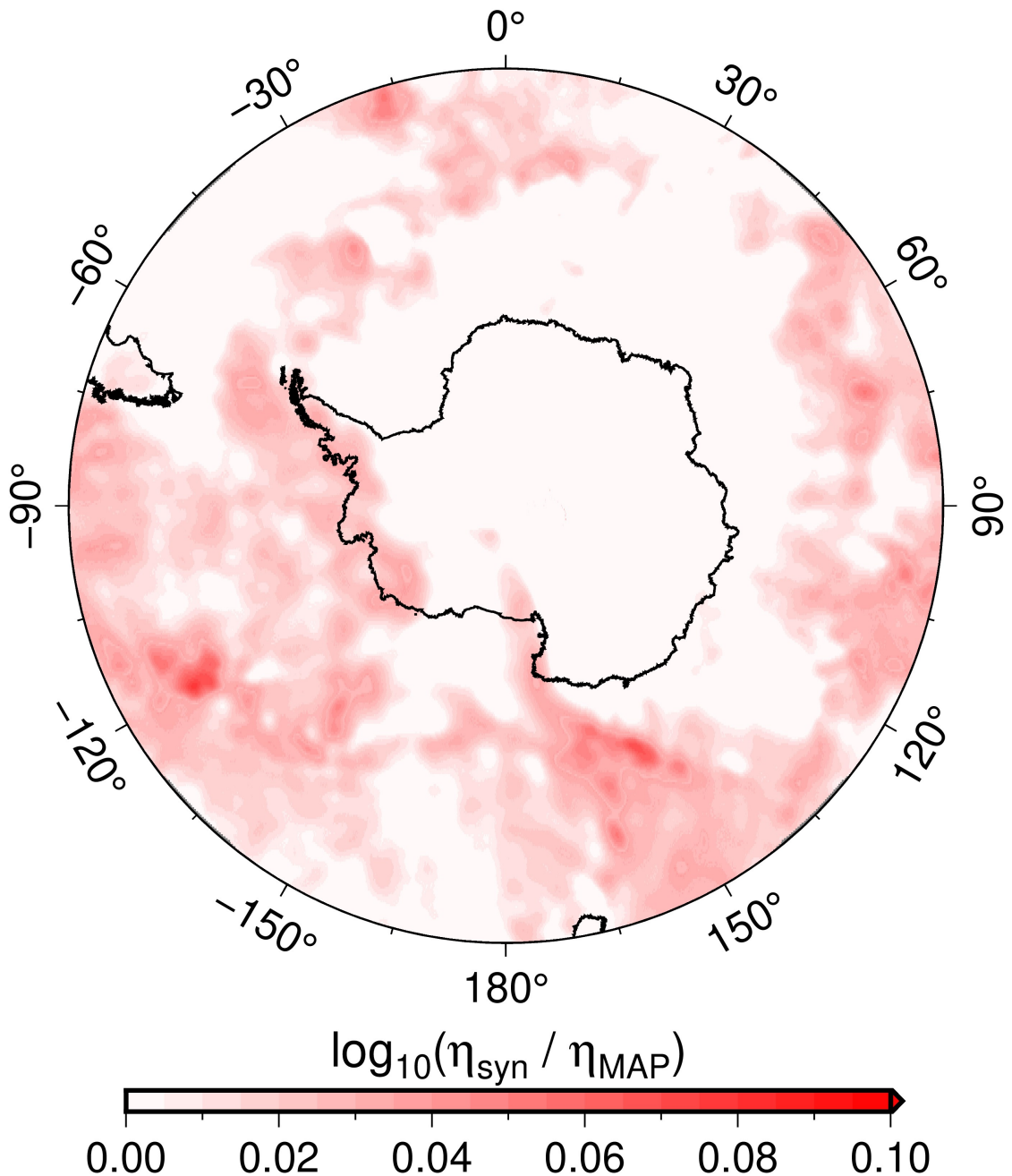


Figure 2.5: Difference between synthetic and inverted viscoelasticity parameters reflected in predictions of Antarctic mantle viscosity. ANT-20 V_S at 150 km depth converted into steady state viscosity using synthetic viscoelasticity parameters, $\boldsymbol{\chi}^{\text{synthetic}}$, as well as maximum *a posteriori* (MAP) viscoelasticity parameters, $\boldsymbol{\chi}^{\text{MAP}}$, taken from the synthetic inversion. The discrepancy between the two viscosity predictions, $\log_{10}\eta_{\text{syn}} - \log_{10}\eta_{\text{MAP}} = \log_{10}(\eta_{\text{syn}}/\eta_{\text{MAP}})$, reveals close agreement between the “true” (synthetic) viscosity and the MAP model.

has been suitably explored (Figure 2.4). By propagating the **ANT-20** V_S model at 150 km depth into viscosity using the **YT16** parameterisation, it is possible to compare the physical predictions of the synthetic model (η_{syn}) to those of the maximum *a posteriori* (MAP) model from the synthetic inversion (η_{MAP} , Figure 2.5). The discrepancy between the two predictions satisfies the condition

$$\log_{10} \left(\frac{\eta_{\text{syn}}}{\eta_{\text{MAP}}} \right) = \log_{10} (\eta_{\text{syn}}) - \log_{10} (\eta_{\text{MAP}}) < 0.01 \quad (2.50)$$

across the vast proportion of Antarctica.

2.4.3 Summarising Posterior Outputs

The result of the inversion is a set of post burn-in models, $\mathcal{X}^{\text{posterior}}$. This serves as a discrete set of samples over the continuous posterior density function, $p(\mathcal{X}|\mathcal{D})$. A greater sampling density is indicative of a more probable region of the model space. Since the sampled posterior distribution (ignoring hyperparameters) is seven-dimensional, it cannot be visualised as a whole. Instead, the sampling density is calculated for each combination of model parameters, \mathcal{X}_i and \mathcal{X}_j . To achieve this, the posterior space of each parameter is discretised into 1,000 blocks, spanning the range of values over which this parameter was sampled. This results in a step-size given by

$$h_i = \frac{\text{maximum}(\mathcal{X}_i) - \text{minimum}(\mathcal{X}_i)}{1,000}. \quad (2.51)$$

The sampling density is then calculated as

$$\rho_{ij}(x, y) = n_{ij}(x, y) / A_{ij}, \quad (2.52)$$

where (x, y) is the grid reference pertaining to each of the $1,000 \times 1,000$ discrete areas in

which density values are calculated, $n_{ij}(x, y)$ is the corresponding number of posterior samples, and $A_{ij} = h_i h_j$ is the corresponding area. To yield further information from the inversion output, the model samples and their corresponding physical predictions must be summarised mathematically. The expectation value of each parameter can be estimated using the discrete summation

$$\hat{E}(\mathcal{X}_i) = \frac{1}{N_s} \sum_{j=1}^{N_s} \mathcal{X}_i^j, \quad (2.53)$$

where N_s is the number of discrete model samples (Gallagher et al., 2009). The corresponding variance of each parameter may be estimated using the formula

$$\hat{V}(\mathcal{X}_i) = \frac{1}{N_s - 1} \sum_{j=1}^{N_s} \left(\mathcal{X}_i^j - \hat{E}(\mathcal{X}_i) \right)^2. \quad (2.54)$$

Although it is helpful to verify that the posterior distribution obtained lies within a sensible region of the model space, the vectors $\hat{\mathbf{E}}(\mathbf{X})$ and $\hat{\mathbf{V}}(\mathbf{X})$ do not tell the full story. The viscoelasticity parameters, \mathbf{X} , combined with the adopted parameterisation of complex compliance, serve as a means for converting V_S into physical predictions of temperature, T , viscosity, η , and density, ρ . The objective is therefore to estimate the expectation value and variance of functions of the model $f(\mathbf{X})$, rather than the model itself. This can be achieved easily, by constructing a vector, \mathcal{F} , where each component is calculated according to the formula

$$\mathcal{F}^i = f(\mathbf{X}^i). \quad (2.55)$$

The expectation value and variance of the physical prediction can be estimated analogously to equations (2.53) and (2.54), resulting in the equations

$$\hat{E}(\mathcal{F}) = \frac{1}{N_s} \sum_{i=1}^{N_s} \mathcal{F}^i, \quad (2.56)$$

and

$$\hat{V}(\mathcal{F}) = \frac{1}{N_s - 1} \sum_{i=1}^{N_s} (\mathcal{F}^i - \hat{E}(\mathcal{F}))^2. \quad (2.57)$$

The estimates for the expectation value, $\hat{E}(\mathcal{F})$, and variance, $\hat{V}(\mathcal{F})$, are referred to as the average and uncertainty, respectively. If it is not practical to calculate all N_s values of \mathcal{F}^i , due to computational expense, a subset N_U of the overall set of post burn-in models may be used (see Section 3.2). The relationship between the uncertainty on a physical prediction, $\hat{V}(f(\boldsymbol{\chi}))$, and the uncertainty on the underlying model parameters, $\hat{\boldsymbol{V}}(\boldsymbol{\chi})$, is dependent on the sensitivity of $f(\boldsymbol{\chi})$ to each parameter, $\boldsymbol{\chi}_i$ (i.e., the gradient, $\partial f(\boldsymbol{\chi})/\partial \boldsymbol{\chi}_i$), and the covariance structure of the model, $\boldsymbol{\Sigma}^{\boldsymbol{\chi}}$ (Champac and Garcia Gervacio, 2018). In the case of the anelasticity parameterisation, $T(\boldsymbol{\chi})$ and $\eta(\boldsymbol{\chi})$ are non-linear functions of V_S , complicating the analytical calculation of their expectation value and variance. This highlights one of the key benefits of taking a Bayesian approach, as it provides a simple way of propagating uncertainties, using the discrete summaries of equations (2.56) and (2.57).

2.5 Analysing Posterior Parameter Distributions

The posterior distribution of viscoelasticity parameters estimated in this study is compared in Table 2.3 to the values obtained by Richards et al. (2020a) via deterministic inversion. The mean posterior parameter values agree with those of Richards et al., 2020a to within two standard deviations, with the exception of $\partial\mu/\partial T$ and $\partial\mu/\partial P$. The parameter $\partial\mu/\partial P$ trades off non-negligibly with both μ_0 and $\partial\mu/\partial T$ (see Section 2.5.1). The direction of these trade-offs helps us to rationalise the fact that a larger value of $\partial\mu/\partial P$ was recovered in Richards et al., 2020a compared to this study, given that they also found a larger μ_0 , and a more negative $\partial\mu/\partial T$. Furthermore, one would expect there to be discrepancy in the recovered viscoelasticity parameters between Richards et al., 2020a and this study, due to the use of different seismic

Model parameter i	This study		Richards et al. (2020a)	
	Posterior μ_i	Posterior s_i	x_i	e_i
μ_0 (GPa)	74.8	0.4	78.2	2.2
$\partial\mu/\partial T$ (GPa K $^{-1}$)	-0.0129	0.0005	-0.020	0.002
$\partial\mu/\partial P$ (unitless)	2.04	0.06	2.67	0.18
$\log_{10} \eta_r$ (Pas)	23.2	0.7	22.6	1.6
E_A (kJ mol $^{-1}$)	542	146	400	288
V_A (cm 3 mol $^{-1}$)	5.35	0.32	0.092	5.560
$\partial T_S/\partial z$ (K km $^{-1}$)	1.63	0.14	0.919	0.257
$\log_{10} \sigma_1$ (unitless)	-0.317	0.024	—	—
$\log_{10} \sigma_2$ (unitless)	0.093	0.148	—	—
$\log_{10} \sigma_3$ (unitless)	0.588	0.105	—	—

Table 2.3: **Comparison of recovered inversion parameters between this study and Richards et al. (2020a).** Posterior μ_i and s_i are estimates of the mean and standard deviation of the posterior distribution for each parameter. The symbols x_i and e_i represent the estimate of each parameter and its uncertainty, respectively, for the study Richards et al. (2020a), which was conducted within a deterministic framework.

tomography models (**SL2013sv**, Schaeffer and Lebedev, 2013 and **ANT-20**, Lloyd et al., 2020, respectively). Differences in $\partial\mu/\partial P$ appear to be mostly caused by the different reference velocities adopted in the **SL2013sv** model used in Richards et al., 2020a, and the **ANT-20** model used here. Velocity increases more strongly with depth in the **SL2013sv** reference model, apparently translating into a steeper sub-oceanic upper mantle velocity gradient in the final model and thus a larger best-fitting $\partial\mu/\partial P$ value of 2.67 ± 0.18 . Interestingly, the value obtained in this study, 2.04 ± 0.06 , is nearer to experimentally determined estimates. This result may indicate that the adopted reference model in **ANT-20** is a more accurate representation of average upper mantle V_S structure. Alternatively, the improved agreement might reflect the fact that shear wave velocities from **ANT-20** are isotropic (Voigt average), whereas **SL2013sv**-derived counterparts represent the vertically polarised (V_{SV}) component only. Since the experimental $\partial\mu/\partial P$ constraints represent isotropic values, it is perhaps no surprise that Voigt average shear-wave velocities give a more consistent result.

2.5.1 Parameter Covariance Structure

To investigate how dependent a particular model parameter is on the choice of another, the posterior sampling density is plotted for each parameter combination (Figure 2.6). This highlights the presence of clear trade-offs, as expected given the need to adapt the proposal sampling scheme to handle non-diagonal model covariance structure. It was found that the anelasticity model \mathbf{m} can be approximately separated into two independent components, $\mathbf{A} = \{\mu_0, \partial\mu/\partial T, \partial\mu/\partial P\}$ and $\mathbf{B} = \{\eta_r, E_A, V_A, \partial T_S/\partial z\}$, such that $\mathbf{m} = \{\mathbf{A}, \mathbf{B}\}$. A reasonable approximation for the model covariance structure therefore takes the form

$$\Sigma^{\mathbf{x}} \approx \begin{bmatrix} \Sigma^{\mathbf{A}} & \mathbf{0} \\ \mathbf{0} & \Sigma^{\mathbf{B}} \end{bmatrix}. \quad (2.58)$$

There exist strong parameter trade-offs within \mathbf{A} and \mathbf{B} separately, but only weak trade-offs between \mathbf{A} and \mathbf{B} . This is in accordance with what is expected physically, whereby \mathbf{A} regulates the elastic component of the physical response, and \mathbf{B} the transient component.

Within \mathbf{A} , a very strong negative trade-off between the reference shear modulus and its temperature derivative is observed. This implies that with respect to the maximum *a posteriori* estimate for this combination of parameters, a similar fit to the data can be obtained by covarying μ_0 and $\partial\mu/\partial T$ in opposite directions. It is possible to verify that this makes sense in the context of the plate model $V_S(T)$ relationship (Figure 2.3a), which serves as the main data constraint on the inversion, as follows. The linear region of the $V_S(T)$ relationship in a given depth bin is well-approximated by assuming a purely elastic response at fixed pressure. Consider the 50 to 75 km depth bin (Figure 2.3a, blue circles), and let us define a reference shear modulus relevant to this depth slice as follows

$$\mu_0^* = \mu_0 + \frac{\partial\mu}{\partial P} (P^* - P_0), \quad (2.59)$$

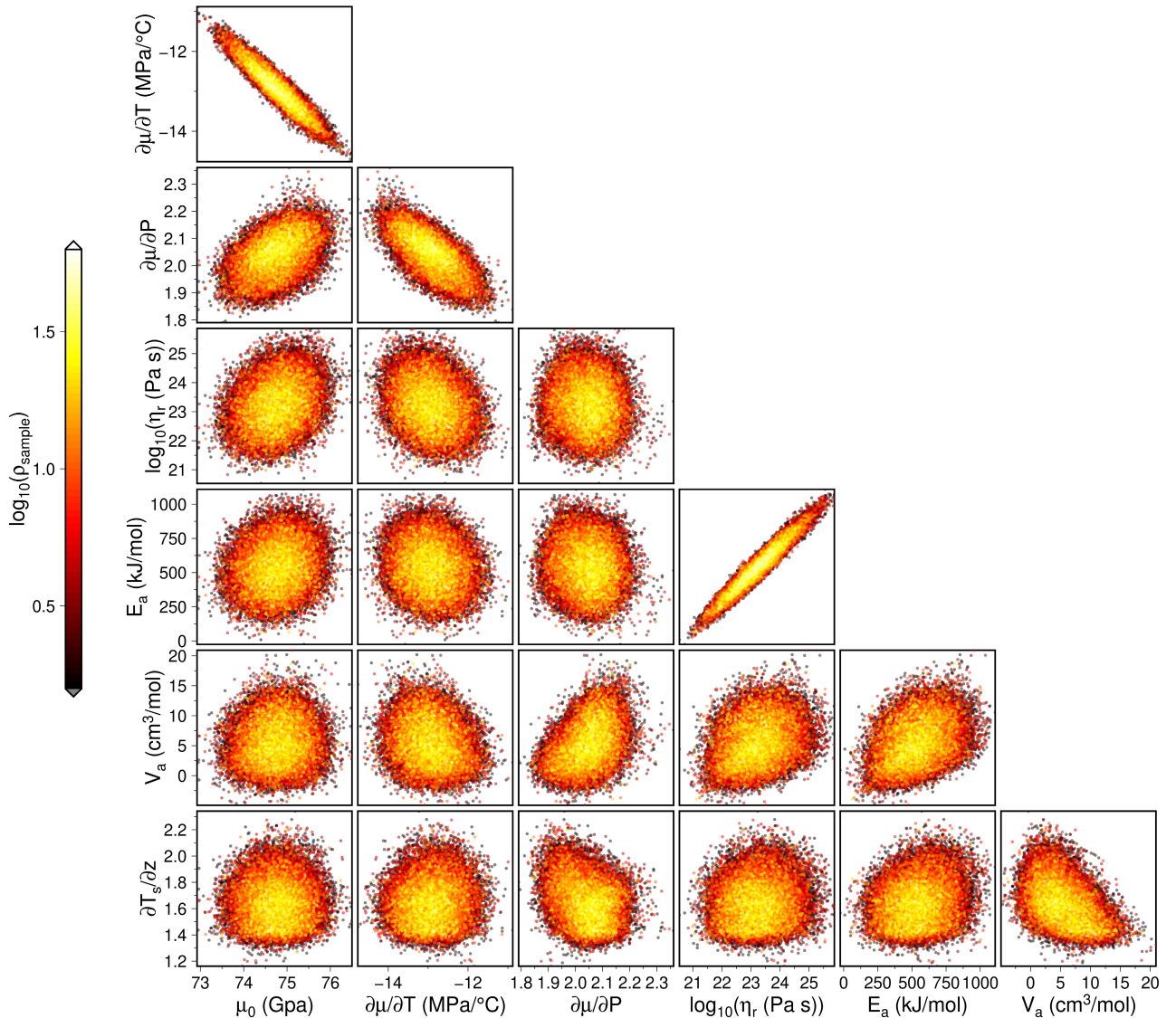


Figure 2.6: **Posterior distributions of viscoelasticity parameters.** Posterior sampling density (ρ_{sample} , arbitrary units) of each combination of anelasticity models, highlighting physical trade-offs between parameters.

where $P^* = 2.1$ GPa is the corresponding pressure value. The $V_S(T)$ relationship can be expressed as

$$V_S(T) = \sqrt{\frac{M_U(T)}{\rho(T)}}, \quad (2.60)$$

and therefore, in terms of the renormalised shear modulus, it can be found that

$$V_S(T) = \sqrt{\frac{\mu_0^* + \partial\mu/\partial T(T - T_0)}{\rho(T)}}. \quad (2.61)$$

Since density is only expected to vary by 2% over the temperature range covered by the 50 km to 75 km depth bin of the plate V_S data, and even less so for the other two depth bins, its variation is ignored for the sake of simplicity. Consider the numerator, $\zeta = \sqrt{\mu_0^* + \partial\mu/\partial T(T - T_0)}$, of Equation (2.61). This may be rewritten in the form

$$\frac{\zeta}{\sqrt{\mu_0^*}} = \left(1 + \frac{\partial\mu/\partial T}{\mu_0^*} \Delta T\right)^{\frac{1}{2}}, \quad (2.62)$$

Assessing the magnitude of each term on the right hand side of this equation, $|\mu_0| \sim 10^2$ GPa and $|(\partial\mu/\partial T)\Delta T| \sim 10^1$ GPa, it is possible to perform a binomial expansion since the ratio

$$\left|\frac{\partial\mu/\partial T}{\mu_0^*} \Delta T\right| < 1. \quad (2.63)$$

Therefore, expanding the square-root, it is found that

$$\zeta = \sqrt{\mu_0} \left(1 + \frac{1}{2} \frac{\partial\mu/\partial T}{\mu_0} \Delta T + \mathcal{O}((\Delta T)^2)\right). \quad (2.64)$$

Ignoring terms of second-order and above, it can be deduced that the form of the linear relationship $\zeta(T)$ looks like

$$\zeta \approx \sqrt{\mu_0} \left(1 + \frac{1}{2} \frac{\partial \mu / \partial T}{\mu_0} \Delta T \right), \quad (2.65)$$

and thus in terms of shear-wave velocity it is found that

$$V_S(T) = \sqrt{\frac{\mu_0}{\rho}} + \frac{1}{2} \frac{\partial \mu / \partial T}{\mu_0 \rho} \Delta T. \quad (2.66)$$

Therefore, an increase in the reference shear modulus has the effect of increasing the V_S value at which the $V_S(T)$ trend is initialised, as well as reducing the absolute gradient of the trend. The temperature gradient of the shear modulus must assume a correspondingly more negative value to compensate, in order to preserve the squared distance between data and model. A symmetric argument can be used to interpret the positive trade-off between reference shear modulus and its pressure gradient. The relative weakness of this $(\mu_0, \partial \mu / \partial P)$ trade-off compared to that of $(\mu_0, \partial \mu / \partial T)$ may, in part, be down to the lower level of information that the geophysical data contains on the variation of V_S with depth. In addition, a negative trade-off between the temperature and pressure derivatives of the shear modulus appears to be present.

By far the strongest parameter trade-off observed within the anelasticity model is contained within \mathbf{B} , between activation energy and reference viscosity; parameters controlling the onset and strength of anelastic effects respectively. The non-linear relationship between parameters in the anelastic regime prevents an analytical derivation of the trade-off between E_A and η_r . However, it appears that while the individual uncertainties on E_A and η_r are very large, the strength of trade-off between the two ensures only a small variation in the misfit between data and model. Importantly, this relationship reduces the extent to which uncertainty in the individual parameters propagates into uncertainty in upper mantle thermomechanical structure (see Section 3.2). Trade-offs between other parameters within \mathbf{B} appear to be present, although relatively weak. In order to further constrain the model covariance, more data containing

information about anelastic behaviour, especially at high pressure, are required.

2.6 Conclusions

A probabilistic approach to the calibration of experimental parameterisations of viscoelasticity, including anelasticity, has been developed to provide a self-consistent mapping between three-dimensional seismic tomographic velocity data and models of thermomechanical structure. By making use of a physical model based on laboratory data, and designed to account for frequency dependence in the mantle stress-strain relationship, it is possible to translate experimentally constrained microphysical behaviour into predictions of macroscopic variables including temperature, viscosity and density, as a function of shear-wave velocity. The calibration procedure was performed using a suite of regional geophysical data constraints associated with the geographical footprint of the chosen velocity model. An integral component of the calibration procedure is its flexibility, allowing it to be deployed with any velocity model, and any parameterisation of mantle viscoelasticity, as preferred. It can easily be adapted to work with other data types, such as xenolith-derived constraints on upper mantle thermal structure. An implementation of the inverse theory is provided, using the Globally Adaptive Scaling Within Adaptive Metropolis (GASWAM) adaptation of the Metropolis-Hastings algorithm to allow ideal sampling efficiency, and thus make the inverse problem tractable. By probing the model covariance structure, model parameter uncertainties and trade-offs can be evaluated in a mathematically robust manner. This breakthrough enables mantle thermomechanical structure and associated uncertainties to be inferred self-consistently from seismic tomography for the first time.

Chapter 3

Probabilistic Assessment of Antarctic Thermomechanical Structure

3.1 Introduction

Antarctica is host to a volume of ice equivalent to 57.9 ± 0.9 m of global mean sea level (GMSL) rise, or roughly 90% of the global cryosphere (Bamber et al., 2018; Morlighem et al., 2020).

The mantle structure, topography, and glacial stability of this continent expresses a dichotomy in tectonic setting between East and West Antarctica. The two regions are separated by the Transantarctic Mountain Range, which spans the continental interior from the Weddell Sea to the Ross Sea. As a result, Antarctica's grounded ice volume is divided into an East and West Antarctic Ice Sheet (EAIS and WAIS, respectively). The EAIS is underlain by thick, cratonic lithosphere owing to minimal tectonic activity in this region since the Mesozoic Era (Noble et al., 2020). The WAIS is underlain by a rift system primarily active between the late Cretaceous and early Cenozoic, and in places still active today, which has given rise to upwelling of low viscosity asthenosphere, and dynamically thinned lithosphere (Noble et al., 2020). Bedrock elevation is predominantly above GMSL in the east, and below GMSL in the west (Figure

3.1a). This exerts a major influence on ice dynamics, due to the increased vulnerability of marine-grounded ice, especially when positioned on a reverse bed slope, as is the case in West Antarctica (Fretwell et al., 2013). The WAIS is therefore considered much more prone to short-term ice mass loss (Coulon et al., 2021). Indeed, it is declining by ~ 200 Gt per year, while the EAIS is approximately in equilibrium (within the error bounds of observational data, Shepherd et al., 2018b).

Seismic shear-wave velocity (V_S) can be used to gain insight into upper mantle structure beneath the ice sheets due to its strong sensitivity to temperature (Faul and Jackson, 2005). Laboratory experiments show sub-solidus temperature changes can induce up to 20% variations in V_S (Priestley and McKenzie, 2013; and references therein). Although volatiles and composition may also influence V_S (Karato and Jung, 1998; Lee, 2003), recent studies show close agreement between xenolith-derived temperature profiles and those inferred from seismic tomographic velocity models using viscoelasticity parameterisations that ignore the potential impact of compositional heterogeneity in the asthenosphere and lower lithosphere, indicating that temperature is indeed the dominant control on shallow mantle V_S variation (Hoggard et al., 2020; Klöcking et al., 2020).

Until recently, Antarctica has suffered from a significant shortage of seismic data due in part to difficulties operating polar seismic stations and the lack of proximal (latitudinally) land masses (Lloyd et al., 2020). For example, global tomographic models such as **SL2013sv** have relied on data from just 9 permanent seismic stations situated in Antarctica (Schaeffer and Lebedev, 2013). However, **ANT-20**, a wave-equation travelttime adjoint tomographic velocity model, has recently been developed utilising data from 270 earthquakes captured at 323 seismic stations, the majority (297) of which reside on the Antarctic continent (Lloyd et al., 2020; see Figure 3.1b for locations). Nearly all of the seismic stations used in **ANT-20** were temporary deployments for the purposes of distinct, regional studies. By integrating seismic data covering

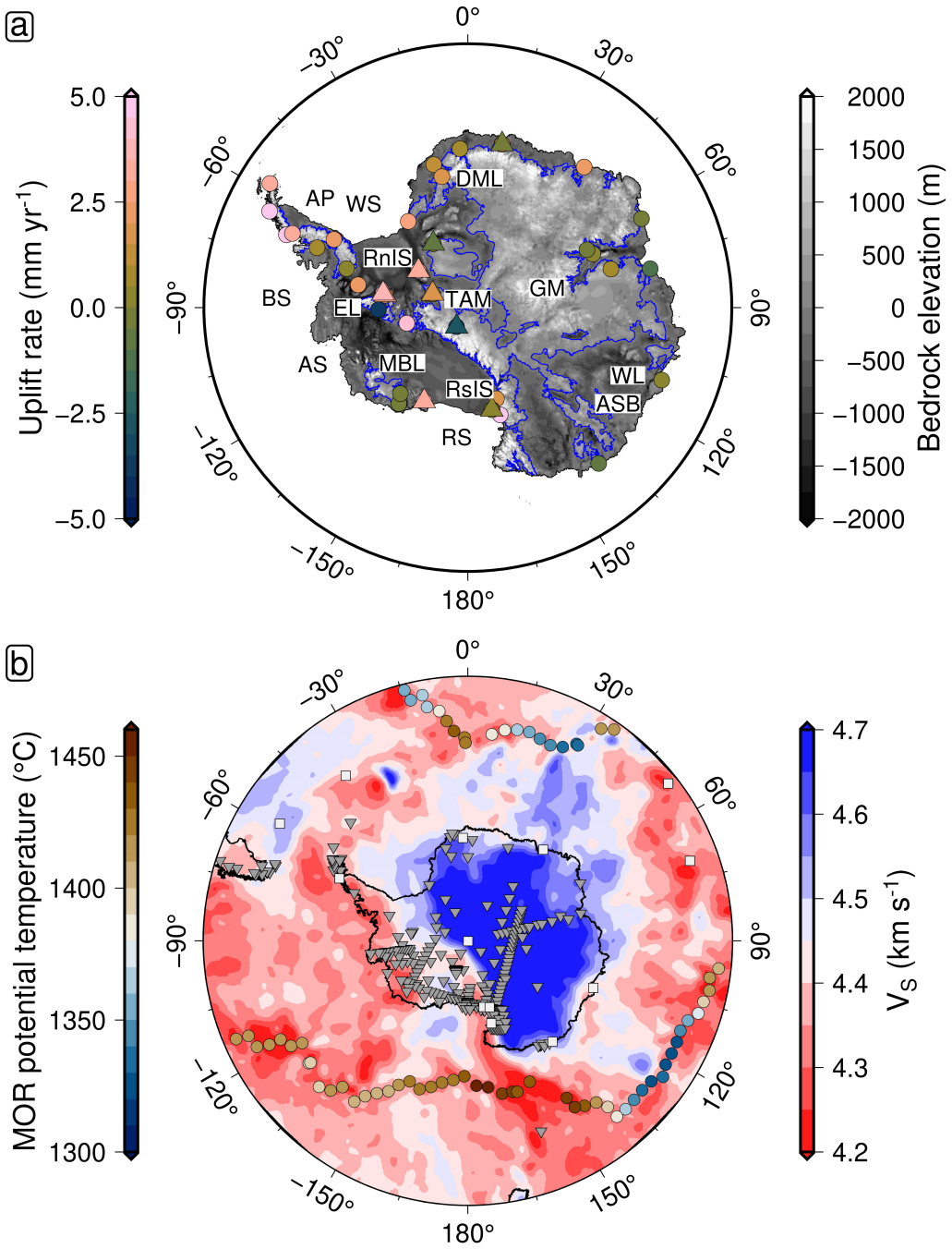


Figure 3.1: Geophysical and geochemical constraints on Antarctic mantle dynamics and structure. (a) Antarctic bedrock elevation taken from **BEDMAP2** data (Fretwell et al., 2013), with elastically corrected GPS uplift rate overlain (Thomas et al., 2011, circles: individual measurement sites; triangles: averages over local sites). Blue contours delineate the transition between positive and negative bedrock elevation. Regions of negative elevation around the periphery of the continent indicate where the AIS is marine-grounded. Text labels indicate reference points within Antarctica and the surrounding ocean (**AP**: Antarctic Peninsula; **RnIS**: Ronne Ice Shelf; **WS**: Weddell Sea; **DML**: Dronning Maud Land; **GM**: Gamburtsev Mountain Range; **WL**: Wilkes Land; **ASB**: Aurora Subglacial Basin; **RS**: Ross Sea; **RsIS**: Ross Ice Shelf; **MBL**: Marie Byrd Land; **TAM**: Transantarctic Mountain Range; **AS**: Amundsen Sea; **EL**: Ellsworth Land; **BS**: Bellingshausen Sea). (b) V_S at 150 km depth from **ANT-20** tomographic model (Lloyd et al., 2020), with mid-ocean ridge (MOR) potential temperature overlain (Dalton et al., 2014, circles). Locations of broadband seismic stations south of -45° latitude used in **ANT-20** shown by grey triangles (temporary stations), and pale grey squares (permanent stations).

a broad range of azimuths from such studies, and combining with that available from a handful of permanent stations, good data coverage could be achieved across the continent (see Figure 9 of Lloyd et al., 2020). As a result, **ANT-20** is the first continental model to image Antarctica at regional-scale resolution (~ 100 km), and thus serves as a suitable starting point for mapping temperature and viscosity with unprecedented fidelity. Promisingly, this tomographic model contains many features that are consistent with independent constraints. For example, lateral variations in V_S beneath the Antarctic mid-ocean ridge system correlate well with point estimates of potential temperature (Dalton et al., 2014; Figure 3.1b). Fast shear-wave velocities below East Antarctica are indicative of high viscosity lithosphere and slow velocities in the West point to low viscosities and thus short viscoelastic response timescales (Coulon et al., 2021).

Here the novel Bayesian inverse framework presented in Chapter 2 is applied for self-consistent quantification of upper mantle thermomechanical structure from seismic data via the calibration of experimental parameterisations of viscoelasticity (including anelasticity). Seismologically derived estimates of viscosity, temperature, LAB depth and GHF are presented. For the first time, uncertainties in each of these outputs are constrained using stochastic methods. Finally, the physical outputs presented herein are evaluated in the context of other studies, and potential implications and remaining challenges are discussed. The principal goal of this chapter is to show how disparate geophysical constraints can be integrated within a probabilistic inverse framework to develop a quantitative understanding of Antarctic upper mantle thermomechanical structure and its associated uncertainties.

3.2 Predictions of Thermomechanical Structure Beneath Antarctica

Given a depth slice of **ANT-20**, it is possible to convert each $V_S(\theta, \varphi)$ value – where θ and φ represent latitude and longitude, respectively – into an estimate of thermomechanical state (viscosity, η , temperature, T , and density, ρ) by assuming a choice of viscoelasticity model \mathcal{X}^i . To assess the improvement achieved by using the inversion procedure to refine this choice of model, a series of three mean and standard deviation viscosity structures are generated, each calculated based on the 150 km depth slice of **ANT-20**. In each case, N_U viscoelasticity models are selected, and their predictions summarised by substituting $\log_{10}\eta$ into equations (2.56) and (2.57). This results in a geometric mean and standard deviation of the viscosity at each location. In case I, each parameter is sampled independently from the prior distribution (Table 2.1). This represents, conservatively, the quality of Antarctic viscosity prediction that can be made based purely on experimental data pertaining to the mechanical behaviour of the upper mantle. In case II, each parameter is sampled independently from the posterior distribution (Table 2.1). This represents the quality of prediction it is possible to make having calibrated the viscoelasticity parameters with independent geophysical data, but ignoring any information on the covariance between parameters. Finally, in case III, the optimal approach laid out in Section 2.4 is taken, using a uniform random sample of posterior viscoelasticity models from the full set of $N_S = 200,000$ post burn-in models. This represents the best constraint on viscosity structure, including not only the refinement of individual parameters based on the data, but also information that the data provides about the model covariance structure. The use of a subset of the post burn-in models ensures computational viability. A suitable value for the sieving ratio N_U/N_S , representing the proportion of total post burn-in models used at the prediction stage, was found by investigating the additional information obtained by increasing N_U in integer

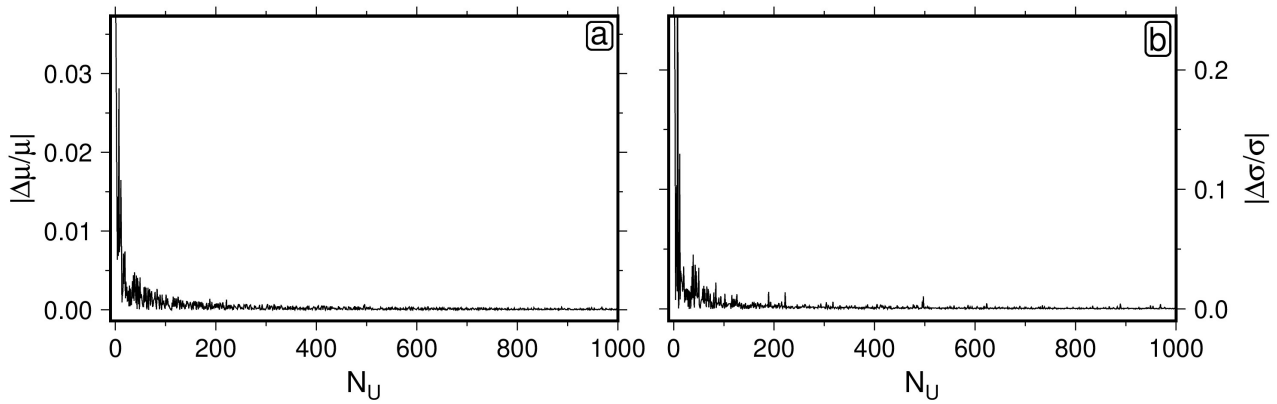


Figure 3.2: Determining the number of models required to accurately characterise posterior expectation and variance. Stability of the expectation value μ , and the uncertainty σ , of predicted viscosity at an arbitrary location ($z = 150$ km, latitude $\theta = -90.00^\circ$, longitude $\varphi = 0.00^\circ$) of the **ANT-20** V_S model, as a function of the number of randomly selected posterior viscoelasticity models used to construct them, denoted by N_U . Calculated by looking at the discrepancy in a physical prediction, X , before and after introducing an extra model, $(\hat{X}(n+1) - \hat{X}(n))/\hat{X}(n+1)$. (a) $X = \mu$. (b) $X = \sigma$.

steps, starting at 1 (Figure 3.2). It was ascertained that N_U as small as 100 was sufficient to bring deviations in the mean and standard deviation viscosity structure down to a fraction of a percentage upon the addition of an extra viscoelasticity model, and therefore a safe choice of $N_U = 1,000$ was taken.

A large reduction in uncertainty (4 to 5 orders of magnitude) is observed from case I-III (Figure 3.3), highlighting the benefit of the inversion as a whole. The most dramatic improvement occurs between case II and III, due to the effect of the highly non-diagonal covariance structure, which, due to compensation, results in muted variation in physical predictions for posterior models that encompass wide parameter ranges. Constraining the covariance structure of the physical model used to convert between shear-wave velocity and thermomechanical parameters is therefore central to the quality of the result obtained. As a result, complementary data sets such as those used to calibrate the inversion here are hugely important. It can be concluded from this assessment that the statistical inverse framework, as utilised optimally in Case III, provides the basis for improved predictions of thermomechanical structure. Therefore, this approach is taken to calculate a range of physical outputs in the results that follow.

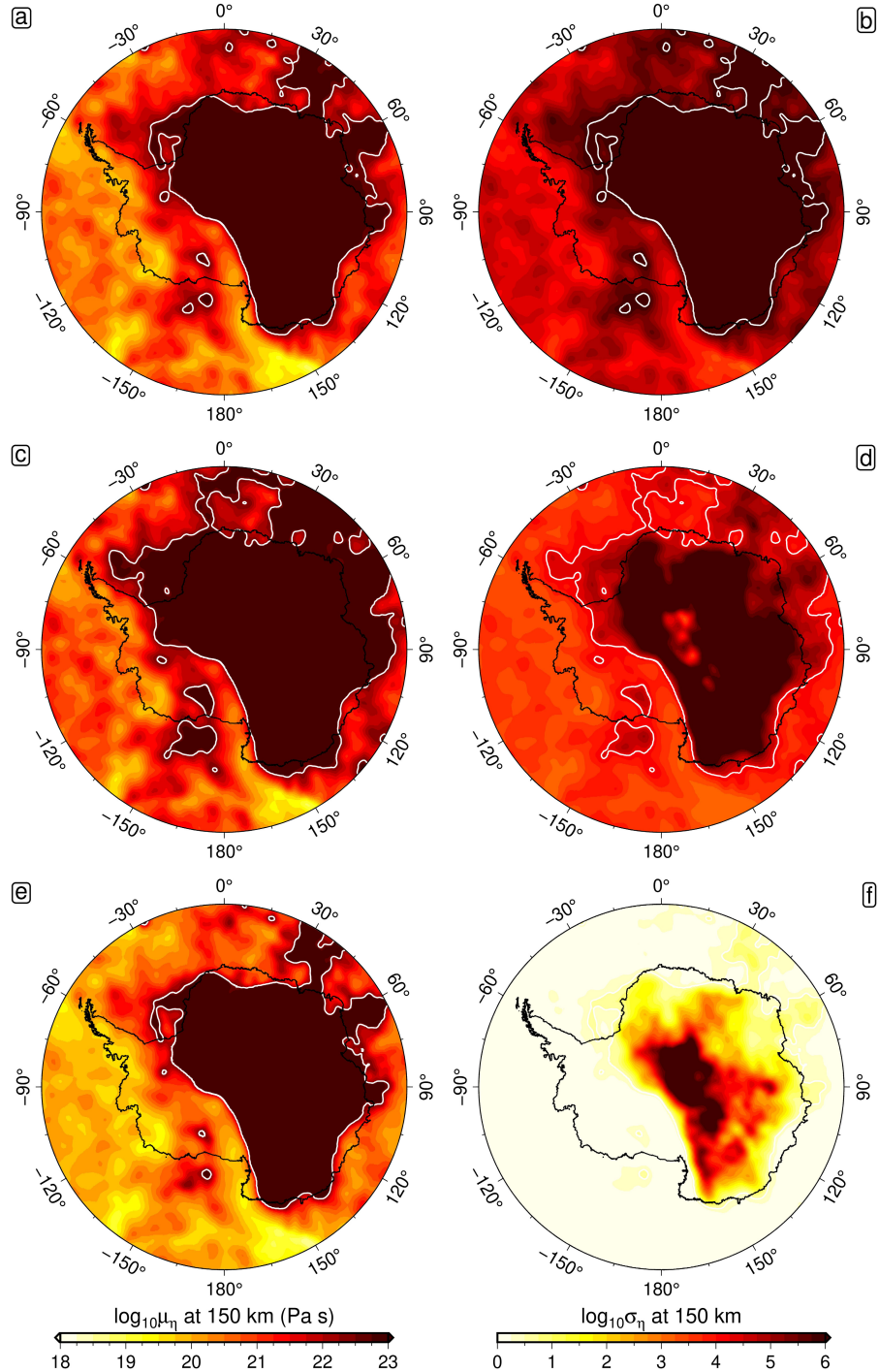


Figure 3.3: Diffusion creep viscosity and uncertainty based on forward and inverse modelling. Geometric mean (left-hand column; panels a, c, e) and standard deviation (right-hand column; panels b, d, f) viscosity structure at 150 km, calculated using three different methods. First (top row; panels a, b), by sampling viscoelasticity parameters independently from the prior distribution (see Table 2.1). Secondly (middle row; panels c, d), by sampling viscoelasticity parameters independently from the posterior distribution. Finally (bottom row; panels e, f), by sampling sets of viscoelasticity parameters from the posterior output. In each case, $N_U = 1,000$ models are used to generate the ensemble of viscosity predictions. White contours denote regions in which mean viscosity $\mu_\eta > 10^{22.5}$ Pa s.

3.2.1 Viscosity Structure

The diffusion creep viscosity structure derived from the application of the thermodynamic conversion method to the **ANT-20** V_S model contains significant lateral heterogeneity beneath the Antarctic continent and surrounding oceans. This is to be expected given the presence of shear-wave velocity anomalies up to 8% in relative amplitude observed in the underlying tomographic velocity (see Figure 11 in Lloyd et al., 2020). To show how this behaviour manifests itself in terms of viscosity variation, geometric mean and standard deviation viscosity structures are calculated as a function of depth (Figures 3.4 and 3.5). Note that at low homologous temperatures, the anelastic contribution to V_S variation is negligible, meaning that viscosities cannot be reliably constrained when $\eta > 10^{22.5}$ Pa s (white contours in Figures 3.4 and 3.5). However, this is an issue of minor significance, since regions with viscosities above this threshold have Maxwell relaxation times exceeding 20 kyr and will behave elastically over the timescales relevant to GIA modelling. In the viscosity structure analysis that follows, the asthenosphere is assumed to be the region in which $\eta < 10^{22.5}$ Pa s.

At 150 km depth, the thermomechanical dichotomy between East and West Antarctica is most obvious; a sharp viscosity boundary follows the path of the Transantarctic Mountain Range (TAM) across the continent from the Ross to the Weddell Sea. The mantle at this depth is lithospheric beneath much of the EAIS, and asthenospheric beneath the WAIS. Within West Antarctica itself, viscosity varies within the range 10^{19-23} Pa s, and it is possible to identify two long-wavelength low-viscosity anomalies. The first arises at the Macquarie Triple Junction, extends to the Balleny Islands, and follows the TAM as it passes into West Antarctica through the western side of the Ross Embayment. The second passes from Marie Byrd Land, through the Amundsen Sea Embayment, to the Antarctic Peninsula. Both anomalies contain viscosities as low as $\eta \sim 10^{19}$ Pa s, and are also identifiable at 75 km, where they form a connected region which is the only portion of asthenosphere within the continental footprint at this depth.

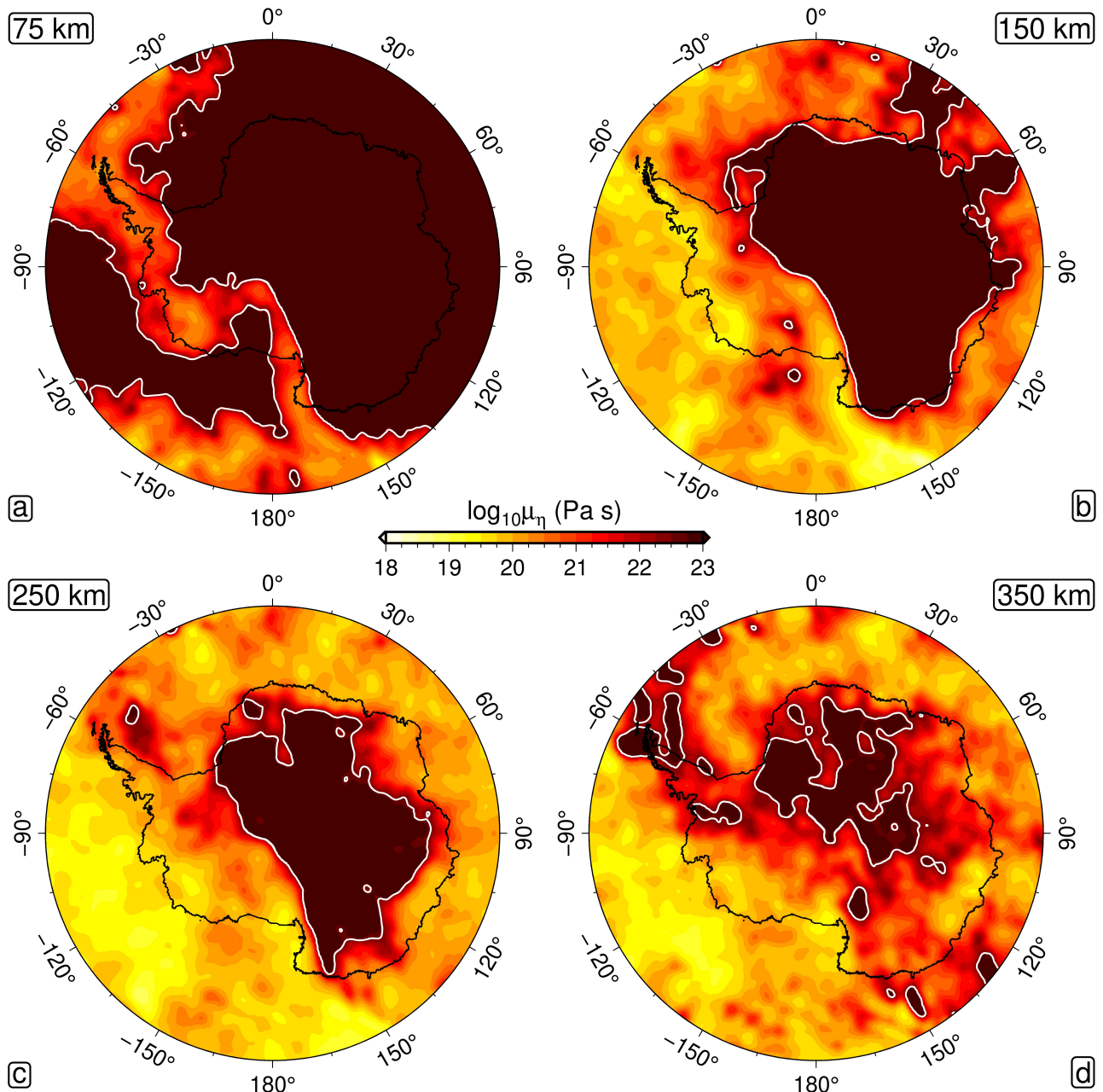


Figure 3.4: Diffusion creep viscosity beneath Antarctica. Geometric mean viscosity structure at 75 km, 150 km, 250 km and 350 km depth (a, b, c and d, respectively). Each structure is calculated by utilising a uniform random sample of $N_U = 1,000$ posterior viscoelasticity models to convert ANT-20 shear-wave velocities into viscosity, and averaging the resulting ensemble.

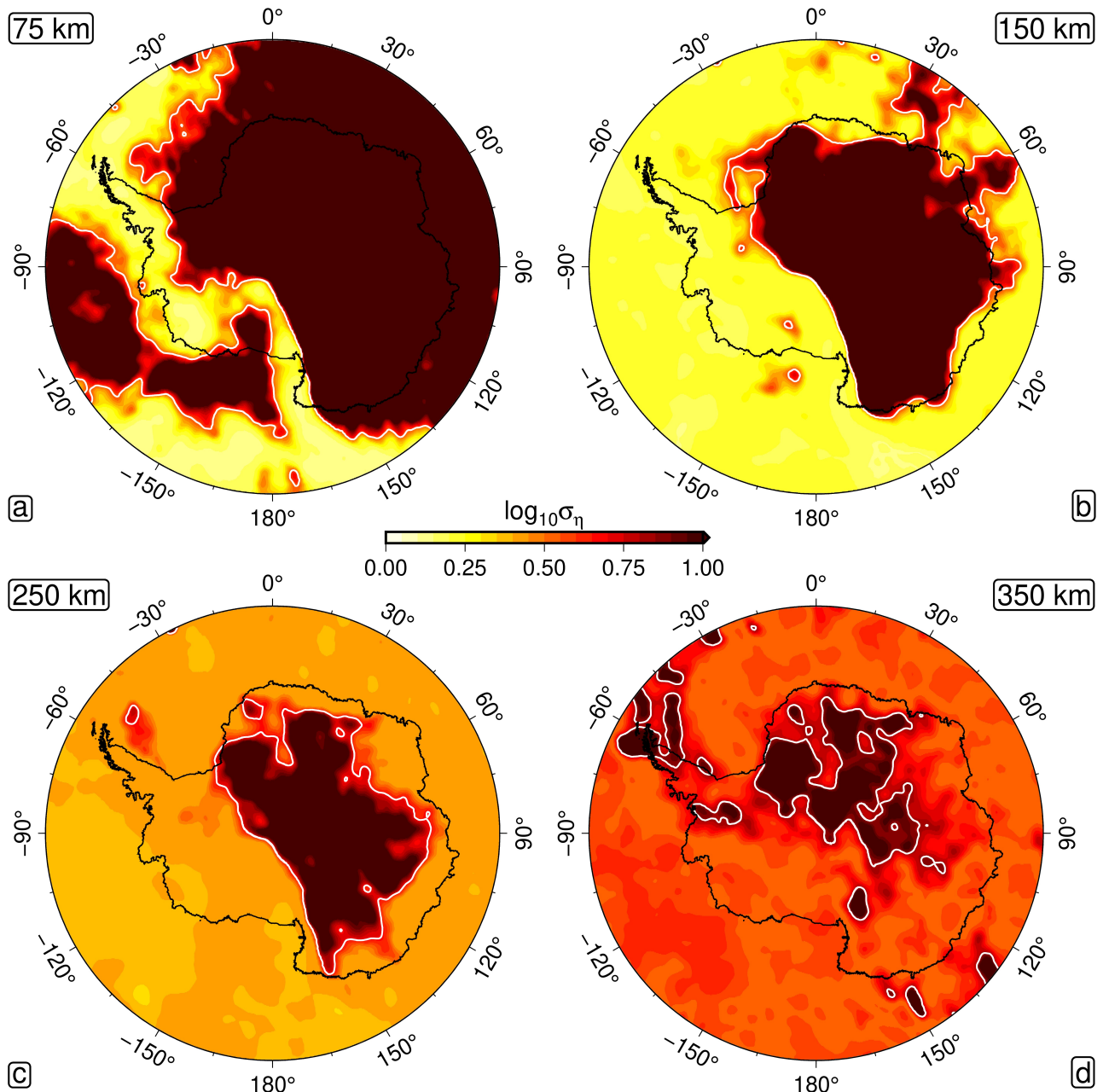


Figure 3.5: Uncertainty in diffusion creep viscosity beneath Antarctica. Geometric standard deviation viscosity structure at 75 km, 150 km, 250 km and 350 km depth (a, b, c and d, respectively). Each structure is calculated by utilising a uniform random sample of $N_U = 1,000$ posterior viscoelasticity models to convert **ANT-20** shear-wave velocities into viscosity, and determining the variance of the resulting ensemble.

Model-based uncertainty in asthenospheric viscosity is very low (~ 0.3 orders of magnitude) at 75 km and 150 km depth, and appears mostly homogeneous, albeit increasing appreciably within localised regions of very high viscosity. Given the small size of these regions (e.g., the higher viscosity patch beneath the Siple Coast at 150 km depth), it is difficult to rule out the possibility that they result from tomographic artefacts.

At deeper depths (250 km and 350 km), average asthenospheric viscosities within the continent are higher ($\bar{\eta} = 10^{20.5 \pm 0.5}$ Pa s and $\bar{\eta} = 10^{21.4 \pm 0.6}$ Pa s, in terms of median and median absolute deviation, respectively) and the area of lithospheric coverage is reduced, leading to an overall more homogeneous structure. The low-viscosity anomaly observed at shallow depths beneath the Antarctic Peninsula has evolved into a high-viscosity anomaly that extends towards the South Scotia ridge by a depth of 350 km, possibly representing a fossil slab (An et al., 2015). Low viscosity regions present beneath the Ross and Amundsen Sea Embayments at 150 km persist at these depths, although the high viscosities that separate the two regions at shallower depths appear muted or absent. In addition, a large low viscosity anomaly can be seen in the Southern Ocean in the vicinity of Marie Byrd Land, consistent with the presence of a mantle plume (Seroussi et al., 2017). Average asthenospheric viscosity uncertainty increases with depth, likely reflecting the lack of deep geophysical data used to constrain the inversion for material properties. In particular, the inversion procedure is unable to constrain activation volume beyond an individual parameter precision of approximately 10%. Since this parameter governs the pressure-dependence of viscosity, deep viscosity uncertainty is highly correlated with activation volume uncertainty. However, lateral variations in uncertainty structure remain minimal, and even at 350 km depth do not exceed an order of magnitude.

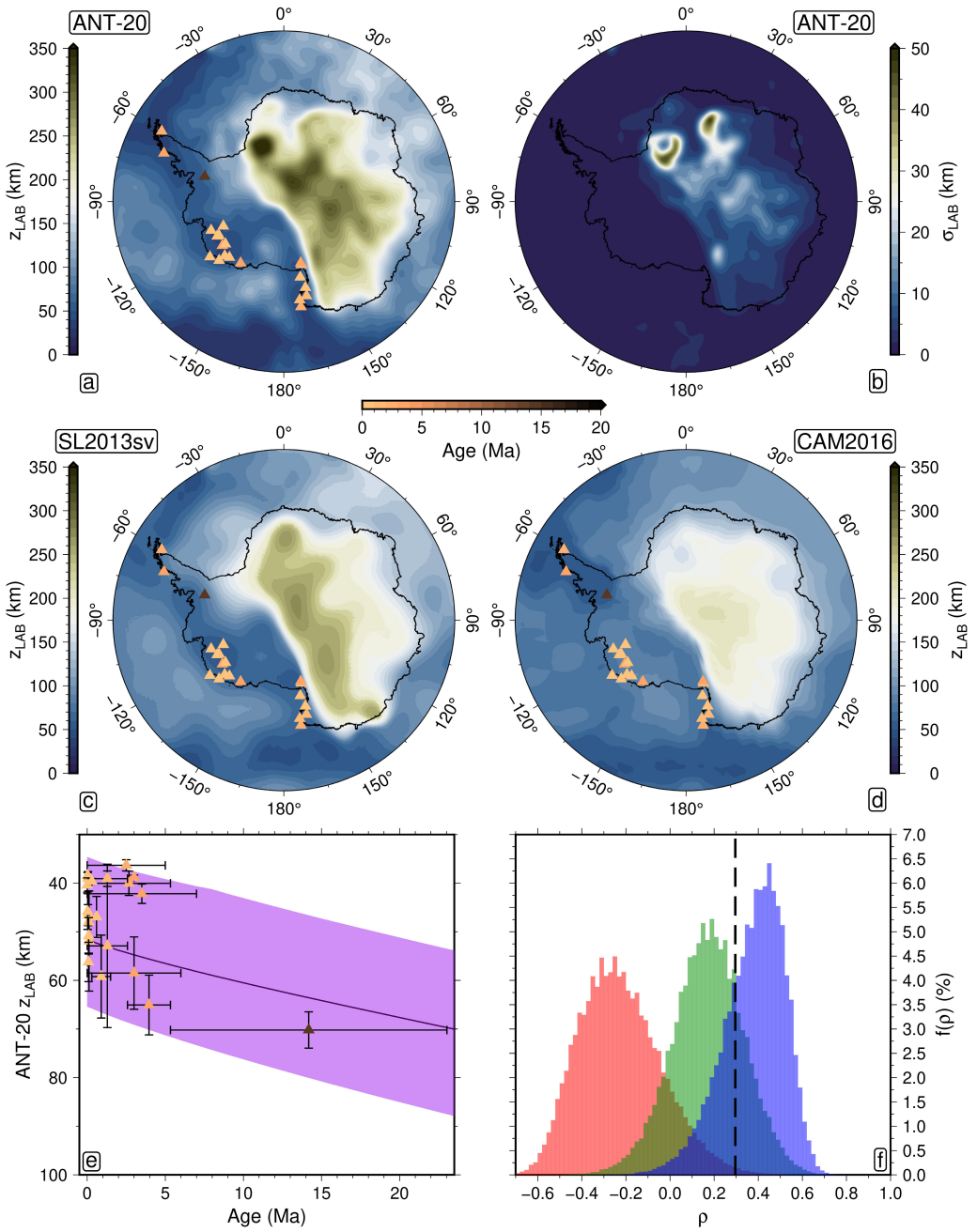


Figure 3.6: LAB depth variations beneath Antarctica. Mean (a) and standard deviation (b) LAB depth derived from **ANT-20**, as estimated from depth to the 1200°C isotherm. **ANT-20**-derived LAB structure is compared to the predictions of Richards et al., 2020a (c) and Priestley et al., 2018 (d), derived from the **SL2013sv** and **CAM2016** seismic tomographic velocity models, respectively. The LAB depth models are overlain with the minimum age since last continental magmatic activity; the relationship between these two variables is shown for **ANT-20** in (e). Histogram (f) displays the distribution of possible Spearman's Rank correlation coefficient values, ρ , between LAB depth and age for each LAB structure (**CAM2016** - red, **ANT-20** - green, **SL2013sv** - blue). Black dashed line = minimum value of ρ required for there to be a statistically significant increase in LAB depth with age at the 95% confidence level.

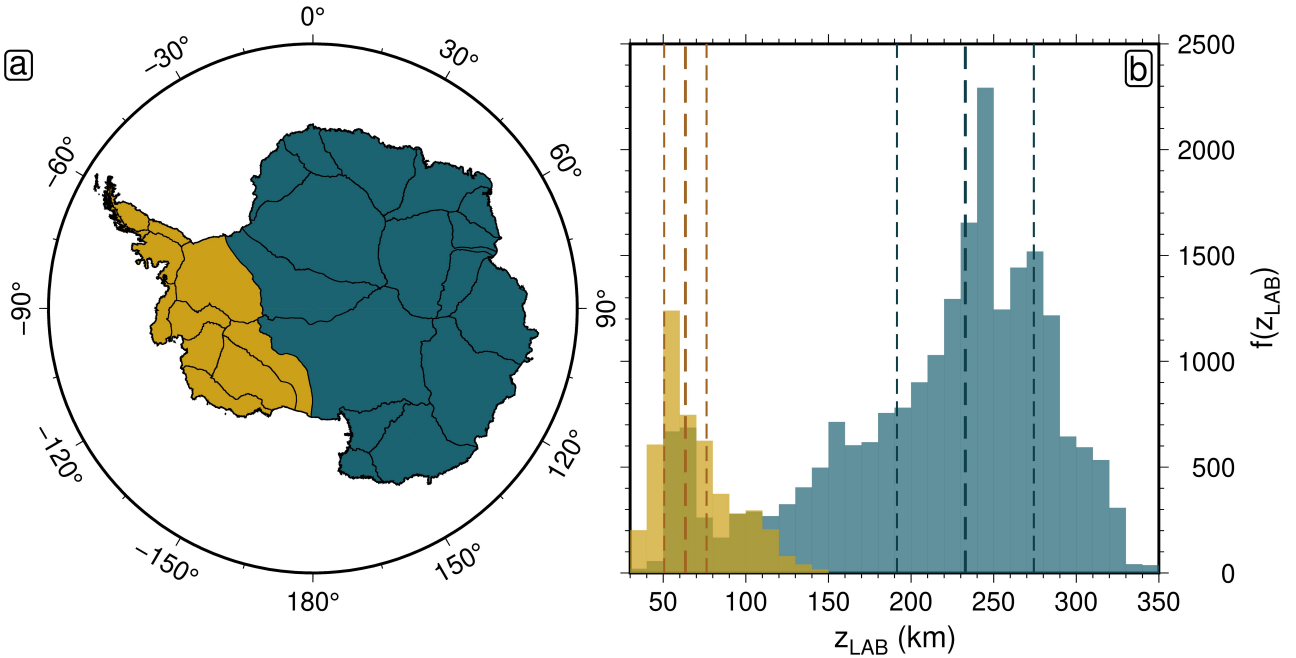


Figure 3.7: **Antarctic LAB depth dichotomy.** (a) Drainage network divides developed by the Goddard Ice Altimetry Group from **ICESat** data (Zwally et al., 2012). (b) Distribution of LAB depths beneath WAIS and EAIS (yellow and blue, respectively).

3.2.2 Lithosphere-Asthenosphere Boundary Depth

The framework used to construct self-consistent predictions of thermomechanical structure beneath Antarctica can also be utilised to constrain other parameters important for GIA and ice sheet modelling studies. First, the ensemble of three-dimensional temperature structures is used to infer LAB depth. For each temperature structure associated with a given choice of viscoelasticity model in the ensemble, the laterally varying geothermal profiles are interpolated to a 1 km depth interval. Prior to interpolation, anomalous temperatures associated with downward bleeding of crustal velocities in the underlying tomographic velocity are removed by identifying spurious reversals of the geothermal gradient and excising temperatures above these loci. In all cases, a temperature of 0 °C is enforced at the basement depth, which can be estimated using the Moho depth and crustal thickness grids associated with the tomographic velocity. Following interpolation, the depth at which the resulting profile intersects a temperature of 1200 °C is extracted, which serves as a proxy for LAB depth (Figure S6, Burgos et al., 2014; Richards et al., 2018). By summarising the set of ensemble predictions of laterally

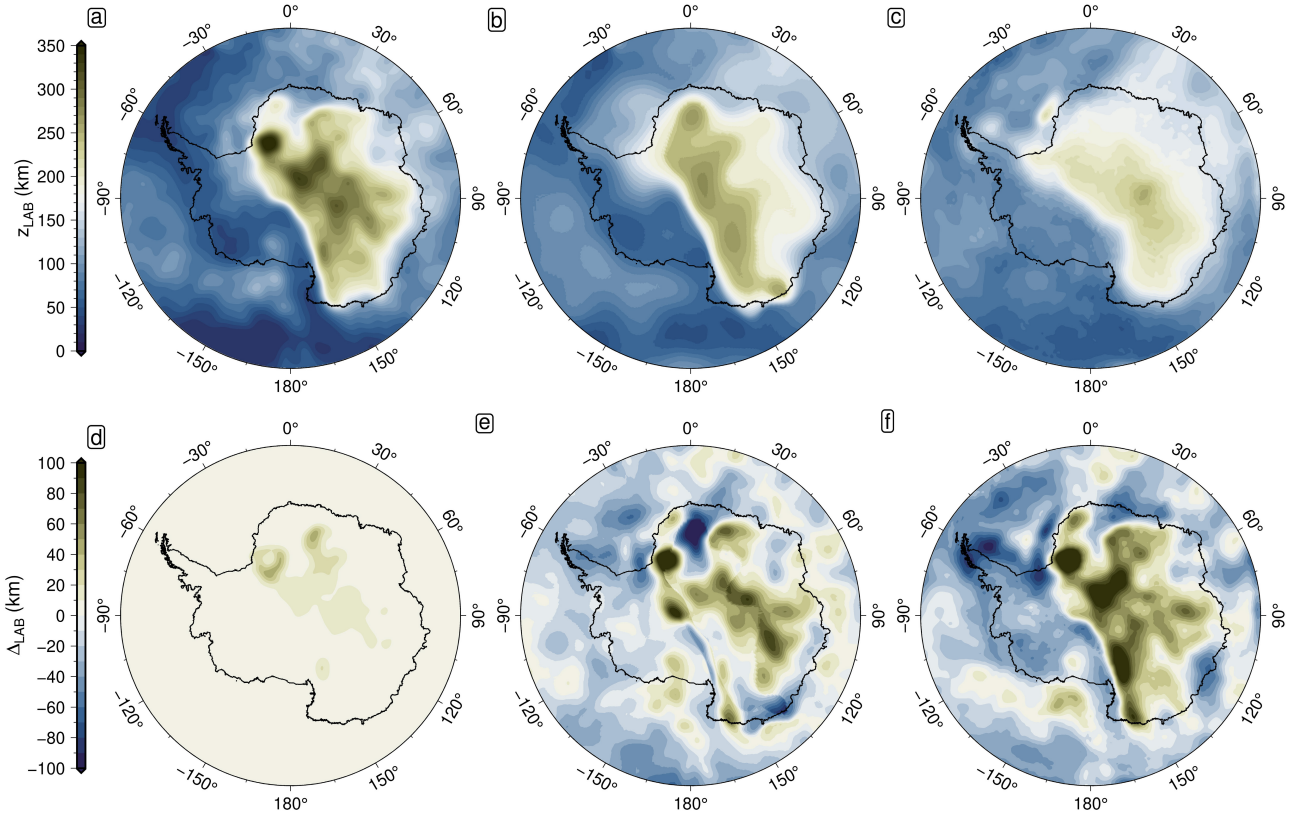


Figure 3.8: **Comparison of LAB depth variations to contemporary studies.** LAB depth estimates from this study (mean *a posteriori* model), Richards et al. (2020a) and Pappa et al. (2019) (panels a, b, and c respectively). LAB depth uncertainty estimate from this study (panel d). Difference in estimated LAB depth between this study and the studies of Richards et al. (2020a) and Pappa et al. (2019) (panels e, and f respectively).

varying LAB depth, according to equations (2.56) and (2.57), a mean and standard deviation LAB depth structure is arrived at (Figure 3.6).

The resulting mean LAB depth displays a number of interesting features. Good agreement is found with long-wavelength structure observed elsewhere in the literature (Priestley et al., 2018; Richards et al., 2020a), whereby LAB depth exceeds 150 km beneath the EAIS, and is much lower beneath the WAIS. Spatially averaged LAB depths of 233 ± 41 km and 63 ± 13 km are found beneath the respective ice sheets, calculated according to the median and median absolute deviation. The overall strength of this heterogeneity is high, involving LAB depths as shallow as 35 km in the West, and as deep as 365 km in the East. A comparison of the LAB depth derived in this study to that of Richards et al. (2020a), as well as Pappa et al. (2019), is shown in Figure 3.8. The work of Richards et al. (2020a) is based on a global

calibration of YT16 viscoelasticity parameters, using the tomography model **SL2013sv**, and a deterministic inversion procedure. The work of Pappa et al. (2019) is based on a combination of satellite gravity data with seismological and petrological modelling. All structures exhibit a clear dichotomy in LAB depth between West and East Antarctica. The largest dichotomy is exhibited in this study's LAB depth estimate, with a range of 35 to 365 km, while the most muted dichotomy is exhibited in the estimate of Pappa et al. (2019), with a range of 70 to 260 km. The average discrepancy between this study's LAB depth estimate and that of the other studies is less than 10 km in each case, and there is reasonable agreement between the studies in West Antarctica. In this region, the model developed in this study is on average 11 ± 7 km shallower than that of Richards et al. (2020a), and 32 ± 8 km shallower than that of Pappa et al. (2019). However, beneath East Antarctica, the discrepancies grow much larger. Here, the model presented in this study is on average 19 ± 22 km deeper than that of Richards et al. (2020a), and 40 ± 25 km deeper than that of Pappa et al. (2019). The full distribution of LAB depths represented by East and West Antarctica are shown in Figure 3.7, along with the classification used to distinguish between the two continental components, which is based on the satellite-mapped drainage network (Zwally et al., 2012).

The maximum ~ 15 km depth resolution and ~ 100 km lateral resolution of the underlying tomographic velocity is the dominant source of uncertainty on the calculated LAB structure over much of Antarctica, as a result of the low variance in LAB depth predictions provided by the ensemble of viscoelasticity models. However, this is not the case in certain areas of East Antarctica, where very large inferred LAB depths are also associated with large uncertainties, of order 30 to 40 km. The statistical uncertainty associated with the ensemble of viscoelasticity models is expected to rise with increasing LAB depth due to elevated temperature uncertainty with depth arising from the previously discussed uncertainty in activation volume.

By comparing the predictions of LAB depth derived from this study to geological con-

straints not linked to the viscoelasticity calibration procedure, it is possible to verify that the temperature structures arrived at via the inversion method are realistic. The location and timing of Cenozoic magmatism was analysed using a compilation of geochemical analyses on volcanic material (Ball et al., 2021; DIGIS Team, 2021). The data were spatially binned over a length scale of 100 km, in accordance with the seismological resolution, with minimum time since last eruption and its associated uncertainty extracted. The data were further processed to remove points with age uncertainties exceeding 10 Ma and the resulting data set mapped (Figure 3.6). Two key observations are immediately apparent when comparing magmatism and LAB depth. First, all sites containing a record of Pliocene or Quaternary (i.e., 5.33 Ma to present) eruptions lie above **ANT-20** derived LAB depths in the range 35 to 70 km; the shallowest continental depths predicted by the present day seismic structure. This result is consistent with geodynamic expectations, since for a reasonable range of mantle temperature and hydration conditions, significant decompression melting is only expected in regions with LAB depth shallower than 80 km (Ball et al., 2021). Secondly, the minimum age since last eruption falls within the Miocene epoch for the remaining site, and here, LAB depth exceeds 70 km. The lack of more recent magmatism in this region indicates that the source of such magmatism has been removed over geological timescales. If this is the case, the LAB would have recovered to an equilibrium depth more representative of mean mantle conditions, thus further validating the model predictions of this study.

To validate this hypothesis, models of conductive cooling were used to determine the expected increase in LAB depth as a function of geological time. The thermal modelling approach of Richards et al. (2020b) was adapted, imposing an initial temperature condition that assumes a steady-state geotherm has been established by the time active magmatism ceases. To model lithospheric rethickening following periods of active magmatism, the one-dimensional

heat equation is solved, which can be expressed as

$$\rho(P, T, X)C_P(T, X)\frac{\partial T}{\partial t} = \frac{\partial}{\partial z} \left[k(P, T, X)\frac{\partial T}{\partial z} \right] + H^*(X), \quad (3.1)$$

where t is time, z is depth, T is temperature, P is pressure, X is composition, ρ is density, C_P is the isobaric specific heat capacity, k is the thermal conductivity, and H^* is the internal radiogenic heat production.

This equation is solved numerically with an unconditionally stable time- and space-centered Crank-Nicholson finite difference scheme and a predictor-corrector step (Press et al., 2007). Accordingly, Equation 3.1 is recast as

$$\begin{aligned} T_j^{n+1} + A \left(-\frac{k_{j+\frac{1}{2}}^m}{\Delta z_j^m} T_{j+1}^{n+1} + \left(\frac{k_{j+\frac{1}{2}}^m}{\Delta z_j^m} + \frac{k_{j-\frac{1}{2}}^m}{\Delta z_{j-1}^m} \right) T_j^{n+1} - \frac{k_{j-\frac{1}{2}}^m}{\Delta z_{j-1}^m} T_{j-1}^{n+1} \right) \\ = T_j^n + A \left(\frac{k_{j+\frac{1}{2}}^m}{\Delta z_j^m} T_{j+1}^n - \left(\frac{k_{j+\frac{1}{2}}^m}{\Delta z_j^m} + \frac{k_{j-\frac{1}{2}}^m}{\Delta z_{j-1}^m} \right) T_j^n + \frac{k_{j-\frac{1}{2}}^m}{\Delta z_{j-1}^m} T_{j-1}^n \right) + AH^* (\Delta z_j^m + \Delta z_{j-1}^m), \end{aligned} \quad (3.2)$$

where

$$A = \frac{\Delta t}{\left(\rho_j^m C_P j (\Delta z_j^m + \Delta z_{j-1}^m) \right)}, \quad (3.3)$$

Δt is the time step, Δz is the depth spacing between nodes, and n and j are the time and depth indices, respectively. Equation 3.2 is solved by tridiagonal elimination (Press et al., 2007). For the initial predictor phase of each time step, $m = n$, whilst in the subsequent corrector phase, $m = n + \frac{1}{2}$. A Lagrangian reference frame is used, whereby Δz_j^m is initially set to 1 km (i.e., when $m = 0$), then scales with thermal contraction in subsequent time steps. The time step,

Δt , is calculated using a Courant-Friedrichs-Lowy condition according to

$$\Delta t = \min_j \left[\frac{\left(\Delta z_j^0 \right)^2 \rho_j^0 C_P^0}{2.2 k_j^0} \right] \sim 5 \text{ kyr.} \quad (3.4)$$

Convergence of T^{n+1} to within a tolerance of 0.001°C is typically achieved after the corrector phase.

The two-layer models employed in this study include a continental crust of thickness, $T_c = 10\text{--}40 \text{ km}$, and an underlying mantle extending from the Moho to the assumed equilibrium plate thickness, $z_p = 250 \text{ km}$. Separate parameterisations are used to define the thermophysical properties of each layer (k , C_P , ρ , and H^*). In the mantle, the temperature- and pressure-dependent formulations specified in Richards et al. (2020b) are adopted, with radiogenic heat production assumed to be negligible ($H^* \sim 0 \text{ mW m}^{-3}$). In the crustal layer, radiative thermal conductivity and density are determined using the Richards et al. (2020b) parameterisation for oceanic crust, but with reference density, ρ_0 , reduced from 2950 kg m^{-3} to 2700 kg m^{-3} , a value more compatible with a continental setting. By contrast, continental crustal heat capacity and lattice thermal diffusivity, κ_{lat} , are calculated using the parameterisation of Whittington et al. (2009), while radiogenic heat production is assumed to be 0.7 mW m^{-3} (Hoggard et al., 2020).

Initial temperature profiles are obtained by combining these parameterisations with the equations of McKenzie et al. (2005) to calculate steady-state temperature profiles for specified values of potential temperature ($T_P = 1358\text{--}1507^\circ\text{C}$), crustal thickness ($T_c = 10\text{--}40 \text{ km}$), and initial LAB depth ($z_{LAB}^0 = 35\text{--}65 \text{ km}$). The aforementioned ranges are based on seismically inferred values beneath the Antarctic magmatic provinces. In all cases kinematic viscosity, ν , is assumed to be $9 \times 10^{19} \text{ Pa s}$. For each combination of T_c and T_P , the steady-state geotherm consistent with a given initial LAB depth value was found by iterating through a range of mechanical boundary layer (MBL) thicknesses (2–60 km), and selecting the temperature profile

with depth to the 1200°C isotherm equal to z_{LAB}^0 .

To simulate the waning of a plume-derived heat source through time, an evolving basal boundary condition is imposed. At $t = 0$, temperature is set to be constant and equal to the values of the relevant input geotherm at depths greater than the base of the thermal boundary layer (i.e., the shallowest depth at which the geothermal gradient, $\frac{\partial T}{\partial z}$, drops below $0.5^\circ\text{C km}^{-1}$). In later time steps, the depth node at which this boundary condition is imposed increases according to a prescribed plume sinking rate, $v_{\text{plume}} = 1 \text{ mm yr}^{-1}$, until the deepest node is reached, whereupon the basal boundary depth remains fixed. At the same time, from $t = 0$ –15 Myr, the temperature applied at the basal boundary decays linearly back towards equivalent values for an ambient mantle adiabat ($T_P = 1333^\circ\text{C}$). This 15 Myr timescale was determined from V_S -derived estimates of Antarctic potential temperature change as a function of age since last eruption. Beyond $t = 15$ Myr, the basal temperature is assumed to remain equal to that of the ambient mantle adiabat at the appropriate depth.

By tracing the depth of the 1200°C isotherm throughout the model runs, predicted conductive rethickening can be directly compared with the magmatic age-dependent LAB depth trends observed across Antarctica (Figure 3.6e). This depth evolution accounts for contraction and subsidence of the lithosphere through time following the isostatic formulation given in Richards et al. (2020b). In order to compare the output of the conductive cooling models to the data, spatially binned eruption age values are tied to a prediction of LAB depth and its uncertainty, calculated by taking the average and standard deviation of the depths within each bin (Figure 3.6e). The magmatic data are fully consistent with the post-magmatic lithospheric thickening models, suggesting that the seismically inferred LAB values are reliable.

To further investigate whether the data implies the existence of a monotonic relationship between LAB depth and minimum age since last eruption, a statistical test was applied. A Monte Carlo approach was employed to simulate the distribution of possible trends according

to the uncertainty reported on each LAB depth-age data point, as follows. For each data point, d_i , initially located at $d_i = (a_i, z_i)$ in age-depth space, a random perturbation, $\Delta_i = (\alpha_i, \zeta_i)$, is added by drawing from a normal distribution with diagonal covariance scaled by the location-dependent age and depth uncertainties. The resulting trend represents one possible combination of “true” age-depth values, and a corresponding Spearman’s Rank correlation coefficient is calculated for this trend. This process is repeated until convergence, resulting in a distribution of possible correlation coefficients for each LAB depth model (Figure 3.6f). For us to associate a given coefficient with statistically significant evidence for the existence of a positive monotonic relationship between LAB depth and minimum age since last eruption at the 95% confidence level, it must exceed a value of $\rho = 0.296$.

It was found that the **ANT-20** and **SL2013sv** derived LAB models satisfied this statistical test to at least the 1σ level, with coefficients $\rho = 0.17 \pm 0.16$ and $\rho = 0.38 \pm 0.14$ respectively. This result suggests that both models make reliable LAB depth predictions in the context of the geological record. It is unlikely however that the improved correlation offered by **SL2013sv** necessarily translates into this being a more realistic LAB model than **ANT-20**. This is because while, in each case, the spatial binning procedure was conducted over a 100 km radius, the true lateral resolution of **SL2013sv** is much poorer than **ANT-20** over Antarctica. The resulting LAB model is therefore laterally smoother, reducing spatially binned LAB depth uncertainties and potentially improving the average trend observed in the age-depth data. It is unlikely that the LAB model derived from **CAM2016** satisfies the test for statistical significance, owing to a coefficient, $\rho = -0.23 \pm 0.19$, such that less than 1% of possible age-depth trends contain a statistically significant positive gradient. This result may indicate that the LAB depth predictions of **CAM2016** are less reliable in the Antarctic region than its counterparts. Nevertheless, there are several limitations on this analysis imposed by the small size of the magmatic dataset, significant clustering of data points within age-depth space, and large age uncertainties on cer-

tain data points. These have a non-negligible impact on the calculated correlation coefficients, and so this analysis does not provide conclusive evidence for the reliability, or lack thereof, of any given seismologically derived LAB depth model.

3.2.3 Geothermal Heat Flow

In addition to calculating LAB depth, it is possible to constrain continental geothermal heat flow by fitting a steady-state, laterally varying geotherm to the ensemble of three-dimensional temperature structures following the procedure laid out in McKenzie et al. (2005). At shallow depths, the downward bleeding of crustal velocities results in anomalously high temperatures, which must be excised from the data prior to fitting. This was achieved by applying two criteria. The first was to remove data points shallower than the Moho depth. The second was to remove any portion of the raw geothermal profile directly beneath the Moho where the temperature gradient is negative ($\partial T / \partial z < 0$). An additional constraint that the temperature reaches 0 °C at the basement depth was added to the data. The resulting temperature profile was interpolated on a 1 km interval. LAB depth was calculated by finding the depth at which the interpolated geothermal profile first reaches 1200 °C (Figure 3.9).

Initially, a constant value for the mantle potential temperature ($T_P = 1333$ °C) was used in the geothermal profile fitting procedure at each location, consistent with the geochemically constrained global average (Richards et al., 2018). This enabled an estimate of the empirical linear fit between LAB depth (as defined by the depth to the 1200 °C isotherm) and thermal boundary layer depth to be calculated, according to

$$z_{\text{TBL}} = a \times z_{\text{LAB}} + b. \quad (3.5)$$

The fitting parameters were determined using orthogonal distance regression to be $a = 1.839 \pm 0.001$, and $b = -16.5 \pm 0.2$ km. Then, a spatially variable mantle potential temperature was

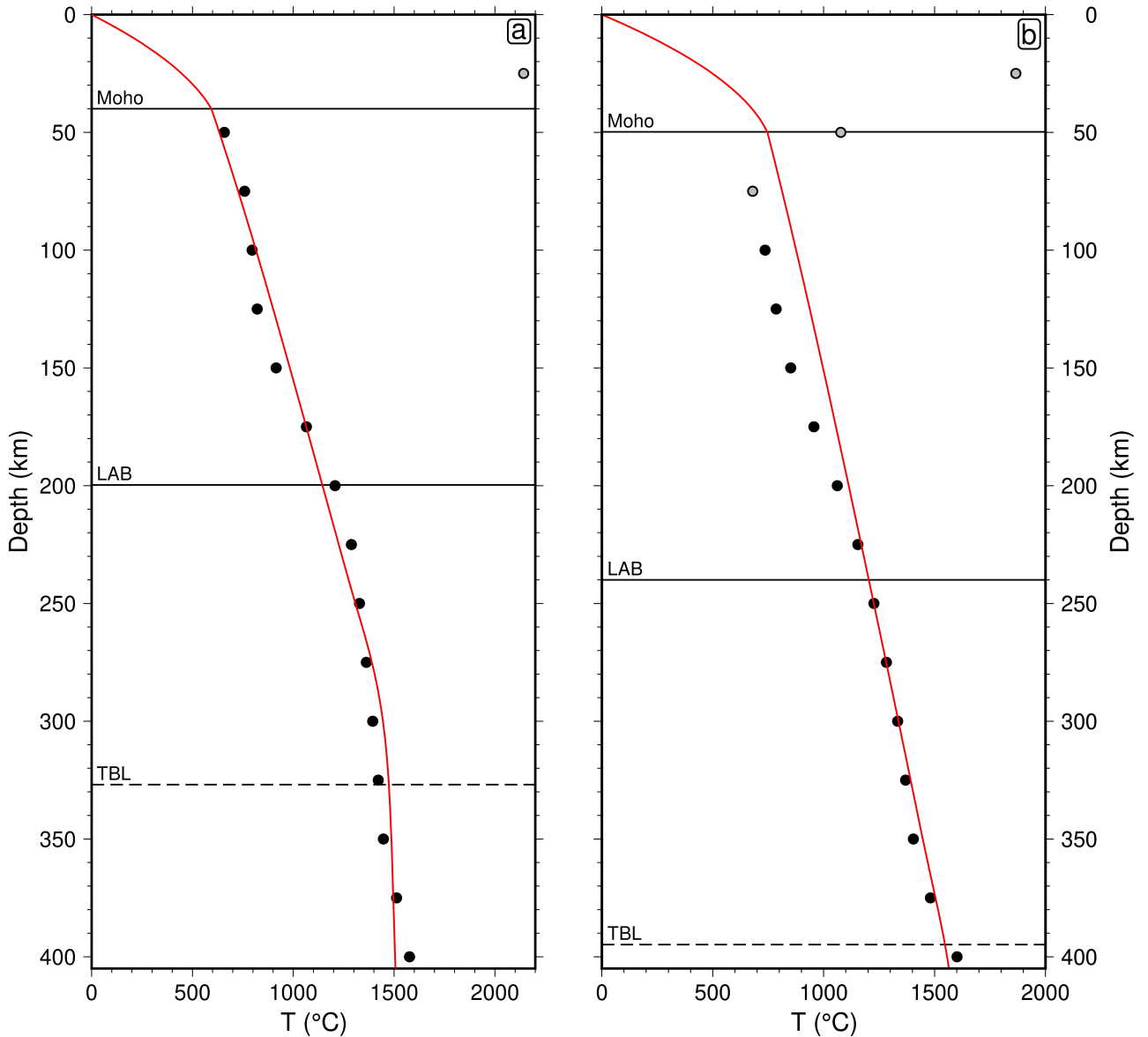


Figure 3.9: Processing and fitting geothermal profiles. Raw (circles) and fitted (red line) temperature structure shown for two different locations (a: latitude $\theta = -79.0^\circ$, longitude $\varphi = 15.0^\circ$; b: latitude $\theta = -80.0^\circ$, longitude $\varphi = 50.0^\circ$). Gray circles are raw data removed prior to interpolation and fitting, based on Moho depth and temperature gradient criteria. Moho depth taken from [ANT-20](#) (Lloyd et al., 2020), LAB depth calculated based on intersection between interpolated geothermal profile and 1200° isotherm. Thermal boundary layer (TBL) depth estimated based on an empirical scaling from LAB depth.

calculated by averaging the interpolated geothermal structure between the empirically fitted thermal boundary layer depth and 400 km. Finally, the geothermal profile fitting procedure was repeated using the spatially variable mantle potential temperature. Geothermal heat flow was calculated by multiplying the crustal conductivity by the temperature gradient at base-
 ment depth. In constructing a modelled geothermal profile at a given location, it is necessary to account for lateral variations in crustal thickness, as well as depth variations in radiogenic heat production and conductivity. As previously, the crustal thickness grid associated with the tomographic velocity model was used, to ensure self-consistency. For crustal heat production, a value of $H_{\text{ocean}}^* = 0.0 \mu\text{W m}^{-3}$ is assumed within the ocean, distributed uniformly throughout the crustal layer. Within the continent, the crust is divided into two layers of equal depth. Values of $H_{\text{cont}}^* = 1.0 \mu\text{W m}^{-3}$ and $H_{\text{cont}}^* = 0.3 \mu\text{W m}^{-3}$ are assumed in the upper and lower crustal layers, respectively. This two-layer continental heat production parameterisation is compatible with globally averaged values obtained from the comprehensive crustal geochemical analysis of Sammon et al. (2022), and is preferred for two main reasons. Firstly, the simplicity of the parameterisation avoids assuming more detailed knowledge of the three-dimensional distribution of heat producing elements within the crust than is currently available. Secondly, it reduces the sensitivity of the crustal radiogenic heat content to regions of anomalously thick crust, as compared to assuming a single crustal layer of constant heat production (although this sensitivity remains non-negligible). Mantle and oceanic crust conductivity are calculated according to the temperature- and pressure-dependent parameterisation of Korenaga and Korenaga (2016). In the continent, crustal conductivity is set to a constant value of $k_{\text{crust}} = 2.5 \text{ W m}^{-1} \text{ K}^{-1}$. These assumptions simplify the true lateral and depth dependence of heat production and conductivity within the continental crust, which are expected to vary within the range $H_{\text{cont}}^* \sim \{0.0, 3.0\} \mu\text{W m}^{-3}$ and $k_{\text{crust}} \sim \{1.0, 4.0\} \text{ W m}^{-1} \text{ K}^{-1}$ (Jennings et al., 2019). Investigating the effect of the variation of these two parameters on the resulting heat flow is not

the focus of this chapter, but is discussed in detail in Chapter 4. However, a close fit between theoretically and V_S -derived geothermal profiles calculated using these simple parameter assumptions suggests the first-order control on GHF estimates is the seismically inferred thermal structure rather than the chosen crustal parameterisation. With this in mind, a laterally varying mantle potential temperature is used during the fitting process, estimated according to the average V_S -derived temperature beneath the base of thermal boundary layer.

Resulting estimates of spatially averaged continental energy transfer rates are $44 \pm 2 \text{ mW m}^{-2}$ into the base of the EAIS, and $76 \pm 7 \text{ mW m}^{-2}$ into the base of the WAIS, where the ‘uncertainty’ in this case relates purely to lateral variations in mean heat flow (Figure 3.10). Both sides of the continent contain GHF variations in excess of 40 mW m^{-2} . However, East Antarctica is less heterogeneous, with over 75% of its area characterised by GHF in the region 40 to 50 mW m^{-2} . By contrast, the WAIS is underlain by bedrock feeding it anywhere from approximately 50 to 100 mW m^{-2} of geothermal energy, with heat flow unevenly distributed across the region. The connection of two long-wavelength (exceeding 10,000 km) thermal anomalies into a single anomaly, observed in the viscosity structure at 75 km depth (Figure 3.4a), can also be seen here to stretch from the Ross Sea through Marie Byrd Land and up to the Antarctic Peninsula, before stretching offshore towards the South Scotia ridge. Most of this anomaly is located within West Antarctica, with the exception of its eastern edge within Marie Byrd Land and Victoria Land. The presence of this anomaly, combined with shorter-wavelength ($\sim 1,000$ – $10,000 \text{ km}$) cold anomalies observed in Marie Byrd Land and Ellsworth Land, together make up a highly heterogeneous West Antarctic GHF structure.

3.3 Discussion

In the text to follow, it is shown how the results presented in this study build upon existing evidence of strong lateral heterogeneity in Earth’s internal thermomechanical structure beneath

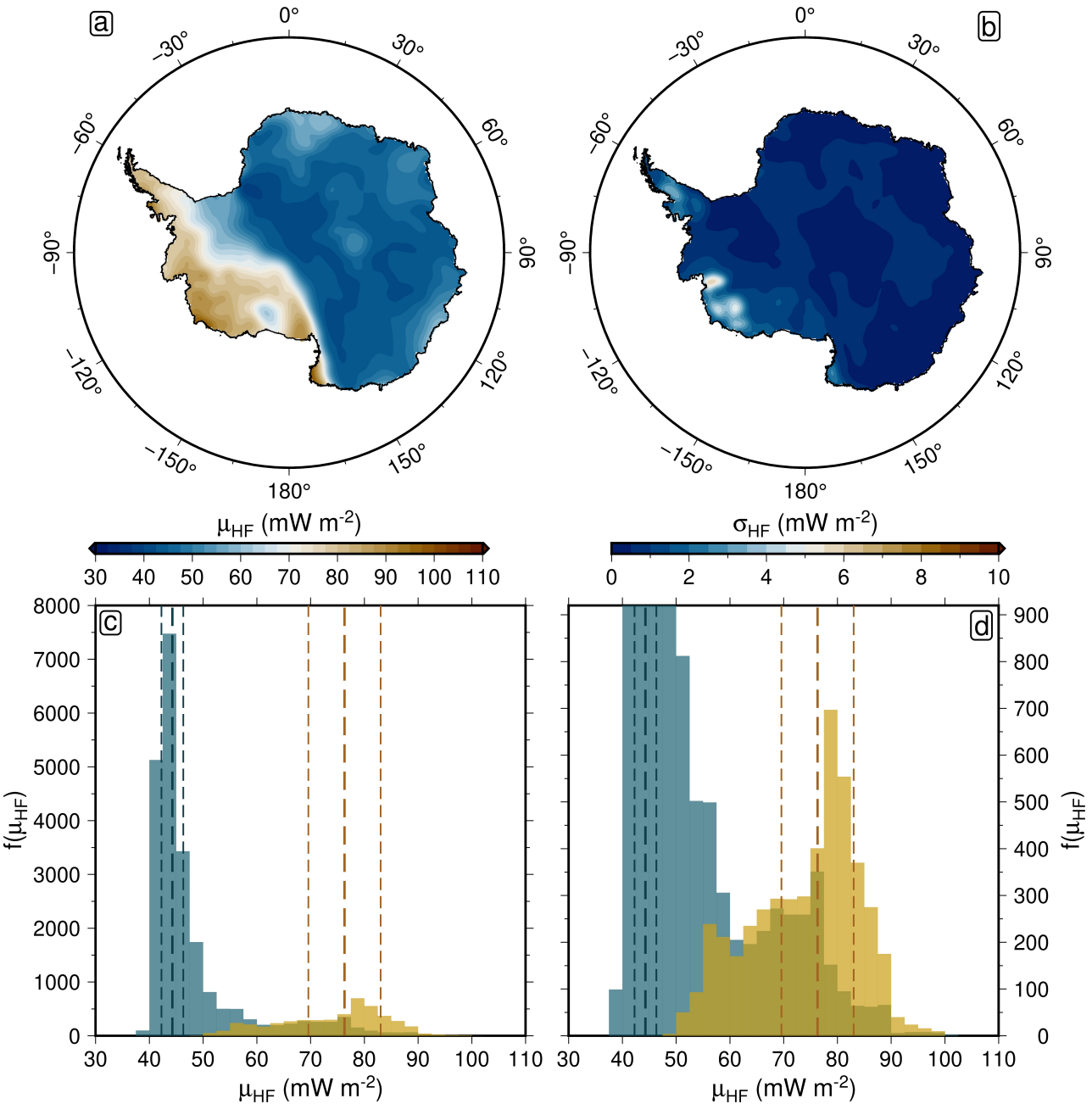


Figure 3.10: GHF variations across Antarctica. Mean (a) and standard deviation (b) GHF derived from ANT-20. Estimated by fitting steady-state geotherms to temperatures inferred from an ensemble of viscoelasticity models. Distribution of GHF into base of West Antarctic and East Antarctic Ice Sheets (c; yellow and blue, respectively). Zoom-in of distributions (d). Regional separation calculated according to the pattern of Antarctic drainage systems, see Figure 3.7. Thick dashed lines show the median of each distribution. Thin dashed lines are located one median absolute deviation away from the median of each distribution.

Antarctica, leading to spatially variable LAB depth and GHF. First, the dichotomy between West and East Antarctic thermomechanical structure is discussed, along with implications for ice sheet stability. Secondly, GHF predictions are compared to those of a recent study by Shen et al. (2020). Thirdly, it is discussed how a consideration of physical forcing timescale can be used to reconcile observations and model predictions of mantle viscosity. Finally, the most significant sources of remaining uncertainty in quantifying mantle structure are summarised.

3.3.1 West and East Antarctic Mantle Structure

Evidence is found that steady-state diffusion creep viscosities reach a lower threshold of $\eta \sim 10^{19}$ Pa s throughout the shallow mantle (150 to 350 km) beneath West Antarctica. Uncertainty in asthenospheric viscosity structure is found to be within one order of magnitude across the full depth range 0 to 400 km of study, and increases with depth. Low-viscosity anomalies observed within the mantle viscosity structure correspond with spatial patterns in LAB depth and GHF structure, whereby negative and positive anomalies are observed, respectively, which is to be expected given the self-consistent framework within which each of these parameters is estimated. For example, viscosities of $10^{19.5 \pm 0.3}$ Pa s present at 150 km depth in western Marie Byrd Land towards the Amundsen Sea Embayment are associated with thin LAB depths (30 to 50 km) and elevated GHF (85 to 95 mW m⁻²), where quoted ranges represent spatial variability within this region. The inference that such low viscosities beneath the WAIS are caused by a thermal anomaly is consistent with the geological record of Cenozoic magmatism (Ball et al., 2021; DIGIS Team, 2021). The combination of high GHF, thin lithosphere and low viscosity points to a highly dynamic ice sheet–solid Earth interaction in regions including western Marie Byrd Land, the eastern Ross Embayment, and the Antarctic Peninsula. Large fluxes of thermal energy into the base of the ice sheet in these regions will likely enhance basal melting, reducing friction and increasing glacial sliding rates (Burton-Johnson et al., 2020; Shen et al., 2020). On

the other hand, a thin lithosphere and low viscosity asthenosphere encourage rapid bedrock uplift and may help to stabilise and reduce grounding line retreat (Gomez et al., 2010).

Much higher viscosities are inferred beneath East Antarctica, with much of this side of the continent exhibiting LAB depths in excess of 150 km. LAB depth is on average 63 ± 13 km beneath West Antarctica, significantly lower than the 233 ± 41 km estimated beneath East Antarctica. The combination of thick lithosphere and moderate GHF suggest a less dynamic interaction between the ice sheet and the solid Earth. While there is evidence for a low viscosity anomaly of order $10^{19.5 \pm 0.7}$ Pa s at a depth of 350 km in Wilkes Land, beneath the Aurora Subglacial Basin, it does not penetrate up to shallower depths of 150 km, and therefore the influence of this anomaly on GIA rates is expected to be greatly reduced compared with the shallow anomalies beneath much of the WAIS. Nonetheless, this region is associated with GHF of 45 to 60 mW m⁻². The upper end of this range is among the highest heat flow values estimated across East Antarctica (with the exception of the eastern Ross Embayment). Ice velocity and mass discharge rates across Wilkes Land are accelerating in response to warming temperatures in the Southern Ocean (Noble et al., 2020). The marine-based Aurora Subglacial Basin is positioned on a reverse bed slope, and may be susceptible to rapid ice mass loss (Shen et al., 2018a). Elevated GHF could therefore enhance this topographic instability by encouraging ice flow across the grounding line.

3.3.2 Comparing Predictions of Geothermal Heat Flow

Estimates of GHF exhibit similar spatial structure to that estimated by Shen et al. (2020), albeit with less short-wavelength variation. The study conducted by Shen et al. (2020) calibrated an empirical mapping between GHF and V_S using the observed relationship across the continental United States between interpolated heat flow measurements and V_S at 80 km depth from a regional tomographic model. When the US-calibrated mapping is applied to their Antarctic

velocity model, resulting GHF ranges from 40 to 90 mW m⁻². The results of this study agree on the presence of anomalously high heat flow (approximately 80 mW m⁻²) stretching from the Ross Sea to the Antarctic Peninsula, avoiding the coast between the Ross and Amundsen Sea. The most obvious discrepancy between the two structures is the presence of a high heat flow anomaly in this study, situated within the footprint of the Gamburtsev Mountain Range. The amplitude of this anomaly is 15% above the East Antarctic average. The reliability of this particular prediction should be doubted, because while the geological origin of the Gamburtsev Mountains is not well known, if it were caused by a mantle plume this would imply thin lithosphere in the region. This is not corroborated by the LAB depth model of this study, or those of Richards et al. (2020a) or Priestley et al. (2018) (Figure 3.6a; b; d). The spatial pattern of elevated GHF coincides with anomalously thick (~ 60 km) crust found in **ANT-20**. Since the total crustal radiogenic heat content in a particular region is proportional to crustal thickness in the employed parameterisation, thick crust steepens the geothermal temperature gradient and therefore increases the inferred GHF. It is therefore hypothesised that the GHF anomaly arises from a combination of two factors. First, a discrepancy between the assumed and true crustal thickness in this region. Secondly, a discrepancy between the assumed and true radiogenic heat production. In addition, anomalously low seismic velocities in the uppermost mantle beneath the Gamburtsev Mountains suggest the presence of a compositional anomaly (Shen et al., 2018b). Although the geotherm fitting methodology is designed to mitigate the impact of locally unphysical temperature estimates that would arise from such an anomaly, it may still reduce the ability to accurately infer heat flow from the seismic velocity structure of this region.

3.3.3 Reconciling Observations and Predictions of Mantle Viscosity

The Antarctic Peninsula (AP) and Amundsen Sea Embayment (ASE) are regions of special interest to the cryosphere and sea level communities, since they are currently experiencing significant ice mass loss and could hold important clues for determining the future stability of the wider West Antarctic Ice Sheet. The northern Antarctic Peninsula is undergoing rapid atmospheric warming, which has increased surface melt rates and contributed to ice shelf collapse (Davies et al., 2014). Recently, three major ice shelves along the AP were lost completely in the space of less than a decade, when Prince Gustav (1993–1995), Larsen A (1995) and Larsen B (2002) collapsed (Nield et al., 2014). As a result, tributary glaciers flowing from the AP plateau are accelerating and thinning (Cook and Vaughan, 2010). While the ASE accounts for less than 4% the area of the AIS, the marine-grounded portion of the WAIS in this region accounts for a quarter of the global present-day cryospheric contribution to GMSL rise (Barletta et al., 2018). Accelerating ice flow and rapidly retreating grounding lines have been observed at both the Pine Island and Thwaites glaciers. This recent change, combined with the reverse bed slope beneath both glaciers, suggests that they are vulnerable to catastrophic collapse (Barletta et al., 2018). Accurately capturing solid Earth structure beneath the AP and ASE is therefore of particular importance, since future ice retreat in these regions is especially sensitive to viscoelastic bedrock uplift rates, which – if sufficiently rapid – may help to stabilise grounding lines. Moreover, the present-day GIA rate is strongly affected by inferred thermomechanical structure beneath sites of recent ice loss, and must be accurately calculated in order to reliably estimate ongoing ice mass change from satellite gravity data.

Bedrock deformation rates observed by GPS can be used to shed light on solid Earth structure, since they depend on the rheology of the underlying mantle. Typically, observed deformation rates are combined with an estimate of the local ice sheet loading history and a Maxwell viscoelastic solid Earth model, to infer a viscosity consistent with the applied constraints. For

Study	Location	Ice loading history	Observation period	$\log_{10}\eta$ estimate
B18	ASE	Retreat from 1900–2014	2002–2014	18.4–19.4
S21	AP	Retreat from 1999–2020	1999–2020	17.5–19.0
I11	AP	Overall retreat from LGM to present, modern phases of advance and retreat	2003–2009	19.3–20.0
W15	AP	Retreat from LGM to present	2009–2013	20.0–20.5

Table 3.1: **Antarctic upper mantle viscosity estimates derived from geodetic observations.** B18 refers to Barletta et al. (2018), S21 to Samrat et al. (2021), I11 to Ivins et al. (2011), W15 to Wolstencroft et al. (2015). Each study assumed a particular ice loading history to estimate the reported viscosity values, a summary of which is reported here. The observation period represents the timeframe that best represents when data was collected.

example, the recent study of Barletta et al. (2018) provides a geodetic analysis of bedrock deformation rates across the ASE using six local GPS stations. Barletta et al. (2018) estimated upper mantle viscosities in the range $\log_{10}\eta = 18.4$ to $\log_{10}\eta = 19.4$. These extremely low viscosities imply Maxwell relaxation times of order 1 to 10 years, meaning that the topographic response to deglaciation following the Last Glacial Maximum (LGM; ca. 21 ka) would have already decayed away in this region. Since models of GIA in response to modern-day ice mass loss typically assume upper mantle viscosities of $\eta \sim 10^{20}$ Pa s, a substantial upward revision of viscoelastic uplift rates would be required in the ASE, implying that local ice mass loss has been underestimated by $\sim 10\%$ in previous GRACE-based assessments. Conversely, the vulnerability of the WAIS in this region to catastrophic collapse would potentially be reduced by the faster GIA response rates, since rapid grounding line uplift might help to stabilise the ice sheet (Gomez et al., 2010).

A question which arises naturally is therefore: How well do geodetically constrained estimates of mantle viscosity beneath the AP and ASE agree with the inferred thermomechanical structure? To determine the answer, the findings of four geodetic studies have been compiled, summarised in Table 3.1. The viscosity range obtained from each study is based on the range of plausible upper mantle viscosities able to fit the geodetically observed horizontal and vertical deformation rates. Corresponding viscosity estimates relevant to this study were extracted

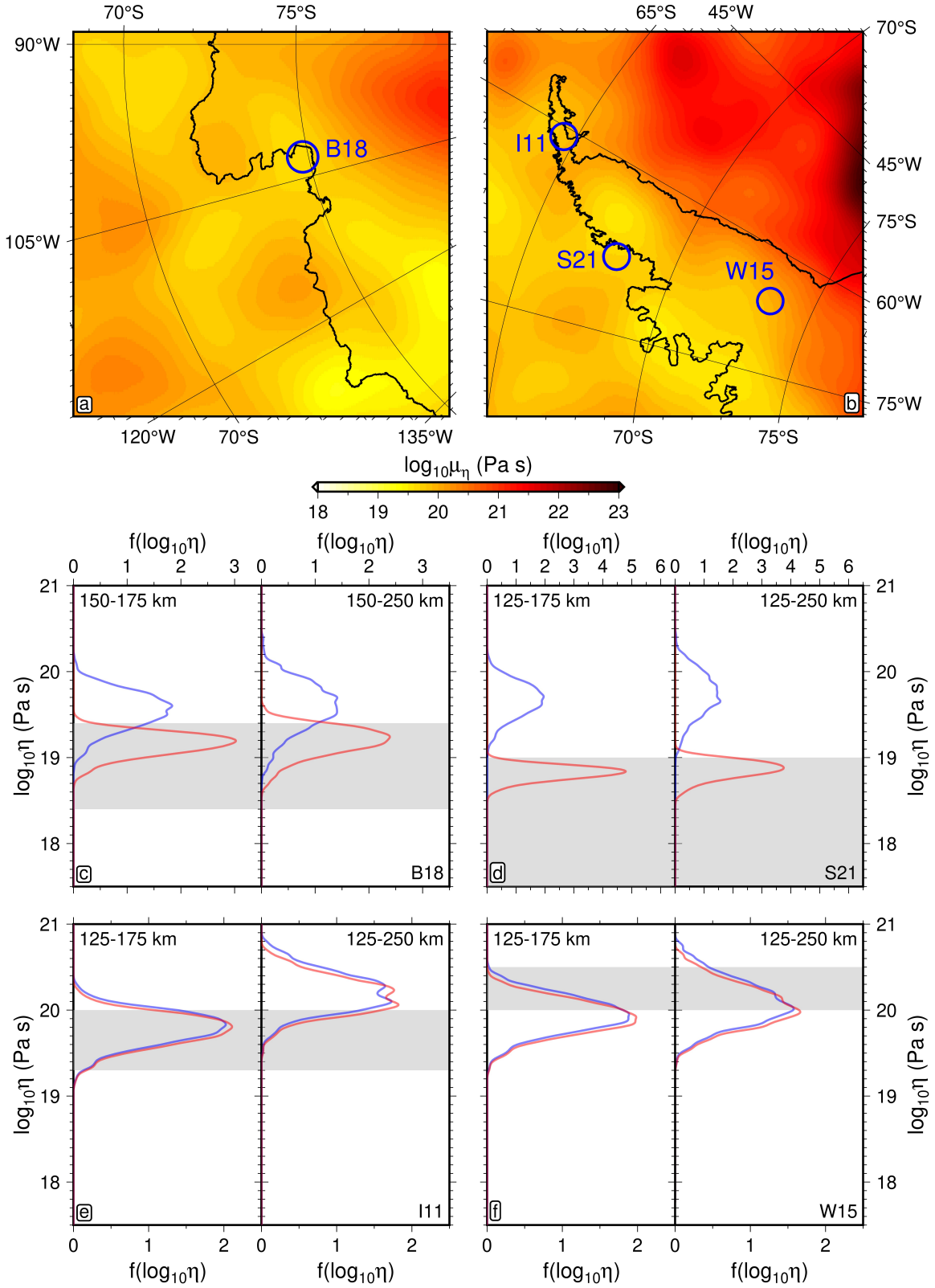


Figure 3.11: Comparison of upper mantle viscosity estimates based on GPS and seismic tomographic velocity. Mean viscosity structure at 150 km depth beneath the ASE and AP (panels a and b, respectively), with lateral sampling regions overlain in blue. Probability density distribution of inferred diffusion creep steady-state (blue) and time-dependent (red) viscosity compared to geodetic estimates (grey) B18, S21, I11 and W15 (panels c, d, e and f, respectively).

based on the ensemble of predicted diffusion creep viscosities beneath the AP and ASE. The ASE location was taken to be 102.667W, 74.833S (in accordance with Lau et al., 2021), to extract viscosities for comparison with the GPS study **B18**. For each of the GPS studies compared to in the AP region, a unique location was used, approximating the region over which satellite data was collected in each case. For **S21**, the location was taken to be 68.000W, 68.000S. For **I11**, 60.750W, 64.600S. For **W15**, 66.000W, 73.500S. A 50 km surface-equivalent lateral averaging radius was used in each case, along with a depth window of 125 to 175 km and 150 to 175 km for the AP and ASE, respectively. The shallow bounds of the respective depth windows were selected to reflect the lowest inferred viscosities in the upper mantle. The motivation for this was to investigate whether the steady-state inferred viscosity structure from this study could match up to the extremely low viscosities indicated by geodetic studies, without the need to invoke time-dependent rheology. A deeper depth window of 125 km to 250 km and 150 km to 250 km for the AP and ASE, respectively, was also used to investigate whether higher viscosities inferred for ice age-related loading might result from deeper stress penetration associated with the larger ice masses in play on these longer timescales (Blank et al., 2021). For each set of parameters within the posterior ensemble, seismic velocity was converted into an estimate of steady-state diffusion creep viscosity at each location within the chosen three-dimensional spatial sampling window. To estimate a single viscosity value for each viscoelasticity model, an average was calculated over all values within the spatial window. This resulted in a posterior ensemble of viscosities associated with the given location, ready for comparison with the geodetic analyses. The resulting probability density distributions of inferred viscosity are shown in comparison to their geodetically derived counterparts in Figure 3.11. A reasonable agreement is found in the case of **I11**, when looking at the shallow depth window, and in the case of **W15**, when looking at the deeper depth window. A poor agreement is found for **B18**, with little overlap between the geodetically and tomographically inferred viscosities. An extremely poor

agreement is found for **S21**, where there is no overlap at all.

Note that the extent to which the geodetic analyses agree with the inferred steady-state viscosities of this study appears to depend on the modelled ice loading timescale. This observation may indicate the presence of transient rheology, wherein the strain response of a viscoelastic body to a given change in the stress field (i.e., loading) depends on the timescale over which it occurs (Lau and Holtzman, 2019). Transient rheological models therefore exhibit a range of apparent viscosities, where the latter refers to the viscosity of the Maxwell model which best fits the observed deformation history. The rheological parameterisation used in this study, YT16, inherently includes transient behaviour because the frequency-dependent complex compliance is derived from a continuous spectrum of underlying relaxation timescales. The viscosity values reported so far in this study have always referred to steady-state deformation, representing the theoretical limit of an infinite forcing timescale. On the other hand, geodetically derived viscosity estimates are relevant to the timescales corresponding with the forcing processes in operation. If such timescales align with the activation of additional relaxation processes due to transient components in the rheological model, there can be a significant discrepancy between the steady-state and apparent viscosities associated with a given region and process. This relationship between forcing timescale and apparent viscosity, within the context of a solid Earth exhibiting transient rheology, could therefore be responsible for the observed discrepancy.

To quantify the potential impact of time-dependent rheology on geodetically inferred viscosity estimates, the transient rheological parameterisation YT16, combined with estimates of steady-state viscosity derived from this study, were used to model the deformation rate one would expect to observe given the ice loading histories pertaining to each of the geodetic studies. This was achieved using the relationship

$$\varepsilon(t) = \int_{-\infty}^t J(t-t') \frac{d\sigma(t')}{dt'} dt', \quad (3.6)$$

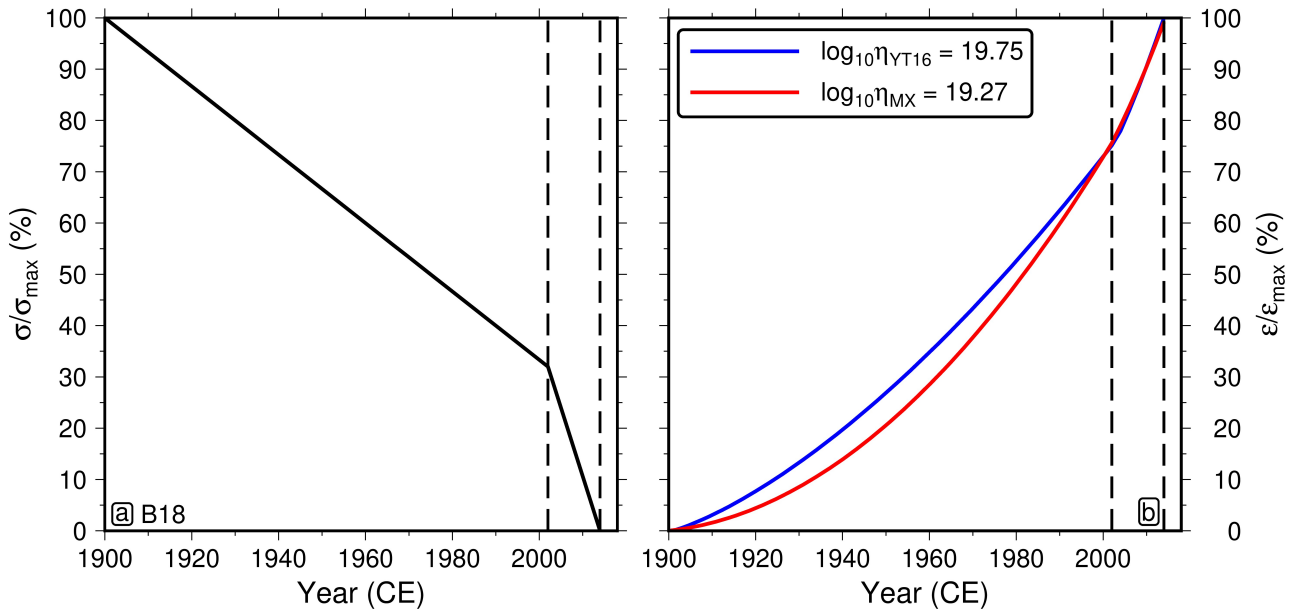


Figure 3.12: Inverting an inferred strain history derived from transient rheology for a best-fitting Maxwell model. Stress evolution consistent with the ice loading history assumed in B18, relevant to the ASE, from 1900 CE to 2014 CE (panel a). Stress shown as a percentage of its maximum value at 1900 CE. Two strain responses, each corresponding with the assumed stress history (panel b). Firstly, a strain response based on the transient rheology parameterised by YT16, assigned a steady-state viscosity ($\log_{10} \eta_{YT16} = 19.75$) selected randomly from the posterior distribution of tomographically inferred values, which were averaged over the depth range 150 to 175 km (blue; see panel c of Figure 3.11 for inferred viscosity distributions). Secondly, a strain response based on Maxwell rheology and a viscosity ($\log_{10} \eta_{MX} = 19.27$) for which the least-squares misfit between ε_{YT16} and ε_{MX} is minimised over the observation period from 2002 CE to 2014 CE (red). This observation period was selected to coincide with the period over which Barletta et al. (2018) collected their data, so as to emulate the geodetic modelling procedure as realistically as possible. Strain normalised by the maximum strain exhibited by the YT16 rheological model, at 2014 CE, and expressed as a percentage of this maximum value.

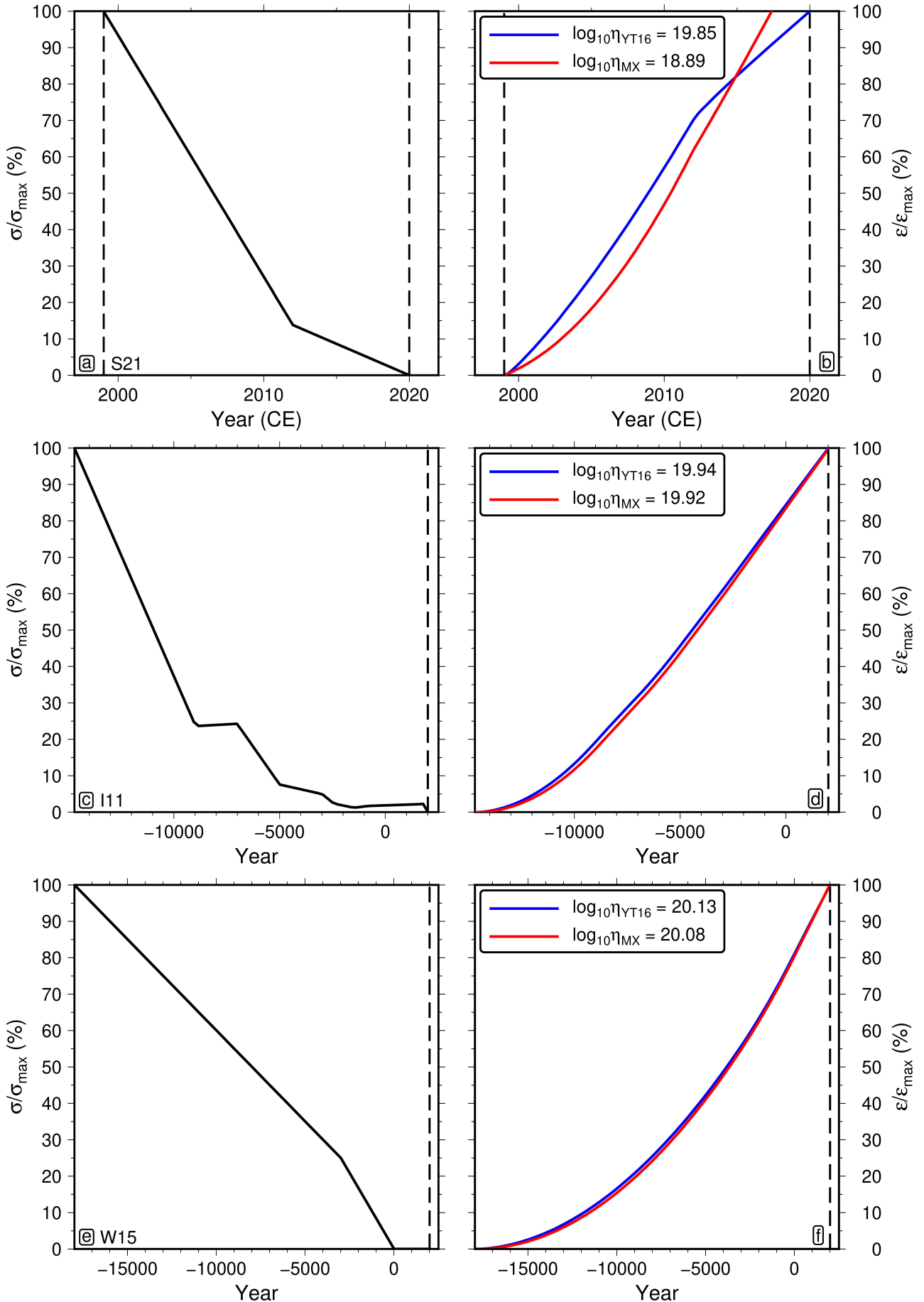


Figure 3.13: Assumed stress history, inferred transient strain, and inverted Maxwell strain for each of the remaining geodetic studies, **S21**, **I11** and **W15**. Format follows Figure 3.12. Year in panels c, d, e and f referenced with respect to 0 CE.

where the creep function, $J(t)$, is the time-domain representation of its frequency-domain counterpart, the complex compliance, and the ice loading history is captured by the stress evolution $\sigma(t)$. The creep function represents the time-dependent strain profile observed in response to a unit applied stress, where the stress evolution follows the profile of a Heaviside step function. By convolving the creep function with the full stress rate history, the total strain at each time t can be obtained, and indeed this is what Equation 3.6 represents. The creep function can be obtained for a general rheology by integrating the relaxation function at constant stress which underlies both $J(t)$ and $J^*(\omega)$, referred to as $X(\tau)$, according to

$$J(t) = J_U + J_U \mathcal{I}(t, X) + \frac{t}{\eta}, \quad (3.7)$$

where

$$\mathcal{I}(t, X) \equiv \int_{-\infty}^{\infty} X(\tau) \frac{1 - \exp(-\frac{t}{\tau})}{\tau} d\tau, \quad (3.8)$$

such that the terms in Equation 3.7 comprise the elastic (instantaneous), transient (intermediary) and viscous (steady-state) components of the deformation response, respectively. The relaxation function represents the continuous spectrum of relaxation strengths associated with each possible forcing timescale. An explicit parameterisation of $X(\tau)$ is provided for YT16, which is defined as

$$X_{YT16}(\tau) = X_B + X_P, \quad (3.9)$$

$$X_B = A_B \tau^{\alpha_B}, \quad (3.10)$$

$$X_P = A_P \exp\left(-\frac{\ln^2(\tau/\tau_P)}{2\sigma_P^2}\right), \quad (3.11)$$

where X_B represents a monotonic relaxation background within which A_B and α_B are constants, and X_P a high-frequency relaxation peak, which broadens and heightens with homologous tem-

perature via the pre-melting functions $A_P(\Theta)$ and $\sigma_P(\Theta)$. For more detail on the relaxation function and its relationship with parameterisations of the creep function and complex compliance, see Section 2.3 of Takei (2017) for discussion in the context of YT16, and Chapter 4 of Nowick and Berry (1972) for a more general treatment.

To parameterise the stress history $\sigma(t)$, constant rates of loading and unloading were used in accordance with the particular geodetic study under consideration (Table 3.1). For example, in the case of B18, a constant rate of unloading $\dot{\sigma}_1$ was assumed from 1900 CE to 2002 CE, after which a significantly faster rate of unloading $\dot{\sigma}_2$ was assumed, such that

$$\frac{\dot{\sigma}_2}{\dot{\sigma}_1} = 4. \quad (3.12)$$

This ratio was selected to correspond with the ratio of ice mass loss rates assumed in the underlying geodetic study Barletta et al. (2018), and the resulting stress evolution is shown in Figure 3.12. The objective was to incorporate a simple ice loading history as consistent with the assumptions of each geodetic study as possible. Consistency in this regard is more important than the accuracy of the ice loading history itself, in ensuring fair comparison. The assumed initial and final stress values, σ_i and σ_f , of each stress history are not important as long as the ratio between relative stress rates is correct, because while the former affect the amplitude of the generated strain response, the apparent viscosity only depends upon the latter.

A synthetically generated pattern of deformation, $\varepsilon_{YT16}(t)$ was calculated for the transient rheological model by substituting η_{YT16} and X_{YT16} into Equation 3.7 via $\mathcal{I}(X_{YT16})$, and combining it with each stress history. The same distributions of η_{YT16} as used in the initial comparison between tomographically and geodetically inferred viscosities were employed here (i.e., blue distributions of Figure 3.11). Then, the synthetically generated deformation histories were fitted under the assumption of Maxwell viscoelasticity, treating the Maxwell steady-state viscosity, η_{MX} , as a free parameter. This was achieved by replacing the creep function relevant to YT16

with its Maxwell counterpart, which is simply expressed as

$$J(t) = J_U + \frac{t}{\eta_{MX}}, \quad (3.13)$$

i.e. there exists no intermediary transient form of deformation in the Maxwell model. By isolating the portion of the calculated strain histories which correspond with the observation period of each geodetic study (Table 3.1), a least-squares fitting procedure could be applied to find the value of η_{MX} for which $\varepsilon_{MX}(t)$ and $\varepsilon_{YT16}(t)$ agree most tightly. This inversion approach was formulated based on the work of Lau et al. (2021). An example of a synthetically generated deformation history, and its corresponding best-fitting Maxwell equivalent, is shown for **B18** in Figure 3.12, using a randomly selected steady-state viscosity from the posterior distribution of tomographically inferred values. For the remaining studies **S21**, **I11** and **W15**, Figure 3.13 shows the assumed stress evolutions and corresponding strain evolutions.

The inverted values of η_{MX} are apparent viscosities, which theoretically correspond with the inferred viscosities of each geodetic study, since they each employed a Maxwell viscoelasticity assumption in modelling their respective observations. A given apparent viscosity is dependent on the relative amplitude and timescale of relaxation processes triggered by the ice loading history, or in other words, its frequency content. When the tomographically inferred time-dependent viscosities derived from this study are compared to those derived from geodetic observations, a much better agreement than before is observed (Figure 3.11). For example, predicted time-dependent viscosity distributions derived from this study lie almost entirely within the range of possible values predicted by **B18** and **S21**, when looking at the shallow depth range. The observation that the shallow depth range provides the best fit to the geodetic observations for the short timescale ice loading histories lends further support to the hypothesis that time-dependent behaviour is at play. This is because one would expect GPS observations to be sensitive to the viscosity within the portion of the mantle activated by the modelled

loading history. In the case of short timescale and lower magnitude loading, dissipation of stress may only have occurred within the shallow upper mantle, thus making the observed deformation rates sensitive only to these depths. For the longer timescale ice loading histories associated with **I11** and **W15**, apparent viscosities are only slightly lower than their steady-state counterparts, suggesting that viscous deformation dominates the geodetic observations relevant to these studies. This is a possible explanation for the fact that the steady-state viscosities inferred from this study are already in good agreement with their geodetic counterparts, prior to time-dependent adjustment. Therefore, each of the results of this time-dependent viscosity analysis are consistent with the notion that the solid Earth may support transient deformation.

3.3.4 Remaining Uncertainties

Despite making major progress in understanding the thermomechanical structure of the Antarctic upper mantle, this work highlights outstanding challenges that limit the ability to utilise seismological data to understand solid Earth structure and its relationship with cryospheric evolution. A lack of geophysical data sets containing information about the deep mantle restricts the precision with which one can estimate pressure-dependent behaviour. For example, the uncertainty present in estimates of activation volume remains high after calibrating the viscoelasticity parameterisation, since the majority of the geophysical data relates to the shallowest 125 km of the mantle. This leads to increasing uncertainty in thermomechanical structure with depth. In addition, the microphysical process or processes responsible for the onset of anelasticity is subject to significant debate, and this translates into competing methods for modelling anelastic effects (Faul et al., 2007; Yamauchi and Takei, 2016). As a result, heavily discrepant predictions may be made depending on the choice of physical model (Ivins et al., 2021). With this in mind, the inverse calibration procedure has been designed structurally to work with any choice of viscoelasticity parameterisation. Further uncertainty relates to the particular

viscous creep mechanism dominating Antarctic upper mantle rheology on timescales relevant to the modelling of geodynamic processes (Lau and Holtzman, 2019). If dislocation creep is the dominant mechanism, the diffusion creep viscosities predicted here will overestimate true steady-state values. Nevertheless, predicted temperatures would remain robust, being reliant only on the correct modelling of diffusionaly controlled anelasticity processes at seismic frequency. It must also be emphasised that this independently constrained thermal structure significantly reduces uncertainty in dislocation creep viscosity, which, like its diffusional counterpart, is strongly temperature dependent.

With respect to secondary structures calculated using estimates of three-dimensional temperature variations, namely LAB depth and GHF, a few specific challenges are yet to be addressed. First, vertical seismic resolution limits make it difficult to infer LAB depth variations smaller than ~ 15 km. Secondly, due largely to the downward bleeding of slow shear-wave velocities associated with discrepancies between the modelled and true crustal structure, seismically inferred temperature structure becomes unreliable close to the Moho. This means that interpolation must be used to estimate shallow temperature structure. While this is not expected to influence estimates of LAB depth, since the 1200°C isotherm is sufficiently deep, it will have an effect on the estimates of heat flow, which are proportional to the surface geothermal gradient. A lack of exposed outcrops where Antarctic GHF can be measured makes it difficult to ground truth geophysical predictions and refine the model. In addition, poor understanding of the range, depth variation, and lateral variation in Antarctic crustal heat production and conductivity prevails. Since both of these parameters must be assumed to fit a steady-state geothermal profile to the temperature-depth data, the GHF estimates produced in this study are directly affected by this limitation. To address this, complementary geophysical methods can be used to gain insight into crustal heat production and conductivity structure, allowing for further refinement of GHF models. This topic is addressed in detail in Chapter 4.

3.4 Conclusions

A probabilistic approach to the calibration of experimental parameterisations of viscoelasticity has been developed to provide a self-consistent mapping between three-dimensional seismic tomographic velocity data and models of thermomechanical structure. The viscoelasticity parameters are calibrated with a suite of regional geophysical data constraints relevant to Antarctica, reducing the discrepancy in physical predictions offered by different seismic tomographic velocity models, and ensuring a set of outputs compatible with well-constrained mantle properties. It is possible to utilise a small subset (in the case of this study, 0.5%) of the overall posterior data set generated by the Bayesian inversion to propagate shear-wave velocity into accurate estimates of thermomechanical structure and its uncertainty, which ensures computational viability. By probing the model covariance structure, this uncertainty is significantly reduced as compared to treating parameters independently (viscosity uncertainty reduced by 4 to 5 orders of magnitude at 150 km depth).

Dramatic differences in viscosity structure, LAB depth and GHF are predicted between East and West Antarctica, in accordance with other studies (Austermann et al., 2021; Barletta et al., 2018; Priestley et al., 2018; Richards et al., 2020a; Shen et al., 2020). Evidence is found for mostly thick lithosphere, high viscosity asthenosphere, and uniformly low GHF beneath the EAIS. Shallow LAB depths and high GHF coincide with regions characterised by the presence of low viscosity anomalies, such as in western Marie Byrd Land where values 30 to 50 km, 85 to 95 mW m⁻², and $\eta = 10^{19.5 \pm 0.3}$ Pa s, respectively, are found. This combination of thermomechanical properties is consistent with the geological record of regional Plio-Pleistocene magmatism (Ball et al., 2021; DIGIS Team, 2021), and indicates that western Marie Byrd Land, along with the eastern Ross Embayment and Antarctic Peninsula, may be amongst the most dynamic in response to climate and ocean forcing. High GHF may significantly increase the flow of ice towards the continental perimeter, whereas the presence of low viscosities and thin

lithosphere suggest much faster bedrock uplift rates than a one-dimensional average rheology, potentially providing a stabilising effect on the grounding line (Gomez et al., 2010).

The outputs presented in this study may be used to refine understanding of ice sheet stability in Antarctica. Models of density structure can be used to improve time-dependent models of convectively supported surface topography, enabling correction of palaeo sea level markers used to inform ice sheet history. Self-consistently determined viscosity and LAB depth structures, that also constrain time-dependent rheological variations, can be applied to three-dimensional glacial isostatic adjustment studies, where uplift rates are intimately tied to rheological structure. These high-resolution estimates of thermomechanical structure will be useful in constraining bedrock uplift rate across the continent, in turn altering corrections needed to produce gravimetric and altimetric estimates of present-day ice mass loss rates. Seismically inferred maps of GHF can be incorporated in new ice sheet modelling studies, where basal sliding rates are highly sensitive to the amount of thermal energy provided from below. As a result, the new methodology for estimating solid Earth inputs and their associated uncertainties may enable accurate probabilistic assessment of ice sheet stability scenarios and projections of future sea level rise.

Chapter 4

Antarctic Geothermal Heat Flow, Crustal Conductivity and Heat Production Inferred From Seismological Data

4.1 Introduction

Heat derived from Earth’s interior, and supplied to its surface, is a crucial component of ice sheet basal conditions. The supply of thermal energy to the ice sheet-solid Earth interface can influence basal melt and sliding, englacial rheology, and erosion, and is therefore a key factor in governing ice dynamics (Burton-Johnson et al., 2020; Larour et al., 2012). Heat supply is quantified by reference to geothermal heat flow (GHF), q_s , which pertains to the amount of thermal energy supplied across Earth’s surface, per unit area and time (units mW m^{-2}). Not only are ice dynamics highly sensitive to the supply of geothermal heat, the latter is expected to vary significantly across Antarctica. Indeed, variations in Antarctic GHF of order 100 mW m^{-2}

were shown in the preliminary investigation of 3.2.3. The result is that a good understanding of the pattern and amplitude of heat supply into the base of the Antarctic Ice Sheet is a requirement for accurately modelling its evolution.

Since thermal conduction is the dominant mechanism of heat transfer in Earth's crust, Fourier's law of conduction is used to relate q_s to Earth's temperature structure,

$$\vec{q}_s = -k(z = z_0) \frac{\partial T}{\partial z} \Big|_{z=z_0} \hat{\mathbf{z}}, \quad (4.1)$$

$$q_s = |\vec{q}_s|. \quad (4.2)$$

Here, k is thermal conductivity, T is temperature, z is a locally vertical depth co-ordinate, and z_0 is located at the surface. Theoretically, then, Equation 4.1 gives us a pathway to estimating q_s , via measurements of laterally varying thermomechanical structure. Indeed, local estimates of Antarctic GHF have been made using observations of temperature and depth from gravity-driven probes in unconsolidated sediment and boreholes drilled into ice or bedrock. However, such measurements can only be used to infer point estimates of GHF, and each class of borehole observation is highly limited in terms of where it can be conducted (Burton-Johnson et al., 2020). Sediment temperature probes require deep enough water (~ 1 km) so as not to be significantly disrupted by long-period (~ 1 kyr) ocean temperature cycles (Dziadek et al., 2019). Ice borehole-derived GHF estimates are based on the assumption of thermal equilibrium between bedrock and ice sheet; an assumption limiting data collection to the summits of ice domes (Engelhardt, 2004). Even here, englacial temperature structure can be affected by other heat sources, potentially contaminating the signal. A lack of accessible bedrock across Antarctica prohibits wide-scale bedrock borehole drilling (Fisher et al., 2015).

Given these limitations on data collection, geophysical methods are the only means of obtaining continental scale maps of GHF needed for ice sheet modelling. A number of methods

based on magnetic, gravity or seismic data have been employed in the past (e.g., An et al., 2015; Haeger et al., 2022; Martos et al., 2017). Whilst useful, such methods have suffered from a range of data- and modelling-derived issues (Burton-Johnson et al., 2020). For example, difficulties in converting field observations into estimates of Earth's thermal structure, and the inference of only a single isotherm, has led to large uncertainty in GHF predictions. Magnetically derived methods suffer from issues related to assumptions on magnetic composition, spatial resolution of magnetic anomaly data, and ability to patch together information from multiple sources. Since gravity data are sensitive only to long wavelength changes in Earth's crust, methods based on these data lack spatial resolution, and require assumptions on crustal conductivity and heat production, both of which can significantly impact predictions of GHF. Despite their potential to vary significantly, conductivity and heat production are parameterised as laterally homogeneous, owing to a lack of good constraint on these parameters.

In the past, seismic inferences of GHF have been limited by similar issues. Until recently, a relative shortage of seismic data in Antarctica has limited the spatial resolution of tomographically inferred GHF (Lloyd et al., 2020). As was the case with methods based on gravity data, poor constraint on crustal parameters has led to lateral variations being ignored, despite their potential for large variations and consequent impact on GHF (An et al., 2015). An alternative approach based on seismic data is to empirically relate velocity anomalies at a given depth beneath Antarctica to those modelled beneath another continent, where densely sampled bore-hole estimates of GHF are accessible (Shapiro and Ritzwoller, 2004; Shen et al., 2020). This method inherently assumes that velocity anomalies imaged by different tomographic velocity models are directly comparable. In reality, subjective choices made in the tomographic modelling process such as starting model, regularisation, and parameterisation influence the result. In addition, this method assumes that two regions with the same crustal thickness, and similar V_S structure in the shallow upper mantle, have comparable GHF. This ignores the effect that

variations in crustal conductivity and heat production due to geochemical heterogeneity have on surface heat supply. This method is therefore subject to a lot of the same drawbacks as the more traditional method.

A number of recent advances allow for the establishment of a novel approach to infer GHF from seismological data sets. Firstly, the development of **ANT-20**, a wave-equation travel-time adjoint tomographic model, lays the groundwork for imaging Antarctic thermomechanical structure and henceforth GHF at regional-scale resolution (~ 100 km; Hazzard et al., 2023; Lloyd et al., 2020). Secondly, the emergence of physics-based parameterisations of mantle rock properties, constrained via laboratory experiments, has opened the door to converting seismic shear-wave velocities (V_S) directly into temperature (Faul and Jackson, 2005; Yabe and Hiraga, 2020; Yamauchi and Takei, 2016). As shown in Chapter 2 and 3, methods to calibrate these parameterisations based on a range of geophysical data constraints allow uncertainty to be rigorously quantified, and reduced, in such conversions. In Section 3.2.3, the aforementioned advances were used to produce a preliminary model of Antarctic GHF and its uncertainty. Thirdly, new geochemical analyses have improved understanding of the likely range of key crustal parameters governing heat supply, their relationship with composition, and to what extent they can be inferred from compressional-wave velocity (V_P) data (Jennings et al., 2019; Sammon et al., 2022). In this chapter, a new method for estimating GHF is developed, incorporating sensitivity to upper mantle thermal structure via V_S , as well as crustal compositional structure via V_P . This method is applied to produce a revised model of Antarctic GHF and its associated uncertainty.

4.2 Methods

My approach to estimating GHF across Antarctica is motivated by the desire to infer geothermal structure in as direct a fashion as possible, without relying on empirical comparisons to

GHF estimates derived from geologically distinct continental environments. Central to this approach is the idea of constraining the relationship between temperature and depth, $T(z)$, across a range of depths, rather than relying on a single isotherm. Therefore, V_S data is made use of, which is especially sensitive to geothermal structure throughout the shallow upper mantle. Since crustal composition also plays a key role in determining heat supply, via variations in thermal conductivity and heat production, these parameters are constrained within the modelling framework. To do so, information is brought in from V_P data, which provides sensitivity to lateral variations in SiO_2 content and therefore crustal conductivity. By fitting steady-state geothermal profiles to V_S -derived counterparts, and looking at how the misfit between the two varies as a function of crustal heat production, it is possible to co-constrain conductivity, heat production and GHF in a thermodynamically self-consistent fashion. This framework serves as the basis for providing reasonable inferences of q_s .

4.2.1 Inferring Thermal Structure from Seismic Data

The sensitivity of V_S to temperature (T) derives from the effect that temperature has on the viscoelastic properties of mantle rock. To reliably parameterise the $V_S(T)$ relationship, the approach of Hazzard et al. (2023) (Chapter 2) is adopted, who calibrated the anelasticity parameterisation of Yamauchi and Takei (2016) against a suite of Antarctic geophysical data constraints. The values of $\vec{\mathcal{X}}_{\text{ve}}$ from the *maximum a posteriori* output of Hazzard et al. (2023) are assumed (Chapter 2). Having established a method for relating seismic velocity and temperature, a geographic location $\{\theta, \phi\}$ (latitude, θ , longitude, φ) within the spatial footprint of the chosen tomographic model **ANT-20** can be selected, and the corresponding radial velocity structure $V_S(z)$ converted into an inferred geotherm $T(z)$ (Figure 4.1a, black cross-hairs).

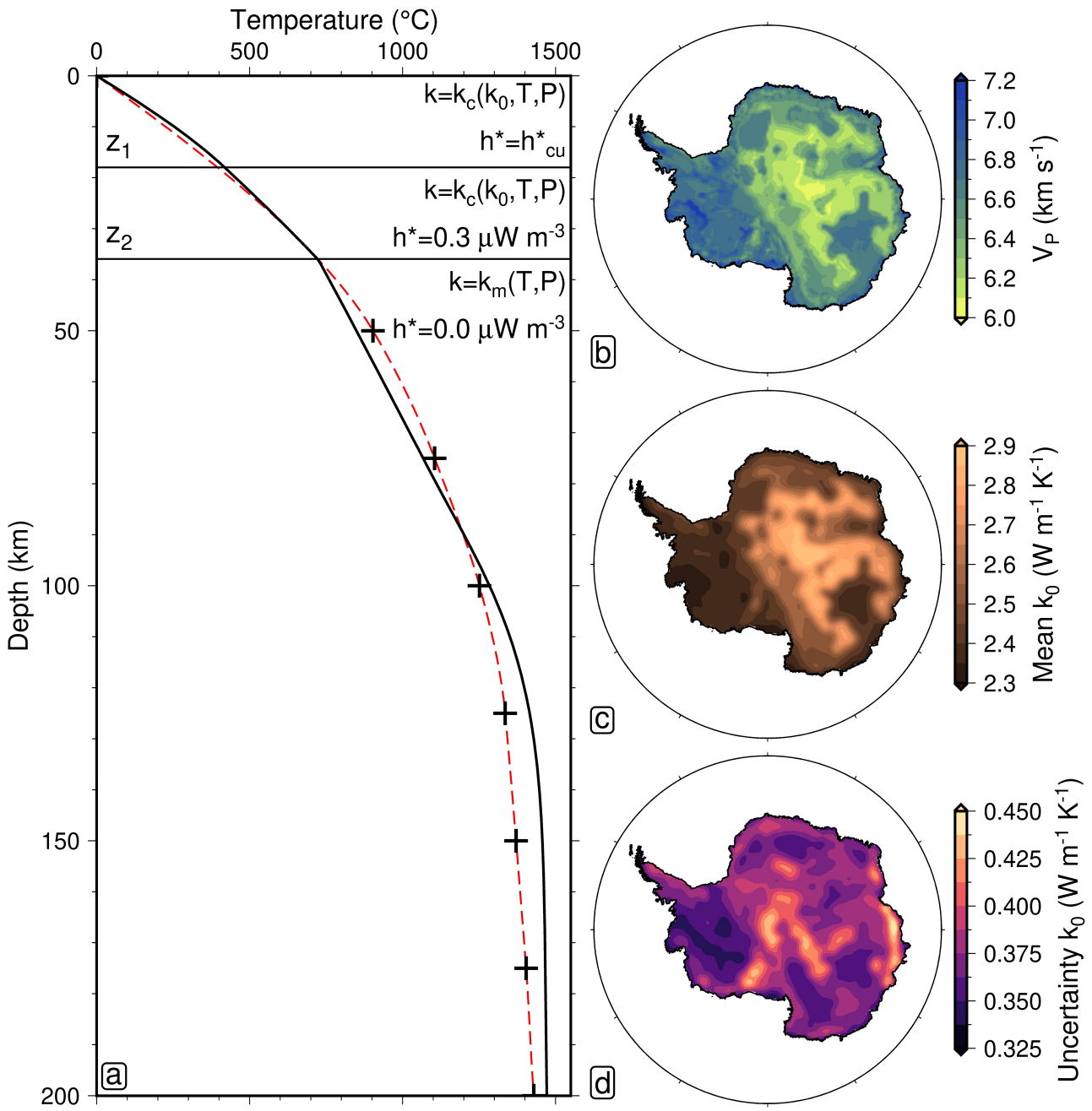


Figure 4.1: Parameterising Earth structure. (a) Temperature-depth data points inferred from **ANT-20** V_S (black cross-hairs) interpolated prior to fitting (red dashed line). Steady-state geotherm fitted to seismic data (black line), subject to depth-dependent thermodynamic constraints within the upper crust ($0 \leq z \leq z_1$), lower crust ($z_1 < z \leq z_2$), and mantle ($z_2 < z$). All depths referenced with respect to the crystalline basement. (b) Average crustal V_P from **ANT-20** across Antarctica. (c) Crustal conductivity (k_0) estimated from V_P (Equation 4.8). (d) Uncertainty in k_0 based on spread in crustal V_P and $k_0(V_P)$ residual (Section 4.2.5).

4.2.2 Fitting Geothermal Profiles

Due to the likely presence of noise and artefacts in the underlying seismic data, as well as the potential for unmodelled compositional seismic velocity variation, estimating q_s directly from seismically inferred geotherms is avoided. Instead, steady-state, thermodynamically self-consistent geotherms are fitted to them. To prepare the V_S -derived geotherms for fitting, they are cleaned according to four algorithmic steps. Firstly, crustal velocities are removed, using the same crustal thickness model assumed in **ANT-20**, for consistency. Secondly, any portion of the geothermal profile directly beneath the Moho where the temperature gradient meets the condition $\partial T / \partial z < 0.4 \text{ } ^\circ\text{C km}^{-1}$ is removed. These two steps were found to effectively excise anomalously slow velocities at shallow depths, which may be associated with downward bleeding of crustal velocities. Thirdly, the constraint that temperature reaches $0 \text{ } ^\circ\text{C}$ at the basement depth is added. Finally, the geothermal profiles are interpolated on a 1 km depth interval, producing a smoothly varying structure suitable for comparison with fitted geothermal profiles. The geotherms are fitted according to a modified version of the procedure laid out in McKenzie et al. (2005). This procedure involves iteratively updating the Moho GHF, and mechanical boundary layer thickness, until the misfit between modelled and V_S -derived geotherms is minimised. Once an optimal geotherm has been arrived at (Figure 4.1a, black solid line), q_s can be calculated according to the surface temperature gradient and associated thermal conductivity.

4.2.3 Parameterising Mantle Structure

In addition to providing a seismically inferred geotherm to the fitting procedure, it is also necessary to provide a suitable parameterisation for thermal conductivity, k ($\text{W m}^{-1} \text{K}^{-1}$), and heat production, h^* ($\mu\text{W m}^{-3}$), in the mantle and crust.

In the mantle, conductivity is calculated according to the temperature- and pressure-dependent parameterisation of Korenaga and Korenaga (2016). The parameterisation is adapted

to assume a grain size of 0.1 cm, relevant to the calculation of radiative thermal conductivity.

This parameterisation will be referred to as $k = k_m(T, P)$. In accordance with the relatively low abundance of heat-producing elements in the upper mantle, a mantle heat production of $h^* = 0.0 \mu\text{W m}^{-3}$ is assumed. Regarding assumptions of adiabatic mantle properties, the constant-pressure heat capacity is set to $C_P = 1187 \text{ J kg}^{-1} \text{ K}^{-1}$, and thermal expansivity to $\alpha = 3 \times 10^{-5} \text{ K}^{-1}$. A mantle kinematic viscosity of $\nu = 9 \times 10^{16} \text{ m}^2 \text{ s}^{-1}$ is assumed.

4.2.4 Parameterising Crustal Structure

To parameterise thermal conductivity in the crust, the following parameterisation is utilised (Goes et al., 2020), which will be referred to as $k = k_c(k_0, T, P)$,

$$k_c(k_0, T, P) = \frac{k_0}{n} (1 + \beta P) \left(n - 1 + \exp \left[\frac{-(T - 25)}{300} \right] \right). \quad (4.3)$$

In this equation, the factors $\beta = 0.1$, and $n = 6.4 - 2.3 \ln(k_0)$, and k_0 is the reference crustal conductivity at atmospheric conditions ($P = 0 \text{ GPa}$, $T = 25 \text{ }^\circ\text{C}$). Note that this parameterisation was misprinted in the original text of Goes et al. (2020); the authors have clarified that the expression above is the correct version.

To parameterise heat production, the crust is divided into two layers of equal depth. A uniformly distributed heat production is assumed throughout each layer, set to $h^* = h_{\text{cu}}^*$ in the upper crust, and $h^* = 0.3 \mu\text{W m}^{-3}$ in the lower crust. This simple parameterisation has been adopted to avoid imposing precise details of the depth-dependence of h^* *a priori*, which are not known. When the upper crustal heat production is set to $h_{\text{cu}}^* = 1.0 \mu\text{W m}^{-3}$, the parameterisation is consistent with globally averaged heat production values obtained from a comprehensive analysis of crustal geochemistry and seismic velocity (Sammon et al., 2022).

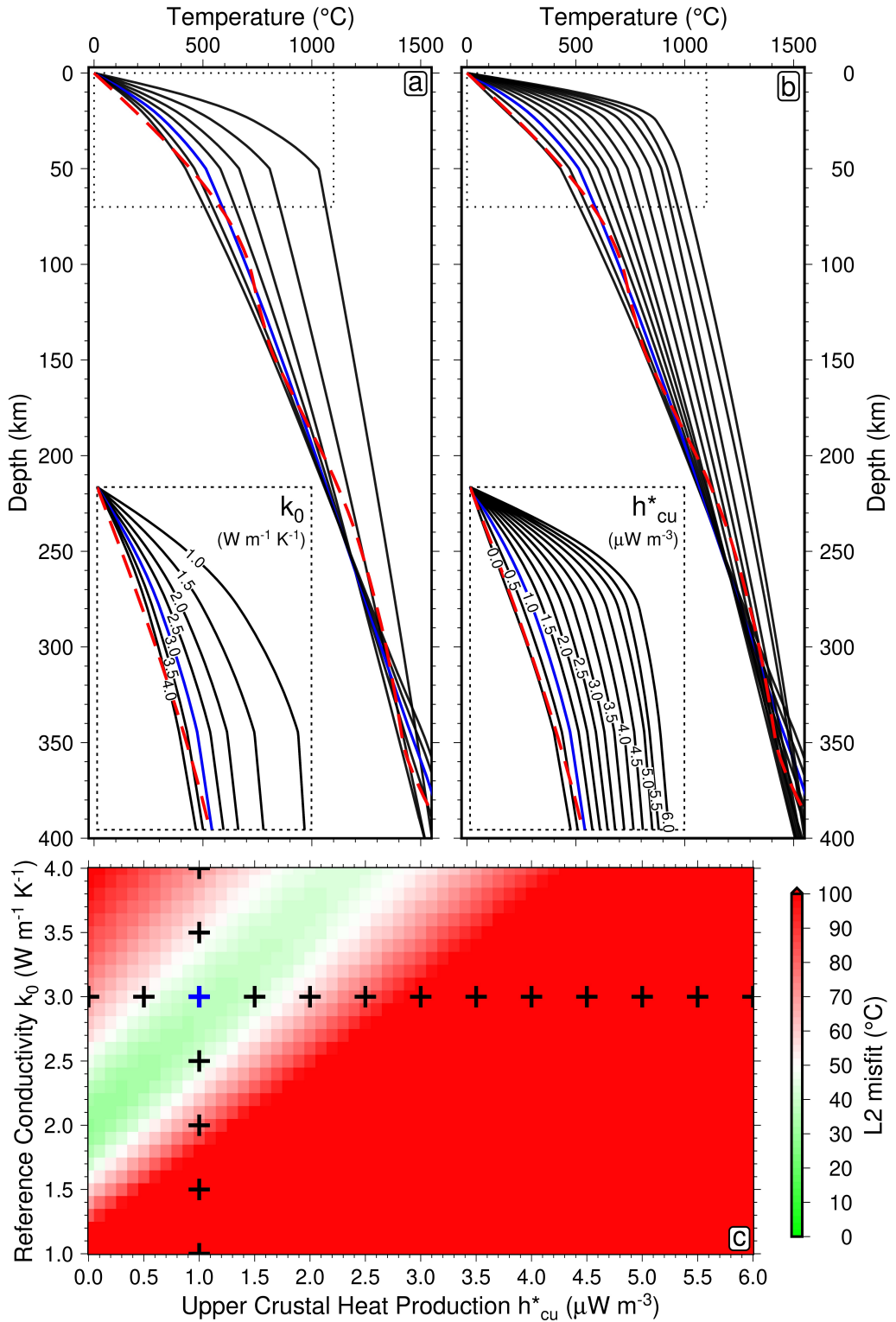


Figure 4.2: Fitting seismically inferred geotherms. (a) Constant reference conductivity, $k_0 = 2.5 \text{ W m}^{-1} \text{ K}^{-1}$, variable upper crustal heat production, h_{cu}^* in range 0.0 to 6.0 $\mu\text{W m}^{-3}$. (b) Variable reference conductivity, k_0 in range 1.0 to 4.0 $\text{W m}^{-1} \text{ K}^{-1}$, constant upper crustal heat production, $h_{\text{cu}}^* = 0.5 \mu\text{W m}^{-3}$. (c) Trade-off between crustal conductivity and upper crustal heat production in misfit between seismically inferred and steady-state fitted geotherm (k_0 and h_{cu}^* combinations used in panels (a) and (b) marked by cross-hairs).

4.2.5 Sampling Crustal Parameters to Optimise GHF

Reference thermal conductivity, k_0 , and upper crustal heat production, h_{cu}^* , are treated as laterally variable parameters in the model, so as to account for the influence of crustal composition on geothermal structure. Both parameters could exhibit lateral variability within the approximate ranges $k_0 \sim 1.0$ to $4.0 \text{ W m}^{-1} \text{ K}^{-1}$ and $h_{\text{cu}}^* \sim 0.0$ to $6.0 \mu\text{W m}^{-3}$ (Hasterok and Chapman, 2011; Jennings et al., 2019; Lösing et al., 2020; Sammon et al., 2022). Such variations can have a significant impact on q_s . For example, it was calculated that for a typical V_S -derived input geotherm, varying k_0 and h_{cu}^* within the aforementioned ranges results in surface GHF variations of $q_s \sim 20$ to 170 mW m^{-2} . The lowest (highest) inferred q_s occurs when both k_0 and h_{cu}^* are minimised (maximised). This observation can be rationalised by considering the dependence of q_s on each crustal parameter in turn. Recall the definition of q_s ,

$$q_s = \left| -k(z = z_0) \frac{\partial T}{\partial z} \Big|_{z=z_0} \right|. \quad (4.4)$$

Firstly, whilst thermal conductivity throughout the crust trades off negatively with the surface geothermal gradient, the presence of the surface thermal conductivity,

$$k(z = z_0) = k_c(k_0, T = 0^\circ\text{C}, P = 0 \text{ GPa}) \approx k_0 \quad (4.5)$$

in Equation 4.4 dominates, meaning that overall, q_s and k_0 trade-off positively with one another. Secondly, to understand the relationship between q_s and h_{cu}^* , consider the simplified case of constant crustal conductivity $k_c = k_0$, in which case surface heat flow can be expressed as

$$q_s = k_0 \frac{\partial T}{\partial z} \Big|_{z=z_1} + \int_{z_1}^{z_0} h^*(z) dz, \quad (4.6)$$

where z_0 represents the surface depth, and z_1 represents the depth to the base of the upper crust.

The parameter z_0 can freely be assigned to $z_0 = 0$ km, according to convention. Upper crustal heat production is uniform in the parameterisation, and so this equation simplifies further to

$$q_s = k_0 \frac{\partial T}{\partial z} \Big|_{z=z_1} + h_{\text{cu}}^* z_1. \quad (4.7)$$

Since the choice of k_0 and h_{cu}^* has a second-order impact on the temperature gradient at the base of the upper crust (first term of Equation 4.7), q_s is approximately proportional to the choice of upper crustal heat production. This conclusion remains valid when the crustal conductivity parameterisation $k_c(k_0, T, P)$ is reintroduced. As a result, both k_0 and h_{cu}^* trade off positively with q_s , in agreement with the aforementioned result that the lowest (highest) inferred q_s occurs when both k_0 and h_{cu}^* are minimised (maximised).

In order to optimise predictions of GHF at each location, k_0 and h_{cu}^* are co-varied, and the least-squared misfit between V_S -inferred and fitted geotherms as a function of the two free parameters is evaluated (Figure 4.2). If the misfit space at each location were to exhibit a global minimum, this would allow for simultaneous extraction of best-fitting k_0 , h_{cu}^* and q_s . However, as might be expected, it is found that k_0 and h_{cu}^* trade off significantly with one another. This trade-off can be visualised by holding k_0 constant and varying h_{cu}^* , and vice versa, and observing the similarity in fitted geotherms (Figure 4.2, panels a-b). Of course, this similarity is also borne out in the misfit space, where valley-like minima are seen (Figure 4.2c). Since q_s trades-off positively with both k_0 and h_{cu}^* , it is vital to be able to locate where in the valley of the misfit space the solution lies. To resolve this issue and break the observed trade-off, additional information is required, which is obtained by utilising an independent geophysical constraint on k_0 .

To gain insight into laterally varying crustal conductivity, a model of crustal V_P (km s^{-1} , Figure 4.1b) is drawn on. The same V_P model as was assumed in **ANT-20** is used, for consis-

tency with the chosen crustal thickness model, and the V_S -derived geotherms. Jennings et al. (2019) relate V_P to k_0 via laboratory measurements on igneous rocks spanning a wide range of compositions. They found that SiO_2 content is the dominant control on thermal conductivity. By making use of the empirical relationship,

$$k_0(V_P) = a_0 + a_1 V_P + a_2 V_P^2 \pm \epsilon, \quad (4.8)$$

$$a_0 = 3.162 \times 10^1 \text{ W m}^{-1} \text{ K}^{-1},$$

$$a_1 = -8.263 \times 10^{-3} \text{ W m}^{-2} \text{ K}^{-1} \text{ s}^{-1},$$

$$a_2 = 5.822 \times 10^{-7} \text{ W m}^{-3} \text{ K}^{-1} \text{ s}^{-2},$$

$$\epsilon = 0.31 \text{ W m}^{-1} \text{ K}^{-1},$$

as provided by Jennings et al. (2019), Antarctic crustal conductivity is estimated by averaging crustal V_P (in km s^{-1}) at each continental location, and converting it into k_0 (Figure 4.1c). In addition, the spread in V_P data within the crust at each location is utilised, along with the $k_0(V_P)$ fitting residual $\epsilon = 0.31 \text{ W m}^{-1} \text{ K}^{-1}$, to estimate an uncertainty in the predicted conductivity (Figure 4.1d).

Since independent predictions of $k_0(\theta, \varphi)$ derived from V_P data are now accessible, it is possible to locate physically plausible regions of k_0 and h_{cu}^* space. The process begins by sampling a value of k_0 from a Gaussian distribution at each location, according to

$$k_0 \sim \mathcal{N} [\mu(k_0), \sigma(k_0)], \quad (4.9)$$

where $\mu(k_0)$ is given by the empirical prediction of Equation 4.8, and $\sigma(k_0)$ is given by the uncertainty associated with this prediction (Figure 4.1). For each sampled value of k_0 , the

corresponding best-fitting value of h_{cu}^* is extracted, as well as the q_s associated with this combination of crustal parameters. By repeating this sampling procedure, distributions of k_0 , h_{cu}^* and q_s are built up. These distributions are summarised at each location using a mean and standard deviation, providing Antarctic GHF predictions along with an estimate of their uncertainty.

4.3 Results and Discussion

In this section, the crustal parameter sampling method described in the previous section is applied. First, statistical summaries of the ensemble predictions of Antarctic upper crustal heat production are shown. Second, estimates of Antarctic GHF are presented. In the discussion that follows, GHF values are compared to those of previous studies, as well as local values derived from in situ temperature probe observations in boreholes and unconsolidated sediment. Then, in the context of these comparisons, the novel procedure developed in this study to infer GHF from V_S and V_P information is appraised. Finally, the most pertinent outstanding challenges in the domain of Antarctic GHF are discussed.

4.3.1 Antarctic Upper Crustal Heat Production Estimates

In Figure 4.3, a summary is shown of the obtained distribution of upper crustal heat production (h_{cu}^*) values. Spatially averaging over the Antarctic continental region, $h_{\text{cu}}^* = 1.2 \pm 1.2 \mu\text{W m}^{-3}$. Owing to the dichotomy between West and East Antarctica in terms of tectonic history, as well as inferred thermal structure, it is instructive to review the inferred h_{cu}^* between the two sub-continents. To do so, the satellite-mapped drainage network of Zwally and Giovinetto (2011) is utilised to separate West and East Antarctica. In West Antarctica, $h_{\text{cu}}^* = 4.2 \pm 1.5 \mu\text{W m}^{-3}$. In East Antarctica, $h_{\text{cu}}^* = 0.3 \pm 0.3 \mu\text{W m}^{-3}$. An interesting feature of the upper crustal heat production inferences is that regions that are inferred to have been impacted in the past ~ 35 Myr by intraplate basaltic magmatism and/or episodes of rifting (e.g., the Alexander Island region of

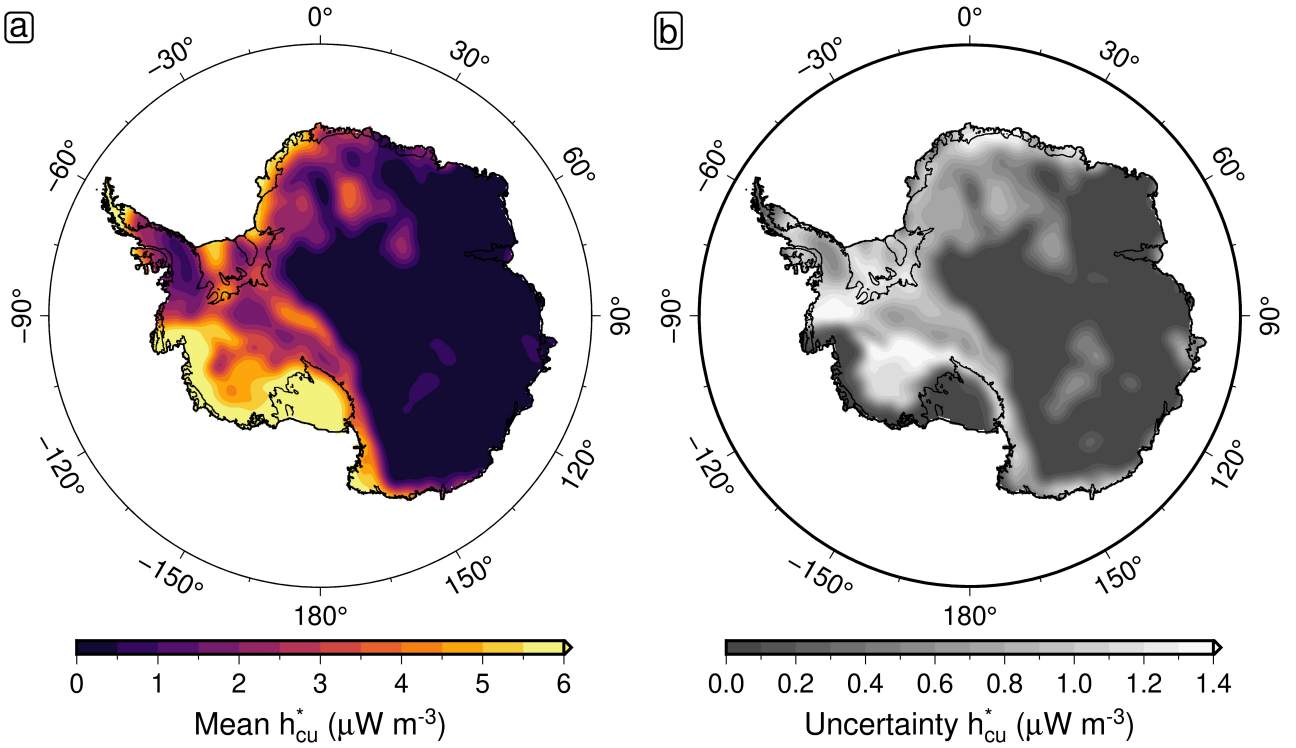


Figure 4.3: **Upper crustal heat production.** (a) Mean. (b) Standard deviation.

the Antarctic Peninsula, Marie Byrd Land and the Victoria Land Basin; LeMasurier, 2008; Sauli et al., 2021) correspond with very high upper crustal heat production values ($h_{cu}^* \geq 4 \mu\text{W m}^{-3}$). Such inferences may be affected by a form of unquantified uncertainty in the modelling framework: the potential for the goothermal profile to be in transient- rather than steady-state. If thermal perturbations associated with these geodynamic events locally thinned the subcontinental lithosphere, present-day geotherms may not be in equilibrium. For identical values of upper crustal heat production and lithospheric thickness, these transient geotherms would have warmer temperatures at crustal levels than steady-state counterparts. The assumption of thermal steady-state in the inverse framework may therefore lead us to infer unrealistically high h_{cu}^* values in order to match these elevated crustal temperatures. Discrepancies in inferred h_{cu}^* and geotherm shape between optimal transient and steady-state temperature profiles may also have some impact on GHF (q_s) predictions; however, steady-state profiles can be used to reasonably approximate transient geotherms predicted for a range of geodynamic settings (Goes et al., 2020).

To test the possible impact of transient heat conduction on h_{cu}^* and q_s inferences, a series of tests focused on Alexander Island and Amundsen Sea Embayment are undertaken, both regions affected by Neogene uplift and volcanism. The timing of peak rock uplift in these regions is inferred from thermochronometric data and assumed to represent the time at which the lithosphere was thinned to its minimum value (t_0). These peaks are inferred to have occurred at ca. 32 ± 4 Ma on Alexander Island, and ca. 29 ± 1 Ma in the Amundsen Sea Embayment, potentially driven by mantle upwelling related to a slab window and a mantle plume, respectively (LeMasurier, 2008; Twinn et al., 2022). The approach outlined in Stephenson et al. (2023), and in the supplements of Hazzard et al. (2023), is used to simulate lithospheric cooling and re-thickening following these periods of active thinning and magmatism, treating mantle potential temperature and upper crustal heat production as free parameters. Optimal values for these parameters, as well as the time since the lithosphere thinned to its minimum extent ($\tau = t - t_0$), are then determined based on the misfit between the V_S -derived geotherm in each region and the simulated geotherms.

Parameterisation

Time-dependent cooling is calculated by solving the one-dimensional heat equation expressed as

$$\rho(P, T, X)C_P(T, X)\frac{\partial T}{\partial t} = \frac{\partial}{\partial z} \left[k(P, T, X)\frac{\partial T}{\partial z} \right] + h^*(X), \quad (4.10)$$

where t is time, z is depth, T is temperature, P is pressure, X is composition, ρ is density, C_P is the isobaric specific heat capacity, k is the thermal conductivity, and h^* is the internal radiogenic heat production. In each region, self-consistency is ensured by parameterising the physical properties that are held fixed (e.g., X , ρ , C_P and k) in an identical manner to the steady-state geotherm calculations.

Equation 4.10 is solved numerically with an unconditionally stable time- and space-centered

Crank-Nicholson finite difference scheme that includes a predictor-corrector step (Press et al., 2007). Accordingly, Equation 4.10 is recast as

$$\begin{aligned} T_j^{n+1} + A \left(-\frac{k_{j+\frac{1}{2}}^m}{\Delta z_j^m} T_{j+1}^{n+1} + \left(\frac{k_{j+\frac{1}{2}}^m}{\Delta z_j^m} + \frac{k_{j-\frac{1}{2}}^m}{\Delta z_{j-1}^m} \right) T_j^{n+1} - \frac{k_{j-\frac{1}{2}}^m}{\Delta z_{j-1}^m} T_{j-1}^{n+1} \right) \\ = T_j^n + A \left(\frac{k_{j+\frac{1}{2}}^m}{\Delta z_j^m} T_{j+1}^n - \left(\frac{k_{j+\frac{1}{2}}^m}{\Delta z_j^m} + \frac{k_{j-\frac{1}{2}}^m}{\Delta z_{j-1}^m} \right) T_j^n + \frac{k_{j-\frac{1}{2}}^m}{\Delta z_{j-1}^m} T_{j-1}^n \right) + A h_*^m \left(\Delta z_j^m + \Delta z_{j-1}^m \right), \end{aligned} \quad (4.11)$$

where

$$A = \frac{\Delta t}{\left(\rho_j^m C_P^m \left(\Delta z_j^m + \Delta z_{j-1}^m \right) \right)}, \quad (4.12)$$

and Δt is the time step, Δz is the depth spacing between nodes, and n and j are the time and depth indices, respectively. Equation 4.11 is solved by tridiagonal elimination Press et al., 2007. For the initial predictor phase of each time step, $m = n$, while in the subsequent corrector phase, $m = n + \frac{1}{2}$. A Lagrangian reference frame is used, whereby Δz_j^m is initially set to 1 km (i.e., when $m = 0$), then scales with thermal contraction in subsequent timesteps.

These timesteps are calculated using a Courant-Friedrichs-Lowy condition calculated according to

$$\Delta t = \min_j \left[\frac{\left(\Delta z_j^0 \right)^2 \rho_j^0 C_P^0}{2.2 k_j^0} \right] \sim 5 \text{ kyr.} \quad (4.13)$$

T^{n+1} typically converges to within a tolerance of 0.001°C after the corrector phase.

Boundary Conditions

All models consist of crustal and mantle layers. Crustal thickness (z_c) is set to locally inferred values, where $z_c = 18$ km for Alexander Island and $z_c = 23$ km for the Amundsen Sea Embayment. In both cases the underlying mantle extends from the Moho to an assumed equilibrium plate thickness, z_p . The initial depth to the LAB, after the cessation of magmatic activity and

lithospheric thinning, is assumed to be $z_{LAB}^0 = 25$ km. To account for the possible presence of a thermal anomaly beneath the plate, initial asthenospheric potential temperature, T_p^0 , can vary between 1333°C, which is assumed to be the temperature of ambient mantle, and 1633°C (i.e. an excess temperature of 300 °C).

If the lithospheric mantle were instantaneously thinned, it is likely that the remaining mantle would not be thermally equilibrated. Nonetheless, since the resulting mechanical boundary layer is thin, temperatures will rapidly reach steady state and minimise the impact of thermal disequilibrium. Consequently, initial temperature profiles are obtained by combining the parameters outlined above with the steady-state geotherm fitting procedure previously outlined. For each combination of h_{cu}^* , and T_p^0 , the steady-state geotherm consistent with z_{LAB}^0 is found by iterating through a range of mechanical boundary layer thicknesses (2–60 km), and selecting the temperature profile for which the depth to the 1200°C isotherm is equal to z_{LAB}^0 . For each value of h_{cu}^* and T_p^0 , the initial thermal structure is found by searching for a steady-state that yields the assumed minimum LAB thickness ($z_{LAB}^0 = 25$ km).

To simulate the potential waning of the imposed heat source through time, an evolving basal boundary condition is imposed. At $t = 0$, $T(z)$ is given by the initial isentrope defined by T_p^0 below the base of the thermal boundary layer (i.e., the shallowest depth at which the geothermal gradient, $\frac{\partial T}{\partial z}$, drops below 0.5°C km⁻¹). In later timesteps, the depth at which this boundary condition is imposed, z_b , increases according to a prescribed sinking rate, $v_z = 1$ mm yr⁻¹, until the deepest model node (i.e. $z_b = z_p = 125$ km) is reached, whereupon the basal boundary depth remains fixed. Simultaneously, from $t = 0$ –100 Myr, the temperature applied at the basal boundary decays linearly to that of the ambient mantle isentrope (i.e. $T_p = 1333$ °C) at the relevant depth. Beyond $t = 100$ Myr, the basal temperature is assumed to remain equal to that of the ambient mantle isentrope at the appropriate depth.

Optimisation Strategy

A three-parameter sweep is carried out to find the combination of initial potential temperature (T_p^0), upper crustal heat production (h_{cu}^*), and time since minimum lithospheric thickness was obtained (τ) that yields optimal fit to the V_S -inferred geotherm in each location. The temperature evolution is then calculated for 150 Myr from this point. Misfit between tomographically determined geotherms and predicted transient temperature profiles is calculated for each geotherm prediction

$$\chi_T = \sqrt{\frac{1}{M} \sum_{i=1}^M (T_i^t - T_i^v)^2}, \quad (4.14)$$

where T_i^v and T_i^t are V_S -derived and calculated temperature profiles for i^{th} measurement, respectively. $M = 126$ is the number of depth points used in the calculation, in which both profiles are interpolated at 1 km intervals from 0–125 km below the basement. Note that although thermal evolution is calculated over 150 Myr, when obtaining optimal parameters for each location the search is restricted to $\tau < \tau_{\max}$, where τ_{\max} represents the maximum thermochronologically constrained age of peak rock uplift, which is presumed to coincide with the time at which minimum lithospheric thicknesses were reached (36 Ma and 30 Ma for Alexander Island and Amundsen Sea Embayment, respectively).

Heat Flow Inference

Three key results emerge from the analysis. First, transient geotherms provide significantly better fit to the V_S -derived geotherms at both sites (\sim 65–80% lower χ_T), implying that these regions of West Antarctica may not be in thermal steady-state. Secondly, the best-fitting transient geotherms have consistently lower h_{cu}^* values than those inferred from the steady-state fits used to construct the revised **HR24** heat flow model. Optimal h_{cu}^* values for Alexander Island and Amundsen Sea Embayment transient geotherms are $4.2 \mu\text{W m}^{-3}$ and $5.2 \mu\text{W m}^{-3}$,

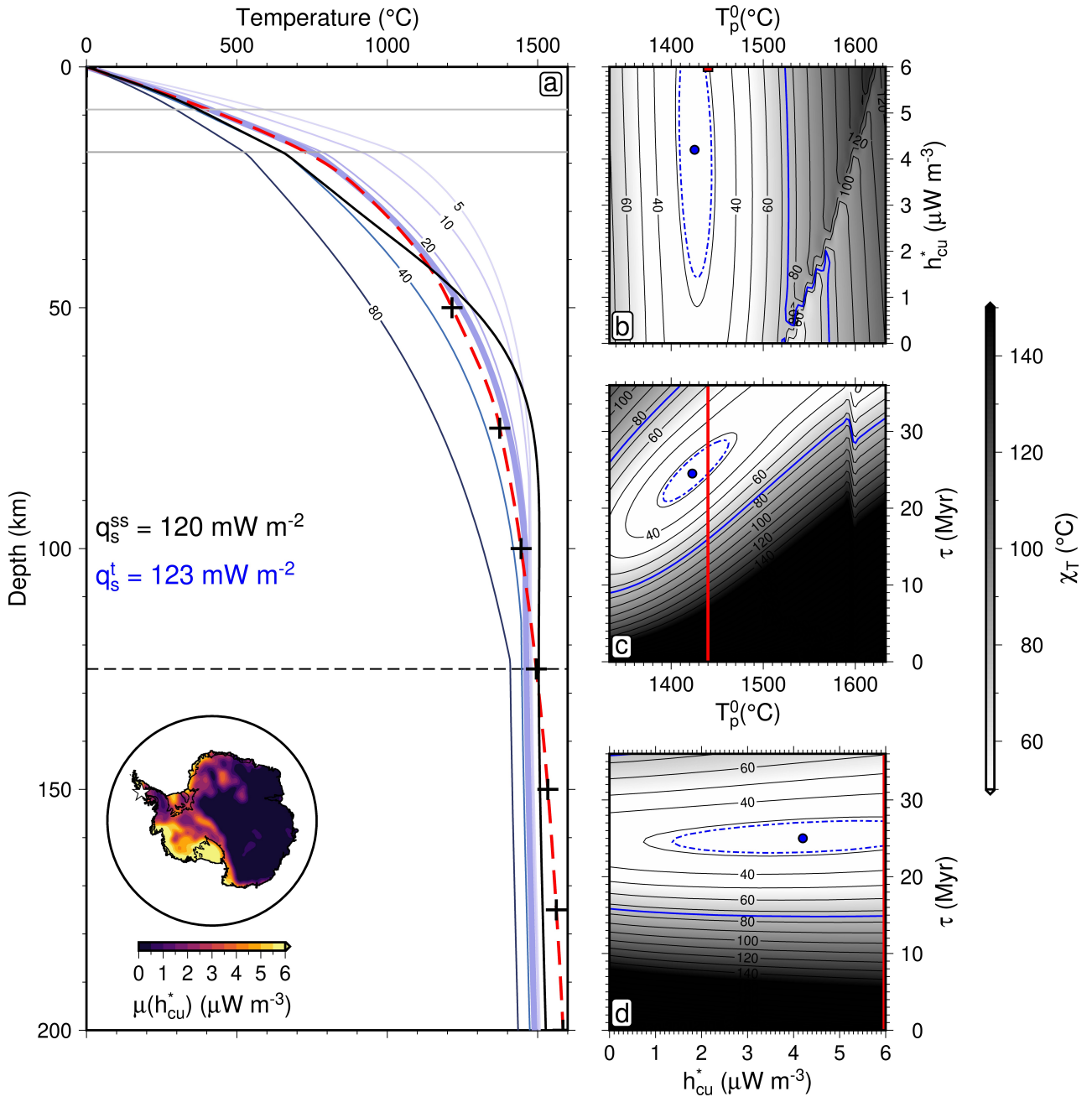


Figure 4.4: Alexander Island transient geotherms. (a) Geotherms. Crosses/red dashed line = raw/interpolated V_S -derived geotherm; black solid line = best-fitting steady-state geotherm (as used in HR24 heat flow model); coloured lines = transient geotherms labelled by time in Myr since lithosphere thinned to minimum value (τ); black dashed line = plate thickness ($z_p = 125 \text{ km}$); dark grey line = Moho; light grey line = upper crust-lower crust boundary; q_s^{ss} = heat flow for best-fitting steady-state geotherm; q_s^t = heat flow for best-fitting transient geotherm. Inset shows mean upper crustal heat production; star = location of Alexander Island. (b) Misfit between V_S -derived and transient geotherms as a function of initial mantle potential temperature (T_p^0) and upper crustal heat production (h_{cu}^*). Blue circle = global minimum; dashed blue line = 110% of global minimum; solid blue line = misfit for best-fitting steady-state geotherm; red square = optimal parameter values for best-fitting steady-state geotherm. (c) Misfit as a function of T_p^0 and time since lithosphere thinned to minimum value (τ). Red line = optimal parameter value for best-fitting steady-state geotherm. (d) Misfit as a function of h_{cu}^* and ΔT .

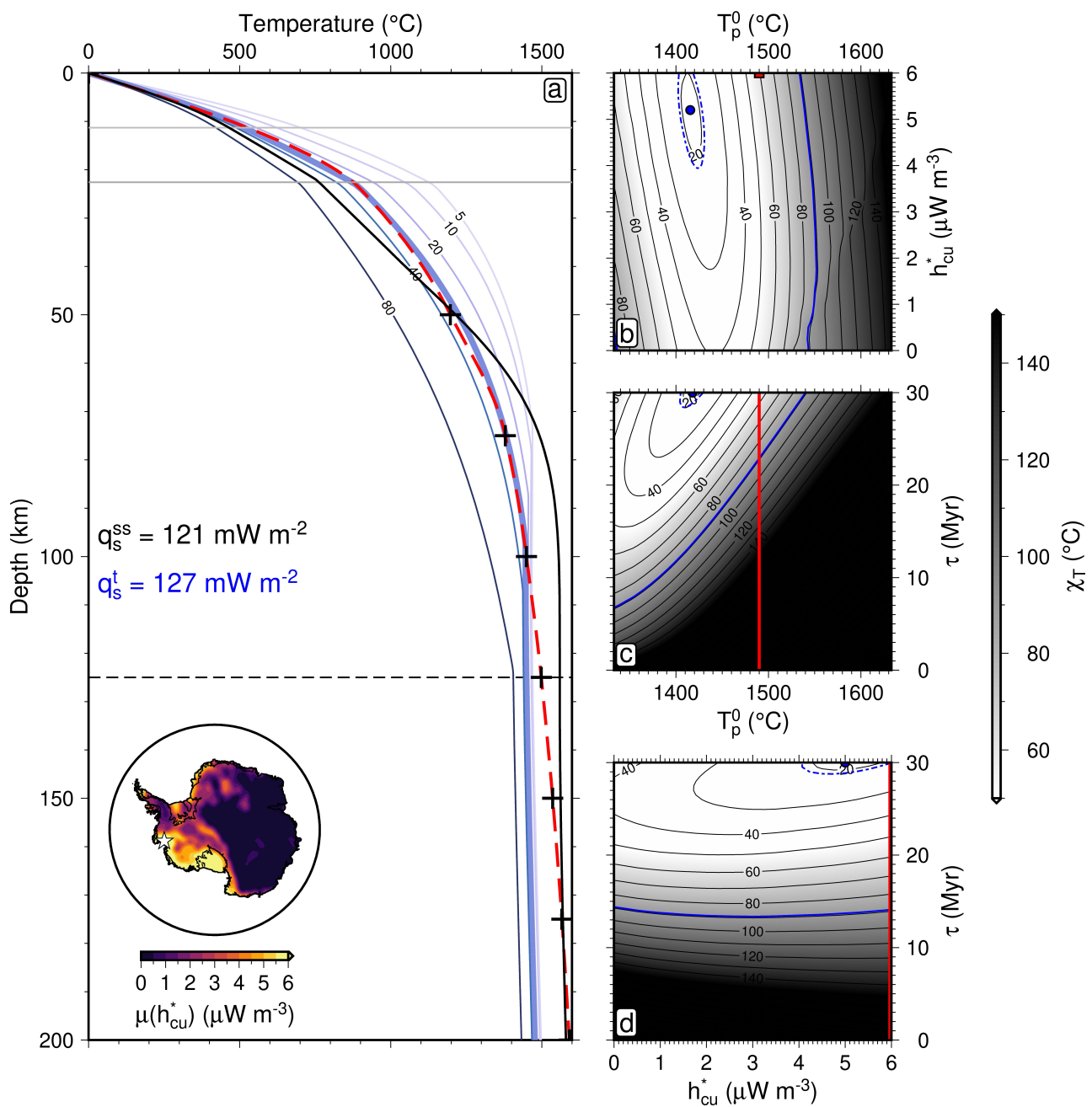


Figure 4.5: Amundsen Sea Embayment transient geotherms. Panels follow Figure 4.4.

respectively. In contrast, the optimal value for both steady-state geotherms is $6.0 \text{ } \mu\text{W m}^{-3}$, the upper limit allowed within the model framework (i.e., if a higher upper bound were set, the discrepancy in optimal h_{cu}^* between transient and steady-state geotherms would likely be larger). Finally, heat flow predictions are demonstrated to be minimally impacted by uncertainty concerning which model parameterisation should be implemented (i.e., transient or steady-state). Optimal heat flow values differ by less than 5% for Alexander Island and Amundsen Sea Embayment. In both cases this mismatch is smaller than the uncertainty on the steady-state inference. Taken together, these results indicate that the steady-state geotherm assumption is likely leading to overestimation of upper crustal heat production in locations like the Amundsen Sea Embayment and Alexander Island. However, the impact of this simplification on heat flow inferences is small. This result corroborates the more qualitative analysis conducted in Goes et al. (2020) and underlines that, although h_{cu}^* inferences may be locally incorrect, significantly, heat flow estimates are accurate.

4.3.2 Antarctic GHF Estimates

Resulting estimates of Antarctic GHF are shown in Figure 4.6. The results indicate high q_s in West Antarctica, where heat supply into the base of the Antarctic Ice Sheet is estimated to vary between 60 and 130 mW m^{-2} , and is on average $97 \pm 14 \text{ mW m}^{-2}$ (median, and median absolute deviation, respectively). Such GHF values are significantly higher than the global continental average, $q_s = 67 \pm 47 \text{ mW m}^{-2}$ (as inferred from gravity-driven probe and borehole temperature-depth data), and are in fact intermediate between the former and the global average over continental rift zones, $q_s = 114 \pm 94 \text{ mW m}^{-2}$ (Lucazeau, 2019). This result is consistent with recent tectonic activity, evidence for Cenozoic magmatism, and inferences of a thermal anomaly beneath West Antarctica (Ball et al., 2021; Barletta et al., 2018; Hazzard et al., 2023). The distribution of q_s values within the aforementioned range is relatively uniform,

implying significant lateral heterogeneity across West Antarctica. Maximum q_s is inferred at the continental perimeter in the Amundsen Sea region, and in the northern Antarctic Peninsula.

In East Antarctica, the results indicate q_s in the range 20 to 120 mW m^{-2} . Note that the presence of above-continental-average GHF values within this range is indicative of the fact that not all of the defined East Antarctic region is underlain by cold, cratonic material. However, the distribution of inferred GHF is heavily skewed towards lower values, which is borne out in the spatial average $30 \pm 8 \text{ mW m}^{-2}$. Such low values are consistent with globally averaged GHF estimates in continental regions of Archean age, $q_s = 46 \pm 21 \text{ mW m}^{-2}$ (Lucazeau, 2019).

For the most part, the spatial pattern of GHF uncertainty, $\sigma(q_s)$, is similar to that of the GHF prediction itself, $\mu(q_s)$. The ratio of these two predictions, $\sigma(q_s)/\mu(q_s)$, is on average $16 \pm 10\%$ over the Antarctic continent. Elevated proportional uncertainty in GHF structure is estimated in Coats Land and Dronning Maud Land in East Antarctica, in parallel with anomalously high uncertainty in heat production. The least-squared misfit between inferred and modelled geotherm is relatively insensitive to the choice of heat production here, reducing the ability to constrain this parameter and hence q_s . Anomalously low q_s uncertainty ($\sigma(q_s) < 10 \text{ mW m}^{-2}$) is estimated at the Amundsen Sea Embayment and Ross Ice Shelf, as well as along the grounding line between these two regions. These areas are characterised by high inferred GHF in the region of 100 to 130 mW m^{-2} . The uncertainty here is artificially low owing to the inferred heat production lying at the top of the parameter sweep range, $h_{\text{cu}}^* = 6.0 \text{ } \mu\text{W m}^{-3}$ (Figure 4.3). Since the seismically inferred geotherm here is systematically hotter than the modelled profile, the inferred value of h_{cu}^* is insensitive to variations in crustal thermal conductivity, and thus exhibits no variation. This causes an artificial reduction in the GHF uncertainty, which can be related back to the discussion of transient geotherms in the previous section. Optimal transient geotherms were found to require less extreme h_{cu}^* values than their steady-state counterparts, meanwhile GHF predictions were near-identical. There-

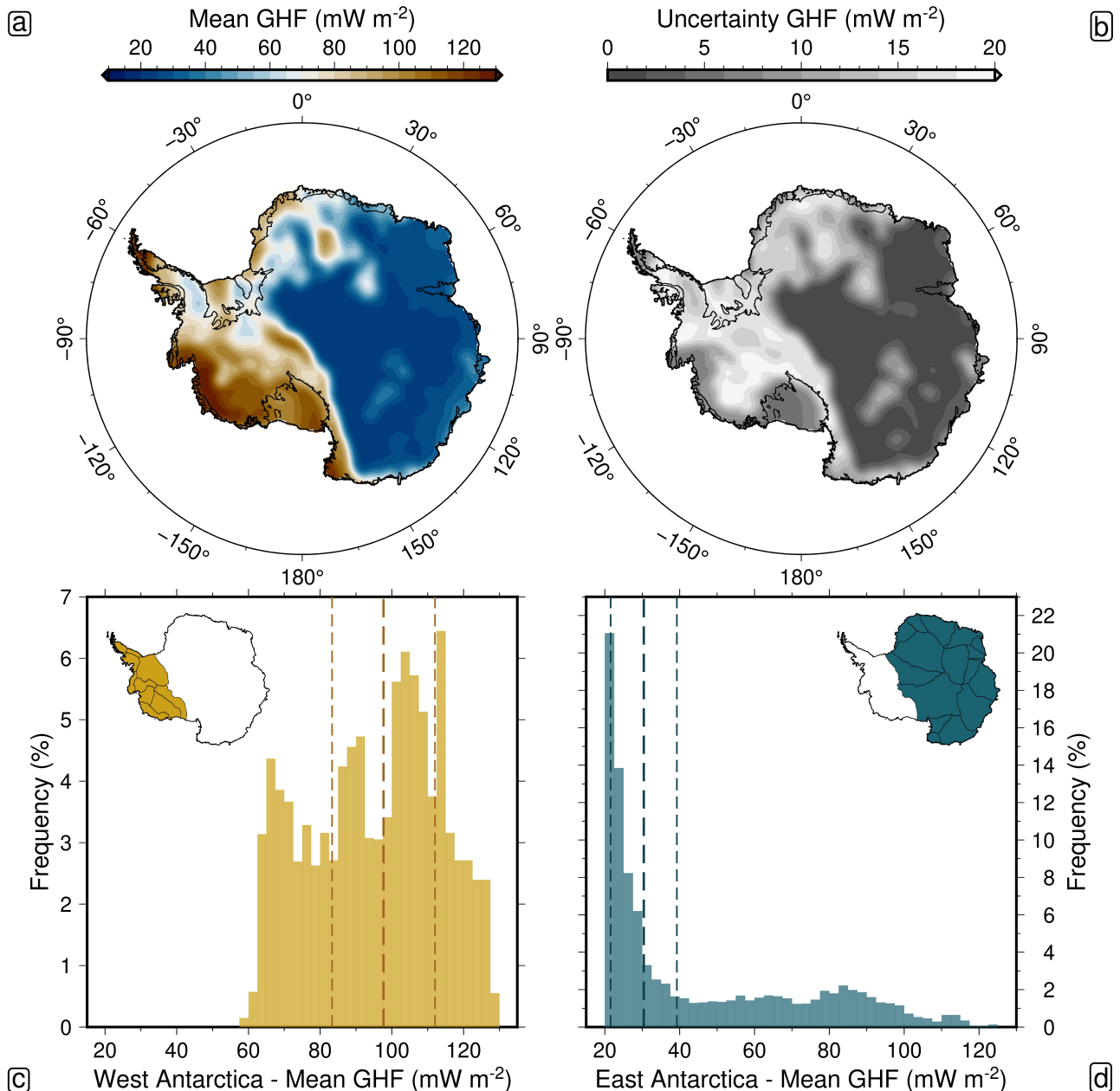


Figure 4.6: **Seismically inferred GHF.** (a) Mean. (b) Standard deviation. (c) Distribution over West Antarctica (region defined according to satellite-mapped drainage networks of Zwally and Giovinetto, 2011). (d) Same as (c), East Antarctica.

fore, the upper limit of the heat production in the modelling framework was not increased, since h_{cu}^* values in excess of $6.0 \mu\text{W m}^{-3}$ are inconsistent with the range of physically plausible values based on continental geology (Artemieva et al., 2017; Sammon et al., 2022), and unreasonable increases in h_{cu}^* would be required to attempt to fit the inferred geotherm. Predictions of GHF uncertainty in these regions are thus artificially suppressed, however the GHF predictions themselves remain trustworthy.

4.3.3 Comparison With Previous Studies

A comparison of the GHF model with those from previous studies utilising a range of approaches is presented in Figure 4.7. Consistent across all studies, a long-wavelength pattern of elevated heat supply in West Antarctica is observed, alongside more uniformly low heat supply in East Antarctica. However, short-wavelength ($\sim 1,000 - 10,000$ km) structure differs significantly between models (both in terms of spatial pattern, and amplitude), reflecting the range of data sets and modelling assumptions used to construct them. In particular, the model (HR24, Figure 4.7) spans a significantly greater range (110 mW m^{-2}) than its comparators, with the exception of the two magnetic studies Maule et al. (2005) and Martos et al. (2017), which exhibit exceedingly high peak GHF values of 190 mW m^{-2} and 240 mW m^{-2} respectively. The higher amplitude of GHF variations in this study compared to most models can be explained by the incorporation of laterally heterogeneous crustal composition. In East Antarctica, below-average crustal heat production is inferred, and in West Antarctica the opposite; the combined effect of which is to broaden the range of inferred q_s . As compared to a directly analogous model assuming constant $k_0 = 2.5 \text{ W m}^{-1} \text{ K}^{-1}$ and $h_{\text{cu}}^* = 1.0 \mu\text{W m}^{-3}$ (HR23, Figure 4.7), a 30% increase in maximum Antarctic q_s , and a 50% reduction in minimum Antarctic q_s is predicted (Hazzard et al., 2023).

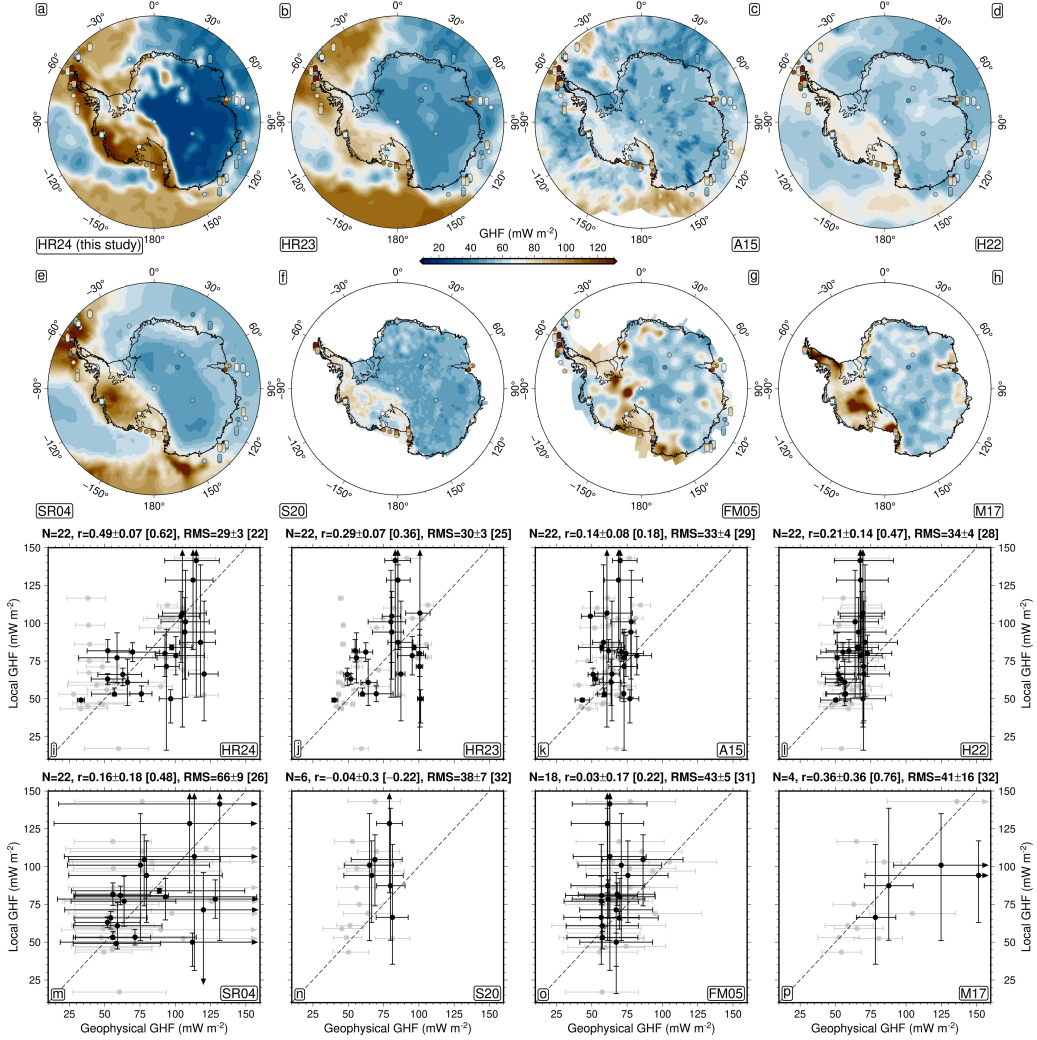


Figure 4.7: GHF Model Comparison. (a)–(h) Geophysical GHF inferences: **HR24** – inferred directly from V_S and V_P (this study); **HR23** – inferred directly from V_S (Hazzard et al., 2023); **A15** – inferred directly from V_S (An et al., 2015); **H22** – inferred via joint seismic and gravity inversion (Haeger et al., 2022); **SR04** – inferred empirically via V_S (Shapiro and Ritzwoller, 2004); **S20** – inferred empirically via V_S (Shen et al., 2020); **FM05** – inferred from magnetic anomaly data (Maule et al., 2005); **M17** – inferred from magnetic anomaly data (Martos et al., 2017). GHF inferences derived from gravity-driven probes and boreholes overlaid as coloured capsules/circles. Capsules used where 2+ local data points available (coloured by lowest-average-highest local estimate from bottom-middle-top). Circles used where 1 local data point available. Note that **HR24** has been extended into the oceanic domain to allow more complete comparison with local data. In the oceanic domain $k_0 = 2.6 \text{ W m}^{-1} \text{ K}^{-1}$ and $h_{cu}^* = 0.0 \mu\text{W m}^{-3}$ are assumed, in keeping with oceanic crustal composition (Grose and Afonso, 2013; Richards et al., 2018). (i)–(p) Relationship between geophysically and locally inferred GHF (Section 4.3.4), same studies as (a)–(h). Data points and associated error bars show the mean and range of local/geophysical GHF values at each location, respectively. Statistics summarising local-geophysical agreement are: r = Pearson’s r -value correlation coefficient; RMS = root-mean-square deviation (values reported in the form $a \pm b$ [c], where a =median, b =median absolute deviation, c =value calculated ignoring data uncertainty). Gray data points correspond to locations where only one local GHF inference is available (i.e., circles in panels (a)–(h)) and are not included in model statistics.

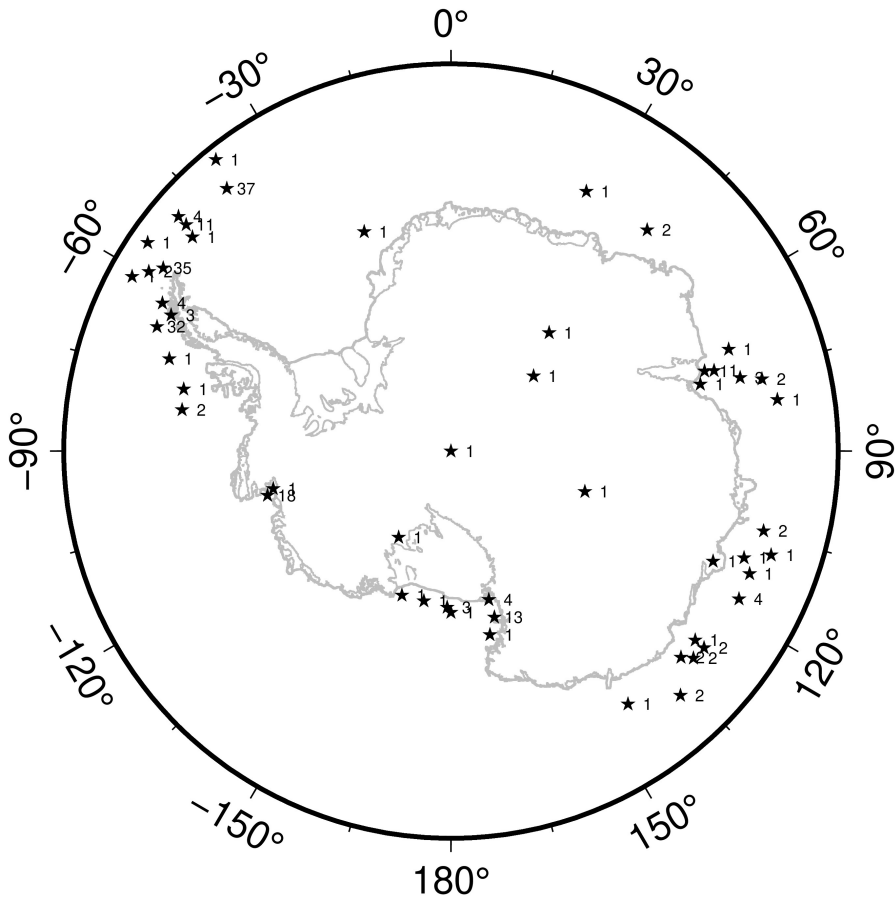


Figure 4.8: Location of GHF inferences derived from local data after collection into distinct spatial groups. Integer values next to data points refer to the number of local GHF inferences compiled at each location.

4.3.4 Comparison With Local Data

Despite the sparsity of Antarctic GHF estimates derived from in situ temperature probe observations in boreholes and unconsolidated sediment, these data can be utilised to independently assess geophysically informed models of q_s . Inferences of GHF from borehole probes into either bedrock or unconsolidated sediment were extracted from the New Global Heat Flow database of Lucazeau, 2019, providing 229 individual measurements within the proximity of Antarctica. Nine additional data points based on boreholes probes into unconsolidated sediment were extracted from Dziadek et al., 2021. A further five GHF inferences based on temperature profile inversions from ice borehole data were added (Dahl-Jensen et al., 1999; Engelhardt, 2004; Hondoh et al., 2002; Price et al., 2002; Salamatian et al., 1998). It is important to treat in situ inferences carefully, since they are representative of localised temperature structure, and are

potentially susceptible to contamination by thermal signals caused by frictional heating at the base of the ice sheet, hydrological circulation, and local topography (Colgan et al., 2021; Shen et al., 2020). In addition, limited lateral resolution in the chosen V_S model will smooth out GHF variations on spatial scales smaller than ~ 100 km, diminishing the ability to accurately compare to local estimates. Therefore, local GHF records from gravity-driven probes and boreholes are collected into spatially separate measurement groups and geophysically inferred GHF values are extracted within a 100 km radius of the centroid of each group. The location of each measurement group, along with the number of local GHF inferences compiled into each record, is shown in Figure 4.8. Note that local GHF inferences exceeding 200 mW m^{-2} are excised. Such values are expected to be representative of localised advective signals (e.g., from hydrological circulation), rather than the conductive heat flow characterising the measurement region as a whole. This expectation stems from the fact that, even for the shallowest LAB depth observed across Antarctica (~ 35 km), optimised plate cooling models find a corresponding oceanic heat flow value of only $\sim 150 \text{ mW m}^{-2}$ (Hazzard et al., 2023). This number will closely approximate the upper bound of the purely conductive contribution to Antarctic heat flow, since oceanic regions are characterised by transient geotherms and thin crust. Local measurement groups contributed to by only one local study were also ignored in the calculation of quantitative model statistics. Such locations lack sufficient information to establish the uncertainty in local data. The geophysical studies used for comparison with local data are **HR24** (this study); **HR23** (Hazzard et al., 2023); **A15** (An et al., 2015); **H22** (Haeger et al., 2022); **SR04** (Shapiro and Ritzwoller, 2004); **FM05** (Maule et al., 2005); **S20** (Shen et al., 2020); **M17** (Martos et al., 2017). Since nearly all local data were obtained off the coast of Antarctica, the number of local-geophysical comparison points available for use was limited in the case of the studies **S20** and **M17**, whose spatial footprints do not extend offshore. Only four locations were close enough to continental Antarctica to enable comparison with **M17** data, and only six

in the case of **S20**. 18 local-geophysical comparison points were available for **FM05**, and 22 points were available for the remaining studies (**HR24**, **HR23**, **A15**, **H22** and **SR04**).

Geophysical Model	N	Range – Local (mW/m ²)	Range (mW/m ²)	Pearson's r	RMS (mW m ⁻²)
HR24 (this study)	22	92.3	87.2	0.49 ± 0.07 [0.62]	29.2 ± 2.6 [22.2]
HR23	22	92.3	61.2	0.29 ± 0.07 [0.36]	30.0 ± 3.3 [24.8]
A15	22	92.3	38.7	0.14 ± 0.08 [0.18]	33.2 ± 4.0 [28.8]
H22	22	92.3	22.3	0.21 ± 0.14 [0.47]	34.3 ± 4.1 [28.0]
SR04	22	92.3	79.5	0.16 ± 0.18 [0.48]	66.2 ± 8.8 [25.6]
FM05	18	91.4	29.6	0.03 ± 0.17 [0.22]	43.4 ± 5.3 [30.7]
S20	6	62.1	16.2	-0.04 ± 0.3 [-0.22]	37.6 ± 6.6 [31.7]
M17	4	34.5	73.1	0.36 ± 0.36 [0.76]	41.2 ± 16.1 [31.6]

Table 4.1: **Local-geophysical GHF comparison statistics.** N is the number of comparison points. Range – local is the spread in locally inferred GHF across all local-geophysical comparison points relevant to the geophysical model of interest. Range is the corresponding spread in geophysically inferred GHF. Pearson's r and RMS are the correlation coefficient and root-mean-square deviation, respectively, between local and geophysical data. Statistics reported in the form $a \pm b$ [c] (a =median, b =median absolute deviation, c =value calculated without consideration of uncertainty).

Three measures are used to quantitatively assess agreement between inferences of GHF from local and geophysical data. Firstly, the range of geophysically predicted GHF is calculated at all local-geophysical comparison points, and evaluated in terms of how it compares to the equivalent range from local data. This measure gives us a broad idea of whether a given model can capture the amplitude of spatial heterogeneity in Antarctic GHF suggested by local observations. Note that these ranges reflect GHF variability only at locations for which local data are available. These data points are limited, so the values do not correspond to the total range of a given GHF model. Secondly, Pearson's product-moment correlation coefficient (r) is used to investigate the extent to which there is a positive linear relationship between local and geophysical predictions. Thirdly, the root-mean-square (RMS) difference between local and geophysical predictions is utilised, which provides a summary of the average level of agreement across all comparison points. The RMS will therefore be reduced if a strong positive linear relationship is present in the data (compared to a weak correlation), but the relationship must also be of the right intercept and gradient to minimise disagreement. The latter two measures, r and RMS, are

calculated both with and without consideration of geophysical and local uncertainty according to the following procedure.

Let the spatially variable n_{local} refer to the number of local GHF inferences compiled into a given local-geophysical comparison point (n_{local} is displayed next to the location of each comparison point in Figure 4.8). If $n_{\text{local}} \geq 10$, it is assumed that the distribution of local GHF values can be well approximated using a normal distribution. If $2 < n_{\text{local}} < 10$, this is not a safe assumption and therefore a uniform distribution covering the range of local inferences is assumed. As mentioned above, due to the inherent noisiness of heat flow data, points are ignored in the case where $n_{\text{local}} = 1$. On the geophysical side, distributions of inferred GHF values within reach of each local measurement group are typically complex (asymmetric and/or multimodal). To circumvent this issue, empirical geophysical GHF distributions are calculated at each local-geophysical comparison point using a kernel density estimation. Having established a method for estimating the uncertainty on each data type, random sampling is used to simulate possible variations of the data. 50,000 trials were conducted, where each trial consists of drawing a random data set from the local and geophysical GHF distributions. Pearson's r-value and RMS was recorded for each trial, and summarised using a median and median absolute deviation at the conclusion of all trials. Ignoring data uncertainty, r and RMS values were also calculated by taking mean local and geophysical GHF as the data vector representative of each comparison point.

Each of the aforementioned statistical measures are reported in Table 4.1. It is found that the model corresponding with this study, **HR24**, contains a range of predicted GHF values most consistent with the local data. Furthermore, **HR24** produces the highest Pearson's correlation coefficient value, $R = 0.49 \pm 0.07$ and lowest root-mean-square deviation, $\text{RMS} = 29.2 \pm 2.6 \text{ mW m}^{-2}$ (when taking data uncertainty into account). The next best performing study in terms of correlation coefficient is **M17**, for which only four local-geophysical comparison

points were available. It is found that **M17** is one of the worst performing studies in terms of RMS deviation. The next best performing study after **HR24** in terms of RMS deviation is **HR23**. It should be noted that two GHF models frequently used in ice sheet modelling studies, **SR04** ($r = 0.16 \pm 0.18$, RMS = $66 \pm 9 \text{ mW m}^{-2}$) and **FM05** ($r = 0.03 \pm 0.17$, RMS = $43 \pm 5 \text{ mW m}^{-2}$) (Maule et al., 2005; Shapiro and Ritzwoller, 2004), perform particularly poorly against independent data as compared to **HR24**.

4.3.5 Methodological Appraisal

There are a few reasons why the modelling approach applied in this study may allow us to arrive at estimates of GHF more consistent with independent data than previous studies. Firstly, the use of a geophysically constrained parameterisation of mantle viscoelasticity enables V_S structure to be mapped directly into temperature over a range of upper mantle depth slices. This stands in contrast to other studies, such as those based on magnetic data, where only a single isotherm associated with the Curie depth is constrained (Martos et al., 2017; Maule et al., 2005). As a result, more reliable estimates of the geothermal gradient can be made. Secondly, the incorporation of crustal V_P information provides us with sensitivity to lateral variations in thermal conductivity, a parameter which affects q_s both directly via its presence in Equation 4.1, and to a lesser extent, indirectly via its effect on the geothermal gradient. Thirdly, by combining insights drawn from V_S and V_P data together with thermodynamic models of geothermal structure, variations in crustal heat production can be constrained. This stands in contrast to previous studies making use of steady-state geotherm modelling, which have assumed constant composition (An et al., 2015; Haeger et al., 2022; Hazzard et al., 2023). In addition, methods based on empirical comparison of seismic data between continents are unable to account for differences in crustal composition between target and comparison sites (Shapiro and Ritzwoller, 2004; Shen et al., 2020). Therefore, whilst their inferred q_s uncertainty

may implicitly capture variations in heat supply associated with crustal composition, their estimates of q_s itself will be agnostic to such variations.

4.3.6 Outstanding Challenges

Although the GHF modelling framework presented herein provides a powerful method to infer GHF from seismological data, a number of outstanding challenges remain. Chief amongst them is the inability to reliably infer temperature structure from V_S at depths shallower than the Moho. This issue has been mitigated in three ways: by assuming a temperature of 0 °C at the crystalline basement, excising anomalous seismic data associated with crustal bleeding, and fitting seismically inferred geotherms using thermodynamically self-consistent models of shallow thermal structure. However, given improved constraints on crustal temperature structure (at vertical resolution of ~ 25 km or higher), it would be possible to generate more reliable predictions of surface geothermal gradient. Such constraints may also help in resolving relative contributions to GHF derived from transient-state geotherms versus crustal heat production. Pn-waves are a type of compressional wave guided along the mantle lid, providing sensitivity to Moho temperature structure. Therefore, a high resolution, continental scale model of Antarctic Pn-velocity (V_{Pn}) would be extremely valuable. Fortunately, this may be on the horizon, with the recent development of a V_{Pn} model of central West Antarctica (Lucas et al., 2021). In general, deployment of additional broadband seismic stations in Antarctica would help to improve the accuracy and spatial resolution of velocity models used to infer geothermal structure.

Another challenge relates to the assumption of steady-state in the geotherm modelling process. Whilst such an assumption is readily applicable in regions of unperturbed cratonic lithosphere, such as East Antarctica, it may not be in areas affected by recent rifting (ca. 60 Ma). In the absence of well-constrained models of the spatiotemporal pattern of West Antarctic rifting, it is currently unfeasible to adapt the modelling framework to incorporate transient geotherms.

It may be possible to estimate GHF associated with a transient geotherm using a steady-state geotherm, as long as the surface geothermal gradient can be appropriately modelled. However, this is not ideal, and therefore in future an alternative solution may be sought. A potential option is to avoid modelling the geotherms at all. Given accurate images of Earth's crust and mantle, one could estimate $k(z = z_0)$ and $\partial T/\partial z|_{z=z_0}$ directly, and hence predict q_s . For this to be possible, self-consistent V_S , V_P and V_{Pn} models are required, with at least regional scale resolution.

Thirdly, a parameterisation of geochemical data pertaining to the relationship between k_0 and V_P is relied upon, in order to estimate lateral variations in crustal thermal conductivity (Jennings et al., 2019). This parameterisation inherently assumes that conductivity is sensitive only to silica content. Further, it assumes that synthetic V_P estimates from thermodynamic calculations on a range of mineral assemblages are accurate, and match up to velocities predicted from real data (Behn and Kelemen, 2003). In reality, systematic errors in modelled V_P associated with the choice of regularisation or starting model will be propagated into systematic errors in predicted k_0 . In addition, artefacts in V_P structure caused by data sparsity and the ill-posed nature of the seismic inverse problem may cause us to improperly estimate k_0 at certain locations. Therefore, further validation of methods used to estimate $k_0(V_P)$ are needed.

Finally, the relative sparsity of Antarctic GHF estimates from gravity-driven probes and boreholes presents a clear challenge in assessing the quality of geophysical predictions. A significant expansion of this data set is needed to address the question: what is the most reliable geophysical method for estimating continental GHF? In addition, multiple boreholes at each field sampling region are needed, in order to properly account for localised variations in GHF associated with geology, hydrothermal circulation, and topography (Burton-Johnson et al., 2020). Promisingly, the Rapid Access Ice Drill (RAID) project seeks to address the lack of local data by drilling down to the deepest portions of the Antarctic Ice Sheet (Goodge and

Severinghaus, 2016). By utilising an autonomous design, providing independence from human intervention, it should be possible to rapidly speed up data capture.

4.4 Conclusions

In this chapter, a novel modelling framework for estimating GHF from seismological data has been presented. Building on the technique used to estimate GHF from V_S -derived geotherms in Chapter 3, Antarctic V_P structure has been used to enhance constraint on shallow geothermal structure. Specifically, a parameterisation of $k_0(V_P)$ derived from laboratory conductivity measurements, major element chemistry analyses, and thermodynamic calculations was used to estimate spatial variations in crustal conductivity. In addition to k_0 , crustal heat production h_{cu}^* was treated as a free parameter within the modelling framework, and inverted for by evaluating the misfit between inferred and modelled geotherms. For the first time, GHF has been estimated from seismic data while accounting for lateral variations in crustal composition. Uncertainty in the predicted GHF structure has been estimated, by accounting for the underlying uncertainty in k_0 and h_{cu}^* .

Crustal conductivity varies from $2.3 \text{ W m}^{-1} \text{ K}^{-1}$ to $2.9 \text{ W m}^{-1} \text{ K}^{-1}$ over Antarctica, with values towards the upper limit of this distribution biased towards East Antarctica. On the other hand, upper crustal heat production is estimated to be uniformly low in East Antarctica, where on average $h_{\text{cu}}^* = 0.3 \pm 0.3 \text{ } \mu\text{W m}^{-3}$, as compared to West Antarctica, where $h_{\text{cu}}^* = 4.2 \pm 1.5 \text{ } \mu\text{W m}^{-3}$. In West Antarctica, the highest inferred heat production values ($h_{\text{cu}}^* \geq 4 \text{ } \mu\text{W m}^{-3}$) should be treated with caution, since these values may be anomalously inflated as a result of the assumption of a steady-state geotherm in regions affected by Cenozoic magmatism or rifting. However, estimates of GHF are shown to be valid and interpretable over the whole Antarctic continent. Variations in GHF from 20 mW m^{-2} to 130 mW m^{-2} are predicted, as compared to the range of values predicted in Chapter 3, 40 mW m^{-2} to 100 mW m^{-2} . The larger amplitude of

GHF variations predicted in this chapter is likely due to the incorporation of laterally variable crustal composition. Predicted GHF values are in better agreement with a compilation of local data than previous studies, implying that crustal composition is an important component of accurate predictions of Antarctic heat supply. The models of Antarctic conductivity, heat production and GHF presented in this chapter provide improved constraints on Antarctic sub-glacial geology and thermal conditions, critical for use in ice sheet modelling studies.

Chapter 5

Thermomechanical Structure of Australian Lithosphere and its Influence on Natural Resource Distributions

5.1 Introduction

In the previous chapters, methods for calculating physically self-consistent models of Antarctica's lithospheric and asthenospheric thermal structure were developed. The resultant high-resolution, three-dimensional maps of viscosity and LAB depth can be used in glacial isostatic adjustment simulations, while the newly derived method for estimating GHF can be integrated into ice sheet models. However, the potential applications of these methods extend beyond tackling problems directly related to ice sheet dynamics and sea level. Maps of thermodynamic parameters, derived from tomographic velocity models, can be used to investigate lithospheric structure in the context of a range of human-related issues. For example, the thickness of

lithosphere influences the distribution of seismic and volcanic hazards (Ball et al., 2021; Craig et al., 2011; Sloan et al., 2011). In addition, the transition between thick and thin lithosphere on the edge of cratons was recently shown to be a powerful indicator of the likely location of sediment-hosted base metal deposits (Hoggard et al., 2020). Such deposits are of critical value to the global economy, due to the role that base metals (copper, lead, nickel and zinc) play in advanced technologies and the transition to renewable energy. In 2017, approximately £6.6 bn was spent in exploration for base metal deposits (The Economist, 2019). The work presented in this chapter focuses on such deposits by developing accurate probabilistic models of Australia's lithospheric structure, to guide future mineral exploration efforts. First, the inverse calibration method developed in Chapter 2 is modified to incorporate the use of xenolith thermobarometric data. This method is then applied to a tomographic velocity model of Australia, and used to infer its lithospheric and asthenospheric thermal structure. Maps of LAB depth and its uncertainty are rigorously quantified, based on a statistical ensemble of modelling outputs. This result builds on the analogous deterministic prediction of Hoggard et al. (2020), integrating new xenolith and xenocryst constraints, to provide the most up to date and reliable lithospheric indicator of the potential location of valuable base metals. The maps generated are of significant economic value. Indeed, the work presented in this chapter was completed as part of a consultancy agreement with Geoscience Australia, via the Exploring for the Future research program, which is dedicated to transforming understanding of Australian continental geology and resource potential.

5.2 Constructing Australian Palaeogeotherms from Xenolith Thermobarometry Data

In oceanic settings, lithospheric temperature-pressure conditions are well constrained by conductive cooling models. In Chapter 2, these models were used to empirically constrain the relationship between V_S and T resulting from oceanic plate cooling, using data from the oceans surrounding Antarctica. By combining the oceanic plate V_S - T constraint with three additional data sets, the resulting calibration of the viscoelasticity parameters within Yamauchi and Takei (2016) could be used to relate V_S to thermodynamic variables beneath the Antarctic continent. The Bayesian inversion framework used to perform the calibration, using the aforementioned geophysical data sets, is flexible in the sense that it can be adapted to use any form of useful information pertaining to the relationship between seismic observables (V_S , Q^{-1}) and thermodynamic parameters (T , P , η , ρ). Since regional tomographic velocity models of Australia have limited resolution in the surrounding oceans, the oceanic plate V_S - T relationship cannot be applied to calibrate viscoelasticity parameters here. Instead, robust constraint on Australia's continental lithospheric structure, derived from mantle xenoliths and xenocrysts (hereafter, simply xenoliths), will be used in the inversion procedure. Xenoliths are fragments of mantle rock brought to the surface by volcanism. By exploiting chemical exchanges between constituent minerals within a given xenolith, their pressure and temperature of equilibration can be determined. This technique in geochemical analysis is referred to as xenolith thermobarometry. By combining multiple xenolith samples derived from the same locality, thermobarometric information can be used to infer regional lithospheric thermal structure.

Here, an inventory of pressure-temperature data points derived from xenolith thermobarometry, compiled by research collaborator Dr. Mark J. Hoggard, is applied to construct a set of Australian palaeogeotherms. The data cover 61 individual localities. At each locality, the

major and minor oxide concentrations for chrome diopsides (clinopyroxene) were obtained. In the case of garnet-periodotite xenoliths, oxide concentrations for orthopyroxene and garnet were also extracted where available. Quality checks were performed according to Ziberna et al. (2016), in order to reduce measurement and lithological classification errors. To calculate equilibrium temperature and pressure, two different thermobarometer pairings were used. The first was applied for xenoliths where data pertaining to clinopyroxene, orthopyroxene and garnet phases were all available. In this case, the thermometer of Taylor (1998) and the barometer of (Nickel and Green, 1985) were used. The second pairing was applied for single-grain clinopyroxene data. For these samples, the thermometer of Nimis and Taylor (2000) was combined with the recently developed barometer of Sudholz et al. (2021), which is more accurate at high pressures than previous parameterisations. There are three main sources of uncertainty in the use of xenolith thermobarometric data to infer mantle geothermal structure. First, uncertainty in the oxide concentrations, which are measured by microprobe analysis. Mather et al. (2011) demonstrate that for the three-phase thermobarometer, microprobe measurement uncertainty introduces a temperature uncertainty of approximately ± 30 °C, and depth uncertainty of approximately ± 10 km at low temperature ($T \approx 700$ °C), reducing to ± 10 °C and ± 3 km at high temperature ($T \approx 1200$ °C). Slightly larger uncertainties are introduced for the single-grain clinopyroxene thermobarometer. However, since the temperature and pressure uncertainties are positively correlated, they tend to shift P - T data points in a direction approximately parallel to the geotherm (M.J. Hoggard, *pers. comm.*), minimising their impact. Therefore, microprobe measurement uncertainty has a relatively small influence on the best-fitting palaeogeotherm.

Table 5.1: Localities used to construct Australian palaeogeotherms (provided by M.J. Hoggard). Inf. = age of eruption has been inferred by indirect means; N.T. = Northern Territory; N.S.W. = New South Wales.

Locality	Region	Lon.	Lat.	Age (Ma)	Age reference	Analysis reference
Argyle	Kimberley	128.389	-16.710	1257 ± 15	Olierook et al. (2023)	Griffin et al. (1999), Jaques and Foley (2018), Jaques et al. (1989a,b, 1990), Luguet et al. (2009), Ramsay (1992), Sobolev et al. (1989), Stachel et al. (2018), and Sudholz et al. (2023a)
Argyle - Bow Hill (WA)	Kimberley	128.183	-16.680	815 ± 20	Pidgeon et al. (1989)	Fielding and Jaques (1986), Griffin et al. (1999), Ramsay (1992), and Sudholz et al. (2023a)
Argyle - Maude Creek	Kimberley	127.768	-16.745	ca. 800 (Inf.)		Jaques et al. (1986) and Sudholz et al. (2023a)
Ashmore	Kimberley	127.293	-14.234	ca. 800 (Inf.)	Jaques and Milligan (2004)	Sudholz et al. (2023a)
Bow Hill (Tas)	Tasmania	147.219	-42.286	25	Sutherland and Wellman (1986)	Ferguson and Sheraton (1982) and Sutherland et al. (1984)
Brigooda	Queensland	151.400	-26.200	18	Robertson et al. (1985)	Griffin et al. (1987) and Sas (1997)
Bullenmerri	Victoria	143.104	-38.252	0	Griffin et al. (1984)	Griffin et al. (1988, 1984), Irving (1974), Lu et al. (2018, 2020), and O'Reilly and Griffin (1985); M.J. Hoggard (<i>pers. comm.</i>)
Bullenmerri - Mount Leura	Victoria	143.157	-38.240			Irving (1974)
Calwynnyardah	Kimberley	124.787	-18.000	21 ± 1	Phillips et al. (2022)	Sudholz et al. (2023a)
Calwynnyardah - Walgidee Hill	Kimberley	124.875	-18.301	17 ± 1	Phillips et al. (2022)	Hutchison (2018) and Sudholz et al. (2023a)

Continued on next page...

Table 5.1 continued...

Locality	Region	Lon.	Lat.	Age (Ma)	Age reference	Analysis reference
Calwynyarah - Laymans Bore	Kimberley	124.837	-17.997	ca. 21 (Inf.)		Sudholz et al. (2023a)
Cone 32	Queensland	144.900	-18.000	ca. 0 (Inf.)	Griffin and McDougall (1975)	Kay and Kay (1983) and Stolz (1987)
Cone 32 - Bachelor Crater	Queensland	144.200	-19.400	ca. 1 (Inf.)		Kay and Kay (1983)
Dolo Hill	Curnamona	142.804	-31.669			M.J. Hoggard (<i>pers. comm.</i>)
El Alamein	Gawler	137.733	-32.583			Gaul et al. (2003) and Sudholz et al. (2022)
Ellendale	Kimberley	124.859	-17.564	22 ± 1	Phillips et al. (2022)	Griffin et al. (1999), Jaques and Foley (2018), Jaques et al. (1984, 1989a, 1994), Ramsay (1992), and Sudholz et al. (2023a)
Ellendale - Water Reserve	Kimberley	124.815	-17.634	21 ± 1	Jaques et al. (1984)	Sudholz et al. (2023a)
Jewill	Yilgarn	122.085	-25.714	1324 ± 4	Phillips et al. (1997)	M.J. Hoggard (<i>pers. comm.</i>)
Jugiong	East N.S.W.	148.268	-34.982			Ferguson and Sheraton (1982)
Jugiong - Eucumbene- Tumut	East N.S.W.	148.500	-35.800			Irving (1974)
Kayrunnera	Curnamona	142.543	-30.670	264 ± 18	Gleadow and Edwards (1978)	Sudholz et al. (2022); M.J. Hoggard (<i>pers. comm.</i>)
Mad Gap Yard	Kimberley	127.242	-17.820	842 ± 8	Downes et al. (2023)	Downes et al. (2023) and Sudholz et al. (2023a)
Merlin	N.T.	136.340	-16.850	380 ± 2	Hell et al. (2003)	Hutchison (2011) and Lee et al. (1997); M.J. Hoggard (<i>pers. comm.</i>)
Monaro	East N.S.W.	149.160	-36.640	45 ± 11	Taylor et al. (1990)	Roach (2004)

Continued on next page...

Table 5.1 continued...

Locality	Region	Lon.	Lat.	Age (Ma)	Age reference	Analysis reference
Monaro - Delegate	East N.S.W.	148.779	-36.838	170 ± 5	Lovering and Richards (1964)	Griffin and O'Reilly (1986), Irving (1974), Lovering and Richards (1964), Lovering and White (1969), and Ramsay (1992)
Mount Anakie	Victoria	144.266	-37.887			Irving (1974) and Wass and Hollis (1983)
Mount Hope	Gawler	135.200	-33.700	191 ± 17	Cooper and Morris (2012)	Gaul et al. (2003) and Sudholz et al. (2022)
Orroroo	Gawler	138.600	-32.542	170 ± 2	Black et al. (1993)	Gaul et al. (2003), Scott Smith et al. (1984), and Sudholz et al. (2022)
Ruby Hill	East N.S.W.	150.592	-30.035	167	Sutherland (1996)	Irving (1974) and Lovering and Richards (1964); M.J. Hoggard (<i>pers. comm.</i>)
Sapphire Hill	Queensland	144.400	-19.300	ca. 1 (Inf.)		Kay and Kay (1983)
Sheep Station Knob	Queensland	147.600	-23.500	27	Griffin et al. (1987)	Griffin et al. (1987)
Table Cape	Tasmania	145.725	-40.959			M.J. Hoggard (<i>pers. comm.</i>)
Terowie - Calcutteroo	Gawler	139.200	-33.120	184 ± 2	Tappert et al. (2019)	Sudholz et al. (2022)
Terowie - Monk Hill	Gawler	139.337	-33.104	190 ± 2	Tappert et al. (2011)	Sudholz et al. (2022) and Tappert et al. (2011)
Terowie - Mungibbie	Gawler	138.965	-33.276			Sudholz et al. (2022)
Terowie - Pitcairn	Gawler	139.223	-32.963	186 ± 7	Tappert et al. (2019)	Sudholz et al. (2022)
Timber Creek	N.T.	130.467	-15.743	179 ± 2	Belousova et al. (2001)	Kolff (2010)
Wandagee	Carnarvon Basin	114.588	-23.978	161 ± 5	Pidgeon et al. (1989)	Hoggard et al. (2020)
Webb	Arunta	128.167	-22.851	806 ± 22	Sudholz et al. (2023b)	Sudholz et al. (2023b)

Continued on next page...

Table 5.1 continued...

Locality	Region	Lon.	Lat.	Age (Ma)	Age reference	Analysis reference
West Leonora	Yilgarn	121.190	-29.494	2061 ± 17	Fiorentini et al. (2020)	Hutchison (2018); M.J. Hoggard (<i>pers. comm.</i>)

On the other hand, uncertainty in the application of the thermobarometers themselves is a more significant source of uncertainty (M.J. Hoggard, *pers. comm.*). Each thermometer and barometer is constructed on the basis of experimental data pertaining to synthetic rock samples, subjected to a specific range of laboratory pressure and temperature conditions. Real xenolith samples may have compositions, or have equilibrated at pressures and temperatures, which do not lie within the ranges tested in the laboratory. To partially mitigate this issue, compositional screening protocols are applied, and results that fall outside of the appropriate pressure and temperature ranges are discarded. However, significant uncertainties within the official calibration ranges of thermobarometers remain. For the three-phase thermobarometer pairing, this corresponds to a temperature uncertainty of approximately ±50 °C, and a depth uncertainty of ±15 km (Nimis and Grüttner, 2010). For the diopside thermobarometer, temperature and depth uncertainties of ±30 °C and 7% are reported, respectively (Sudholz et al., 2021). These uncertainties have no obvious correlation, and therefore impact inferences of regional palaeogeothermal structure more significantly than oxide concentration uncertainty.

Finally, an additional source of uncertainty is introduced via the use of P – T data points derived from xenolith thermobarometry to infer present-day geothermal structure. The xenolith P – T data points are relevant to the time at which equilibration occurred, which is anywhere between 0 and 2061 Ma (Table 5.1). Therefore, an implicit assumption is being made, that modern mantle thermal conditions at the locality of interest are equivalent to those at the time of equilibration. Furthermore, where multiple xenoliths are combined to construct a single geotherm relevant to a particular locality, this assumption applies to all equilibration times. In locations affected by transient geothermal evolution, this assumption is unlikely to be valid.

Therefore, it will not always be possible to obtain a reasonable fit between inferences of the present-day geotherm derived from tomographic velocities and xenolith thermobarometry data. This issue is explored in more detail in the next section, regarding the adaptation of the inverse calibration procedure to incorporate P - T information derived from xenolith thermobarometry.

Having applied the thermobarometers to the compiled xenolith data, M.J. Hoggard inspected the resulting P - T data points and removed any obvious anomalies. Then, localities in close proximity to one another were examined, and merged into a single locality where consistent. Localities for which only one data point was available, or the derived P - T structure was physically implausible were removed from the data set. The latter phenomenon may be related to thermal or chemical alteration of xenolith samples after their emplacement, or measurement errors (M.J. Hoggard, *pers. comm.*). Ultimately, these steps resulted in a set of 28 localities for which high quality P - T data was available (see Table 5.1). To construct a best-fitting palaeogeotherm at each locality, the approach used to model GHF in Chapter 3, and again in Chapter 4, was applied. This involves solving the one-dimensional conductive heat flow equation, and optimising the thickness of the mechanical boundary layer, in order to fit a steady-state geothermal profile to the P - T data points. The temperature-dependent lattice thermal conductivity parameterisation of Whittington et al. (2009) was used within continental crust, and the temperature- and pressure-dependent parameterisation of Grose and Afonso, 2013 was used in the mantle. In both domains radiative thermal conductivity is included using the parameterisation of Grose and Afonso, 2013, assuming a mean grain size of 1 mm. Bulk crustal radiogenic heat production was set to $0.4 \mu\text{W m}^{-3}$, mantle potential temperature to 1330°C , and kinematic viscosity to $2 \times 10^{16} \text{ m}^2 \text{s}^{-1}$. Crustal thickness was determined based on regional variations in the Moho depth model **AusMoho** (Kennett et al., 2011), resulting in a thickness of 30 km for localities in the Tasmanides (eastern Australia), and 40 km elsewhere. The resulting set of 28 Australian palaeogeotherms are shown in Figure 5.1 and 5.2. They im-

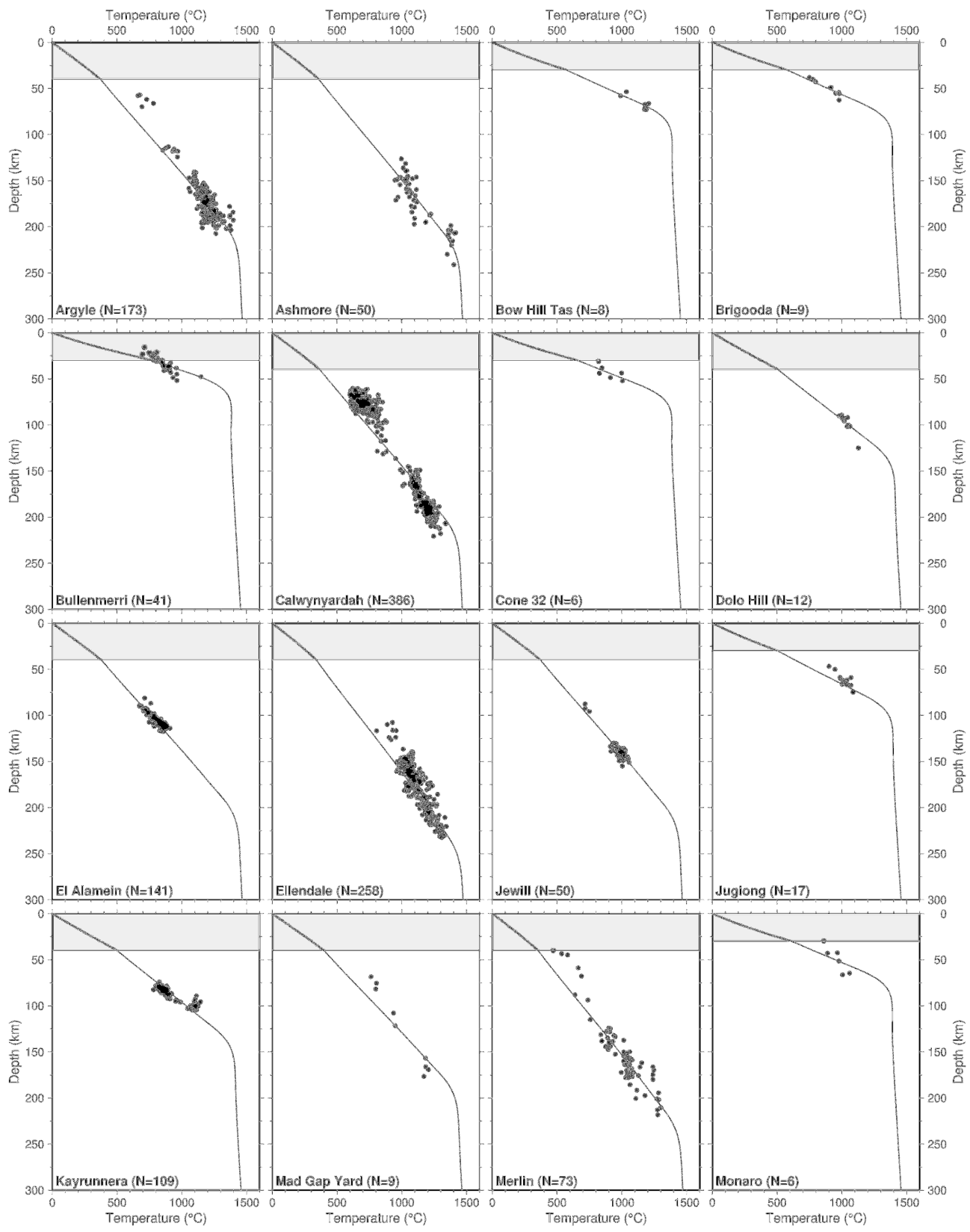


Figure 5.1: Australian palaeogeotherms (1 of 2). Steady-state geotherms (black solid lines) are fitted to xenolith P - T constraints derived from thermobarometry (black circles). Crust demarcated by grey shaded region. Name of locality (and number of P - T constraints, N) shown in panel inset.

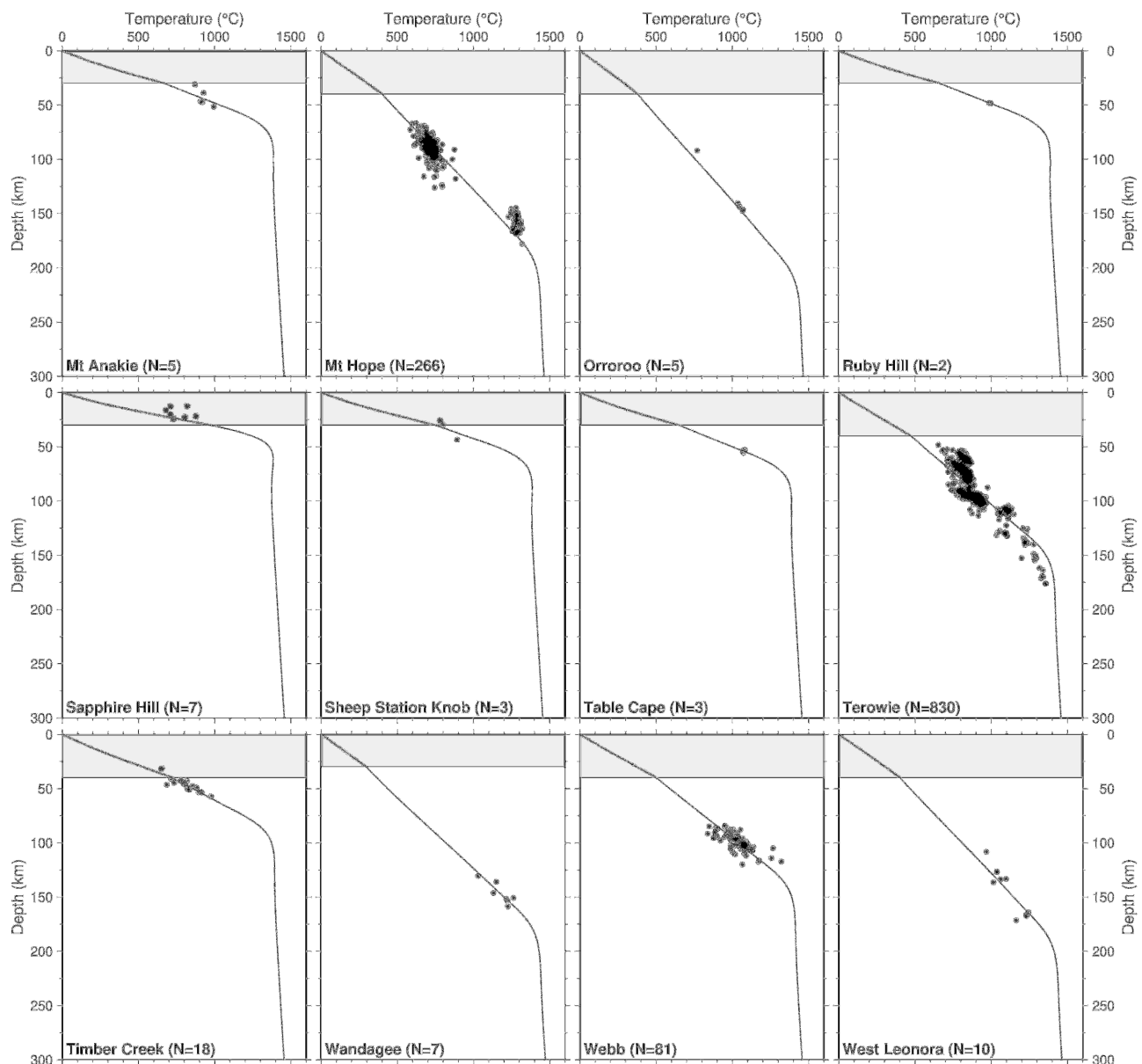


Figure 5.2: Australian palaeogeotherms (2 of 2). Format follows previous figure.

ply a large range of LAB depths over the Australian continent, e.g. from \sim 60 km at Cone 32 (eastern Australia) to \sim 200 km at Ellendale (Kimberley Craton, northwestern Australia), as estimated by the depth to the 1200 °C isotherm. In terms of palaeogeotherm reliability, one would expect this to be positively correlated with both the number of P - T constraints, and the range of depths covered by the constraints. A handful of localities (Argyle, Calwynyardah, El Alamein, Ellendale, Kayrunnera, Merlin, Mount Hope, Terowie and Webb) offer more than 50 P - T constraints. Of these, six localities (Argyle, Calwynyardah, Ellendale, Merlin, Mount Hope and Terowie) have P - T data covering a depth range of at least 100 km. Meanwhile, several sites offer less than 10 P - T constraints (Bow Hill, Brigooda, Cone 32, Mad Gap Yard, Monaro, Mount Anakie, Orroroo, Ruby Hill, Sapphire Hill, Sheep Station Knob, Table Cape and Wandagee), covering depth ranges anywhere between 0 km (Ruby Hill, 2 P - T constraints) and 108 km (Mad Gap Yard, 9 P - T constraints). As with the issue of palaeogeotherm relevance to modern lithospheric conditions, palaeogeotherm reliability will be dealt with as part of the viscoelasticity calibration framework.

5.3 Adapting the Bayesian Modelling Framework to Incorporate Palaeogeotherms

Having obtained a set of Australian palaeogeotherms, it is necessary to adapt the Bayesian modelling framework outlined in Chapter 2 used to calibrate viscoelasticity parameterisations, in order to incorporate this data type. At each locality, predictions of temperature (T) derived from shear-wave velocity (V_S) are compared to temperatures from the corresponding best-fitting palaeogeotherm. V_S information was obtained from the Rayleigh wave travel time tomography model **FR12** (Fishwick and Rawlinson, 2012). Although **FR12** is not the most recent tomographic model of Australia, it remains one of the most reliable, as shown by its compatibility

with xenolith-derived temperatures in Hoggard et al. (2020). This is likely due to the use of high quality input data, and manual quality control of waveforms used in the inversion procedure. In constructing the palaeogeotherm inversion constraint, V_S from **FR12** was matched to T from the constructed palaeogeotherm at each locality using a 25 km depth interval, consistent with the approximate vertical resolution of the tomographic velocity model. The shallowest depth sampled at each locality, $z_{\text{top}} \geq 50$ km, was selected to be half the LAB depth or the shallowest point beneath the Moho, whichever was deeper. The deepest depth, $z_{\text{bottom}} \leq 350$ km, was chosen to coincide with the base of the thermal boundary layer, as estimated via the geotherm fitting procedure outlined in Section 5.2.

To integrate sensitivity of the viscoelasticity model parameters to the palaeogeotherm data into the inversion procedure, a likelihood function is required. For consistency with the approach used to model the four geophysical constraints presented in Chapter 2, a Gaussian distribution was used to represent the likelihood of each geotherm, according to Equation 2.41. The likelihood pertaining to the complete set of palaeogeotherms could then be calculated by multiplying together the individual palaeogeotherm likelihood densities. A unique hyperparameter was applied to each individual locality. By doing so, palaeogeotherms which are not representative of modern lithospheric conditions could be objectively downweighted in the inversion procedure. For example, suppose that at one of the localities used, a mantle plume made lithospheric conditions significantly hotter when xenoliths were emplaced than they are at present. Using a sensible set of viscoelasticity model parameters, it will not be possible to accurately reconstruct the xenolith-inferred geotherm from V_S data. The V_S -inferred temperature will consistently underestimate palaeogeotherm temperatures. However, by treating the average uncertainty assigned to each palaeogeotherm as a free parameter within the model, the unreliability of data at this particular locality can be iteratively learnt by the inversion. This approach also aids mitigation of other sources of uncertainty in the xenolith-derived geotherm

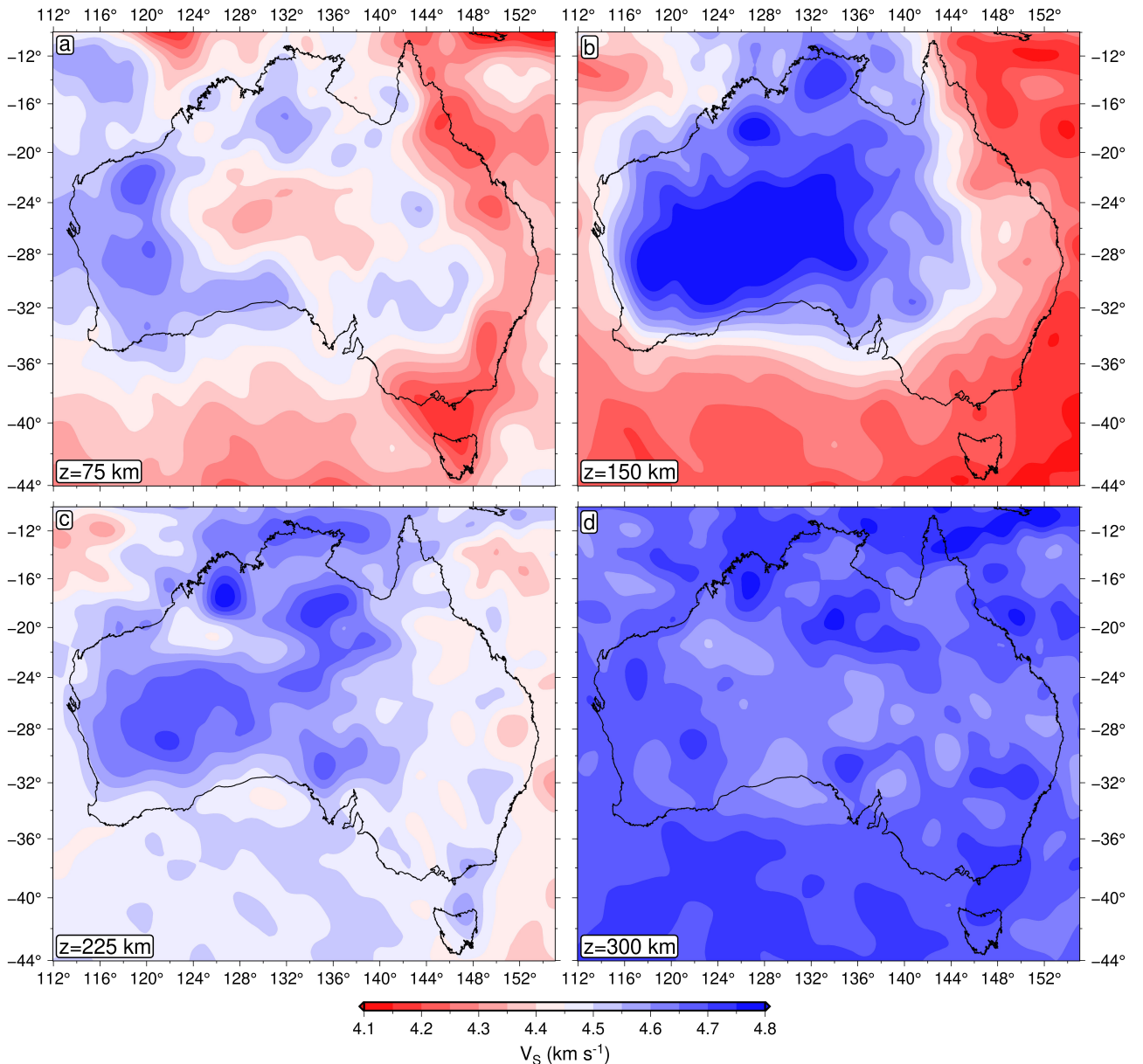


Figure 5.3: Tomographic shear-wave velocity model **FR12**, shown at 75 km, 150 km, 225 km and 300 km depth (panels a-d, respectively). Eastern Australia is characterised by slower than average V_S down to at least 225 km depth, consistent with thinner lithosphere. By contrast, fast velocities across northern, western and southern Australia are consistent with the presence of cratonic lithosphere.

constraints, such as analytical error. Therefore, the inversion procedure is progressively tuned to establish which data sets it should rely most on for optimising model parameters.

In combination with the palaeogeotherm data, a mantle adiabat was used to constrain asthenospheric temperatures. A mantle potential temperature of $T_P = 1300$ °C was assumed, in accordance with the global average (Richards et al., 2018). The adiabat data constraint was constructed in the same way as presented in Chapter 2, by calculating spatially averaged V_S beneath Australia from **FR12** (at 25 km depth intervals between 225 km and 350 km), and tying these values to the corresponding adiabatic temperature at each depth slice. The 28 palaeogeotherm data sets and single adiabat constraint constitute the complete set of geophysical data used in the inversion. For each constraint, the data and corresponding model prediction were compared in temperature space (as opposed to V_S space, e.g., Chapter 2). This was found to improve the stability of the inversion procedure, and therefore aid convergence on optimal regions of model space. The prior distribution for each of the viscoelasticity parameters was assumed to be the same as in Chapter 2, as were all other aspects of the inversion. Full details of the inversion code, and how it can be accessed open-source, are provided in Appendix A.

5.4 Inversion Performance

Applying the inversion algorithm as specified in Section 5.3 produces the viscoelasticity parameters shown in Table 5.2. The posterior parameters each lie within 1 standard deviation of their respective prior distributions, with the exception of $\frac{\partial\mu}{\partial T}$ and $\frac{\partial\mu}{\partial P}$. However, as noted in Chapter 2, these two parameters have a strong negative trade-off with each other. In comparison with the best-fitting parameters obtained in Hoggard et al. (2020), MAP values obtained in this study for μ_0 , E_A , V_A and $\frac{\partial T_S}{\partial z}$ appear much more reasonable with respect to published experimental constraints. This encouraging result suggests that the Bayesian inverse approach allows a more thorough exploration of the parameter space and is better able to escape local minima in the

misfit space (i.e., maxima in probability density space). Credible intervals highlighting the model fit to each of the 29 geophysical data constraints (28 palaeogeotherms, 1 adiabat) are shown in Figure 5.4, 5.5 and 5.6. The following summary statistics, pertaining to each data set, are shown in Table 5.3. First, s_T is the assumed temperature uncertainty on each data point within the data set of interest. Second, $\hat{E}(\log_{10} \sigma)$ is the mean hyperparameter value obtained for each data set, reported as a base-10 logarithmic value. This value is an average calculated over the posterior ensemble of models. Third, the scaled error s'_T is found according to

$$s'_T = 10^{\hat{E}(\log_{10} \sigma)} s_T. \quad (5.1)$$

The scaled error is the uncertainty on each data set implied by the average hyperparameter value. Fourth, $\hat{E}(\text{RMS})$ is the mean RMS misfit between V_S -inferred and data-constrained temperature. As for the mean hyperparameter, the mean RMS misfit is an average over the posterior ensemble. In Table 5.3, close agreement is observed between the scaled error and the mean RMS misfit. This result is indicative of desirable hyperparameter behaviour. Data sets with a larger average RMS misfit are associated with higher average hyperparameter values, and therefore lower weights in the likelihood function. This ensures that data sets providing sensible data-model misfits are prioritised in the parameter space exploration, increasing the likelihood that optimal parameter combinations are found.

Visual inspection of Figure 5.4 indicates a high level of agreement between the adiabat constraint and the posterior ensemble of V_S -inferred asthenospheric temperatures. This is corroborated by an average misfit of $\hat{E}(\text{RMS}) = 23$ °C. Eight localities provide palaeogeotherm data in close alignment with the posterior ensemble of local V_S -inferred temperatures, such that $\hat{E}(\text{RMS}) \leq 100$ °C. These are Bullenmerri, Calwynyardah, El Alamein, Ellendale, Mount Hope, Orroroo and Wandagee. Of the remaining 20 localities, 12 exhibit data-model agreement in the range $100 < \hat{E}(\text{RMS}) \leq 200$ °C. The remaining 8 localities are least reliable, exhibiting

Model parameter i	Prior μ_i	Prior s_i	Posterior μ_i	Posterior s_i	MAP	x_i (Hoggard et al., 2020)
μ_0 (GPa)	81	8	77.5	0.8	78.0	69.0
$\partial\mu/\partial T$ (GPa K $^{-1}$)	-0.014	0.003	-0.0200	0.0010	-0.0207	-0.0117
$\partial\mu/\partial P$ (unitless)	1.6	0.2	2.72	0.12	2.73	2.83
$\log_{10} \eta_r$ (Pa s)	22	3	23.1	1.8	24.2	22.11
E_A (kJ mol $^{-1}$)	400	200	535	201	485	963
V_A (cm 3 mol $^{-1}$)	6	4	4.04	3.8	4.69	0.00
$\partial T_S/\partial z$ (K km $^{-1}$)	2.25	2.25	1.17	1.02	0.63	4.50

Table 5.2: Inverted viscoelasticity parameters. Prior μ_i and s_i represent the mean and standard deviation of the Gaussian prior distribution for each parameter. Posterior μ_i and s_i represent the mean and standard deviation of the posterior distribution for each parameter. MAP represents the maximum *a posteriori* model. x_i represents parameters obtained for FR12 in Hoggard et al. (2020).

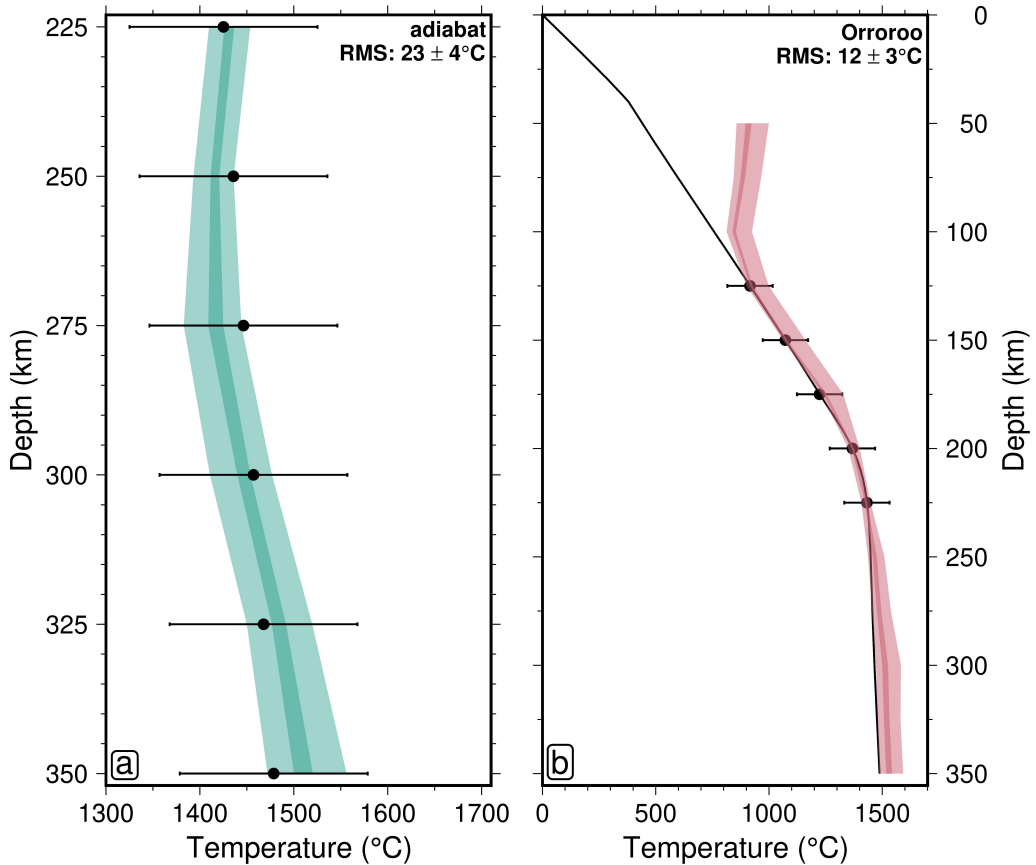


Figure 5.4: Fit of inverted viscoelasticity parameters to adiabat and Orroroo palaeogeotherm. Adiabat temperature data (black circles) compared to average asthenospheric V_S -inferred temperature (dark shaded region=50% credible interval, pale shaded region=99% credible interval) in panel a. Palaeogeotherm temperature data (black circles) compared to local V_S -inferred temperature (shading follows panel a) in panel b. RMS values refer to \hat{E} (RMS), i.e., a mean over the posterior ensemble.

Data set	s_T (°C)	$\hat{E}(\log_{10} \sigma)$	s'_T (°C)	\hat{E} (RMS) (°C)
Adiabat	100	-0.608	24	23
Argyle	100	0.292	195	175
Ashmore	100	0.079	119	108
Bow Hill (Tas)	100	0.240	173	146
Brigooda	100	0.238	172	147
Bullenmerri	100	-0.206	62	45
Calwynnyardah	100	0.010	102	89
Cone 32	100	0.299	199	165
Dolo Hill	100	0.447	279	238
El Alamein	100	-0.933	11	10
Ellendale	100	-0.190	64	58
Jewill	100	0.537	344	324
Jugiong	100	0.442	276	238
Kayrunnera	100	0.366	232	210
Mad Gap Yard	100	0.652	448	425
Merlin	100	0.178	150	142
Monaro	100	0.189	154	125
Mount Anakie	100	0.090	123	100
Mount Hope	100	0.025	105	92
Orroroo	100	-0.828	14	12
Ruby Hill	100	0.305	201	165
Sapphire Hill	100	0.357	227	144
Sheep Station Knob	100	0.221	166	127
Table Cape	100	0.213	163	123
Terowie	100	0.299	199	183
Timber Creek	100	0.624	420	391
Wandagee	100	-0.242	57	51
Webb	100	0.730	537	498
West Leonora	100	0.630	426	391

Table 5.3: Inversion data fit summary statistics. Data set refers to each of the 29 constraints used in the inversion. s_T is the assumed temperature uncertainty on each data point within the data set of interest. $\hat{E}(\log_{10} \sigma)$ is the average hyperparameter value obtained for each data set, represented on a base-10 logarithmic scale. The scaled error s'_T is an implied uncertainty on each of the data sets. \hat{E} (RMS) is the root-mean-square misfit between data and model for each data set, reported as an average over the posterior distribution.

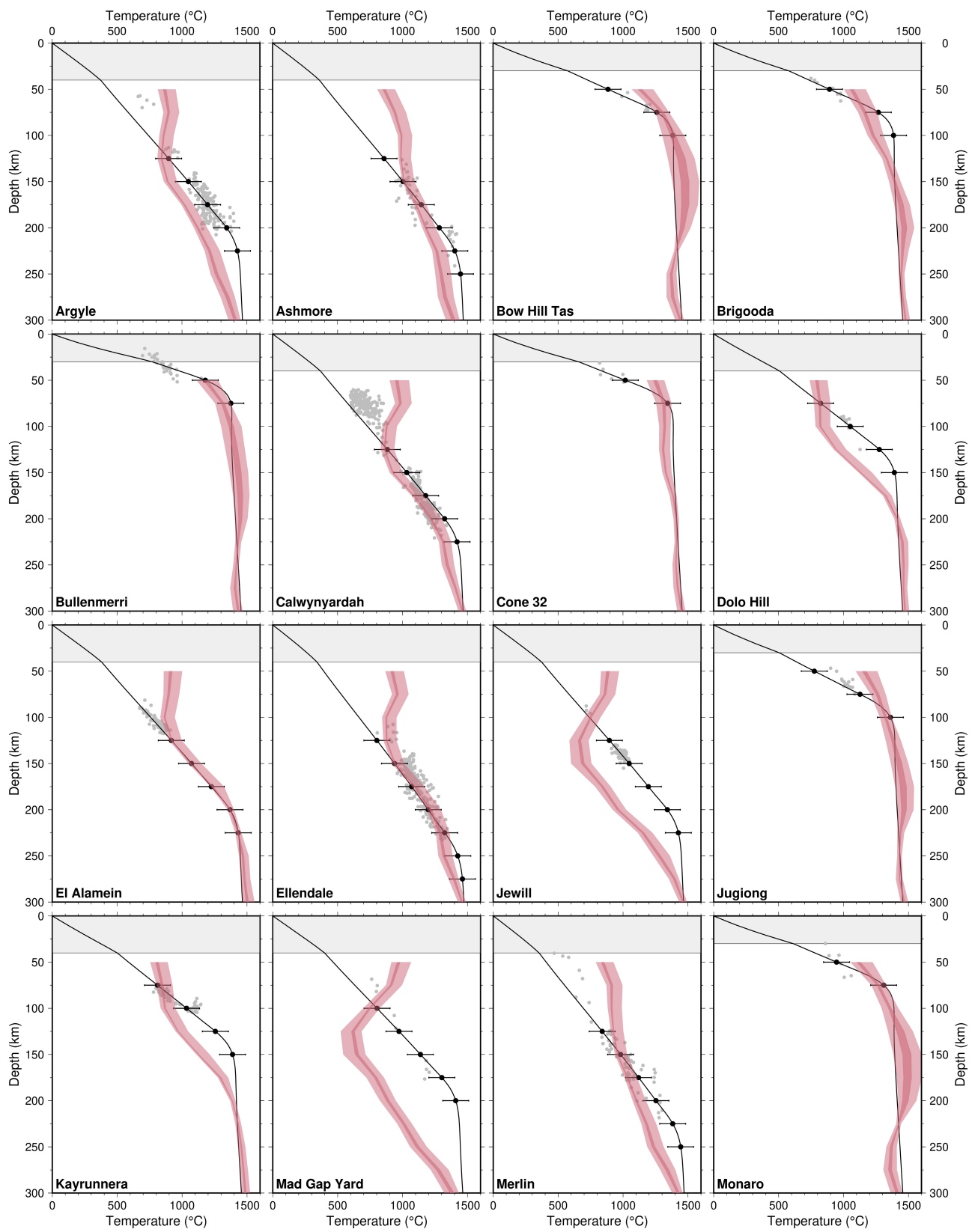


Figure 5.5: Fit of inverted viscoelasticity parameters to Australian palaeogeotherms (1 of 2). Palaeogeotherm temperature data (black circles) compared to local V_S -inferred temperature (dark shaded region=50% credible interval, pale shaded region=99% credible interval). Original xenolith P - T constraints derived from thermobarometry (grey circles). Crust demarcated by grey shaded region. Name of locality shown in panel inset.

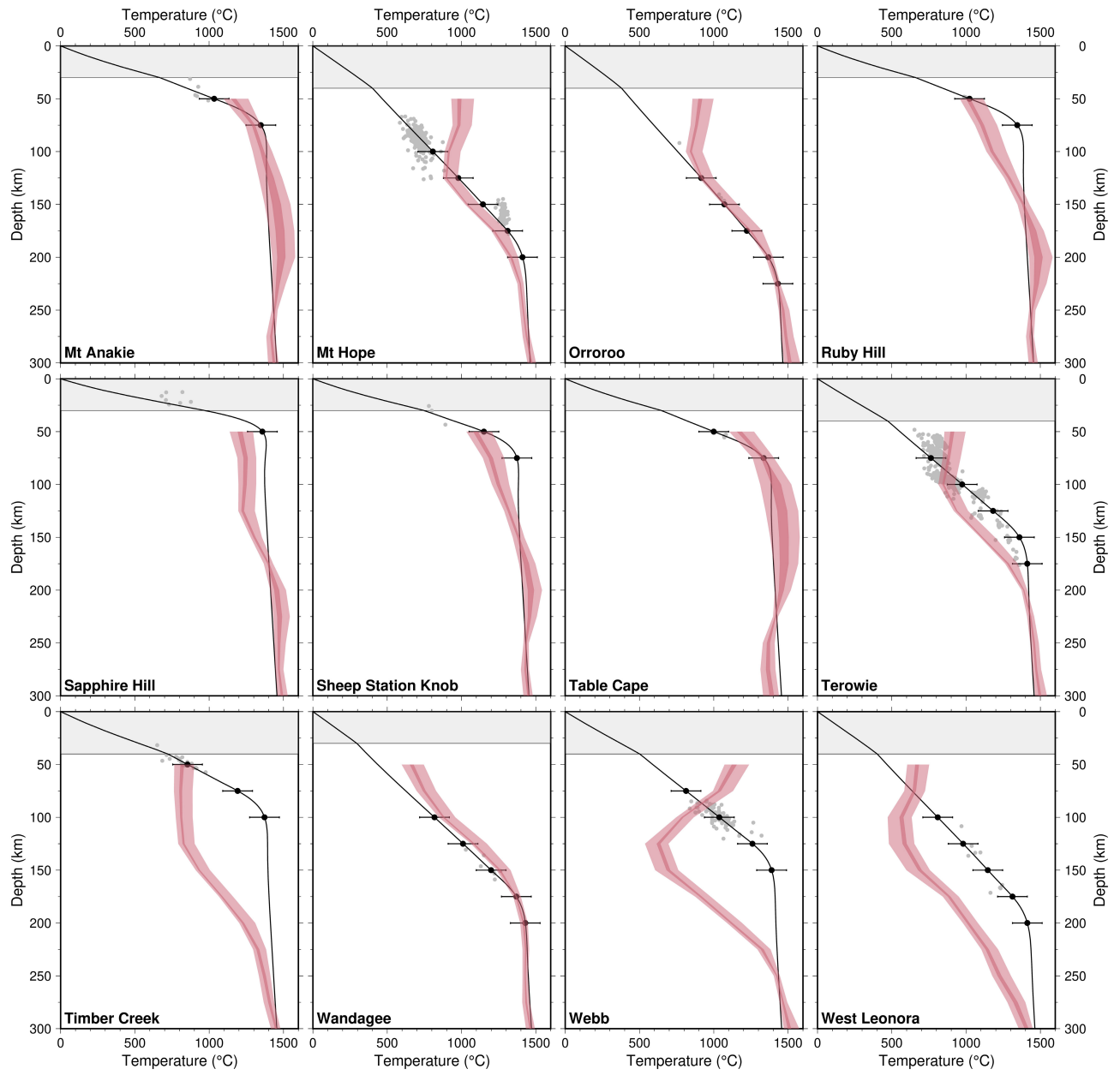


Figure 5.6: Fit of inverted viscoelasticity parameters to Australian palaeogeotherms (2 of 2). Format follows previous figure.

misfits $\hat{E}(\text{RMS}) > 200$ °C, namely: Dolo Hill, Jewill, Jugiong, Kayrunnera, Mad Gap Yard, Timber Creek, Webb and West Leonora. These localities may be influenced by a range of issues affecting data-model agreement. For example: evolution of lithospheric thermal conditions between xenolith emplacement and present-day, presence of unmodelled compositional anomalies or radial anisotropy changes influencing V_S , or measurement and/or human error during geochemical analysis.

5.5 Probabilistic Assessment of Australian Lithosphere-Asthenosphere Boundary Depth

To infer LAB depth at each location within the chosen tomographic velocity model, **FR12**, a random subset of 1,000 post burn-in viscoelasticity models is used to generate an ensemble of three-dimensional temperature structures. This follows the procedure laid out in Section 3.2.2. As previously, the laterally varying geothermal profiles are interpolated to a 1 km depth interval. Prior to interpolation, anomalous temperatures associated with downward bleeding of crustal velocities in the underlying tomography are removed by identifying spurious reductions of the geothermal gradient in the shallow mantle, and excising predicted temperatures above these loci. In all cases, a temperature of 0 °C is enforced at the surface, which is estimated using **SRTM15+** topographic grids (Tozer et al., 2019). Following interpolation, the depth at which the resulting profile intersects the 1200 °C is extracted, which is used as a proxy for LAB depth (Burgos et al., 2014; Richards et al., 2018). In the following, the results of applying the LAB depth inference procedure are shown, and discussed in the context of sediment-hosted metal distribution in Australia.

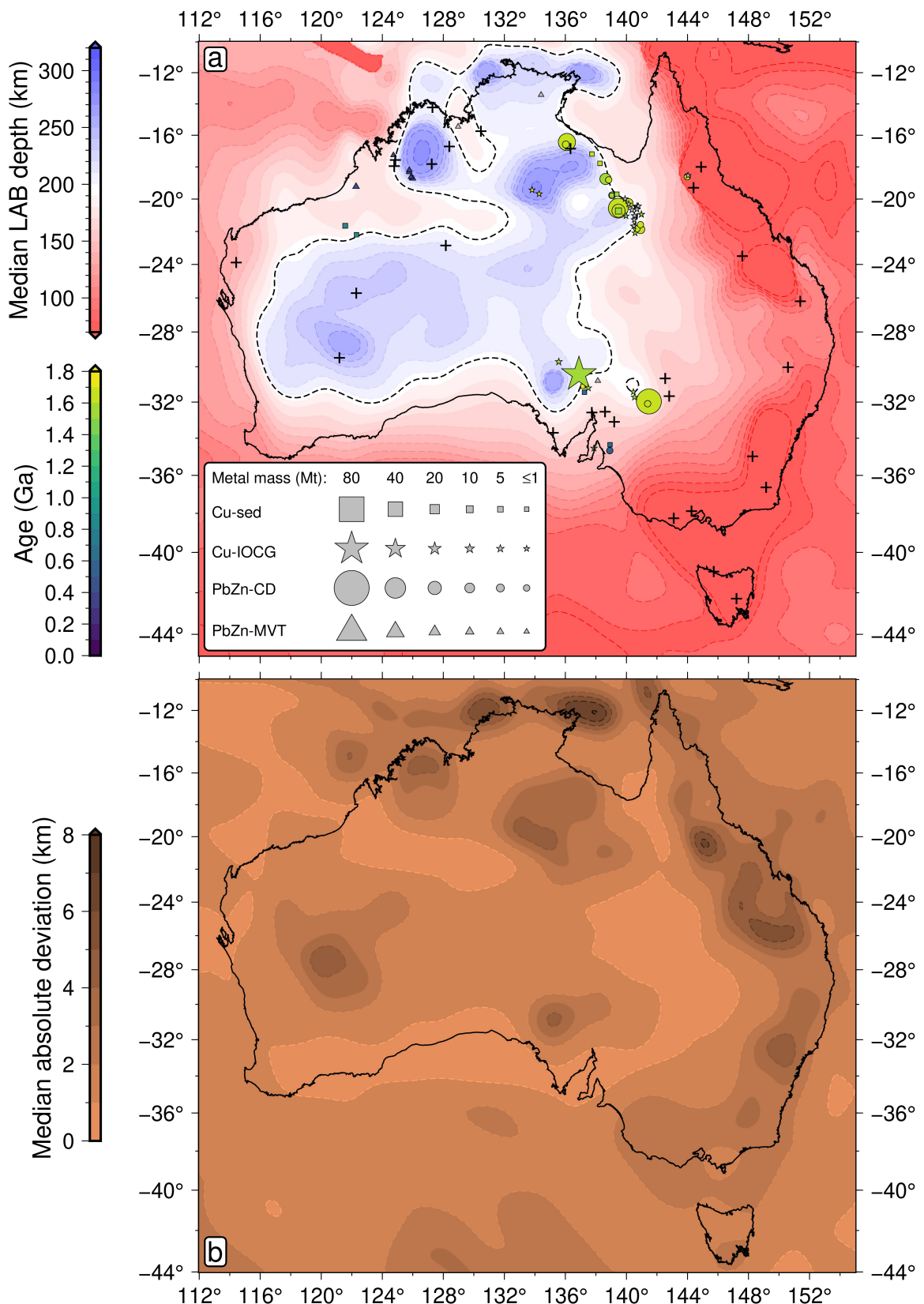


Figure 5.7: Australian LAB depth inferred from FR12 V_S , constrained using xenolith-derived palaeogeotherm data. Median (panel a) and median absolute deviation (panel b). Distribution of sediment-hosted (panel a; circles=clastic-dominated lead-zinc, triangles=Mississippi Valley-type lead-zinc), squares=sedimentary copper, stars=copper from iron oxide-copper-gold ore) metal deposits appears concentrated around the 195 km LAB depth contour (panel a; black dashed line). Location of 28 palaeogeotherms used to constrain inversion (panel a; black crosshairs).

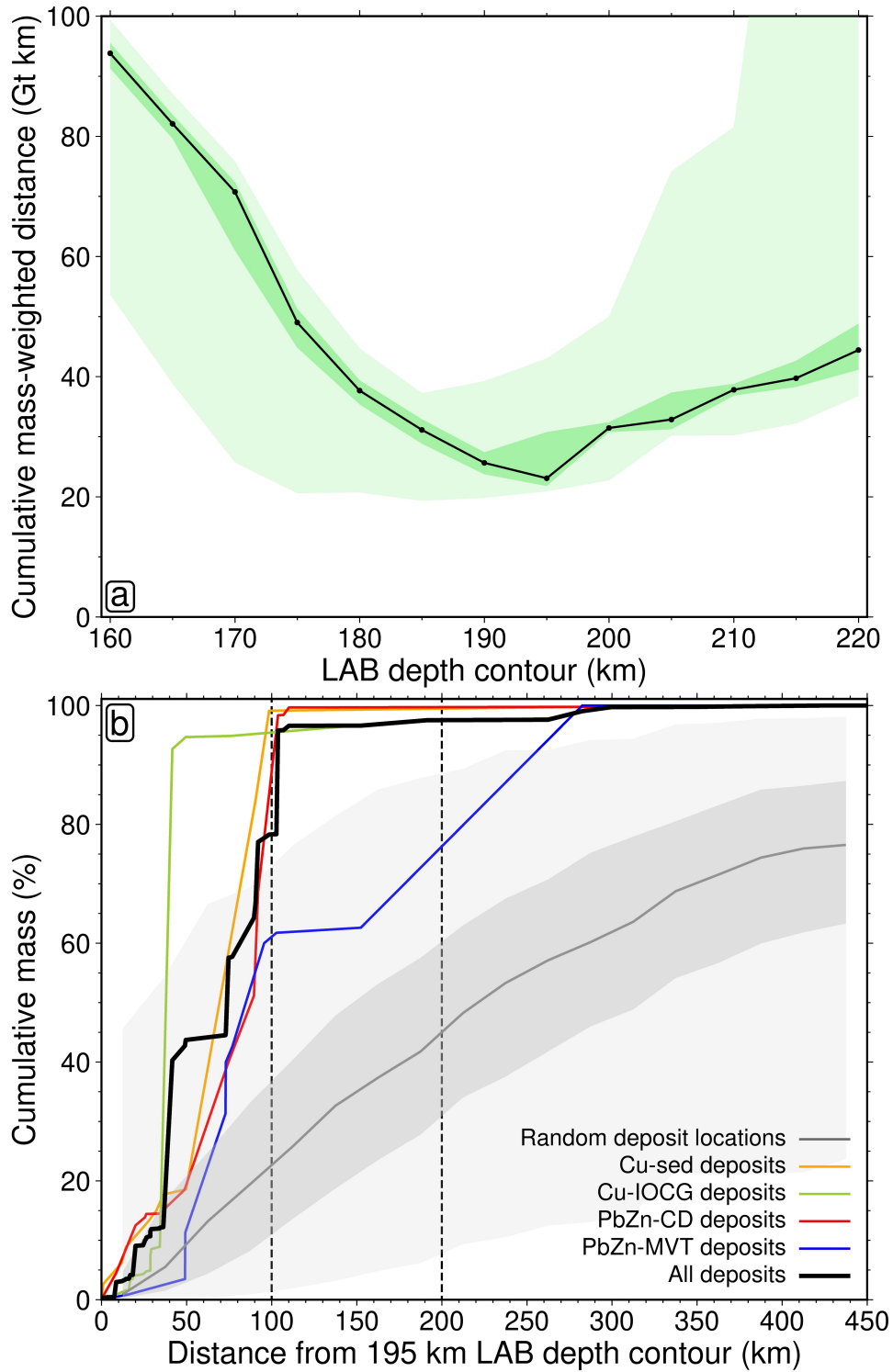


Figure 5.8: Investigating the relationship between sediment-hosted base metal deposit location and the transition from thick to thin lithosphere in Australia. Cumulative distance between LAB depth contour and each Mt of metal, as a function of chosen contour depth (panel a; black circles/line=median, dark shaded region=50% credible interval, pale shaded region=99% credible interval). Percentage of total deposit mass found within each distance of the 195 km LAB depth contour (panel b; see panel inset for deposit types in which Cu-sed=sedimentary copper, Cu-IOCG=copper from iron oxide-copper-gold ore, PbZn-CD=clastic-dominated lead-zinc, PbZn-MVT=Mississippi Valley-type lead-zinc). Synthetic relationship for random distribution of deposit locations (grey line=median, dark shaded region=50% credible interval, pale shaded region=99% credible interval), where distribution of synthetic deposit masses is equivalent to that observed in real data.

5.5.1 Results and Discussion

By summarising the distribution of values at each location within the spatial footprint of **FR12**, it is possible to arrive at an ensemble prediction of Australian LAB depth and its uncertainty (Figure 5.7). Here, the median and median absolute deviation were used, as opposed to the mean and standard deviation. The former two measures were found to significantly reduce the contribution of a small number of anomalous LAB depth predictions, which were present at a handful of locations where the V_S -inferred temperatures are prone to spurious values at shallow depth, despite the geotherm conditioning procedure used to mitigate this issue. Median LAB depth varies from 40 km around the perimeter of eastern Australia, up to 270 km at the Kimberley Craton of northwestern Australia. On average, uncertainty in Australian LAB depth arising due to uncertainty in the viscoelasticity model parameters is ~ 2 km, however this value reaches up to 8 km in certain locations.

By overlaying the location of Australian sediment-hosted base metal deposits on top of the median LAB depth prediction (Figure 5.7a), the relationship between lithospheric structure and natural resource distribution can be investigated. Four types of deposit were analysed: sedimentary copper (Cu-sed), copper derived from iron oxide-copper-gold ore (Cu-IOCG), clastic-dominated lead-zinc (PbZn-CD), and Mississippi Valley-type lead-zinc (PbZn-MVT). Australian deposits containing at least 0.1 Mt of metal were considered. The resulting inventory consisted of 10 Cu-sed deposits (total mass $m = 11.3$ Mt), 25 Cu-IOCG deposits ($m = 100.1$ Mt), 15 PbZn-CD deposits ($m = 175.9$ Mt) and 10 PbZn-MVT deposits ($m = 11.5$ Mt). In agreement with Hoggard et al. (2020), there is a close link between the location of base metal deposits and the edge of cratonic lithosphere. The transition between thick and thin lithosphere provides optimal conditions for the generation of sediment hosted base metal deposits for a number of reasons. Firstly, for a given stretching factor, rifting cratonic lithosphere produces thicker synrift sediment piles than other extensional settings, owing to increased buoyancy as a result of

chemical depletion (Hoggard et al., 2020). These larger volumes of source and sink lithologies serve to increase the potential size of the eventual mineral deposit. Secondly, since cratonic lithosphere is thicker than standard continental lithosphere, it is associated with lower basal heat flow during rifting. This means that greater amounts of lithospheric thinning can occur, producing thicker sediment piles, while still maintaining brine temperatures below the $\sim 250^{\circ}\text{C}$ threshold necessary for metal precipitation reactions to remain effective (Hoggard et al., 2020; Huston et al., 2016). Finally, the rheological contrasts present at cratonic edges help to focus strain associated with successive cycles of tectonic extension and contraction, concentrating the distribution of source and sink lithologies and localising faults that enable mineralising fluids to be transported between them (Gibson et al., 2016; Sloan et al., 2011). Furthermore, the development of deeper, longer and more widely spaced faults during rifting of cratonic lithosphere leads to greater interaction between hydrothermal fluid and sedimentary rock (Biggs et al., 2010). These faults also tend to remain active for longer than in standard continental lithosphere, allowing more time for mineralisation to occur. These factors combine to encourage the development of giant deposits, and can explain why no sediment-hosted deposits of this size are found in non-cratonic rift systems (Hoggard et al., 2020). To quantitatively assess the relationship between the location of base metal deposits and the edge of cratonic lithosphere, a series of LAB depth contours between 160 km to 220 km were selected on 5 km intervals. For each contour, the cumulative mass-weighted distance to each base metal deposit Z was determined. Each contour-deposit distance, ζ , was calculated using the shortest great-circle path connecting the contour to the deposit location, such that

$$Z = \sum_i m_i \zeta_i, \quad (5.2)$$

where i is an integer index referring to each deposit in turn, and m_i is the mass of metal in each deposit. Carrying out this procedure for each LAB depth map in the posterior ensemble of 1,000

viscoelasticity models, a distribution of Z values was obtained for each contour, which could be summarised in terms of a median and a set of credible intervals (Figure 5.8a). Inspecting the results, it can be seen that the 195 km LAB depth contour is most strongly correlated with the location of base metal deposits. Indeed, for the median LAB depth model, all deposits of mass in excess of 10 Mt are located within 105 km of this contour. The 195 km contour is 25 km deeper than that obtained in Hoggard et al. (2020), whose analysis was based on global LAB depths and deposit locations. Therefore, it is possible that the mechanism responsible for deposit generation may regionally operate at greater depths than indicated by the globally best-fitting value. Alternatively, the discrepancy could be caused by differences in LAB depth inferred by different tomographic models.

Looking more closely at the optimal 195 km contour, a cumulative distribution function (CDF) was used to investigate the proportion of total deposit mass found within a given distance of this contour. It was found that 78% of all deposit mass is located within 100 km of the 195 km contour, and 97% within 200 km (Figure 5.8b, black line). To gauge the statistical significance of this trend, it was compared with an analogous CDF obtained using a synthetic data set, within which all deposit locations were generated randomly (Hoggard et al., 2020). The synthetic data set was equivalent to the real data in terms of size (60 deposits) and mass distribution. Randomised locations were found by sampling two parameters, u and v , from a uniform random distribution on $(0, 1)$, and projecting onto a spherical coordinate system using

$$\theta = \cos^{-1} (2v - 1), \quad (5.3)$$

and

$$\varphi = 2\pi u, \quad (5.4)$$

where θ and φ become geodetic coordinates by conversion into degrees. Equation 5.3 and 5.4

derive from the differential solid angle

$$d\Omega = \sin \theta \, d\theta \, d\varphi, \quad (5.5)$$

$$= d(\cos \theta) \, d\varphi, \quad (5.6)$$

which is linked to differential surface area on a sphere of radius r by $dA = r^2 d\Omega$. Therefore (to within the accuracy of the assumption that Earth is spherical), this method ensures that the expected sampling density within a region of unit area is constant over Earth's surface. Pairs of u and v were drawn, and converted into geodetic coordinates, until 60 locations pertaining to onshore Australia had been drawn. Each deposit location was assigned a mass drawn from the real deposit mass distribution. A CDF was then made by obtaining the shortest distance between each deposit and the 195 km LAB depth contour, and calculating cumulative deposit mass as a function of distance away from this contour. Due to the inherent stochasticity of the randomised deposit data, 1,000 synthetic CDFs were generated (each based on a unique set of 60 random deposit locations). This ensemble of CDFs was summarised by binning as a function of distance from the 195 km LAB depth contour, using a bin width of 25 km. Within each bin, a median value (and set of 50% and 99% credible intervals) for the cumulative mass proportion were calculated. By analysing the resultant binned CDF, it was found that only 23% of total deposit mass was found within 100 km, and 44% within 200 km (Figure 5.8b, grey line). This corresponds to 55 and 53 percentage points less than the real deposit data, respectively. Furthermore, for each CDF within the synthetic ensemble, a two-sample Kolmogorov-Smirnov test was applied to assess the likelihood that the real deposit data is drawn from the same underlying distribution (i.e., uniform random) as the synthetic data. The Kolmogorov-Smirnov test is applied by calculating the maximum absolute difference in probabilities between the two CDFs, known as a D-value. The D-value was found to vary between 0.26 and 0.96 over the ensemble of synthetic data sets, with a mean value (and standard deviation) of 0.71 ± 0.17 .

The mean D-value corresponds to a less than 1 in 10^{18} probability that the real deposit data is drawn from a set of uniform random locations across onshore Australia, showing that the LAB depth-deposit relationship obtained for the real data is of extremely high statistical significance. Separating out the CDF for each deposit type, it can be seen that the PbZn-MVT appear least correlated with the 195 km LAB depth contour of the four deposit types. This is to be expected given that, unlike the other deposit types, many MVT deposits are associated with tectonic compression, potentially resulting in substantial topographically driven lateral transport of mineralising fluids away from intracratonic basin margins (Hoggard et al., 2020). On the other hand, the 195 km LAB depth contour appears to be a very powerful indicator for Cu-sed, Cu-IOCG and PbZn-CD deposit location.

5.6 Conclusions

In this chapter, a methodology for the use of xenolith-derived palaeogeotherms to calibrate inferences of continental thermomechanical structure from V_S data has been developed. An expanded inventory of geochemical analyses on Australian xenoliths, obtained from research collaborator M.J. Hoggard, has been used as the basis for applying this methodology to understand Australian lithospheric architecture. Building on the Bayesian approach set out in Chapter 2, hyperparameters have been used to objectively up- and down-weight palaeogeotherm data constraints within the inversion procedure, based upon their individual reliability. It was found that 28 palaeogeotherms, combined with an adiabat pertaining to asthenospheric thermal structure, were sufficient to numerically characterise the posterior distribution of viscoelasticity model parameters.

Using the 1200 °C isotherm as a proxy for LAB depth, an ensemble of posterior models were used to obtain estimates of laterally varying LAB depth in Australia from **FR12** V_S information. Summarising these estimates using a median, and median absolute deviation, it

was shown that LAB depth varies between 40 km and 270 km in this region, with a typical uncertainty due to variations in viscoelasticity parameters of only ~ 2 km. A clear relationship between the 195 km LAB depth contour and the location of natural deposits containing in excess of 0.1 Mt of base metal was observed. The depth of this contour is 25 km deeper than estimated based on a global analysis, a discrepancy which may be caused by regional geology. 78% of metal mass associated with such deposits was found to be located within 100 km of this LAB depth contour, and 97% within 200 km. This relationship was proven to be statistically significant by comparison with a synthetic data set, of equal size and mass distribution to the real data, but with randomised locations over Australia. For the randomised synthetic data, only 23% of mass is found within 100 km of the LAB depth contour, and only 44% within 200 km. The location of Mississippi Valley-type lead-zinc deposits was shown to be the least strongly connected to the LAB depth contour out of all deposit types. However, the connection still appears much stronger than expected based on randomised deposit locations. All three remaining deposit types (sedimentary copper, copper from iron oxide-copper-gold ore, and clastic-dominated lead-zinc) from the data set appear very strongly correlated with the 195 km LAB depth contour. By exploiting the tendency for very large deposits to exist in close proximity to this contour, companies involved in mineral exploration can greatly reduce their search space. This increase in exploration efficiency is likely to play an important role in boosting the supply of key minerals that are needed in the transition to renewable energy.

Chapter 6

Relationships Between Transient Rheology, Ice Sheet Stability, and Sea Level

6.1 Introduction

Glacial isostatic adjustment (GIA) represents the rotational, gravitational and viscoelastic response of the Earth to changes in the distribution of ice and water over its surface. GIA is an important physical process to model due to its influence on our understanding of Earth's cryosphere, and the climate system more widely. For example, palaeo sea level records corrected for GIA-derived vertical displacement can be used to infer past global mean sea level, which combined with records of past climate are indicative of ice sheet-climate sensitivity. In the present day, estimates of ice sheet mass balance (i.e., the net balance of mass gain and loss of an ice sheet, measured in Gt/yr) derived from satellite gravimetry data require correcting for rates of solid Earth deformation in response to Last Glacial Maximum (ca. 21 ka) to present deglaciation. Furthermore, future relative sea level changes depend upon the influence of hydro-

logical mass redistribution on the shape of the solid Earth, its gravitational field, and its state of rotation. The extent to which numerical models of GIA are able to reconstruct or predict spatiotemporal patterns of deformation to Earth’s surface, gravitational field, and rotational state, is dependent on how accurately they can represent Earth’s mechanical behaviour.

Typically, Earth is assumed to act as an elastic or Maxwell viscoelastic body, depending on the timescale of the surface load redistribution under consideration (Watts et al., 2013). If Earth’s structure can be described by an average stiffness $\mu_r \approx 10^{11}$ Pa and viscosity $\eta_r \approx 5 \times 10^{21}$ Pa s, the Maxwell relaxation timescale $\tau_M \approx 1,000$ years indicates an approximate transition point between these two modelling assumptions. Accounting for lateral variations in viscosity $\eta = \eta(r, \theta, \varphi)$, the relaxation timescale relevant to a given region of interest will be locally modified by $\tau'_M = \tau_M \frac{\eta}{\eta_r}$. In the case of relatively rapid ($\tau \ll \tau'_M$ years) deglaciation signals, the assumption of an elastically deforming Earth is usually made, since the strain contribution from viscous deformation is expected to be negligible. For example, Meltwater Pulse 1A (14,650 years ago) took place between Last Glacial Maximum and present, consisting of a period of rapid deglaciation lasting around 500 years. So-called “fingerprinting” studies seek to break down deglaciation events such as Meltwater Pulse 1A in terms of the relative contribution arising from each ice sheet. The idea is that while numerous ice sheet histories could account for the barystatic sea level change associated with Meltwater Pulse 1A, only a handful of histories will be able to reconstruct departures from barystatic sea level change recorded by global relative sea level data to within the measurement uncertainty. Such histories should theoretically correspond closely with the real ice history and therefore provide insight into palaeo ice sheet evolution. Fingerprinting studies have inferred that the dominant meltwater contribution came from North America (5.6 to 15.4 m), while a minor contribution may have come from Antarctica (0 to 5.9 m), from the total 17.9 m GMSL rise (Lin et al., 2021). However, the assumption of elasticity ignores the potential contribution of transient viscous deformation in

response to deglaciation. If viscoelastic deformation on Earth is more complex than described by a Maxwell body, multiple stress relaxation processes across a range of physical timescales between the elastic limit ($\tau \rightarrow 0$) and the Maxwell timescale ($\tau = \tau'_M$) may be supported. This type of deformation behaviour is known as transient rheology, characterised by a range of apparent viscosities, dependent on the deformation and observation times. If Earth exhibits transient rheology, elastic deformation may not be the only contributor towards deformation over periods of order 1 to 1,000 years. Indeed, Lau (2023) showed that for a viscoelastic Earth describable by an Extended Burgers rheology, significant deviations in relative sea level over the duration of Meltwater Pulse 1A are predicted as compared to a purely elastic response. These results imply that it will be necessary to re-evaluate ice sheet history constraints derived from fingerprinting studies, leading to new insights regarding the sensitivity of Antarctica's ice to past climate. Since the additional relaxation timescales introduced by transient rheology are intermediate between elasticity and Maxwell viscoelasticity, transient rheology is not only an important consideration for the applicability of elastic fingerprinting, but also for treatment of longer timescale ($\tau \sim \tau'_M$ and longer) deglaciation signals. As a result, it is important to assess the timescales over which transient rheology on Earth is significant, and to what extent it may affect patterns of deformation.

In the past decade, substantial geophysical evidence has mounted for the presence of transient rheology. For example, Ivins et al. (2020) showed evidence for viscous deformation in response to tidal forcing on timescales between 12 h and 18.6 years. Nield et al. (2023) found that adding a Kelvin-Voigt deformation unit (consisting of a spring and dashpot in parallel) to the traditional Maxwell setup, forming a transient rheological description known as the Burgers model, improved fit to GPS observations of postseismic deformation (1 day to 10 year timescale) in the northern Antarctic Peninsula, following 2003 and 2013 earthquakes in the nearby Scotia Sea. Barletta et al. (2018) showed that the contemporary GIA response (10 year to 1,000 year

timescale) to ice sheet retreat in the Amundsen Sea Embayment between 1900–2014 cannot be explained by purely elastic deformation, indicating an extremely low apparent viscosity of $\eta \approx 10^{18}$ Pas. As shown in Chapter 2, it is difficult to reconcile such a low apparent viscosity with inferences from V_S without taking transient deformation into account, indicating that such anomalously low viscosities are not simply due to Earth’s laterally heterogeneous structure. A similar, and even stronger example of the same behaviour was identified in relation to ice retreat on the Antarctic Peninsula by Samrat et al. (2021). Taken together, the aforementioned studies are a powerful suggestion that transient rheology may be in operation, particularly considering that the data presented in each study are sensitive to a different range of deformation timescales. Despite the growing body of geophysical evidence, the most robust indicator of the existence of transient rheology comes from experimental data. Laboratory investigations have probed the strain response of mantle-like rock samples to applied oscillatory stresses of variable frequency (Faul et al., 2007; Yamauchi and Takei, 2016). Faul et al. (2007) used synthetic olivine aggregates in an effort to emulate the real mineralogical make-up of Earth’s upper mantle. Yamauchi and Takei (2016) used a synthetic borneol-diphenylamine analogue of the olivine-basalt system, which is expected to deform similarly, and allows testing at frequencies corresponding to mantle conditions. While the two laboratories conduct their experiments using separate procedures, and parameterise their observations using different mathematical forms, they both find that grain-boundary-scale deformation processes exhibit frequency-dependence. Such frequency-dependence cannot be captured by a simplistic Maxwell description of viscoelastic deformation, which implies the presence of a single relaxation timescale. Instead, a continuous relaxation spectrum must be used, which implies an infinite number of relaxation timescales, each associated with a given strength. To describe the rheology of such a material in terms of springs and dashpots, one would require an infinite number of Kelvin-Voigt elements, positioned in series with a Maxwell element representative of steady-state behaviour. Alterna-

tively, the same setup can be achieved using infinite Maxwell elements, positioned in parallel with each other. In either setup, the stiffness and viscosity of each unit is tuned to match the strength of relaxation at each frequency. Transient rheologies therefore contain additional relaxation modes (on top of the steady-state Maxwell mode) via which stress can be dissipated, the strength of which depend on the forcing timescale. They therefore exhibit time-dependent apparent viscosities lower than that observed at steady-state (i.e., in the limit $\tau \rightarrow \infty$, where τ represents the forcing timescale).

In recognition of the potential impact of transient rheology on the character of solid Earth deformation, a handful of studies have attempted to incorporate time-dependent deformation behaviour into solid Earth deformation models. As mentioned above, Nield et al. (2023) utilised the Burgers model of transient rheology to model postseismic deformation in the northern Antarctic Peninsula following a $M_w = 7.7$ strike-slip earthquake in the Scotia Sea in 2013. Klein et al. (2016) followed a similar approach in order to fit GPS observations of postseismic deformation following the 2010 $M_w = 8.8$ Maule earthquake in Chile. The Burgers model was also used by Boughanemi and Mémin (2024) to gain insight into GIA-induced deformation in Antarctica. The Burgers model consists of a single Kelvin-Voigt element positioned in series with a Maxwell element. It is therefore the first step towards transforming a Maxwell viscoelastic rheology into a generalised transient rheology represented by a continuous relaxation spectrum. As such, the Burgers rheology is the least computationally expensive type of transient rheology to implement within a finite element model of solid Earth deformation, since only one additional relaxation element must be added. However, there is a key issue associated with using a Burgers model to approximate the expression of transient rheology. Namely, the chosen rheology has no clear relationship back to experimentally determined mechanical properties of mantle rock. This presents many of the same drawbacks as are present for the pure Maxwell approach: one cannot safely assume that such an approximate description of Earth's

rheology is representative of its true deformation character, and one cannot easily generalise the information learned about Earth's structure from studies using a Burgers model to processes operating at different forcing timescales. Furthermore, the lack of grounding in experimentally verified behaviour means that it is impossible to tell, *a priori*, how viscosity should be partitioned between the two elements of the model. For example, Nield et al. (2023) arbitrarily fix the ratio between the viscosity of the transient Kelvin-Voigt element, and the steady-state Maxwell element, to $\eta_{\text{KM}}/\eta_{\text{M}} = 1/10$. This assumption was taken to avoid the number of parameter combinations expanding beyond what was feasible to test, but significantly adds to the uncertainty regarding whether the chosen rheological parameterisation is a valid description of Earth's deformation character, and serves to abstract the meaning of the recovered best-fitting viscosity values.

In order to properly address the issue of transient rheology in numerical models of solid Earth deformation, including GIA, rheologies such as the Burgers model should be substituted with broadband parameterisations derived from experimental data, such as Yamauchi and Takei (2016). To do so would bring two major advantages. Firstly, it would enable the use of calibrated maps of mantle structure derived from V_S in a self-consistent fashion. For example, estimates of laterally variable steady-state viscosity and lithospheric thickness, such as those presented in Chapter 3, could be integrated into finite element deformation models. Secondly, it would provide the ability to model time-dependent deformation as realistically as possible, according to the latest experimental data pertaining to the mechanical properties of mantle rock. Since the parameterisation of Yamauchi and Takei (2016) characterises relaxation across a broad range of normalised frequencies, such a formalism could be applied to model physical processes ranging from tidal loading, to postseismic deformation, to GIA. This would be an important step towards a unified understanding of mantle rheology, as opposed to the currently fragmented approach in which different rheologies and viscosities are assumed depending on the

physical process considered. Successful implementation of a so-called “transient GIA model” would motivate the revisiting of a plethora of canonical GIA studies, to identify potential caveats in our current understanding of past, present and future sea level change arising due to the assumption of elastic or Maxwell viscoelasticity (Lau, 2023). In this chapter, the theoretical steps needed to apply experimentally constrained parameterisations of mantle viscoelasticity to GIA models are made. Firstly, a Generalised Maxwell Model framework is developed to represent an arbitrary mechanical parameterisation across a broad spectrum of timescales, which can be readily applied to a range of numerical models, including finite-element descriptions, which are commonly used to model continuum mechanics. Secondly, the parameterisation of Yamauchi and Takei (2016) is adapted to speed up computation of the complex compliance, by combining the original experimental data with a modified mathematical form, within which an array of free parameters is optimised via Bayesian inversion. Finally, the adapted parameterisation is integrated within a simple model of solid Earth deformation to demonstrate its effectiveness, highlight differences in behaviour between Maxwell and transient deformation, and provide a pathway towards transient GIA simulations on a laterally variable solid Earth.

6.2 Translating Experimental Parameterisations of Mechanical Behaviour Into Generalised Maxwell Form

GIA studies utilise numerical models of deformation induced by surface load changes to understand changes in topography and sea level. Such models invoke conservation of momentum to form a governing equation, which combined with a chosen rheological description of the relaxation modulus (e.g. in the time-domain, $M(t)$), can be used to solve for spatiotemporal strain changes. On the other hand, rheological descriptions derived from laboratory data such as Yamauchi and Takei (2016) employ the creep compliance, $J(\omega)$, to parameterise viscoelasticity.

The purpose of this section is to understand how such experimental parameterisations can be translated into a form applicable to numerical models. To do so, it is necessary to begin with the foundations of linear viscoelasticity.

Consider a general mechanical body which behaves viscoelastically, which is initially at equilibrium, to which a stress σ_1 is applied at a time t'_1 . Then, the corresponding strain is described at times t after t'_1 by

$$\varepsilon(t) = J(t - t'_1)\sigma_1. \quad (6.1)$$

In this equation, $J = J(t)$ is the creep relaxation function (or simply creep function), capturing the time-dependent strain profile in response to a unit applied stress (Nowick and Berry, 1972). The creep function is the time-domain representation of its equivalent in the frequency-domain, the complex compliance $J^* = J^*(\omega)$, such that the two are related by the Fourier transform

$$J^*(\omega) = \int_{-\infty}^{\infty} J(t)e^{-i\omega t}dt. \quad (6.2)$$

Assuming linearity in the relationship between stress and strain, the principle of superposition can be applied, which states that the strain response to a series of applied stresses can be found by taking the strain response to each stress applied individually, and summing. Then, for a discrete series of stresses, the strain response is given by

$$\varepsilon(t) = \sum_{i=1}^{i=n} J(t - t'_i)\sigma_i. \quad (6.3)$$

Generalising further to the case of a stress function applied continuously, $\sigma = \sigma(t)$, the discrete summation can simply be replaced with the integral

$$\varepsilon(t) = \int_{-\infty}^t J(t - t') \frac{d\sigma(t')}{dt'} dt'. \quad (6.4)$$

By inspection of equation 6.4, it can be seen that to calculate the strain displacement at time t , for a material describable by a creep function $J(t)$, its entire stress history $\sigma(t)$ from the earliest time at which a non-zero stress was applied until the present time t is required. As stated by Nowick and Berry (1972), this property derives from the fact that viscoelastic materials contain internal variables, whose values affect the stress-strain relationship, but respond non-instantaneously to the material's evolution. The strain response to an applied stress has been used to highlight such time-dependent behaviour above, however a directly analogous approach can be taken to calculate the stress response of a general viscoelastic material to a continuous strain evolution, which is given by

$$\sigma(t) = \int_{-\infty}^t M(t-t') \frac{d\varepsilon(t')}{dt'} dt', \quad (6.5)$$

where the creep compliance $J(t)$ is replaced by its analogue $M(t)$, known as the stress relaxation function, or the relaxation modulus (Nowick and Berry, 1972). In this case, the entire strain history is required to calculate the stress at time t .

In the laboratory, the complex compliance $J(\omega)$ is readily accessible, due to the fact that experiments are conducted using an applied stress (at known amplitude, σ_0 , and frequency, ω – i.e., stress is the dependent variable), and measuring the strain response (the independent variable). Furthermore, descriptions of $J(\omega)$ from the laboratory are continuous functions, consistent with the observation that anelastic relaxation occurs over a spectrum of relaxation timescales. On the other hand, numerical models use mathematical descriptions of the relaxation modulus to track the relationship between stress and strain. If Earth's mantle is assumed to be spherically symmetric, a spectral approach using Love numbers can be employed, in which case rheology must be expressed in the Laplace-domain form $M(s)$ (where $s = \gamma + i\omega$ is a complex frequency variable) (Mitrovica and Peltier, 1992). Finite element formulations allow lateral variations in Earth's viscosity structure to be accounted for, and in this type of model,

rheology must be expressed using the time-domain form $M(t)$. In either case, it is necessary to perform some kind of $J \rightarrow M$ transformation (Lau, 2024). Furthermore, finite element models of continuum mechanics use mathematical representations of a discrete combination of spring and dashpot components to form a given rheological description, such as the Maxwell or Burgers models. For example, the generalised Maxwell model is commonly used, which consists of a spring arranged in parallel with a finite number (N_M) of Maxwell elements (spring and dashpot in series), which themselves are arranged in parallel with one another. In such a setup, the total strain is the same as the strain exhibited by each element, such that

$$\varepsilon = \varepsilon_1 = \varepsilon_2 = \dots = \varepsilon_{N_M}, \quad (6.6)$$

and the total stress is given by the sum of the stresses acting on individual elements, such that

$$\sigma = \sum_{i=1}^{i=N_M} \sigma_i. \quad (6.7)$$

Utilising these constraints in combination with expressions defining spring- and dashpot-like behaviour, provided by

$$\sigma = M\varepsilon \quad (6.8)$$

and

$$\sigma = \eta \frac{d\varepsilon}{dt} \quad (6.9)$$

respectively, the stress-strain relationship of the generalised Maxwell model as a whole can be derived. The resulting relationship takes the form of a linear homogeneous ordinary differential equation of second order, the solution of which yields the following relaxation function, referred to as a Prony series:

$$\tilde{M}(t) = \tilde{M}_U - \sum_{i=1}^{i=N_M} \alpha_i \left(1 - e^{-t/\tau_i} \right), \quad (6.10)$$

where $\tilde{M}_U = \tilde{M}(t = 0)$ is the unrelaxed (instantaneous) modulus associated with the isolated spring, α_i and τ_i (for $i = 1, 2, \dots, N_M$) are the discrete relaxation moduli and timescales associated with the spring and dashpot of each Maxwell element, respectively. Alternatively, the Prony series can be represented as

$$\tilde{M}(t) = \tilde{M}_\infty + \sum_{i=1}^{i=N_M} \alpha_i e^{-t/\tau_i}, \quad (6.11)$$

where

$$\tilde{M}_\infty = \tilde{M}_U - \sum_{i=1}^{i=N_M} \alpha_i \quad (6.12)$$

represents the relaxed modulus of the material. Here, the symbol $\tilde{M}(t)$ is used to refer to Prony series approximations of the true relaxation function of a given material, $M(t)$. Equation 6.11 represents the time-dependent stress response of a generalised Maxwell body to a unit instantaneous strain. For completeness, note that instead of a generalised Maxwell model a generalised Kelvin-Voigt model can be used. In the Kelvin-Voigt model, a spring is arranged in series with a finite number (N_K) of Kelvin-Voigt elements (spring and dashpot in parallel), each of which are arranged in series with each other. In this case, $\tilde{J}(t) \approx J(t)$ can be expressed analogously to equation 6.11. This series can be used for problems in which creep is modelled. The number of elements (N_M or N_K) chosen in each case represents the number of unique relaxation timescales the material is assumed to exhibit. Therefore, in the limit $N_M \rightarrow \infty$ (or $N_K \rightarrow \infty$), the generalised model perfectly describes materials characterised by a continuous spectrum of relaxation timescales. The more elements (i.e., larger N_M or N_K) present, the more computationally expensive a given rheology will be to implement in numerical simulations. This limitation is related to the earlier observation that numerical models must track the entire strain history of a material throughout a simulation, in order to calculate the corresponding stress field at a given time. Therefore, for every additional Maxwell or Kelvin-Voigt element in the generalised

model, an additional stress or strain history must be calculated and stored in memory.

The above observations point towards the requirement to translate experimental parameterisations of mechanical behaviour into a form that can feasibly be implemented in numerical models. Finite element applications are of most interest here, since they enable consideration of three-dimensional variations in Earth's viscosity structure. However, it would also be beneficial to develop a framework which can be applied to Love number formulations, which are discussed in more detail in Section 6.4.1. Practically, such a translation method needs to allow one to convert a continuous, frequency-dependent complex compliance parameterisation $J(\omega)$ into a discrete, time-dependent relaxation function $M(t)$ (and its Laplace-domain counterpart, $M(s)$, for spectral applications [Lau, 2024](#)). The first step in this process is to use the relationship

$$M^*(\omega) = \frac{1}{J^*(\omega)}, \quad (6.13)$$

where $M^*(\omega) = M_1 - iM_2$ is the frequency-domain representation of $M(t)$, to convert experimental parameterisations of J_1 (storage compliance) and J_2 (loss compliance) into analogous forms for M_1 (storage modulus) and M_2 (loss modulus). This results in the expressions

$$M_1(\omega) = \frac{J_1(\omega)}{|J^*(\omega)|^2}, \quad (6.14)$$

and

$$M_2(\omega) = \frac{J_2(\omega)}{|J^*(\omega)|^2}. \quad (6.15)$$

The second step involves utilising the frequency-domain representation of a Prony series, which looks like

$$\tilde{M}_1(\omega) = \tilde{M}_\infty + \sum_{i=1}^{i=N_M} \alpha_i \frac{(\omega\tau_i)^2}{1 + (\omega\tau_i)^2}, \quad (6.16)$$

and

$$\tilde{M}_2(\omega) = \sum_{i=1}^{i=N_M} \alpha_i \frac{\omega \tau_i}{1 + (\omega \tau_i)^2}. \quad (6.17)$$

By treating $\tilde{M}^*(\omega) = \tilde{M}_1 - i\tilde{M}_2$ as a discrete approximation of the experimental parameterisation $M^*(\omega)$ obtained from equation 6.14, it is possible to fit the former to the latter using a least-squares inversion approach, finding optimised values for the free parameters \tilde{M}_U and α_i (at optimised values of τ_i) in the process. The elegance of this approach is that the fitted parameters \tilde{M}_U and $\alpha_i(\tau_i)$ can be substituted directly into the time-domain representation presented in equation 6.11. Therefore, a generalised Maxwell model can be fitted to experimental data in the frequency domain, and then easily translated for usage in continuum mechanics models operating in the time domain. However, this approach is complicated by the fact that experimental parameterisations of $J^*(\omega)$, such as the pre-melting parameterisation of Yamauchi and Takei (2016), are dependent on state variables: pressure (P), temperature (T), composition (X) and grain size (d). In effect, state-dependence means that a unique best-fitting Prony series exists for each possible combination of state variables. To circumvent this issue, one can utilise the fact that, momentarily ignoring the high-frequency dissipation peak associated with pre-melting, the complex compliance of polycrystalline materials appears to follow the so-called master curve (Figure 6.1, McCarthy and Takei, 2011). The issue of how to deal with pre-melting will be returned to later, in Section 6.2.2, after the necessary foundations are built. The master curve parameterisation implies that the frequency-dependence of the complex compliance is identical across different physical states, when expressed as a function of the normalised frequency,

$$f' = \frac{f}{f_M}, \quad (6.18)$$

where

$$f_M = \frac{1}{\tau_M}, \quad (6.19)$$

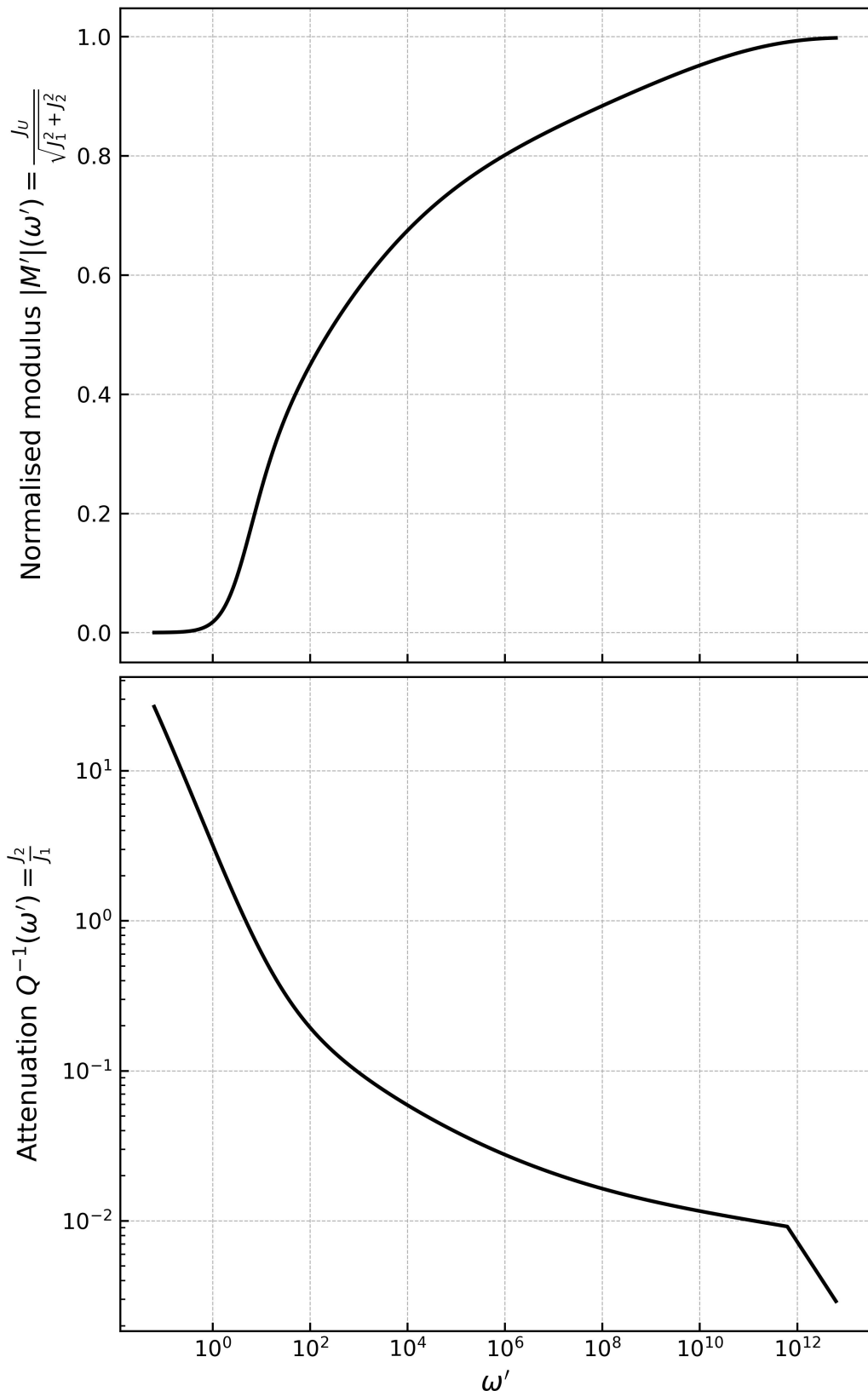


Figure 6.1: Normalised modulus and attenuation, as parameterised by the master curve of McCarthy and Takei (2011). The master curve provides a state-independent parameterisation of the complex compliance, when expressed as a function of normalised angular frequency, $\omega' = \omega/f_M$, which all polycrystalline materials may approximately obey.

and the normalised Maxwell timescale τ_M is given by

$$\tau_M = \frac{\eta(P, T, X, d)}{M_U(P, T, X)}, \quad (6.20)$$

in which the steady state viscosity of diffusion creep is

$$\eta = \eta_r(X) \left(\frac{d}{dr} \right)^m \exp \left[\frac{E_A}{R} \left(\frac{1}{T} - \frac{1}{T_r} \right) \right] \exp \left[\frac{V_A}{R} \left(\frac{P}{T} - \frac{P_r}{T_r} \right) \right], \quad (6.21)$$

and the instantaneous shear relaxation modulus is

$$M_U = \mu_0(X) + \frac{\partial \mu}{\partial T} \Delta T + \frac{\partial \mu}{\partial P} \Delta P. \quad (6.22)$$

By making the substitution $\omega \rightarrow \omega'$, where $\omega' = \omega/f_M$, the frequency-domain Prony series \tilde{M}^*

may be expressed as a function of normalised frequency, ω' , which results in the form

$$\tilde{M}_1(\omega') = \tilde{M}_\infty + \sum_{i=1}^{i=N_M} \alpha_i \frac{(\omega' \tau'_i)^2}{1 + (\omega' \tau'_i)^2}, \quad (6.23)$$

and

$$\tilde{M}_2(\omega') = \sum_{i=1}^{i=N_M} \alpha_i \frac{\omega' \tau'_i}{1 + (\omega' \tau'_i)^2}, \quad (6.24)$$

where each Maxwell element is now defined according to a discrete normalised timescale, $\tau'_i = \tau_i/\tau_M$. Therefore, the relaxation function can be calculated at a given frequency, $\omega = 2\pi f$ by first calculating the normalised Maxwell timescale (τ_M) associated with the present physical state, and converting ω into its equivalent normalised frequency, ω' , before substituting ω' in to the normalised Prony series expression. The final step required to fully account for the dependence of rock viscoelasticity on state variables is to make the substitution $\alpha_i \rightarrow \tilde{M}'_i$, where $\tilde{M}'_i = \alpha_i/\tilde{M}_U$, which normalises for the state-dependent $M_U(P, T, X)$ and transforms the

Prony series expression into its final form, where the normalised storage modulus is given by

$$\tilde{M}'_1(\omega') = \tilde{M}'_\infty + \sum_{i=1}^{i=N_M} \alpha'_i \frac{(\omega' \tau'_i)^2}{1 + (\omega' \tau'_i)^2}, \quad (6.25)$$

and the corresponding expression for the normalised loss modulus is

$$\tilde{M}'_2(\omega') = \sum_{i=1}^{i=N_M} \alpha'_i \frac{\omega' \tau'_i}{1 + (\omega' \tau'_i)^2}. \quad (6.26)$$

The resulting Prony series fits provided by equation 6.25 and 6.26 can now be used to encode self-consistency into numerical continuum mechanics models since the coefficients $\alpha'_i(\tau'_i)$ can be re-dimensionalised using an appropriate state vector (P, T, X, d) at each model node.

6.2.1 Application to the Master Curve Parameterisation

As mentioned in the previous section, the master curve parameterisation of McCarthy and Takei (2011) expresses complex compliance as a function of normalised frequency. The storage compliance is given by

$$J_1(\omega') = \frac{J_U}{F(\omega')}, \quad (6.27)$$

where J_U is the unrelaxed (instantaneous) compliance and $F(\omega')$ is an empirically defined function, given by

$$F(\omega') = \begin{cases} \sum_{i=0}^{i=6} a_k \ln \left(\frac{\omega'}{2\pi} \right)^k & \text{for } \frac{\omega'}{2\pi} \leq 10^{-13}, \\ 1 & \text{for } \frac{\omega'}{2\pi} > 10^{-13}, \end{cases} \quad (6.28)$$

where a_k are empirical constants ($a_0 = 0.55097$; $a_1 = 0.054332$; $a_2 = -0.0023615$; $a_3 = -5.7175 \times 10^{-5}$; $a_4 = 9.9473 \times 10^{-6}$; $a_5 = -3.4761 \times 10^{-7}$; and $a_6 = 3.9461 \times 10^{-9}$). The loss compliance is found by applying the Kramers-Kronig constraint, which ensures causality

is observed, i.e. that $J(t) = 0$ when $t < 0$, resulting in the expression

$$J_2(\omega') = J_U \left(\frac{\pi}{2} X(\omega') + \frac{2\pi}{\omega'} \right), \quad (6.29)$$

where $X(\omega')$ is an additional empirically defined function known as the relaxation spectrum, given by

$$X(\omega') = \begin{cases} 0.32 \times \left(\frac{2\pi}{\omega'} \right)^{0.39 - \frac{0.28}{1+2.6 \times \left(\frac{2\pi}{\omega'} \right)^{0.1}}} & \text{for } \frac{\omega'}{2\pi} \leq 10^{-11}, \\ 1853 \times \left(\frac{2\pi}{\omega'} \right)^{0.5} & \text{for } \frac{\omega'}{2\pi} > 10^{11}. \end{cases} \quad (6.30)$$

To calculate $M'_1(\omega')$ and $M'_2(\omega')$ spectra associated with the master curve parameterisation, prior to fitting, normalised versions of equation 6.14 and 6.15 are derived, such that

$$M'_1(\omega') \equiv \frac{M_1}{M_U}, \quad (6.31)$$

$$= \frac{J_U J_1}{|J|^2}, \quad (6.32)$$

$$= \frac{(J_1/J_U)}{(J_1/J_U)^2 + (J_2/J_U)^2}, \quad (6.33)$$

$$= \frac{J'_1}{|J^{*\prime}|^2}, \quad (6.34)$$

where $M_U = 1/J_U$, $J'_1 \equiv J_1/J_U$ and, by symmetry,

$$M'_2(\omega') \equiv \frac{M_2}{M_U}, \quad (6.35)$$

$$= \frac{J'_2}{|J^{*\prime}|^2}, \quad (6.36)$$

where $J'_2 \equiv J_2/J_U$. Substituting in the master curve parameterisation, the following expressions are found:

$$M'_1(\omega') = \frac{F}{1 + F^2 \left(\frac{\pi}{2} X(\omega') + \frac{2\pi}{\omega'} \right)^2}, \quad (6.37)$$

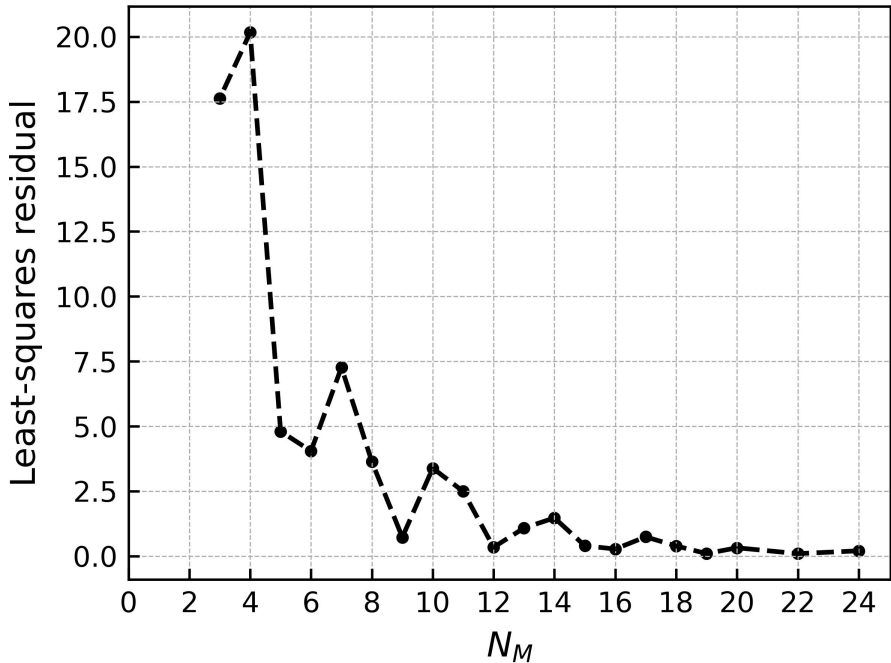


Figure 6.2: Least-squares residual between generalised Maxwell fit and underlying master curve parameterisation, as a function of the number of Maxwell elements (N_M).

and

$$M'_2(\omega') = \frac{\frac{\pi}{2}X + \frac{2\pi}{\omega'}}{F^{-2} + \left(\frac{\pi}{2}X + \frac{2\pi}{\omega'}\right)^2}. \quad (6.38)$$

The Prony series, \tilde{M}'_1 and \tilde{M}'_2 (equation 6.25 and 6.26, respectively) are used to obtain a best-fitting generalised Maxwell representation of M'_1 and M'_2 , and therefore the master curve's rheological behaviour. By varying the number of Maxwell elements (N_M) used in the Prony series fitting procedure and the corresponding timescale of each element, the residual misfit between each generalised Maxwell model and the underlying master curve spectra was calculated. It was found that at least $N_M = 9$ elements are needed to provide a good approximation in the frequency domain (Figure 6.2). In Figure 6.3, the fit of the Prony series to the underlying M'_1 and M'_2 spectra is shown. For a given value of N_M , the normalised storage modulus M'_1 is better approximated by the Prony series than the normalised loss modulus M'_2 . The oscillatory behaviour observed in both M'_1 and M'_2 is an inherent feature of the finite Prony series, but becomes less pronounced if N_M is increased.

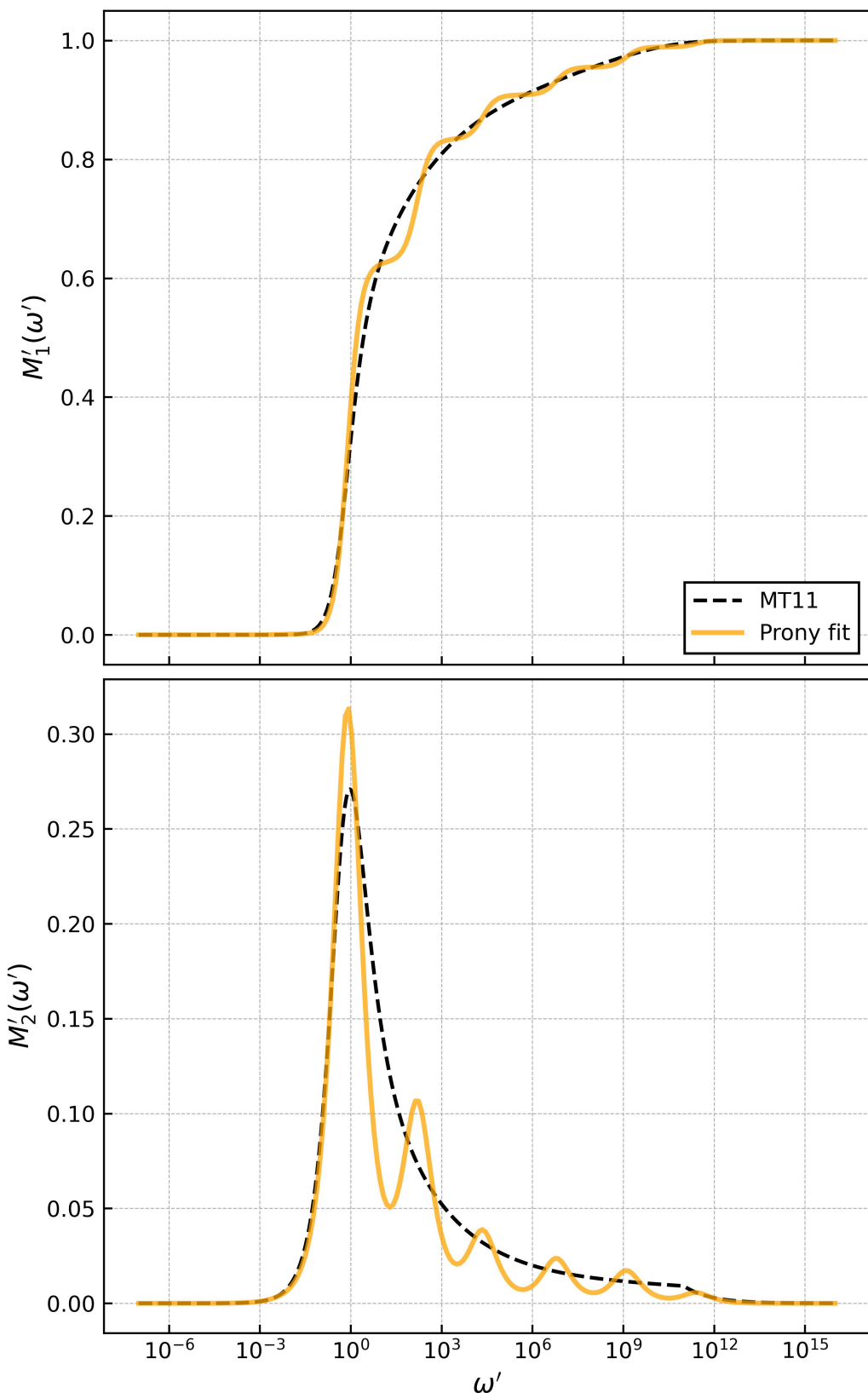


Figure 6.3: Prony series approximation of $M'_1(\omega')$ and $M'_2(\omega')$, for the master curve parameterisation of McCarthy and Takei (2011), using $N_M = 9$ Maxwell elements.

6.2.2 Application to the Pre-Melting Parameterisation

Applying the normalised Prony series approach to the pre-melting parameterisation of Yamauchi and Takei (2016) is more challenging than the master curve parameterisation, because the high-frequency dissipation peak of the former model breaks the normalised frequency scaling, such that a different normalised complex compliance spectrum will be exhibited depending on the homologous temperature

$$\Theta \equiv \frac{T}{T_S}, \quad (6.39)$$

of the material represented (T_S is the solidus temperature, see Figure 6.4). This behaviour is inferred to be caused by diffusional grain boundary sliding, exhibited at near-solidus temperatures, where small amounts of melt at the grain interface provide a lubricating effect. The result is that the Prony series coefficients α'_i are no longer state-independent, and will only apply to the homologous temperature at which they were calculated. A potential solution to this issue might be to generate a look-up table of Prony series coefficients at a series of discrete homologous temperatures. Then, for any given value of Θ , linear interpolation could be used to estimate a set of appropriate Prony series coefficients that best represent the deformation behaviour of mantle rock at that particular temperature. However, there is no theoretical basis for predicting how the individual Prony series coefficients, for a chosen number of Maxwell elements N_M , should vary as a function of temperature, and therefore how best to generate a look-up table of this kind. Here, a more rigorous solution is sought, which first involves constructing a normalised Prony series representation of Yamauchi and Takei (2016) at an arbitrary reference temperature, Θ_r , given by

$$\tilde{M}'_1(\omega', \Theta_r) = \tilde{M}'_\infty(\Theta_r) + \sum_{i=1}^{i=N_M} \alpha'_i(\Theta_r) \frac{(\omega' \tau'_i)^2}{1 + (\omega' \tau'_i)^2}, \quad (6.40)$$

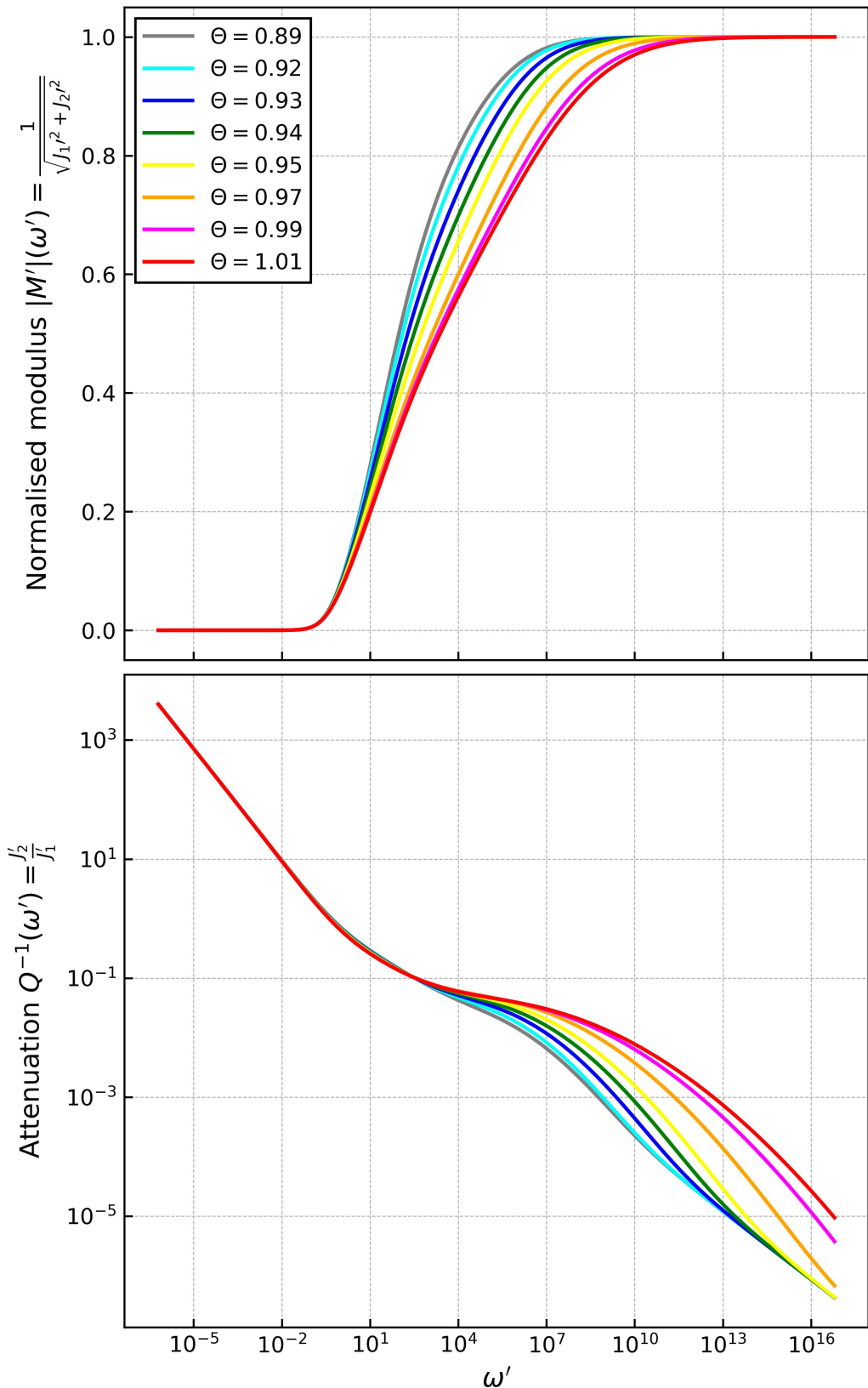


Figure 6.4: Normalised modulus and attenuation, as parameterised by the pre-melting curves of Yamauchi & Takei (2016). The pre-melting parameterisation disobeys the state-independent master curve.

where $\tilde{M}'_1(\omega', \Theta_r) \approx M'_1(\omega', \Theta_r)$ and

$$M'_1 = \frac{J'_1(\omega', \Theta_r)}{|J^{*'}(\omega', \Theta_r)|^2}. \quad (6.41)$$

Then, an equivalent expression can be written for a general temperature, Θ , i.e.

$$\tilde{M}'_1(\omega', \Theta) = \tilde{M}'_\infty(\Theta) + \sum_{i=1}^{i=N_M} \alpha'_i(\Theta) \frac{(\omega' \tau'_i)^2}{1 + (\omega' \tau'_i)^2} \approx \frac{J'_1(\omega', \Theta)}{|J^{*'}(\omega', \Theta)|^2}, \quad (6.42)$$

where in general the Prony series coefficients $\alpha_i(\Theta)$ are different to $\alpha_i(\Theta_r)$, and a relationship between the unknown $\alpha_i(\Theta)$ and the known $\alpha_i(\Theta_r)$ is sought. To find it, consider the ratio between \tilde{M}'_1 at both Θ_r and Θ , which looks like

$$\frac{\tilde{M}'_1(\omega', \Theta)}{\tilde{M}'_1(\omega', \Theta_r)} = \frac{\tilde{M}'_\infty(\Theta) + \sum_{i=1}^{i=N_M} \alpha'_i(\Theta) \frac{(\omega' \tau'_i)^2}{1 + (\omega' \tau'_i)^2}}{\tilde{M}'_\infty(\Theta_r) + \sum_{i=1}^{i=N_M} \alpha'_i(\Theta_r) \frac{(\omega' \tau'_i)^2}{1 + (\omega' \tau'_i)^2}} \approx \frac{J'_1(\omega', \Theta) |J^{*'}(\omega', \Theta_r)|^2}{J'_1(\omega', \Theta_r) |J^{*'}(\omega', \Theta)|^2}. \quad (6.43)$$

As it stands, this equation acts as a single constraint on a set of N_M unknowns, and so it is not possible to isolate the individual $\alpha'_i(\Theta)$ without some further simplification or addition of information. To this end, it is possible to utilise the fact that when

$$\omega' < \sqrt{\frac{1-\beta}{\beta}} \frac{1}{\tau'_{N_M-1}}, \quad (6.44)$$

where $\beta = 0.9$ is an arbitrarily set dominance factor, the dominant contribution towards the storage modulus $\tilde{M}'_1(\omega', \Theta)$ comes from the $\alpha'_{N_M}(\Theta)$ component (Figure 6.5), and thus the discrete summation in the numerator of equation 6.43 can be reduced to

$$\tilde{M}'_1 \left(\omega' < \sqrt{\frac{1-\beta}{\beta}} \frac{1}{\tau'_{N_M-1}}, \Theta \right) \approx \tilde{M}'_\infty(\Theta) + \alpha'_{N_M}(\Theta) \frac{(\omega' \tau'_{N_M})^2}{1 + (\omega' \tau'_{N_M})^2}. \quad (6.45)$$

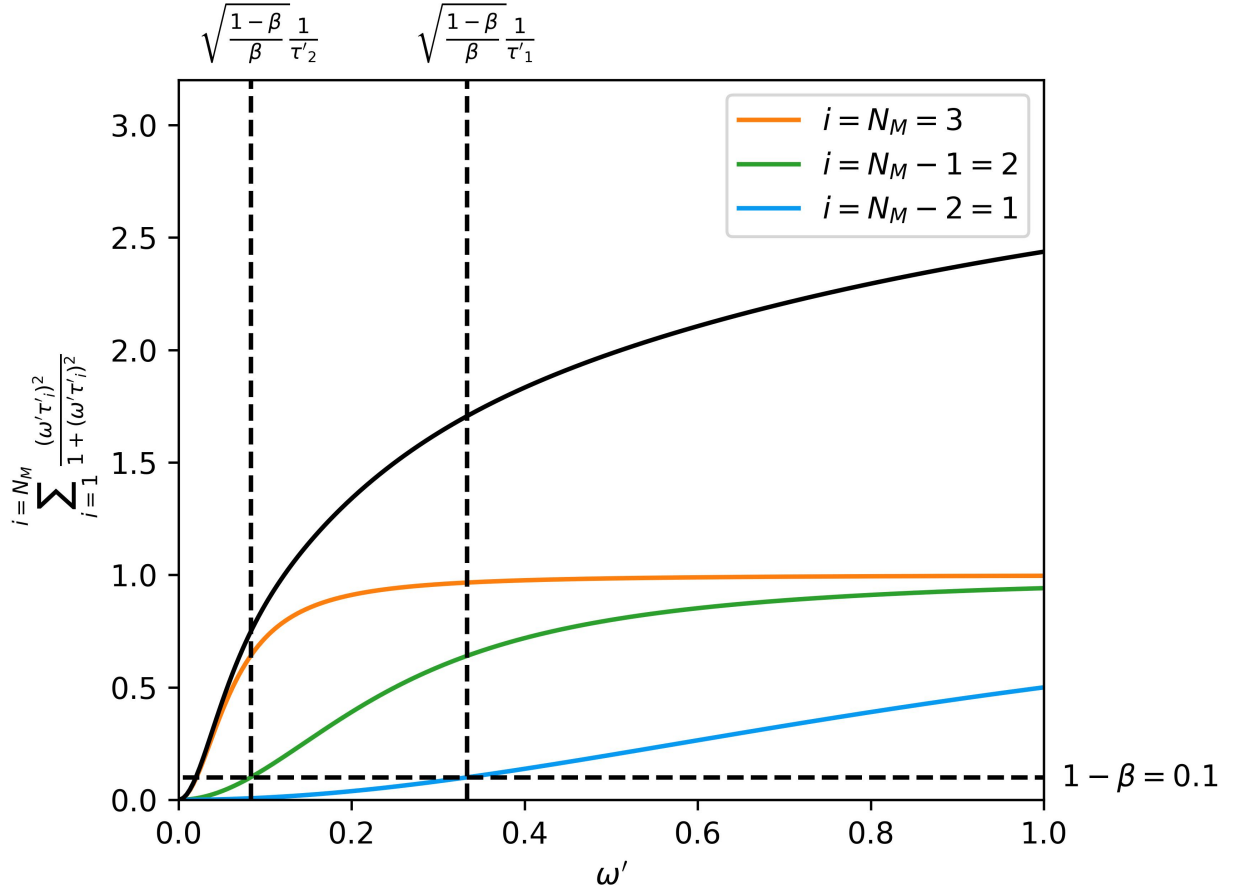


Figure 6.5: Contributions towards $\tilde{M}'_1(\omega', \Theta)$ from $\alpha'_i(\Theta)$ as a function of ω' . N.B. that ω' , τ'_i and α'_i are defined arbitrarily in this schematic diagram. When $\omega' < \sqrt{\frac{1-\beta}{\beta}} \frac{1}{\tau'_{N_M-1}}$, the α'_{N_M} (orange) component dominates the total signal (black), where $\beta = 0.9$. When $\sqrt{\frac{1-\beta}{\beta}} \frac{1}{\tau'_{N_M-2}} > \omega' \geq \sqrt{\frac{1-\beta}{\beta}} \frac{1}{\tau'_{N_M-1}}$, the α'_{N_M} and α'_{N_M-1} (green) components together dominate the total signal. When $\omega' \geq \sqrt{\frac{1-\beta}{\beta}} \frac{1}{\tau'_{N_M-2}}$, all three components α'_{N_M} , α'_{N_M-1} and α'_{N_M-2} (blue) contribute.

Rearranging this simplified version of equation 6.43 for $\alpha'_{N_M}(\Theta)$, and using the approximation $\tilde{M}'_\infty(\Theta) \approx \tilde{M}'_\infty(\Theta_r)$, the following expression is found

$$\alpha'_{N_M}(\Theta) = \frac{1 + (\omega' \tau'_{N_M})^2}{(\omega' \tau'_{N_M})^2} \left[\tilde{M}'_1(\omega', \Theta_r) \mathcal{J}(\omega', \Theta, \Theta_r) - \tilde{M}'_\infty(\Theta_r) \right], \quad (6.46)$$

where

$$\mathcal{J}(\omega', \Theta, \Theta_r) \equiv \frac{J'_1(\omega', \Theta) |J^{*'}(\omega', \Theta_r)|^2}{J'_1(\omega', \Theta_r) |J^{*'}(\omega', \Theta)|^2}. \quad (6.47)$$

Having solved for $\alpha'_{N_M}(\Theta)$, knowledge of this parameter can now be used to find $\alpha'_{N_M-1}(\Theta)$, by utilising the fact that when

$$\sqrt{\frac{1-\beta}{\beta}} \frac{1}{\tau'_{N_M-2}} > \omega' \geq \sqrt{\frac{1-\beta}{\beta}} \frac{1}{\tau'_{N_M-1}}, \quad (6.48)$$

the dominant contribution towards the storage modulus comes from the $\alpha'_{N_M}(\Theta)$ and $\alpha'_{N_M-1}(\Theta)$ components, and thus it is found that

$$\alpha'_{N_M-1}(\Theta) = \frac{1 + (\omega' \tau'_{N_M-1})^2}{(\omega' \tau'_{N_M-1})^2} \left[\tilde{M}'_1(\omega', \Theta_r) \mathcal{J}(\omega', \Theta, \Theta_r) - \tilde{M}'_\infty(\Theta_r) - \alpha'_{N_M}(\Theta) \frac{(\omega' \tau'_{N_M})^2}{1 + (\omega' \tau'_{N_M})^2} \right]. \quad (6.49)$$

This relationship is recursive, such that one can solve for all parameters $\alpha_i(\Theta)$ by working in order down from $i = N_M$ to $i = 1$, and using the formula

$$\alpha'_i(\Theta) = \frac{1 + (\omega' \tau'_i)^2}{(\omega' \tau'_i)^2} \left[\tilde{M}'_1(\omega', \Theta_r) \mathcal{J}(\omega', \Theta, \Theta_r) - \tilde{M}'_\infty(\Theta_r) - \sum_{j=i+1}^{j=N_M} \alpha'_j(\Theta) \frac{(\omega' \tau'_j)^2}{1 + (\omega' \tau'_j)^2} \right], \quad (6.50)$$

where

$$\sqrt{\frac{1-\beta}{\beta}} \frac{1}{\tau'_{i-1}} > \omega' \geq \sqrt{\frac{1-\beta}{\beta}} \frac{1}{\tau'_i} \quad \text{if } i \geq 2, \quad (6.51)$$

$$\omega' > \sqrt{\frac{1-\beta}{\beta}} \frac{1}{\tau'_i} \quad \text{if } i = 1. \quad (6.52)$$

Each time the formula is applied, a piece of information is added: that $\tilde{M}'_1(\Theta)$ within a certain frequency band (defined by equation 6.51 and 6.52) is controlled only by components α'_j whose corresponding relaxation timescale, τ'_j , is long enough that the expression

$$\alpha'_j(\Theta) \frac{(\omega' \tau'_j)^2}{1 + (\omega' \tau'_j)^2} \quad (6.53)$$

exhibits significant variation over this region of frequency space, such that a non-negligible contribution is made to the overall storage modulus. This information allows a single constraint on N_M unknowns to be transformed into a set of N_M constraints on the same number of unknowns, allowing each component to be isolated.

The accuracy of the scaling approach to estimating $\alpha'_i(\Theta)$ based on a set of Prony coefficients corresponding to a reference temperature, Θ_r , depends firstly on how accurately the reference series approximates the underlying pre-melting parameterisation. This accuracy can be improved by moving to larger N_M , with tests (evaluating the residual misfit between the approximate reference series and the underlying parameterisation it is derived from) implying that $N_M \geq 9$ is favourable. However, assumptions on the dominant contribution towards the shear modulus at a given frequency, ω' , rely on there being sufficient spacing between individual components of the series. If $\Delta\tau_i = \tau_i - \tau_{i-1}$ (for $i = 2, 3, \dots, N_M$) becomes too small, one will no longer be able isolate the contribution of α'_i from that of α'_{i-1} , and the recursion relationship

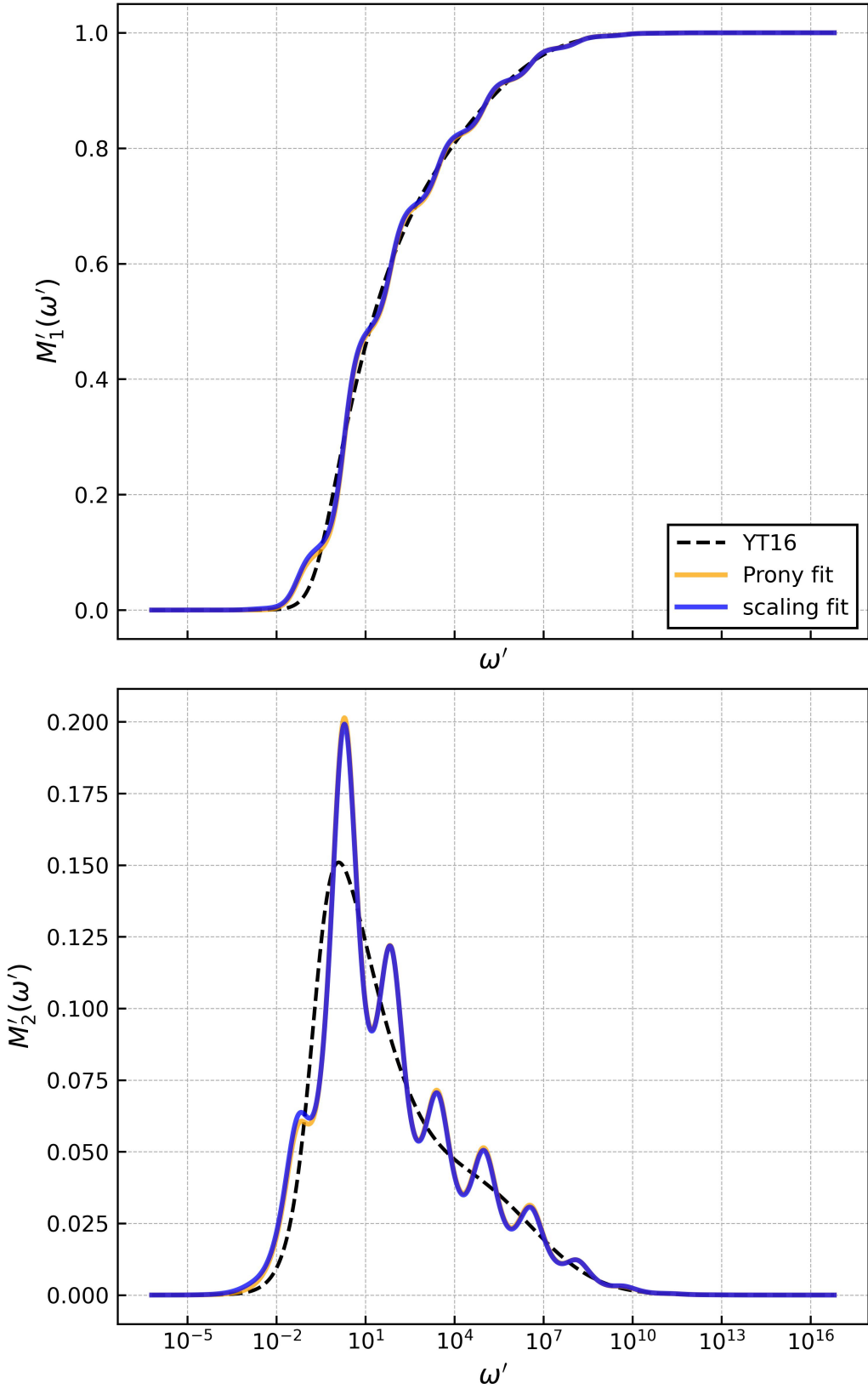


Figure 6.6: Prony series approximation of $M'_1(\omega')$ and $M'_2(\omega')$ for the pre-melting parameterisation of Yamauchi & Takei (2016), using $N_M = 15$ Maxwell elements, and a homologous temperature $\Theta = 0.95$. The Prony series fit (orange) appears almost identical to the scaling fit (blue), which was produced by obtaining a Prony series fit at a reference temperature, $\Theta = 0.80$, and utilising the recursive formula of equation 6.50 to approximate the corresponding series at $\Theta = 0.95$.

will become unstable. This is not expected to be an issue for

$$N_M \leq \log_{10} \left(\frac{\tau'_{N_M}}{\tau'_1} \right), \quad (6.54)$$

such that there is less than one discrete Prony coefficient per decade in normalised frequency space. In the case of transient rheology, a parameterisation is sought over the normalised frequency range $\omega' = 2\pi \times 10^{-7}$ to $\omega' = 2\pi \times 10^{16}$, in which case $N_M \leq 23$ satisfies condition 6.54. Therefore, a generalised Maxwell model containing between 9 and 23 elements is found to be suitable for application of the pre-melting parameterisation within numerical models of continuum mechanics. The recursive formula of equation 6.50 was tested using $N_M = 15$ Maxwell elements to scale from a reference temperature, $\Theta_r = 0.8$, up to an arbitrarily selected temperature, $\Theta = 0.95$. Figure 6.6 shows that the resulting fit is almost identical to that which is produced by constructing an approximate Prony series fit of the same number of elements at $\Theta = 0.95$, which means that the method is working as intended. As a result, the difference between the reference Prony series approximation and the true reference spectrum is by far the dominant control on the accuracy of the constructed model at an arbitrary temperature, Θ , as compared to the error introduced by performing the recursive scaling method. This means that more complicated descriptions of viscoelasticity, such as Yamauchi and Takei (2016), can just as accurately be implemented in numerical models as their more simple counterparts, such as McCarthy and Takei (2011). The focus should therefore be on using the most realistic description of mantle rock available, and optimising N_M and τ'_i such that a good quality reference Prony series fit is obtained.

6.3 Adapting Pre-Melting Parameterisation For Computational Efficiency

Having shown that the pre-melting parameterisation of Yamauchi and Takei (2016) can be accurately converted into a normalised Prony series, which can be scaled to any physical state of interest, attention can be turned towards making its implementation in numerical models computationally efficient. Consider a finite element discretisation of Earth's volume, within which each node has a unique physical state, represented by a given temperature (T), pressure (P) and grain size (d). For simplicity composition (X) will be treated as constant, but it is not necessary to do so. Then, the stress relaxation function $M(t)$ relevant to each model node should be calculated. To do so, a parameterisation of the solidus must be used to calculate the node-variable homologous temperature Θ . Having obtained Θ , the temperature-dependent normalised Prony coefficients, $\alpha'_i(\Theta)$, can be calculated at each node using the recursive scaling relation expressed in equation 6.50. Each time this calculation is performed, multiple calls are made to the parameterisation of complex compliance within the pre-melting framework, which looks like

$$J_1 = J_U \left(1 + \frac{A_B \tau_S^{\alpha_B}}{\alpha_B} + \frac{\sqrt{2\pi}}{2} A_P \sigma_P \left(1 - \text{erf} \left[\frac{\ln(\tau_P/\tau_S)}{\sqrt{2}\sigma_P} \right] \right) \right), \quad (6.55)$$

$$J_2 = J_U \left(\tau_S + \frac{\pi A_B \tau_S^{\alpha_B}}{2\alpha_B} + \frac{\pi}{2} A_P \exp \left[\frac{-\ln^2(\tau_P/\tau_S)}{\sqrt{2}\sigma_P} \right] \right). \quad (6.56)$$

To redimensionalise the obtained normalised Prony series, normalised Prony series coefficients must be converted into moduli, using knowledge of the unrelaxed modulus, M_U . In addition, normalised timescales $\tau'_i = \tau_i/\tau_M$ must be converted into real timescales using knowledge of the Maxwell timescale, $\tau_M = \eta/M_U$, where the steady state viscosity of diffusion creep is provided by

$$\eta = \eta_r \left(\frac{d}{dr} \right)^m A_\eta \exp \left[\frac{E_A}{R} \left(\frac{1}{T} - \frac{1}{T_r} \right) \right] \exp \left[\frac{V_A}{R} \left(\frac{P}{T} - \frac{P_r}{T_r} \right) \right]. \quad (6.57)$$

In the above equations, the three homologous temperature-dependent functions $A_P(\Theta)$, $\sigma_P(\Theta)$, and $A_\eta(\Theta)$ define the amplitude and width of the high-frequency dissipation peak, and the effect of pre-melting on viscosity, respectively. They are piecewise functions, constructed using several sub-functions, which taken together cover the full domain of possible Θ values. The dissipation peak amplitude is given by

$$A_P(\Theta) = \begin{cases} 0.01 & \text{if } \Theta < 0.91, \\ 0.01 + 0.4(\Theta - 0.91) & \text{if } 0.91 \leq \Theta < 0.96, \\ 0.03 & \text{if } 0.96 \leq \Theta < 1, \\ 0.03 + \beta(\phi) & \text{if } \Theta \geq 1, \end{cases} \quad (6.58)$$

the peak width is given by

$$\sigma_P(\Theta) = \begin{cases} 4 & \text{if } \Theta < 0.92, \\ 4 + 37.5(\Theta - 0.92) & \text{if } 0.92 \leq \Theta < 1, \\ 7 & \text{if } \Theta \geq 1, \end{cases} \quad (6.59)$$

and the effect of pre-melting on steady state diffusion creep viscosity is given by

$$A_\eta(\Theta) = \begin{cases} 1 & \text{if } \Theta < \Theta^\eta, \\ \exp\left[-\frac{\Theta-\Theta^\eta}{\Theta-\Theta^\eta} \ln \gamma\right] & \text{if } \Theta^\eta \leq \Theta < 1, \\ \gamma^{-1} \exp(-\gamma\phi) & \text{if } \Theta \geq 1. \end{cases} \quad (6.60)$$

where melt fraction is assumed to be negligible (i.e., $\phi = 0$), and the parameters $\gamma = 5$ and $\Theta^\eta = 0.94$ are taken from the observations of Yamauchi and Takei (2016) pertaining to borneol sample 41, which are considered to be of highest available quality. Numerical implementation

of the above functions requires the use of “if else” statements, which are notoriously slow to implement computationally because they obfuscate the vectorisation of function calls. Since computing the viscoelastic properties relevant to each discrete node of a finite element model requires A_P , σ_P and A_η to be calculated, it is preferable to replace their piecewise parameterisations with a smoothly varying, continuous function which covers the entire domain. Furthermore, the parameterisations of A_P , σ_P and A_η were defined subjectively (Yasuko Takei pers. comm.). That is, Yamauchi and Takei (2016) did not use numerical optimisation to find best-fitting parameterisations of A_P , σ_P and A_η to the underlying experimental data. This aspect is unideal because parameterisations of physical behaviour based on experiments should remain as faithful to the observations as possible, and this can only be ensured in an objective fashion by using some form of numerical optimisation. Furthermore, applications of the pre-melting parameterisation inherently assume that it is a true representation of mantle rock deformation. In fact, if an optimisation technique is used to characterise the range of possible forms for A_P , σ_P and A_η which fit the underlying data, it starts to become possible to take this source of phenomenological uncertainty into account when applying the pre-melting model to geophysical applications. Therefore, when replacing the piecewise A_P , σ_P and A_η definitions with functions for which only a single expression is required to define each function across the whole domain of possible Θ values, optimisation will be used to obtain the best-fitting parameterisation.

To within a change of sign, each of the functions A_P , σ_P and A_η as defined by Yamauchi and Takei (2016) behave very similarly, particularly in the absence of melt (Figure 6.7). The amplitude and width of the dissipation peak maintain a constant value beneath some lower threshold Θ , above which they increase linearly, until they reach a maximum value at a higher threshold, which is then preserved for all higher temperatures. The viscosity reduction factor is initially of unit value, then decreases approximately linearly, until it reaches a minimum value, preserved for all higher temperatures. While Yamauchi and Takei (2016) choose a unique

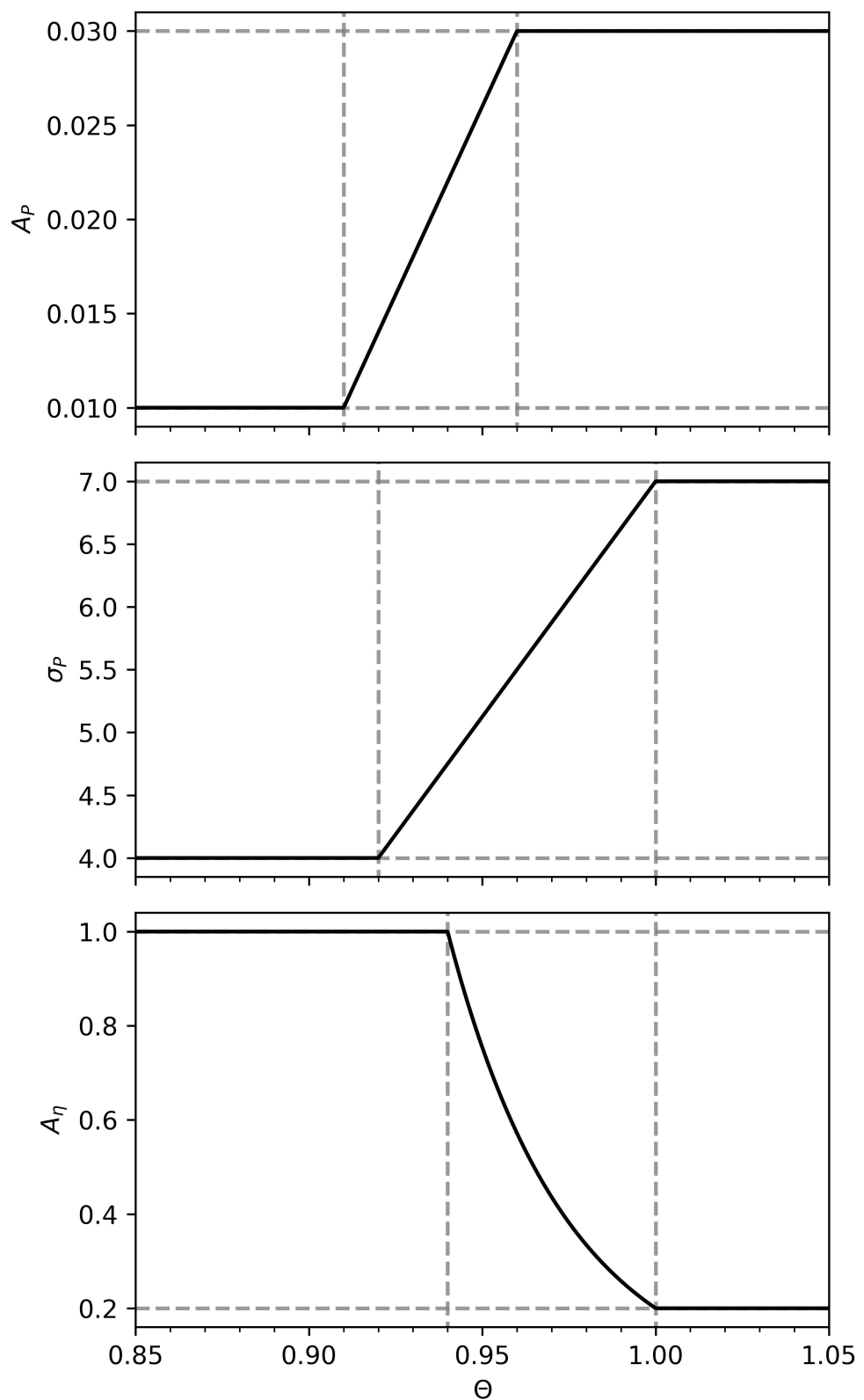


Figure 6.7: Homologous temperature dependence of A_P , σ_P and A_η as parameterised by Yamadachi and Takei (2016).

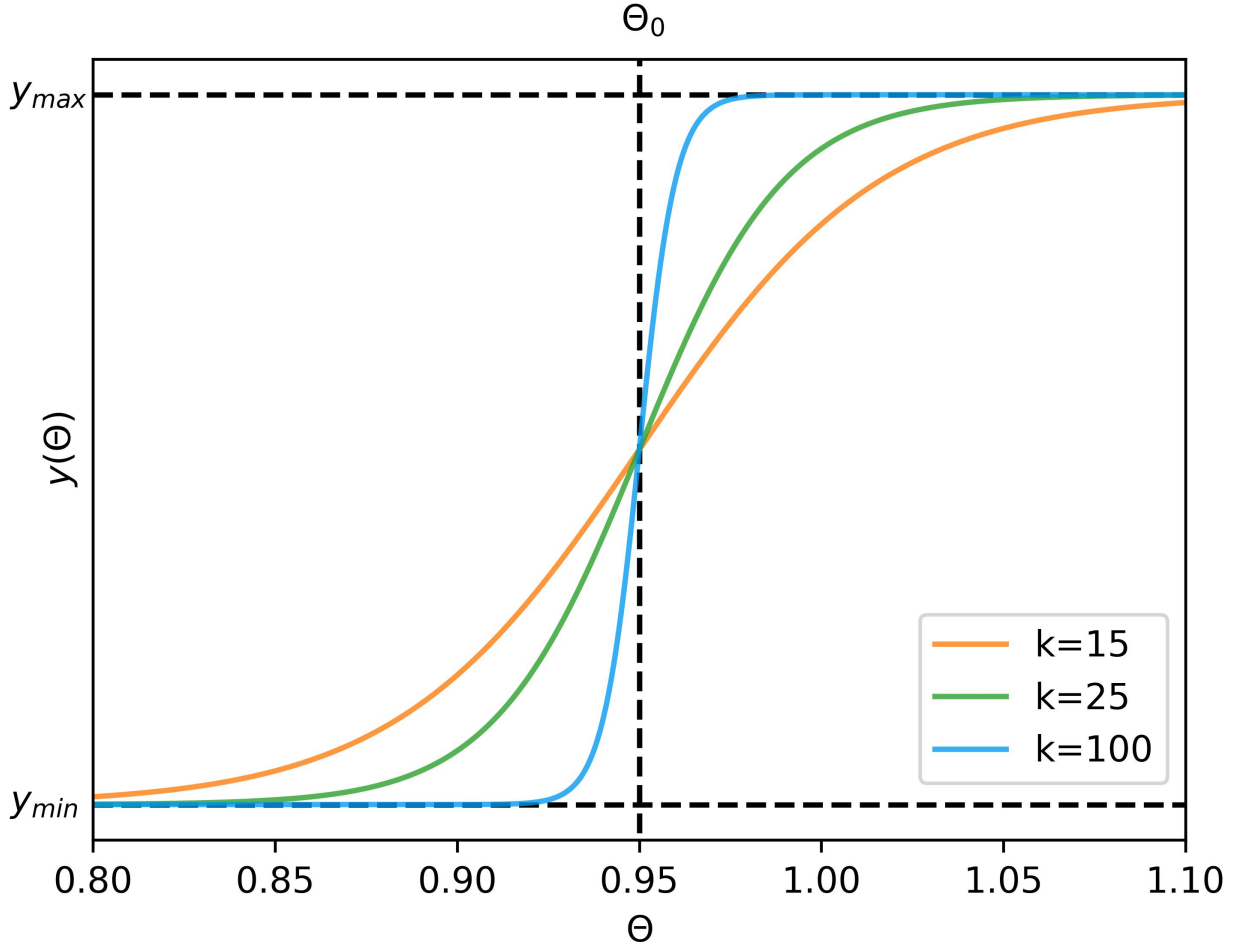


Figure 6.8: Schematic representation of the scaled hyperbolic tangent function.

lower and higher threshold, determining the position in homologous temperature space across which variations in the individual functions occur, for each of A_P , σ_P and A_η , the lower and higher thresholds presumably pertain to the onset and saturation of pre-melting as a physical phenomenon, respectively. Therefore, it may be preferable to parameterise A_P , σ_P and A_η according to universal temperature thresholds. A reasonable approximation of the shapes of A_P , σ_P and A_η can be obtained using scaled hyperbolic tangent functions, which are represented generally as

$$y(\Theta) = (y_{\max} - y_{\min}) \left[1 + \exp(-2k(\Theta - \Theta_0)) \right] + y_{\min}, \quad (6.61)$$

where y_{\min} defines the minimum value, $y_{\max} - y_{\min}$ is the amplitude of variation, Θ_0 is the threshold temperature about which functional variations are symmetric, and k is a scaling factor

representing the range of temperatures over which variations occur. A schematic representation of the scaled hyperbolic tangent function is shown in Figure 6.8, highlighting the effect of each parameter on the function's shape. Applying the assumption that each of A_P , σ_P and A_η should exhibit variations over the same range of pre-melting temperatures, it follows that k and Θ_0 are treated as constant with respect to the choice of pre-melting function. On the other hand, y_{\min} and y_{\max} should be treated as unique to each particular function. In the case of A_η , it is known that $y_{\min} = 1$ and $y_{\max} = \gamma^{-1} = 0.2$, as constrained by Yamauchi and Takei (2016).

6.3.1 Fitting A_P , σ_P and A_η to Experimental Data

In order to invert for a set of best-fitting pre-melting parameters, anelasticity and diffusion creep viscosity data from the original experiments of Yamauchi and Takei (2016) were obtained. The anelasticity data consist of a set of measurements of the storage and loss compliance (J_1 and J_2 , respectively) as a function of homologous temperature and normalised forcing frequency. These data allow for the constraint of A_P and σ_P , since these functions control the effect of pre-melting on frequency-dependent shear relaxation, and therefore J_1 via equation 6.55, and J_2 via equation 6.56. The viscosity data consist of a series of inferred viscosities as a function of homologous temperature. These data are collected by performing a series of creep tests, which involve applying a small shear stress, σ , and tracking how the strain response evolves over time, $\varepsilon(t)$ (see Figure 8, Yamauchi and Takei, 2016). Since σ is held constant throughout the study, $\varepsilon(t)$ is a simple linear relationship corresponding to steady state diffusion creep. Viscosity is the constant of proportionality linking the observed strain rate to the applied stress, meaning it can be calculated from the creep test using

$$\eta = \sigma \left(\frac{d\varepsilon}{dt} \right)^{-1}. \quad (6.62)$$

Function	Parameter	Prior l_i	Prior u_i	Posterior μ_i	Posterior s_i	MAP
A_P, σ_P and A_η	k	5	200	8.55	5.72	16.0
	Θ_0	0.9	1.0	0.949	0.023	0.932
A_P	y_{\min}	0	0.02	0.01275	0.00484	0.00235
	y_{\max}	0.02	0.04	0.0292	0.0054	0.0325
σ_P	y_{\min}	3.0	5.0	4.03	0.28	3.95
	y_{\max}	6.0	8.0	6.99	0.29	6.58
$\ln \eta$	a_0	-46.1	-23.0	-33.5	6.3	-26.9
	$\frac{a_1}{1000}$	11.5	23.0	19.4	1.9	17.5

Table 6.1: Prior and posterior estimates of the pre-melting parameters. For each parameter, a lower and upper uniform prior bound is reported (l_i and u_i , respectively), as well as the mean and standard deviation posterior estimate (μ_i and s_i), and the *maximum a posteriori* estimate.

The relationship between viscosity and temperature is given by equation 6.57. Taking the natural logarithm, it looks like

$$\ln \eta = \ln A_\eta + \ln \eta_r + m \ln \left(\frac{d}{d_r} \right) - \frac{E_A + V_A P_r}{R T_r} + \frac{E_A + V_A P}{R} \frac{1}{T}, \quad (6.63)$$

from which it can be seen that at constant grain size and pressure, the pre-melting function $A_\eta(\Theta)$ controls deviations of the $\ln \eta \left(\frac{1}{T} \right)$ relationship away from linearity, i.e.

$$\ln \eta = \ln A_\eta + a_0 + a_1 \frac{1}{T}, \quad (6.64)$$

where

$$a_0 \equiv \ln \eta_r + m \ln \left(\frac{d}{d_r} \right) - \frac{E_A + V_A P_r}{R T_r} \quad (6.65)$$

and

$$a_1 \equiv \frac{E_A + V_A P}{R} \quad (6.66)$$

are unknown parameters relating to the reference viscosity, grain size, activation energy, activation volume and reference pressure of the tested borneol sample, and therefore a_0 and a_1 are to be fitted alongside A_η as part of the inversion procedure. Since the three pre-melting functions

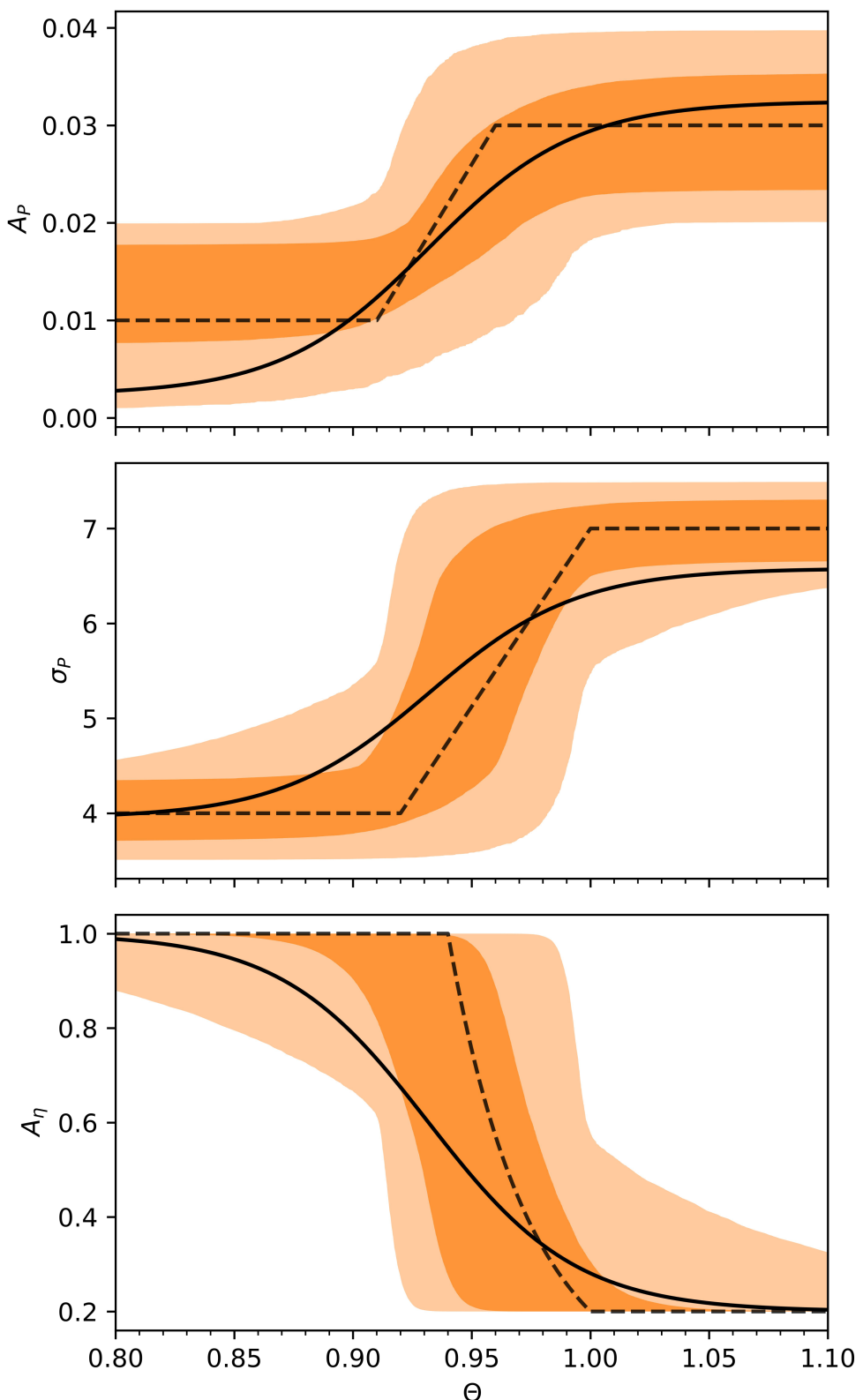


Figure 6.9: Best-fitting pre-melting functions (solid line=MAP; pale shaded region=central 99% credible interval; dark shaded region= 1σ (68%) credible interval) compared to original functional forms from Yamauchi and Takei (2016, dashed line).

are connected by the same underlying variables k and Θ_0 , the anelasticity and viscosity data are treated simultaneously, using a joint inversion procedure. This is because variations in k and Θ_0 made to accommodate the structure of the anelasticity data will affect the fit to the viscosity data, and vice versa. In order to evaluate the distribution of possible values the free inversion parameters could reasonably take, and therefore the uncertainty in the parameterisation of pre-melting behaviour, a Bayesian inversion approach was taken, analogous to that applied in the context of geophysical data in Chapter 2. There were eight parameters to be fitted in total: k , Θ_0 , y_{\min} and y_{\max} for each of A_P and σ_P , and a_0 and a_1 , which determine the linear component of the $\ln \eta \left(\frac{1}{T} \right)$ relationship. Together they form the model vector \mathcal{X} . A uniform prior distribution was assumed for each parameter, such that the inversion results were driven purely by the applied data constraints. For a general parameter \mathcal{X}_i with corresponding prior lower bound l_i , and upper bound u_i , the prior probability density on \mathcal{X}_i is given by

$$p(\mathcal{X}_i) = \begin{cases} \frac{1}{u_i - l_i} & \text{for } l_i \leq \mathcal{X}_i \leq u_i, \\ 0 & \text{otherwise.} \end{cases} \quad (6.67)$$

The prior bounds (l_i, u_i) for each parameter were chosen based on the most conservative view of the possible range of parameter values when plotting fits between the model and the data (Table 6.1). The overall prior density was then constructed by multiplying together the prior density on each parameter, such that

$$p(\mathcal{X}) = \prod_{i=1}^{i=N_p} p(\mathcal{X}_i), \quad (6.68)$$

where $N_p = 8$ is the number of free parameters in the model vector \mathcal{X} .

A Gaussian likelihood function was used for each of the three data sets, $J'_1(\omega', \Theta)$, $\log_{10} J'_2(\omega', \Theta)$

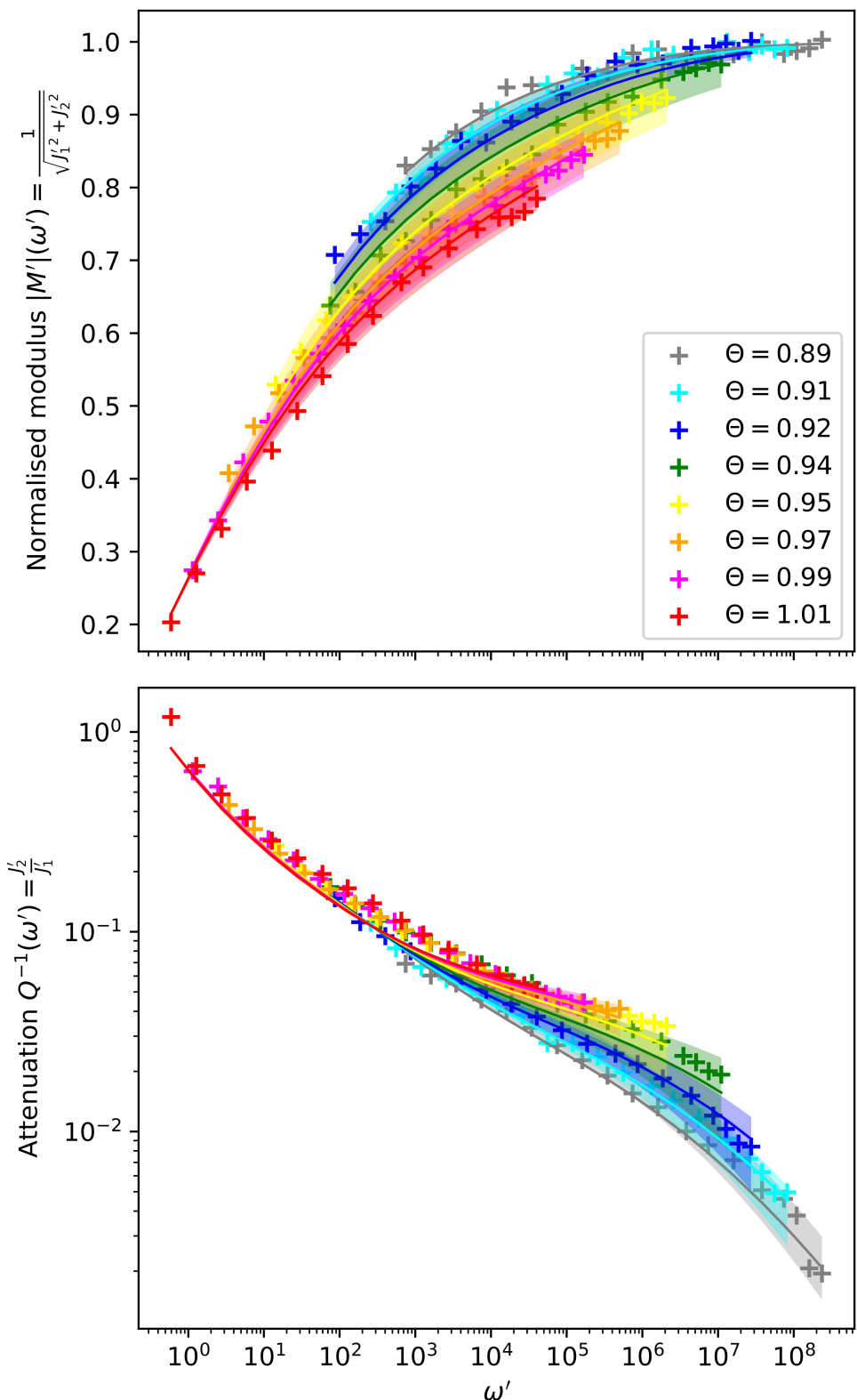


Figure 6.10: Fit of scaled hyperbolic tangent pre-melting parameterisation to anelasticity data (solid line=MAP; shaded region= 1σ (68%) credible interval).

and $\ln \eta\left(\frac{1}{T}\right)$, given by

$$p(d_k | \mathcal{X}) = \frac{1}{(2\pi)^{N_k/2} |\Sigma_k|^{1/2}} \exp\left(-\frac{1}{2} (d_k - \hat{d}_k)^T \Sigma_k^{-1} (d_k - \hat{d}_k)\right), \quad (6.69)$$

where d_k represents the k^{th} data set containing N_k data points, $\hat{d}_k = \hat{d}_k(\mathcal{X})$ the corresponding model prediction, and Σ_k the data covariance matrix containing the uncertainty on each data point. Note that the use of hyperparameters was neglected in this inversion for simplicity; this issue will be returned to during the more rigorous treatment described in Section 6.3.3. The overall likelihood was then constructed, as usual, by multiplying together the likelihood on each parameter, such that

$$p(\mathcal{D} | \mathcal{X}) = \prod_{k=1}^{k=N_d} \frac{1}{(2\pi)^{N_k/2} |\Sigma_k|^{1/2}} \exp\left(-\frac{1}{2} (d_k - \hat{d}_k)^T \Sigma_k^{-1} (d_k - \hat{d}_k)\right), \quad (6.70)$$

where $N_d = 3$ is the total number of data sets. As in Chapter 2 with the inversion for best-fitting viscoelastic parameters using geophysical data, the GASWAM sampling algorithm was used to ensure efficient sampling of the multidimensional parameter space. The inversion was run for a total of 1,000,000 trials, with a burn-in phase of 10,000 trials, after which random sampling around a region of high-likelihood parameter combinations occurred. A summary of the inverted parameters is provided in Table 6.1. The *maximum a posteriori* (MAP) model from the inversion corresponds simply to the highest likelihood, and therefore lowest misfit set of parameters, owing to the assumption of uniform priors. Predictions of A_P , σ_P and A_η using the MAP model are shown in Figure 6.9, alongside 99% and 1σ (68%) credible intervals, and the original parameterisation of Yamauchi and Takei (2016). They show that a wide range of pre-melting models are plausible, within the constraints of the experimental data. This includes models exhibiting sharp changes in pre-melting behaviour over a narrow range of homologous temperatures, as well as models exhibiting a much smoother transition, as

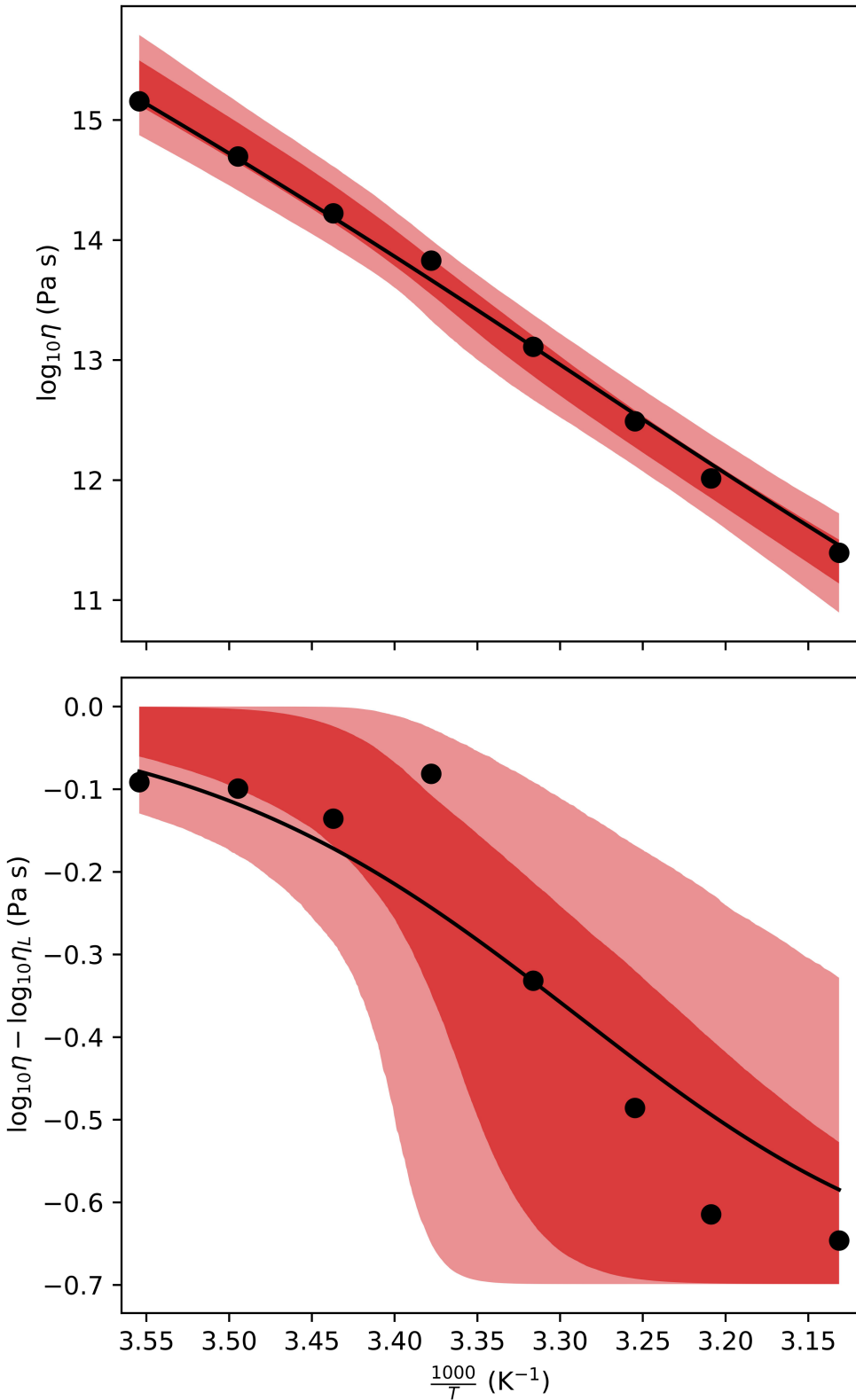


Figure 6.11: Fit of scaled hyperbolic tangent pre-melting parameterisation to viscosity data (solid line=MAP; pale shaded region=central 99% credible interval; dark shaded region= 1σ (68%) credible interval). Pre-melting effect $\log_{10}A_\eta$ shown in lower panel by removing the linear portion of the trend, $\log_{10}\eta_L \equiv \log_{10}e(a_0 + a_1\frac{1}{T})$, from the viscosity. N.B. that data shown in lower panel is based on $\log_{10}\eta_L$ derived from the MAP values of a_0 and a_1 , and is therefore not entirely free from modelling assumptions.

compared to Yamauchi and Takei (2016). The MAP model falls into the latter category. Fits between the inverted pre-melting models and the anelasticity data are shown in Figure 6.10. A high level of agreement is observed across a wide range of frequencies and temperatures, which is corroborated by a root-mean-square (RMS) misfit analysis. The RMS between measured and predicted values of the normalised modulus, for the MAP model, is given by

$$E(|M'|) = \sqrt{\frac{1}{N_{|M'|}} \sum_{i=1}^{i=N_{|M'|}} (d(|M'|)_i - \hat{d}(|M'|)_i)^2}, \quad (6.71)$$

where $N_{|M'|}$ is the number of anelasticity testing data points, $d(|M'|)$ is the normalised modulus data, and $\hat{d}(|M'|)$ the corresponding model prediction. In the case of Yamauchi and Takei (2016), $E(|M'|) = 0.0139$. For the optimised pre-melting parameterisation based on scaled hyperbolic tangent functions, $E(|M'|) = 0.0135$, which corresponds to a 3% improvement in fit. To compute RMS values for attenuation, the following measure is used

$$E(Q^{-1}) = \sqrt{\frac{1}{N_{Q^{-1}}} \sum_{i=1}^{i=N_{Q^{-1}}} (d(\log_{10} Q^{-1})_i - \hat{d}(\log_{10} Q^{-1})_i)^2}, \quad (6.72)$$

where $\log_{10} Q^{-1}$ is used to better account for attenuation variations which span multiple orders of magnitude. For the original parameterisation of Yamauchi and Takei (2016), $E(Q^{-1}) = 0.0796$. For the optimised parameterisation, $E(Q^{-1}) = 0.0570$, which corresponds to a 28% improvement in fit. Therefore, not only does the revised parameterisation offer improvements in terms of computational efficiency, crucial for implementation in numerical models of Earth deformation, but it is also arguably more faithful to the underlying experimental data.

Finally, the fit of the optimised pre-melting parameterisation to the creep test data is shown in Figure 6.11. For this data set, RMS values are calculated according to

$$E(\eta) = \sqrt{\frac{1}{N_\eta} \sum_{i=1}^{i=N_\eta} (d(\log_{10} \eta)_i - \hat{d}(\log_{10} \eta)_i)^2}. \quad (6.73)$$

For the original parameterisation of Yamauchi and Takei (2016), $E(\eta) = 0.0675$, and for the optimised parameterisation, $E(\eta) = 0.0789$. Therefore, in this case, it appears as if the original parameterisation performs 14% better. However, note that the $\eta(T)$ data set is limited to eight data points, which makes $E(\eta)$ highly sensitive to potential outliers. The data point for which

$$\frac{1000}{T} = 3.38 \quad (6.74)$$

and

$$\log_{10}\eta = 13.8 \quad (6.75)$$

appears anomalously high in Figure 6.11, particularly when viewing the non-linear component of the viscosity-temperature trend, which may indicate some kind of error arose during measurement. If this data point is removed from the analysis, the viscosity RMS is revised to $E(\eta) = 0.0721$ for Yamauchi and Takei (2016), and $E(\eta) = 0.0580$ for the optimised parameterisation, such that the latter performs 20% better than the former.

6.3.2 Influence of Optimised Pre-Melting Parameterisation on Predictions of Antarctic Mantle Structure

By altering the functional form of the pre-melting parameterisations A_P , σ_P and A_η , the form of the complex compliance $J^* = J_1 + iJ_2$ and therefore the relationship between seismic observables (V_S , Q^{-1}) and thermodynamic parameters (T , η) is altered as well. For example, at a fixed temperature, increasing A_P or σ_P directly increases the storage modulus and therefore reduces V_S , meanwhile decreasing A_η indirectly has the same effect by shifting the normalised frequency towards a lower value (Figure 6.12). Mathematically, this can be seen by noting that

$$A_\eta \propto \eta \propto \tau_M \propto \omega', \quad (6.76)$$

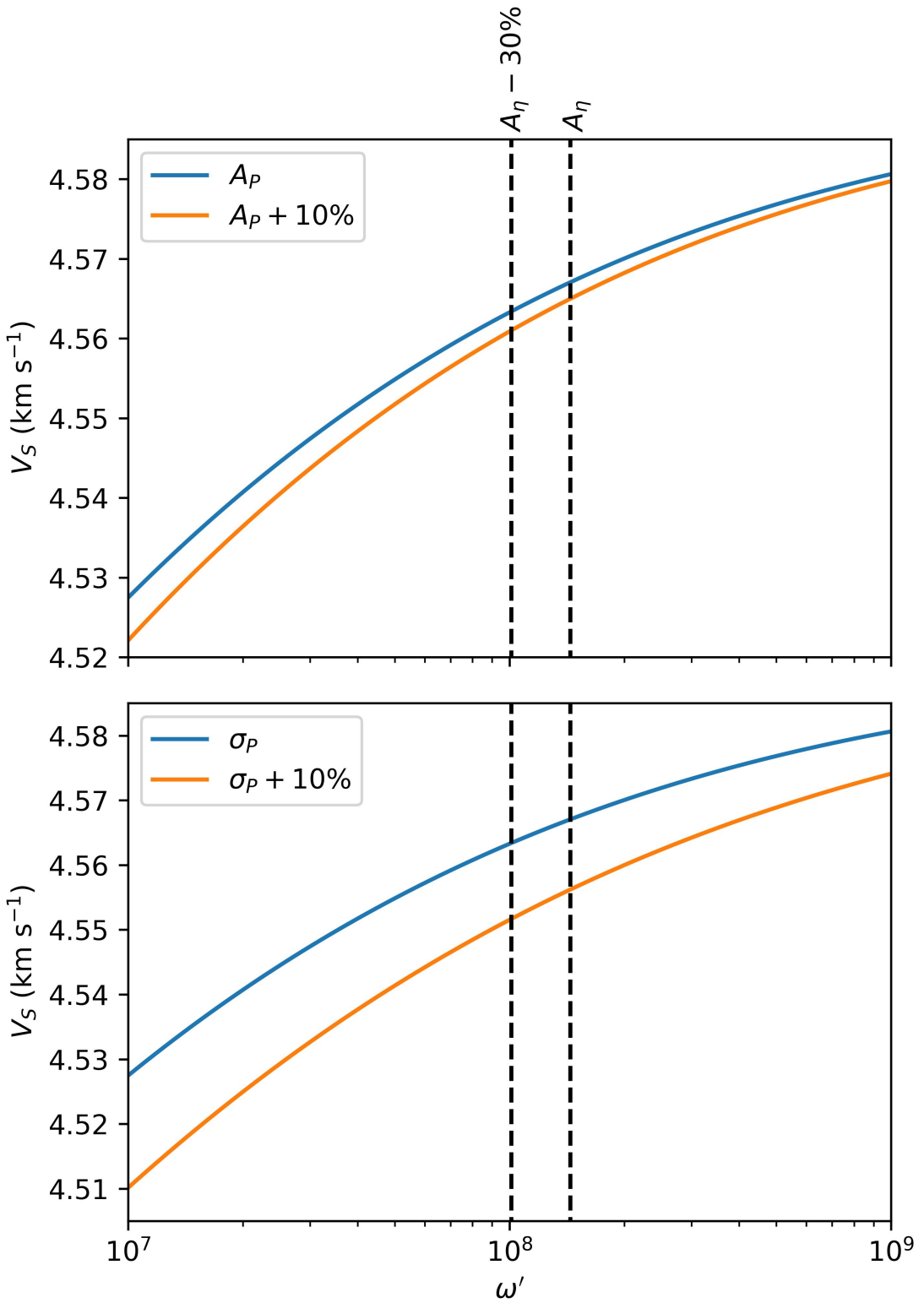


Figure 6.12: Visualising the influence of pre-melting parameter values on $V_S(\omega')$ at fixed temperature. Upper panel shows the effect of increasing A_P by 10%, lower panel shows the effect of increasing σ_P by 10%. Dashed lines show the effect of decreasing A_η by 30% on the normalised angular frequency associated with seismic waves.

and

$$\frac{\partial V_S}{\partial \omega'} > 0, \quad (6.77)$$

such that

$$V_S \propto A_\eta. \quad (6.78)$$

Given that modifying the pre-melting parameterisation causes an alteration to the $V_S(T)$ relationship, it is important to explore the implications on predictions of Antarctic thermomechanical structure. Therefore, the Bayesian inverse calibration procedure introduced and applied in Chapters 2 and 3, was reapplied using the same geophysical data as before, but using the new MAP forms for A_P , σ_P and A_η . The resulting collection of posterior samples exhibits a very similar covariance structure to that observed using the original parameterisation of Yamauchi and Takei (2016), as can be seen by the shape of the parameter trade-offs in Figure 6.13. Likewise, a similarly good fit to the underlying geophysical data is observed (Figure 6.14), although the effect of anelasticity on the oceanic lithosphere $V_S(T)$ relationship appears enhanced for the adapted parameterisation, as compared to Yamauchi and Takei (2016). Referring back to Figure 6.12, this could be caused by the fact that σ_P is higher, and A_η is lower, for the modified parameterisation as compared to their Yamauchi and Takei (2016) counterparts over a wide range of temperatures less than $\Theta \sim 0.97$. As a consequence of the enhanced anelastic behaviour, a low wave-speed anomaly of given amplitude is associated with a lower temperature. To visualise the impact of this effect on predictions of temperature at each depth slice, the difference between potential temperature predictions from the original and modified parameterisation (referred to as YT16 and YT16m in equations, respectively) for a collection of posterior models was calculated according to

$$\Delta T_i(r, \theta, \varphi) = T_{\text{YT16m}}^i - T_{\text{YT16}}^i, \quad (6.79)$$

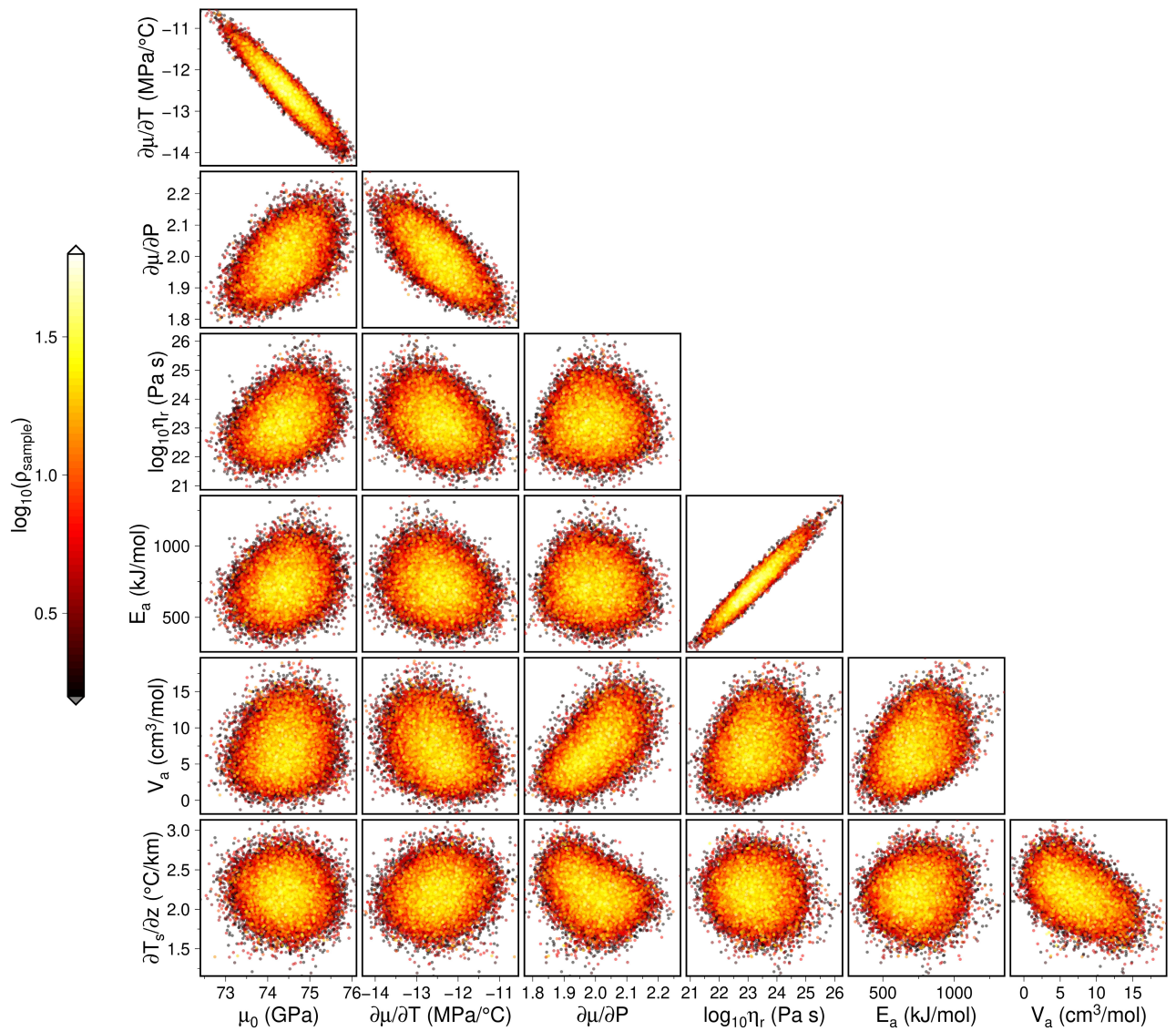


Figure 6.13: Covariance between posterior distributions of viscoelasticity parameters for the modified pre-melting parameterisation.

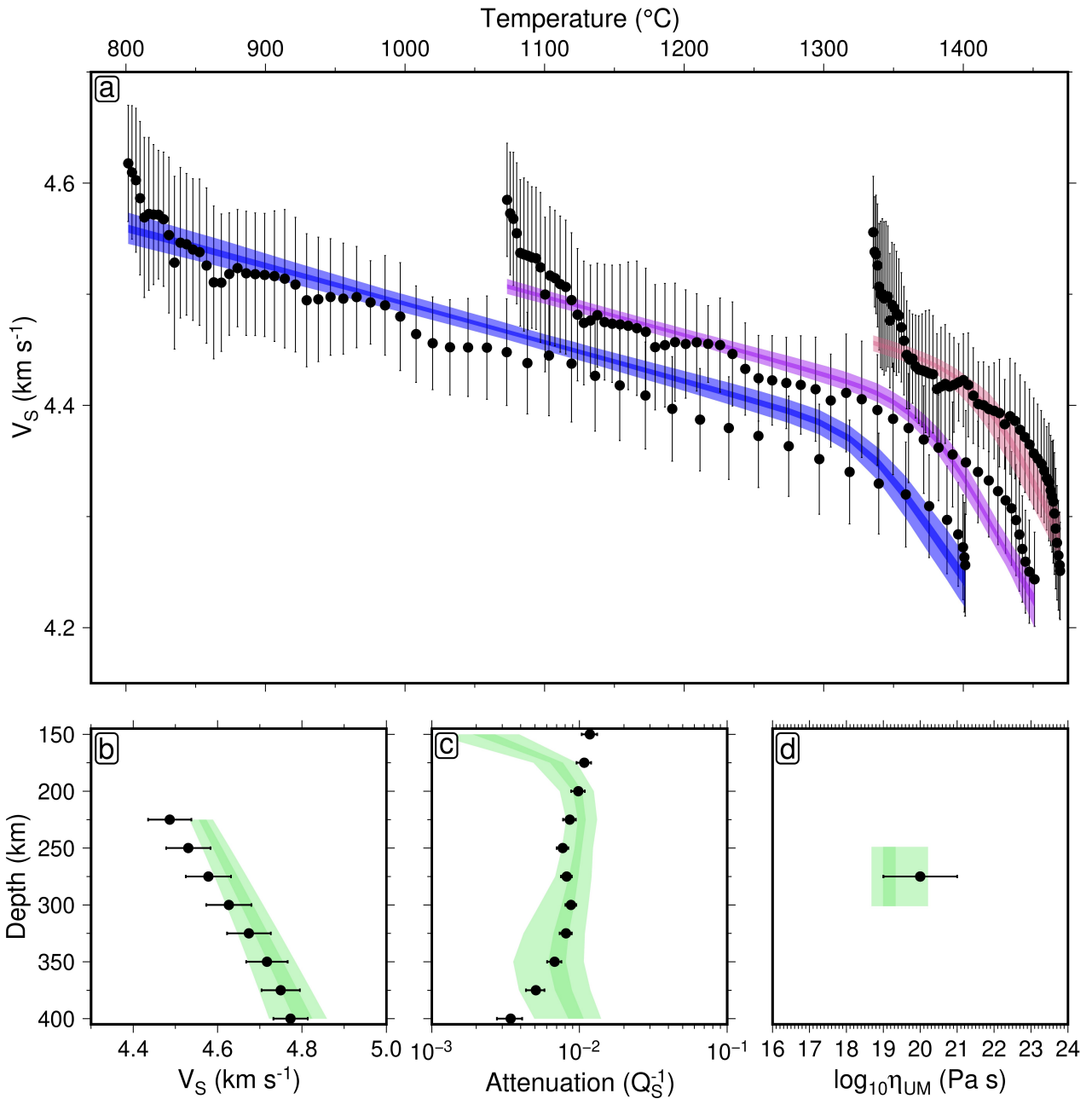


Figure 6.14: Assessing fit of inverted viscoelasticity parameters for the modified pre-melting parameterisation. Fit of post burn-in models to the four geophysical data sets used to constrain the inversion procedure (circles/error bars; see Chapter 2). Pale shaded regions represent the 99% credible interval, and dark shaded regions represent the 50% credible interval. (a) Plate cooling model fit for depth ranges 50–75 km (blue), 75–100 km (purple), and 100–125 km (red). (b) Adiabatic model fit for depth range 225–400 km. (c) QRFSI12 seismic attenuation model fit at depths 150–400 km beneath ocean floor for ages ≥ 100 Ma. (d) Average viscosity between 225 and 400 km compared to $\eta = 10^{20} \pm 1$ Pa s estimate.

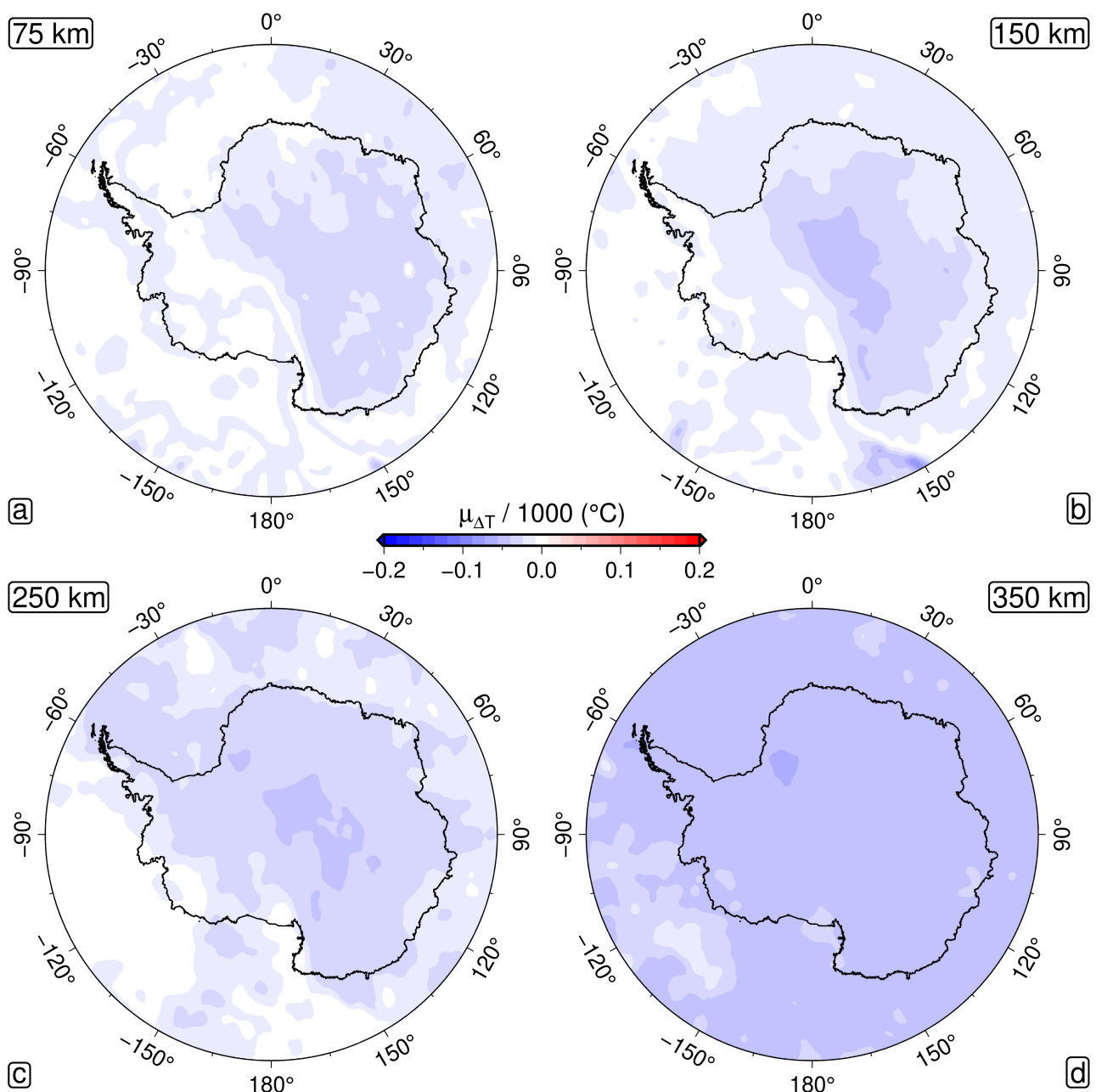


Figure 6.15: Mean potential temperature difference between original and modified pre-melting parameterisation, $\mu_{\Delta T} = T_{\text{YT16m}}^i - T_{\text{YT16}}^i$.

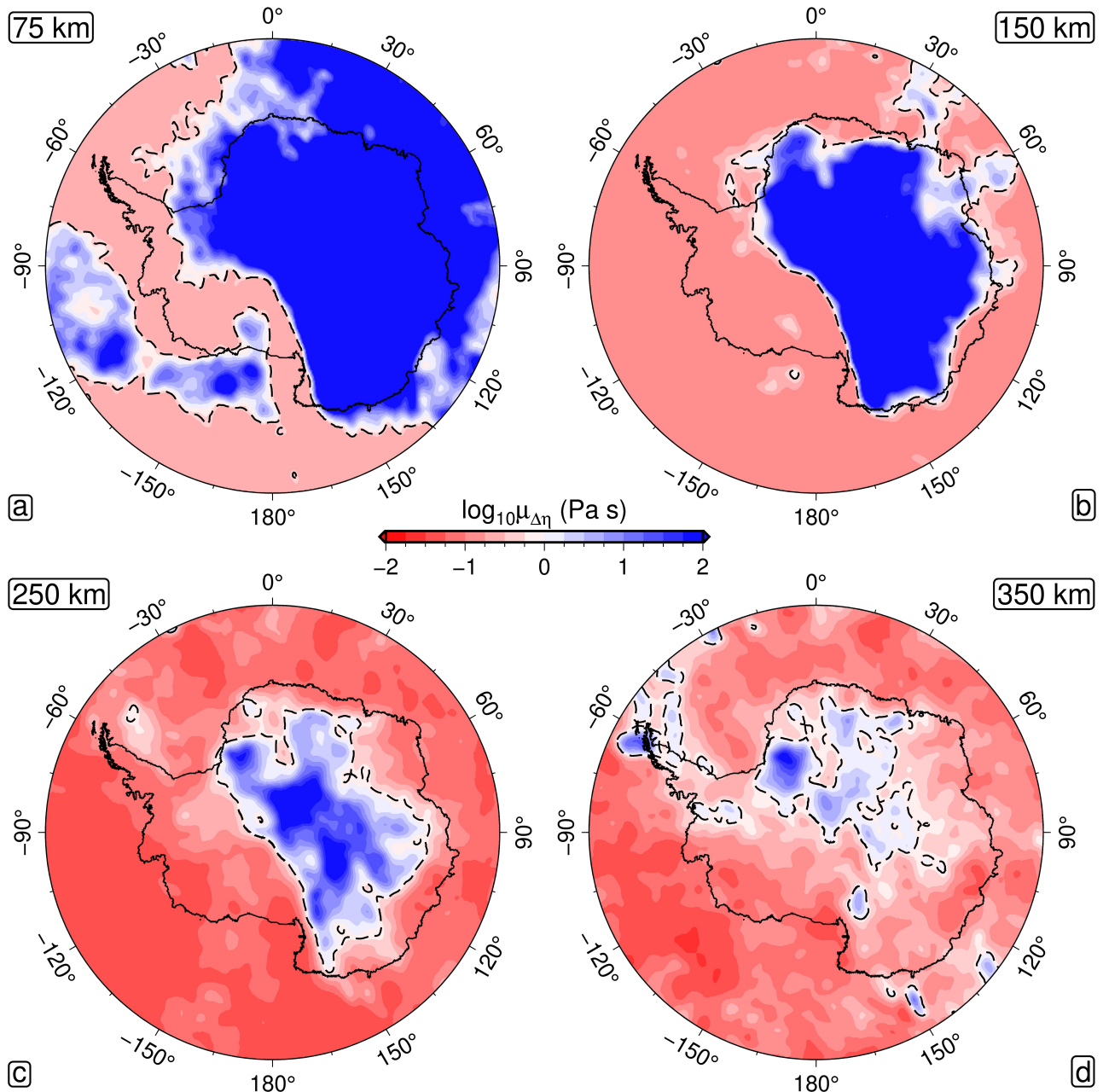


Figure 6.16: Mean viscosity difference between original and modified pre-melting parameterisation, $\mu_\eta = \eta_{\text{YT16m}}^i - \eta_{\text{YT16}}^i$. Dashed line demarcates regions for which $\eta \geq 10^{22.5}$ Pa s, where $\eta = \eta_{\text{YT16m}}$.

where i refers to a particular model selected from the posterior distribution. The mean value

$$\mu_{\Delta T} = \sum_i \Delta T_i \quad (6.80)$$

corresponds to the expected difference in potential temperature between the two models, shown in Figure 6.15. The modified pre-melting parameterisation predicts temperatures on average 3.7°C, 1.5°C, 4.7°C and 27.3°C cooler than its Yamauchi and Takei (2016) counterpart, for the depth slices 75 km, 150 km, 250 km and 350 km respectively. Such temperature differentials are relatively insignificant in comparison to variations due to uncertainty in the viscoelasticity parameters, which are typically 10 °C to 50 °C, and increasing with depth. On the other hand, viscosity estimates are more heavily impacted, as shown in Figure 6.16. Despite the presence of cooler temperatures, viscosity values outside of the lithosphere are up to 1.5 orders of magnitude lower. A contribution towards this differential arises from the fact that A_η of the modified parameterisation is lower than that of Yamauchi and Takei (2016) when $\Theta \leq 0.98$. However, the ratio

$$\frac{A_\eta^{\text{YT16m}}}{A_\eta^{\text{YT16}}} \quad (6.81)$$

only reaches its minimum, 0.55 when $\Theta = 0.94$, which would only cause a viscosity reduction of 0.26 orders of magnitude. Therefore, the dominant contribution is from the shift in inverted viscoelasticity parameters. In particular, an increase in the average value of E_A from 542 kJ mol⁻¹ to 727 kJ mol⁻¹, and V_A from 5.35 cm³ mol⁻¹ to 7.11 cm³ mol⁻¹.

6.3.3 Co-Inverting For Pre-Melting and Viscoelasticity Parameters With Experimental and Geophysical Data

In the previous section, it was shown that modifying the pre-melting parameterisation of Yamauchi and Takei (2016) has a noticeable impact on predictions of Antarctic mantle structure,

even if the corresponding viscoelasticity parameters are re-calibrated. In particular, predictions of upper mantle viscosity can be significantly impacted. However, only the MAP pre-melting parameters defining the modified $A_P(\Theta)$, $\sigma_P(\Theta)$ and $A_\eta(\Theta)$ relationships were considered, whereas a considerable range of possible relationships were obtained upon fitting the experimental data (Figure 6.9). In order to robustly account for the effect of uncertainty in the complex compliance on conversions between V_S and thermodynamic variables, uncertainty in both the pre-melting and viscoelasticity parameters must be considered. In addition, since both classes of parameters affect inferences of thermodynamic variables, there is likely to be trade-off between parameters coming from each class. This warrants an analysis in which the pre-melting and viscoelasticity parameters are co-inverted. Therefore, the Bayesian framework used previously to invert separately for viscoelasticity parameters using geophysical data, and for pre-melting parameters using experimental data, was adapted into a unified method to invert for both sets of parameters using both types of data. This adaptation is simple to implement, following the steps described below.

The model space is extended to include all seven viscoelasticity parameters, as well as all eight pre-melting parameters, i.e.

$$m = \left[\mu_0, \frac{\partial \mu}{\partial T}, \frac{\partial \mu}{\partial T}, \eta_r, E_A, V_A, \frac{\partial T_S}{\partial z}, k, \Theta_0, y_{\min}(A_P), y_{\max}(A_P), y_{\min}(\sigma_P), y_{\max}(\sigma_P), a_0, a_1 \right]^T. \quad (6.82)$$

The prior density is calculated by multiplying the prior density on each individual parameter, where the viscoelasticity priors follow Gaussian distributions, and the pre-melting priors follow uniform distributions. A summary of the prior assumption used for each parameter is given in Table 6.2. As before, the overall likelihood is constructed by multiplying the likelihood on each data set. In order to appropriately assign hyperparameters to each experimental data point, the anelasticity data pertaining to $J^*(\omega', \Theta)$ are separated out by homologous temperature,

Function	Parameter	Prior	Posterior μ_i	Posterior s_i	MAP
$M_U(T, P)$	μ_0 (GPa)	$\mathcal{N} \sim (81, 8)$	74.6	0.4	74.8
	$\partial\mu/\partial T$ (GPa K $^{-1}$)	$\mathcal{N} \sim (-0.014, 0.003)$	-0.0127	0.0005	-0.0132
	$\partial\mu/\partial P$ (unitless)	$\mathcal{N} \sim (1.6, 0.2)$	2.04	0.07	2.14
$\eta(T, P)$	$\log_{10} \eta_r$ (Pas)	$\mathcal{N} \sim (22, 3)$	22.5	0.3	22.7
	E_A (kJ mol $^{-1}$)	$\mathcal{N} \sim (400, 200)$	528	56	581
	V_A (cm 3 mol $^{-1}$)	$\mathcal{N} \sim (6, 4)$	7.00	2.04	9.56
$T_S(z)$	$\partial T_S/\partial z$ (K km $^{-1}$)	$\mathcal{N} \sim (2.25, 2.25)$	2.11	0.17	2.14
A_P, σ_P and A_η	k	$\mathcal{U} \sim (5, 200)$	29.1	4.1	31.7
	Θ_0	$\mathcal{U} \sim (0.9, 1.0)$	0.939	0.003	0.939
A_P	y_{\min}	$\mathcal{U} \sim (0, 0.02)$	0.00903	0.00095	0.00946
	y_{\max}	$\mathcal{U} \sim (0.02, 0.04)$	0.0328	0.0019	0.0323
σ_P	y_{\min}	$\mathcal{U} \sim (3.0, 5.0)$	4.30	0.09	4.33
	y_{\max}	$\mathcal{U} \sim (6.0, 8.0)$	6.20	0.18	6.12
$\ln \eta$	a_0	$\mathcal{U} \sim (-46.1, -23.0)$	-26.5	1.9	-26.1
	$\frac{a_1}{1000}$	$\mathcal{U} \sim (11.5, 23.0)$	17.3	0.6	17.2

Table 6.2: Prior and posterior estimates of the viscoelasticity and pre-melting parameters as constrained via joint inversion. For each parameter, a prior distribution is specified, as well as the mean and standard deviation posterior estimate (μ_i and s_i), and the *maximum a posteriori* estimate.

with a hyperparameter assigned to each set of measurements at given Θ . This decision is taken to reflect the fact that the experimental data were collected by heating a sample of borneol to a given target temperature, before measuring the strain response to an applied oscillatory stress over a spectrum of frequencies. Therefore, the data are inherently grouped by Θ , and it is reasonable to assume that a different average uncertainty may apply to each group. For each set of anelasticity data associated with a given Θ , referred to as $d_{\text{an}, \Theta}$, the components of $J'^*(\omega')$ are expressed in terms of a normalised shear modulus

$$|M'|(\omega') = \frac{1}{\sqrt{J_1'^2 + J_2'^2}}, \quad (6.83)$$

and attenuation

$$Q^{-1}(\omega') = \frac{J_2'}{J_1'}, \quad (6.84)$$

where

$$J'^* = \frac{1}{|M'|} e^{i \tan^{-1}(Q^{-1})}. \quad (6.85)$$

Then, the likelihood function for each Θ is calculated using the expression

$$\log_{10} p(d_{\text{an},\Theta} | \mathcal{X}) = \frac{\log_{10} p(|M'|_\Theta | \mathcal{X}) + \log_{10} p(Q_\Theta^{-1} | \mathcal{X})}{2}, \quad (6.86)$$

where Θ is used as an index to refer to data points collected at this particular homologous temperature, normalised modulus likelihoods $p(|M'|_\Theta | \mathcal{X})$ are given by

$$p(|M'|_\Theta | \mathcal{X}) = F_{|M'|,\Theta} \exp \left(-\frac{1}{2} \left(|M'|_\Theta - |\hat{M}'|_\Theta \right)^T \Sigma_{|M'|,\Theta}^{-1} \left(|M'|_\Theta - |\hat{M}'|_\Theta \right) \right), \quad (6.87)$$

where the prefactor

$$F_{|M'|,\Theta} \equiv \frac{1}{(2\pi \Sigma_{|M'|,\Theta})^{N_\Theta/2} |\Sigma_{|M'|,\Theta}|^{1/2}}, \quad (6.88)$$

and attenuation likelihoods $p(Q_\Theta^{-1} | \mathcal{X})$ are given by

$$p(Q_\Theta^{-1} | \mathcal{X}) = F_{Q^{-1},\Theta} \exp \left(-\frac{1}{2} \left(Q_\Theta^{-1} - \hat{Q}_\Theta^{-1} \right)^T \Sigma_{Q^{-1},\Theta}^{-1} \left(Q_\Theta^{-1} - \hat{Q}_\Theta^{-1} \right) \right), \quad (6.89)$$

where

$$F_{Q^{-1},\Theta} \equiv \frac{1}{(2\pi \sigma_\Theta)^{N_\Theta/2} |\Sigma_{Q^{-1},\Theta}|^{1/2}}, \quad (6.90)$$

such that the hyperparameters σ_Θ are applied to all data points within the data set pertaining to the temperature Θ . In these equations, $\Sigma_{|M'|,\Theta}$ and $\Sigma_{Q^{-1},\Theta}$ refer to the data covariance matrices, containing the uncertainty on each data point. In the absence of experimentally determined measurement uncertainties, a standard percentage error of 10% was applied to all data points, which could be scaled up and down between data sets of different Θ by the hyperparameters. N_Θ refers to the number of data points within $d_{\text{an},\Theta}$ i.e., the number of frequencies sampled at

a given temperature Θ .

A single hyperparameter is applied to the creep test data, reflecting the fact that this data set is one dimensional, depending only on temperature. The likelihood function for the laboratory viscosity data therefore takes the form

$$p(\eta_{\text{lab}} | \mathcal{X}) = F_{\eta_{\text{lab}}} \exp \left(-\frac{1}{2} (\log_{10} \eta_{\text{lab}} - \log_{10} \hat{\eta}_{\text{lab}})^T \Sigma_{\eta_{\text{lab}}}^{-1} (\log_{10} \eta_{\text{lab}} - \log_{10} \hat{\eta}_{\text{lab}}) \right), \quad (6.91)$$

where

$$F_{\eta_{\text{lab}}} \equiv \frac{1}{(2\pi\sigma_{\eta_{\text{lab}}})^{N_{\eta_{\text{lab}}}/2} |\Sigma_{\eta_{\text{lab}}}|^{1/2}} \quad (6.92)$$

The likelihood function for the experimental data is calculated by multiplying together the likelihood of each of the nine individual laboratory data sets (eight homologous temperatures for which anelasticity data were collected, and one creep test data set), such that

$$p(d_{\text{lab}} | \mathcal{X}) = p(\eta_{\text{lab}} | \mathcal{X}) \prod_{\Theta} p(d_{\text{an},\Theta} | \mathcal{X}). \quad (6.93)$$

Finally, the overall likelihood function is found by multiplying together the likelihood functions derived from the geophysical and laboratory data constraints, such that

$$p(\mathcal{D} | \mathcal{X}) = p(d_{\text{geo}} | \mathcal{X}) p(d_{\text{lab}} | \mathcal{X}), \quad (6.94)$$

where $p(d_{\text{geo}} | \mathcal{X})$ is the likelihood function for all four geophysical constraints combined, calculated as described in Chapter 2.

Applying the Bayesian inversion method, including the aforementioned adaptations, leads to a set of posterior outputs which simultaneously provide a good fit to each of the geophysical (Figure 6.17) and experimental (Figure 6.18 and 6.19) data sets. Revisiting the RMS metrics used to assess the fit of a given pre-melting parameterisation to the experimental compliance

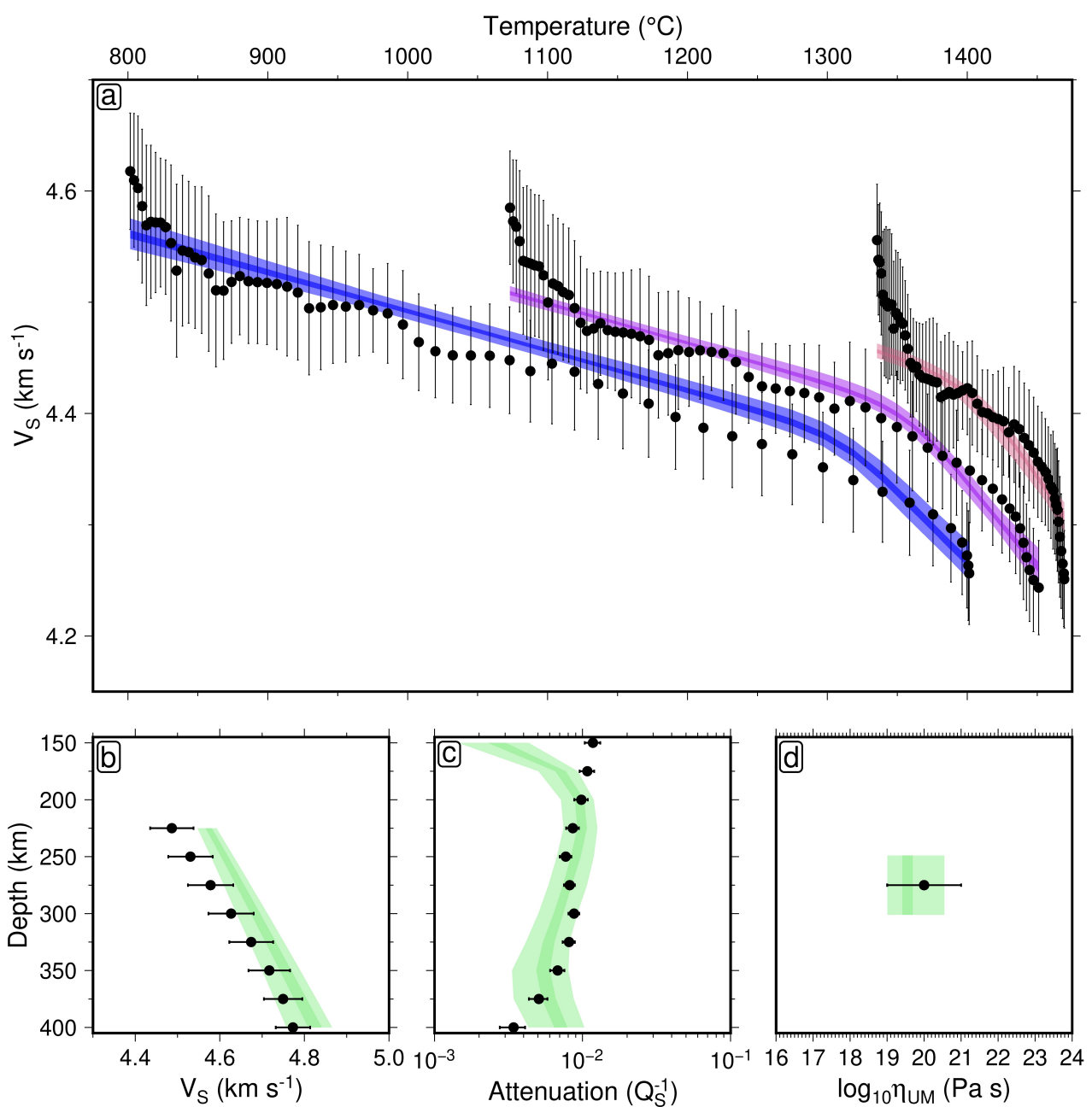


Figure 6.17: Assessing fit of inverted viscoelasticity and pre-melting parameters to geophysical data constraints (circles/error bars; see Chapter 2). Pale shaded regions represent the 99% credible interval, and dark shaded regions represent the 50% credible interval.

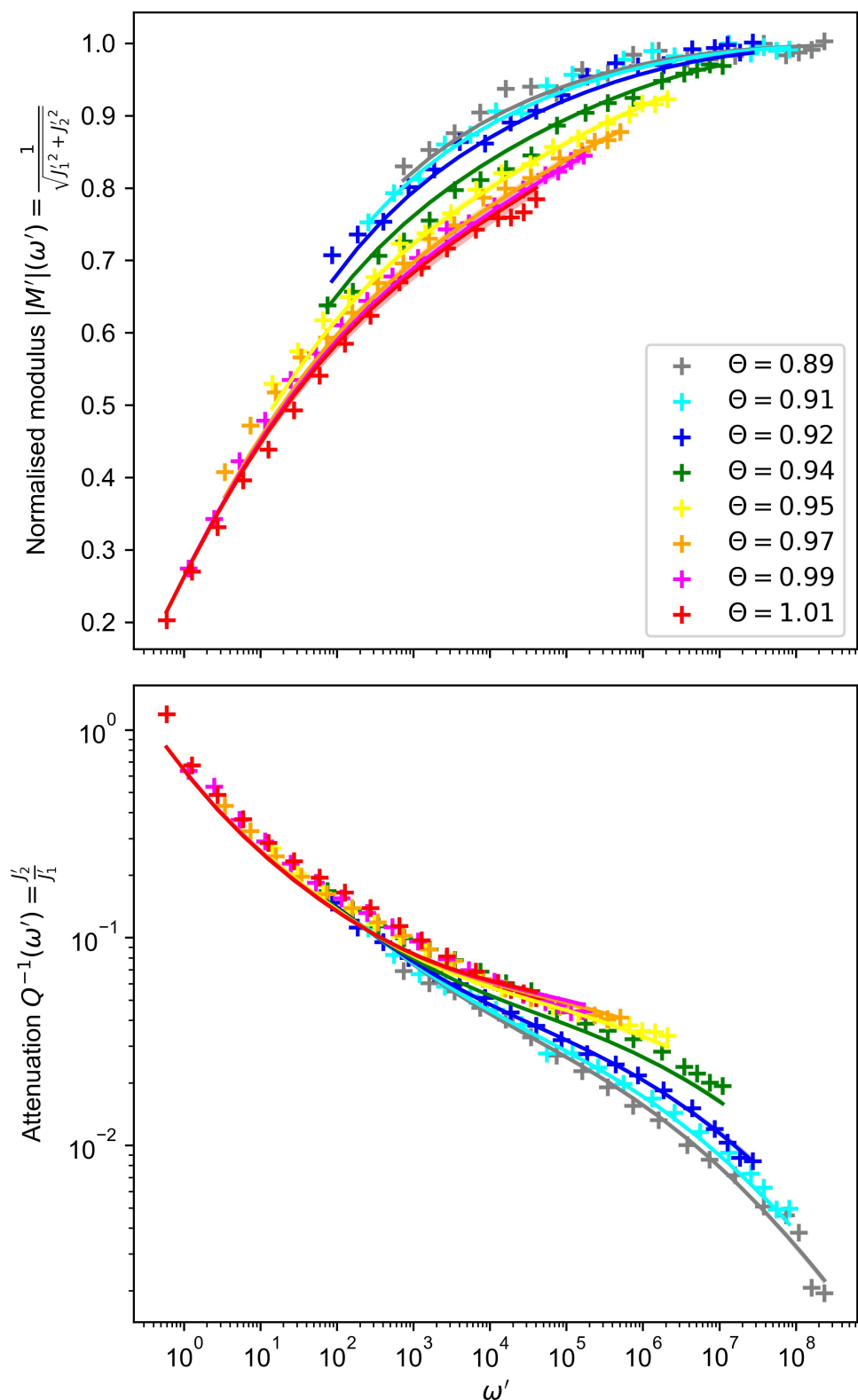


Figure 6.18: Fit of inverted pre-melting parameters constrained via joint inversion approach to anelasticity data (solid line=MAP; shaded region= 1σ (68%) credible interval).

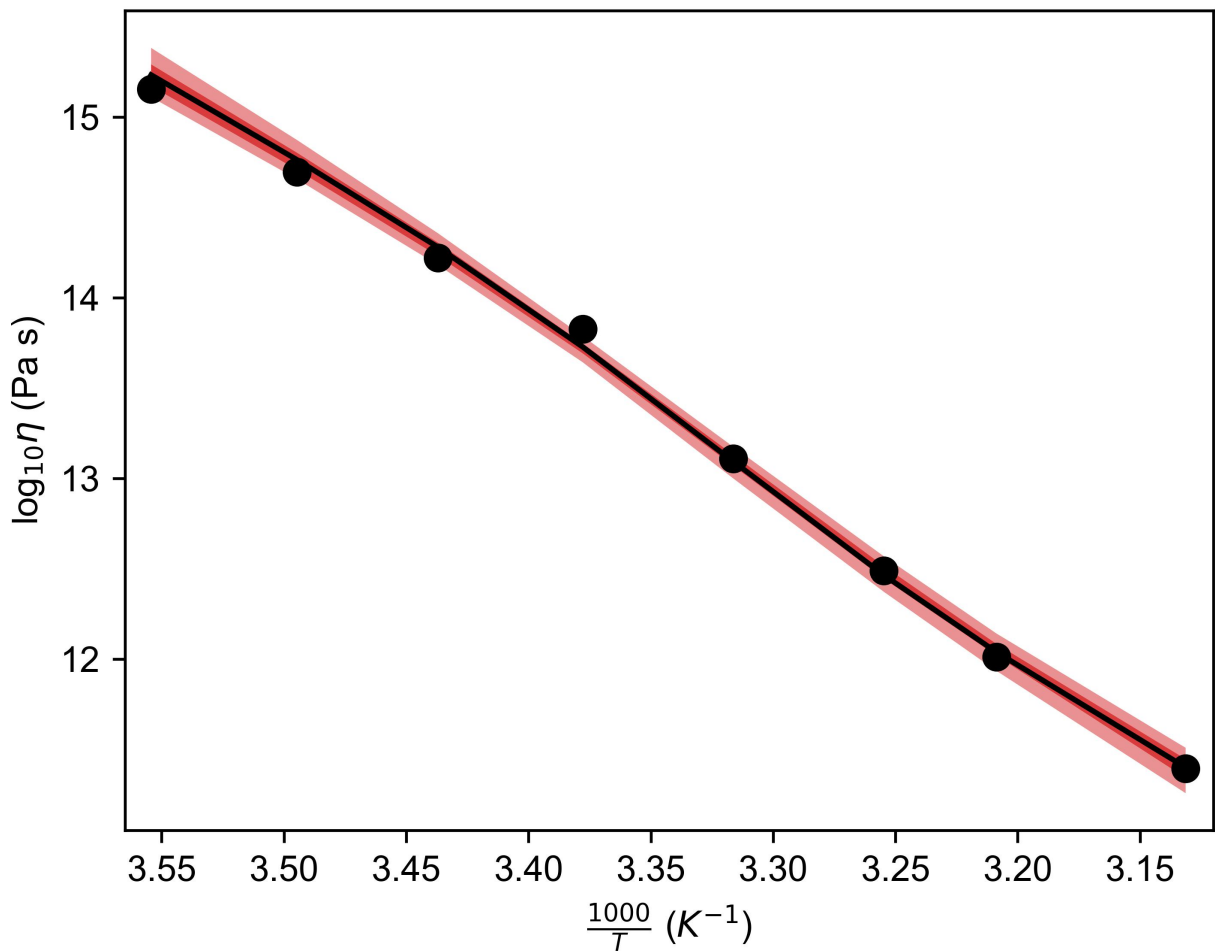


Figure 6.19: Fit of inverted pre-melting parameters constrained via joint inversion approach to laboratory viscosity data (solid line=MAP; pale shaded region=99% credible interval; dark shaded region= 1σ (68%) credible interval).

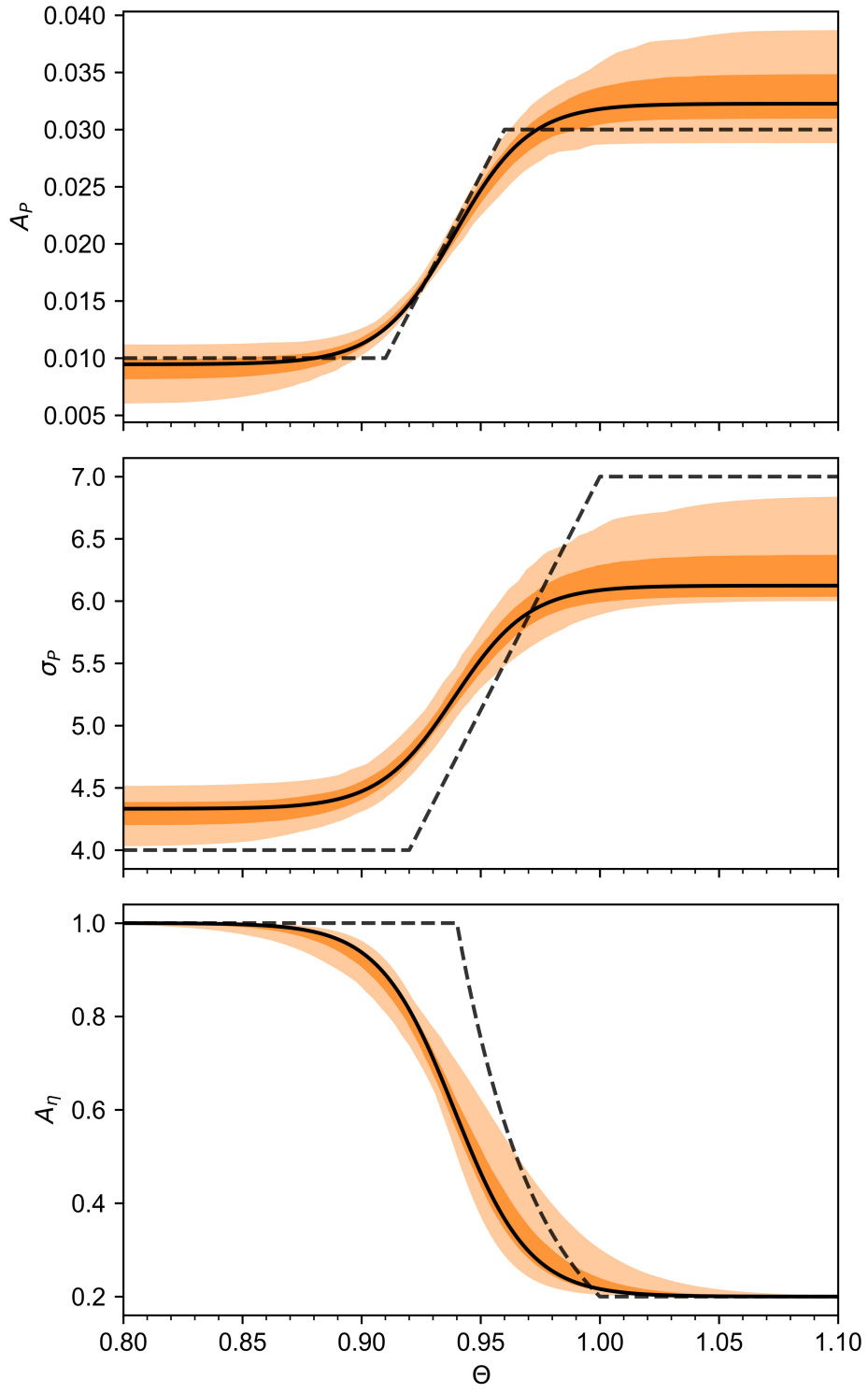


Figure 6.20: Best-fitting pre-melting functions (solid line=MAP; pale shaded region=99% credible interval; dark shaded region= 1σ (68%) credible interval) compared to original functional forms from Yamauchi and Takei (2016, dashed line).

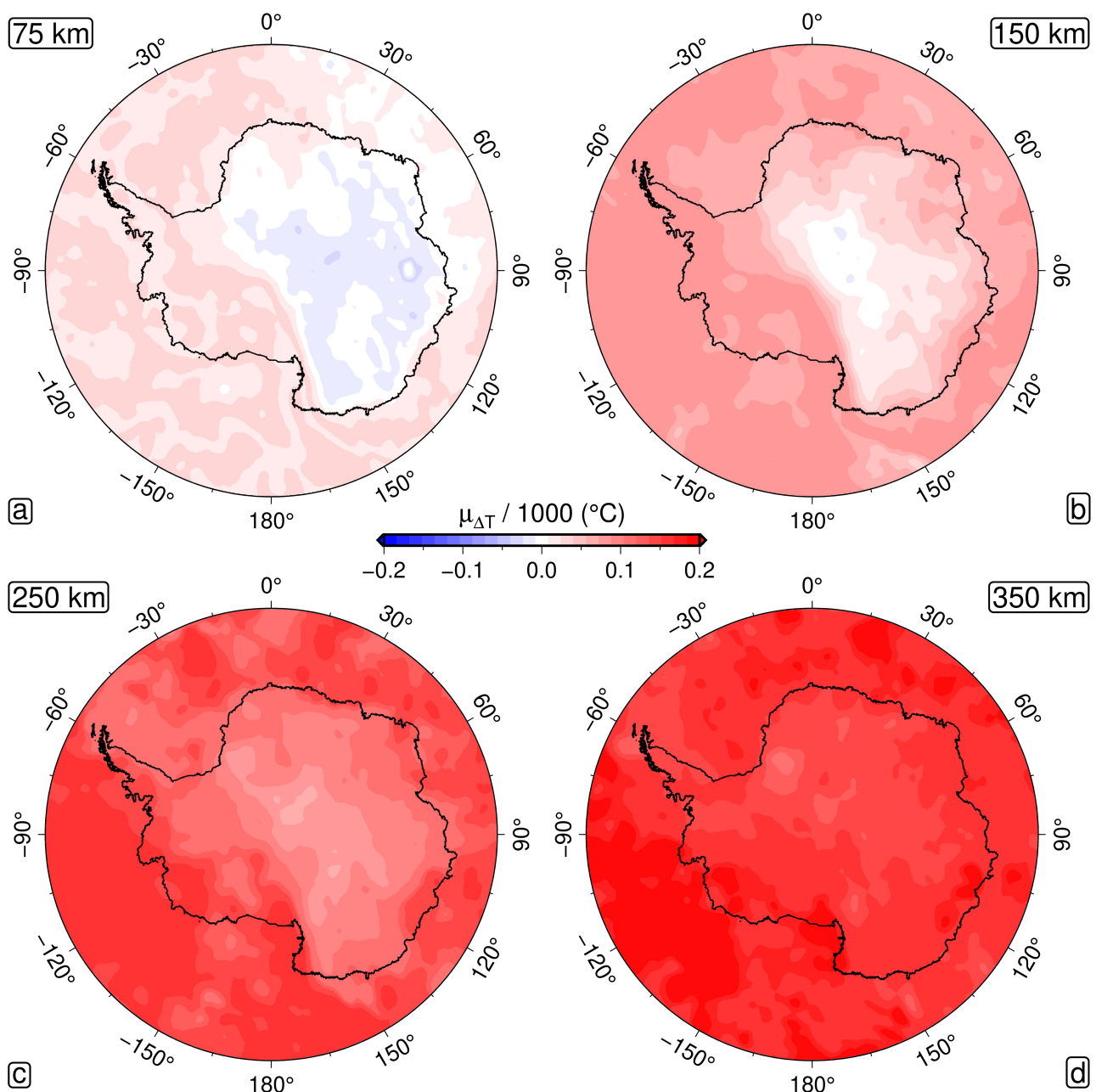


Figure 6.21: Mean potential temperature difference between original and co-inverted pre-melting parameterisation. Format follows Figure 6.15.

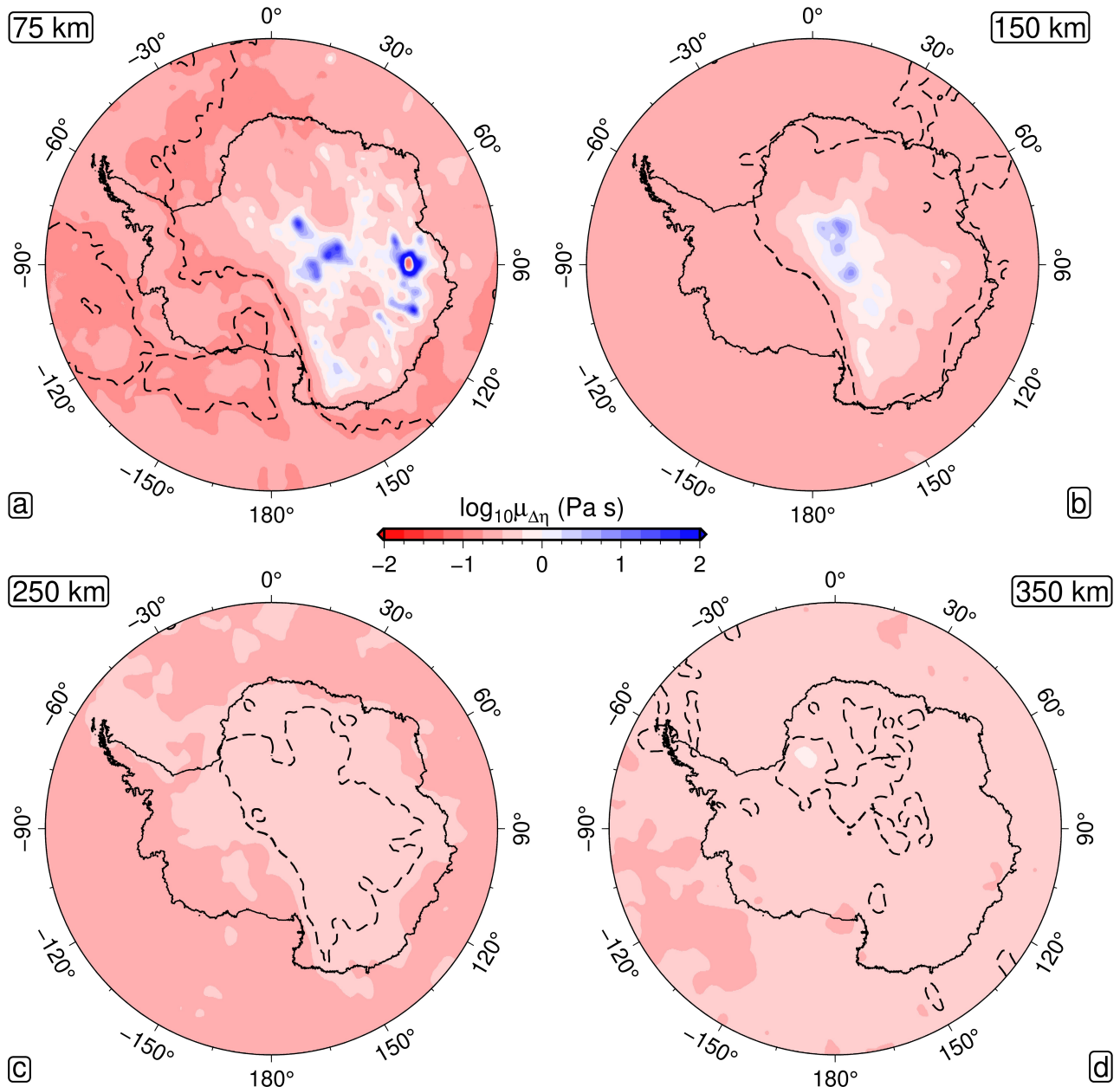


Figure 6.22: Mean viscosity difference between original and co-inverted pre-melting parameterisation. Format follows Figure 6.16

and viscosity data, the following values are obtained: $E(|M'|) = 0.0140$, $E(Q^{-1}) = 0.0520$ and $E(\eta) = 0.0567$. Therefore, the fit to the normalised modulus data is almost identical between the original and adapted parameterisations, whereas $E(Q^{-1})$ and $E(\eta)$ are improved by 35% and 16%, respectively, for the adapted parameterisation relative to that of Yamauchi and Takei (2016). Compared to the previous section in which the pre-melting parameters were inverted separately to the viscoelasticity parameters, a much narrower range of predicted pre-melting functions is predicted (Figure 6.20). This may suggest that the geophysical data provide helpful information regarding the structure of the pre-melting relationship, which can be harnessed to tighten the range of plausible pre-melting functions. Regarding predictions of mantle thermomechanical structure made using the co-inverted viscoelasticity parameterisation, temperature and viscosity results are shown in Figure 6.21 and 6.22, respectively. As for the previous section, temperature and viscosity predictions are shown compared to the original pre-melting parameterisation of Yamauchi and Takei (2016), which was calibrated in Chapter 2. For the co-inverted parameterisation, temperatures are on average hotter than the original parameterisation of Yamauchi and Takei (2016), with the discrepancy increasing with depth: 20 °C at 75 km, 70 °C at 150 km, 130 °C at 250 km, and 160 °C at 350 km. The net effect of the co-inverted parameterisation is to reduce predictions of average mantle viscosity by ~ 0.5 orders of magnitude. The effect on viscosity is relatively uniform with depth, although more muted at 350 km depth (~ 0.3 orders of magnitude). Importantly, the effect on mantle viscosity; the parameter of most interest for simulating GIA, is smaller (in relative terms) than that on predicted temperatures.

Having verified that the optimised viscoelasticity parameterisation provides a high quality fit to the inversion data sets, it is instructive to look at its performance compared to experimental data not used within the inversion framework. In particular, anelasticity data obtained from experiments on polycrystalline olivine (Jackson, 2019; Jackson et al., 2014; Qu et al., 2021).

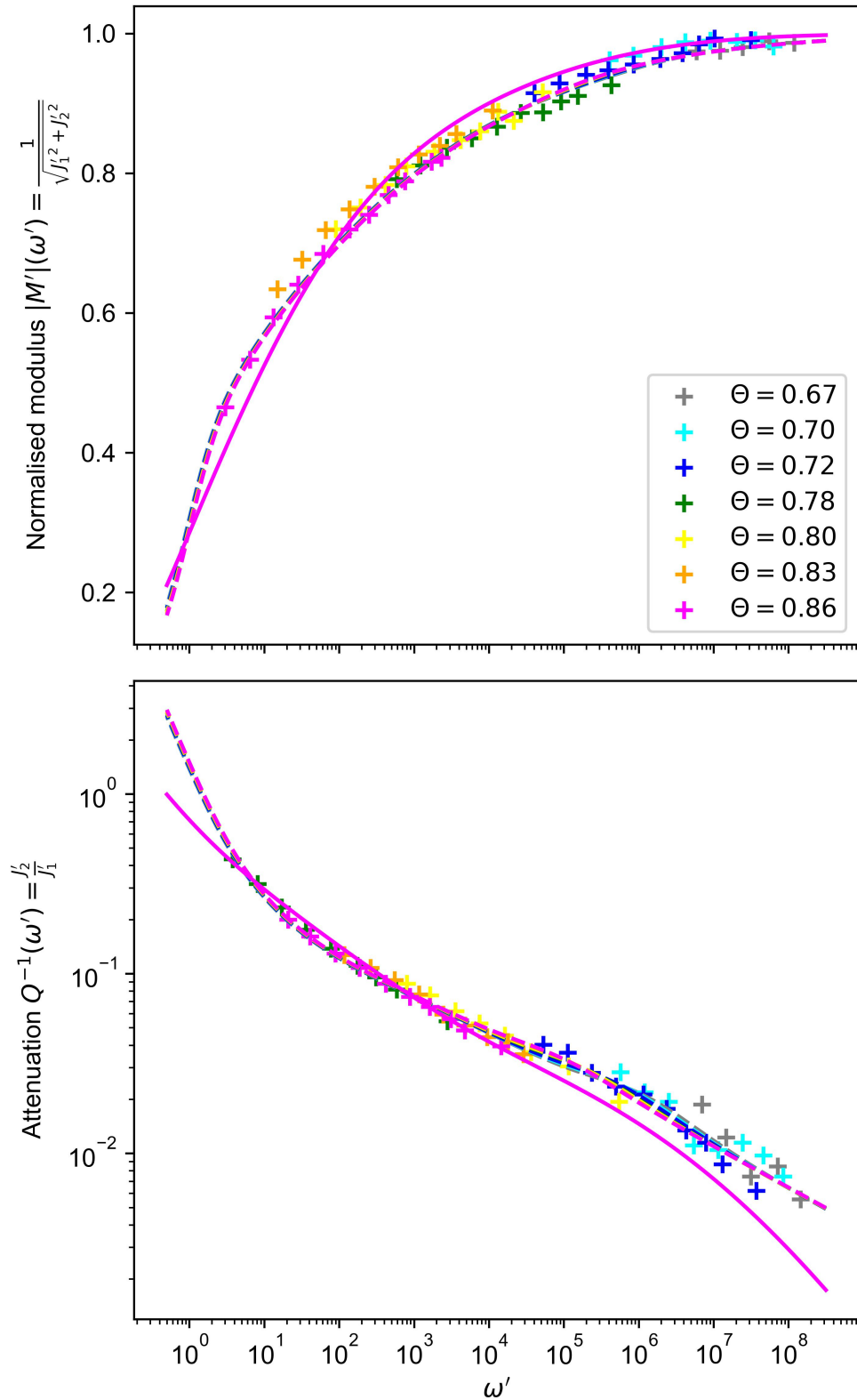


Figure 6.23: Fit of inverted viscoelasticity parameterisation to anelasticity data obtained from experiments on olivine (Jackson, 2019; Jackson et al., 2014; Qu et al., 2021, solid line=MAP, shaded region= 1σ (68%) credible interval). Data retrieved from Priestley et al. (2024), who performed Maxwell frequency normalisation based on best-fitting parameters obtained for Ol₉₅Px₅ in Qu et al. (2021). Due to low homologous temperature of experimental data, pre-melting relationships overlap, meaning only $\Theta = 0.86$ line (pink) can be seen. Extended Burgers model fits (dashed lines) are based on parameters reported for their Ol₉₅Px₅ sample in Table 2 of Qu et al. (2021).

These data have previously been parameterised using an Extended Burgers model (e.g., Jackson, 2019). Analogously to the pre-melting parameterisation of Yamauchi and Takei (2016), the Extended Burgers relaxation function consists of a monotonic background, and a superimposed dissipation peak (Equation 5 of Jackson, 2019). However, while the magnitude and width of the dissipation peak in the pre-melting model is homologous-temperature-dependent, these characteristics are assumed to be invariant with temperature in the Extended Burgers model. This assumption is consistent with the interpretation that, at the microphysical scale, the observed dissipation peak is caused by elastically accommodated grain boundary sliding (EAGBS, Jackson and Faul, 2010). The magnitude of the dissipation peak attributed to EAGBS was originally thought to be large, with a value of $\Delta_P = 0.057 \pm 0.002$ quoted in Jackson and Faul (2010). However, more recent data, collected after improvements to experimental apparatus were made, reduced this amplitude by a factor of over 5; in Qu et al. (2021), $\Delta_P = 0.011$. In the recent study of Qu et al. (2024), the authors concluded that, contrary to their previous conclusions (e.g., Jackson and Faul, 2010), EAGBS cannot account for the sharp drop in V_S across the oceanic LAB observed in several seismological datasets. The lack of temperature dependence in the dissipation peak characteristics of the Extended Burgers model leads to a fundamentally discrepant complex compliance parameterisation, as compared to the pre-melting model. However, the olivine anelasticity data underpinning the Extended Burgers model generally agree well with the co-inverted viscoelasticity parameterisation derived in this section, with the exception of attenuation when $\Theta \leq 0.72$ (Figure 6.23). Calculating the RMS misfit between the olivine data and the MAP co-inverted pre-melting model, it is found that $E(|M'|) = 0.026$, and $E(Q^{-1}) = 0.156$. Since their parameterisation was optimised using this olivine anelasticity data, Qu et al. (2021)'s expressions (see Ol₉₅Px₅ specimen in their Table 2) provide comparably better fit ($E(|M'|) = 0.017$, and $E(Q^{-1}) = 0.051$). However, the olivine data do not cover homologous temperatures high enough to assess the potential im-

pact of pre-melting on these samples. Therefore, while different studies and laboratories may offer discrepant parameterisations of anelasticity, based on different interpretations of microphysical behaviour, it now appears that all experimental data are reasonably consistent with a pre-melting model. On the other hand, the borneol data of Yamauchi and Takei (2016) is not consistent with an Extended Burgers model, since the latter does not incorporate homologous temperature-dependent anelastic behaviour. These observations are a positive sign for the geophysics community, because they imply that phenomenological uncertainty regarding how to describe anelasticity is now much smaller than previously thought. The impact of transient rheology on important geodynamic phenomena like GIA can therefore be more confidently quantified using the approach outlined here.

6.4 Implementing Adapted Pre-Melting Parameterisation in a Numerical Simulation of Glacial Isostatic Adjustment

In Section 6.2, the theoretical groundwork was laid for translating arbitrarily complex parameterisations of viscoelasticity into a form applicable to finite element models of continuum mechanics. It was shown that an experimentally constrained model such as Yamauchi and Takei (2016) can be implemented, combining Prony series with a recursive scaling method to express $M(t)$ as a function of state variables including temperature. Since the recursive scaling method requires computationally efficient access to the complex compliance, an optimised form of Yamauchi and Takei (2016) was developed in Section 6.3, using experimental and geophysical constraints within a joint inversion framework. Ultimately, these steps will enable the use of realistic descriptions of Earth’s mechanical behaviour, grounded in laboratory observations, within finite element GIA models incorporating three-dimensional variations in mantle struc-

ture. To this end, I am one of several collaborators (alongside Bob Myhill, Fred Richards, John Naliboff, Cedric Thieulot and Harriet Lau) working on such an implementation in **ASPECT**, an open-source code used to simulate geodynamic processes. This project is in an early phase of its development, and therefore a finite element implementation of transient rheology is not presented here. Instead, the well-established Love number approach is applied, which uses Green's functions describing the response of Earth's surface and gravity field to an impulse load change. Utilising the adapted form of Yamauchi and Takei (2016) developed earlier in this chapter, combined with the techniques developed to approximate this form with Prony series, transient rheology is incorporated into the Love number theory. The resulting Green's functions are combined with a pseudo-spectral procedure for solving the generalised sea level equation, enabling RSL changes in response to a synthetic deglaciation history to be computed, and compared between Maxwell and transient rheological models. These outputs bring to light how strongly sea level and ice sheet stability are affected by transient rheology.

6.4.1 Love Number Formulation of the GIA Problem

The Love number formulation is a powerful method for computing spatiotemporal patterns of deformation in response to surface loading (Farrell, 1972; Love, 1909; Peltier, 1974; Shida, 1912). In a spherically symmetric domain, the surface displacement response to an impulse load applied as a point-source is given by

$$\mathbf{u}(\psi, t) = \frac{r_E}{m_E} \sum_{\ell=0}^{\infty} \left[h_\ell(t) P_\ell(\cos \psi) \hat{\mathbf{r}} + l_\ell(t) \frac{\partial}{\partial \psi} P_\ell(\cos \psi) \hat{\boldsymbol{\psi}} \right], \quad (6.95)$$

where $\hat{\mathbf{r}}$ is the unit radial displacement vector, and $\hat{\boldsymbol{\psi}}$ the unit angular displacement vector, which points from the loading source at (θ_L, φ_L) to the point of interest (θ, φ) along the great

circle intercepting both locations, such that (Mitrovica et al., 1994)

$$\cos \psi = \cos \theta \cos \theta_L + \sin \theta \sin \theta_L \cos(\varphi - \varphi_L). \quad (6.96)$$

The constants r_E and m_E represent Earth's radius and mass, respectively. The function P_ℓ represents the Legendre polynomial of degree ℓ , which can be expressed as

$$P_\ell(x) = \frac{1}{2^\ell \ell!} \frac{d^\ell}{dx^\ell} (x^2 - 1)^\ell. \quad (6.97)$$

The radial and angular displacement coefficients at each degree are the time-dependent Love and Shida numbers, $h_\ell(t)$ and $l_\ell(t)$, respectively. An analogous set of Love numbers, $k_\ell(t)$ determine how Earth's gravitational field, \mathbf{g} , is perturbed by impulse surface load changes according to the expression

$$\mathbf{g}(\psi, t) = \frac{g}{m_E} \sum_{\ell=0}^{\infty} [\ell \delta(t) + 2h_\ell(t) - (\ell + 1)k_\ell(t)P_\ell(\cos \psi)]. \quad (6.98)$$

Note that a further expression, involving both $h_\ell(t)$ and $k_\ell(t)$, must be used to calculate the perturbation to Earth's axial tilt introduced by GIA (Peltier, 1974). Taken together, the Love and Shida numbers encode Earth's rheology and determine a set of Green's functions which, when combined with a surface loading history $\boldsymbol{\sigma}_L(\mathbf{r}, t)$, can be used to predict how Earth's surface and external gravity field change shape over time.

Each of $h_\ell(t)$, $l_\ell(t)$ and $k_\ell(t)$ can be split into instantaneous and time-dependent components, e.g. in the case of h_ℓ this looks like

$$h_\ell(t) = h_\ell^E \delta(t) + h_\ell^V(t), \quad (6.99)$$

where h_ℓ^E derives from the elastic component of the response, and $h_\ell^V(t)$ derives from the non-

elastic component of the response (Peltier, 1974). The instantaneous components h_ℓ^E , l_ℓ^E and k_ℓ^E are the solutions on a purely elastic Earth, for which analytical solutions are available. If Maxwell viscoelasticity is assumed, and Earth's density and viscosity structure is totally uniform, the time-dependent components $h_\ell^V(t)$, $l_\ell^V(t)$ and $k_\ell^V(t)$ would exhibit the general form

$$p(t) = p \exp(-st), \quad (6.100)$$

i.e. pure exponential decay, where $s = \frac{2\pi}{\tau_M}$ (Peltier, 1974). The Love and Shida numbers decay asymptotically to zero as $t \rightarrow \infty$, due to the establishment of isostatic equilibrium. The presence of only a single relaxation frequency s is consistent with the lack of radial stratification, which would introduce additional relaxation modes and corresponding harmonic overtones (Peltier, 1976). If the assumption of radial uniformity is now relaxed, as is necessary to find a realistic solution to the GIA problem, the Love and Shida numbers can still be expressed exactly, using a discrete series of exponential decay functions of general form

$$p(t) = \sum_i p_i \exp(-s_i t). \quad (6.101)$$

The characteristic relaxation frequencies s_i and their associated weights p_i represent the set of eigenvalue and eigenfunction solutions of the viscoelastic Earth model (Peltier, 1976). In other words, s_i and p_i represent a set of normal modes via which Earth accommodates deformation. The modes are found by solving the governing equations of the GIA system in the Laplace transform domain (Peltier, 1974). The governing equations comprise Poisson's equation (Farrell, 1972)

$$\nabla^2 \tilde{\phi}(s) = -4\pi G \nabla \cdot \rho \tilde{\mathbf{u}}(s) \quad (6.102)$$

incorporating gravity, and a set of linearised Stokes equations

$$\nabla \cdot \tilde{\boldsymbol{\sigma}}(s) - \nabla \rho g \tilde{\mathbf{u}}(s) \cdot \hat{\mathbf{r}} - \rho \nabla \tilde{\phi}(s) + g \nabla (\rho \tilde{\mathbf{u}}(s)) \hat{\mathbf{r}} = \mathbf{0}, \quad (6.103)$$

incorporating conservation of momentum. In these equations, $\tilde{\phi}$ and $\tilde{\mathbf{u}}$ are perturbations to Earth's gravitational potential and outer surface, respectively. The Laplace transform variable s represents a complex frequency, $s = \gamma + i\omega$. The symbol $G = 6.674 \times 10^{-11} \text{ N m}^2 \text{ kg}^{-2}$ is the gravitational constant, meanwhile $g = 9.81 \text{ m s}^{-2}$ is the acceleration due to gravity on Earth. Mechanical behaviour is specified using the following relationship between stress and strain:

$$\boldsymbol{\sigma}(s) = \Lambda(s) \text{Tr}(\boldsymbol{\varepsilon}) \mathbf{1} + 2M(s) \boldsymbol{\varepsilon}, \quad (6.104)$$

where $\text{Tr}(\boldsymbol{\varepsilon}) \equiv \varepsilon_{ii}$ is the trace of the strain tensor. The s -dependent Lamé moduli, $\Lambda(s)$ and $M(s)$ are expressed for a Maxwell solid as

$$\Lambda(s) = \frac{\lambda s + K \tau_M^{-1}}{s + \tau_M^{-1}}, \quad (6.105)$$

and

$$M(s) = \frac{M_U s}{s + \tau_M^{-1}} \quad (6.106)$$

where λ is a constant related to the bulk modulus, K , and the unrelaxed shear modulus, M_U , via $\lambda = K - \frac{2}{3}M_U$, and $\tau_M = \frac{\eta}{M_U}$ as previously. In the Laplace transform domain, the exponential decay series of Equation 6.101 becomes

$$\tilde{p}(s) = \sum_i \frac{p_i}{s + s_i}. \quad (6.107)$$

The normal mode eigenvalues s_i are located at the poles of $\tilde{p}(s)$ on the negative-real s -axis,

since

$$\lim_{s+s_i \rightarrow 0} \tilde{p}(s) \rightarrow \infty. \quad (6.108)$$

The corresponding p_i are the residues of $\tilde{p}(s)$ at each pole s_i . For a Maxwell solid, s_i and p_i can be found by normal mode analysis, which can be applied numerically using matrix methods (Peltier, 1985). Therefore, the time-dependent component of the Love and Shida numbers can be constructed by combining the exponential decay series presented in Equation 6.101 with the solved residues and poles.

In the context of transient rheological models such as Yamauchi and Takei (2016), the structure of $M(s)$, $\tilde{h}_\ell^V(s)$, $\tilde{l}_\ell^V(s)$ and $\tilde{k}_\ell^V(s)$ becomes more complicated, inhibiting the ability to locate the poles and residues relevant to each Love or Shida number via normal mode analysis (Lau, 2024). This is caused by difficulties in implementing a numerical algorithm which can locate all simple poles, particularly when $\tilde{p}(s)$ may be affected by other types of singularity such as branch cuts (Mitrovica and Peltier, 1992). Despite this difficulty, the original exponential decay series shown in Equation 6.101 remains applicable, but now as an approximation of the time-dependent structure (rather than an analytical solution, as is the case for Maxwell rheology). In this case, the estimated s_i and p_i no longer represent the eigenvalues and eigenfunctions of the underlying problem, but are instead used to empirically fit the frequency-dependent behaviour. This is in many ways analogous to the use of a Prony series to approximate the deformation behaviour of a given transient model of viscoelasticity (Lau, 2024). In order to determine sensible values of s_i and p_i , the collocation method is applied (Mitrovica and Peltier, 1992; Peltier, 1974). This involves evaluating $\tilde{p}(s)$ at a pre-determined selection of real points in s -space, represented as s_j , and optimising s_i and p_i by minimising the vector

$$f(s_j) = \tilde{p}(s_j) - \sum_i \frac{p_i}{s_j + s_i}. \quad (6.109)$$

Lau (2024) find that a suitable specification of s_j spans real frequencies from $1 \times 10^{-19} \text{ s}^{-1}$ to $1 \times 10^{-7} \text{ s}^{-1}$, using four samples per decade, equidistant in logarithmic space. Therefore, the full procedure for establishing a set of Love and Shida numbers relevant to a general description of mechanical behaviour, parameterised in terms of the complex compliance, is as follows. Firstly, the Fourier transform domain $J(\omega)$ spectrum must be converted into its complex reciprocal $M(\omega)$. Secondly, the resultant modulus spectrum must be fitted using a Prony series. In this case, the relaxed modulus \tilde{M}_∞ will be ignored for mathematical simplicity, i.e.

$$\tilde{M}_1(\omega) = \sum_{i=1}^{i=N_M} \alpha_i \frac{(\omega\tau_i)^2}{1 + (\omega\tau_i)^2}, \quad (6.110)$$

and

$$\tilde{M}_2(\omega) = \sum_{i=1}^{i=N_M} \alpha_i \frac{\omega\tau_i}{1 + (\omega\tau_i)^2}. \quad (6.111)$$

Third, the coefficients α_i and τ_i of the fitted Prony series can be used to express the modulus spectrum in the Laplace transform domain, by making the substitution $s \rightarrow i\omega$, resulting in the form

$$\tilde{M}(s) = \sum_{i=1}^{i=N_M} \alpha_i \frac{s\tau_i}{1 + s\tau_i}, \quad (6.112)$$

which replaces the analogous Maxwellian expression (Equation 6.106) in the stress-strain relationship used to solve the governing equations of the GIA problem. Fourth, the governing equations must be solved to find the Laplace transform domain Love and Shida numbers, $\tilde{h}_\ell^V(s)$, $\tilde{l}_\ell^V(s)$ and $\tilde{k}_\ell^V(s)$, which can then be transferred into the time domain using the collocation method described earlier (Equation 6.109). In order that the Love and Shida numbers derived for an arbitrary rheology (using the approximate collocation method) agree with Maxwell rheology in the fluid limit, the collocation Love and Shida numbers are normalised using a multiplicative factor K . For example, the radial displacement Love numbers for an arbitrary

rheology are given by

$$\tilde{h}_\ell(s) = h_\ell^E + K \sum_i \frac{p_i}{s + s_i}, \quad (6.113)$$

and their Maxwell counterparts are given by

$$\tilde{h}_\ell^{\text{MX}}(s) = h_\ell^E + \sum_i \frac{p_i^{\text{MX}}}{s + s_i^{\text{MX}}}. \quad (6.114)$$

In the fluid limit $s \rightarrow 0$, $\tilde{h}_\ell(s)$ and $\tilde{h}_\ell^{\text{MX}}(s)$ should be consistent with one another. Thus, the normalisation factor is constrained to be

$$K = \frac{\sum_i \frac{p_i}{s_i}}{\sum_i \frac{p_i^{\text{MX}}}{s_i^{\text{MX}}}}. \quad (6.115)$$

The Love and Shida numbers derived for the arbitrary rheology via collocation are then adjusted by making the substitution $p_i \rightarrow K p_i$. The resulting p_i and s_i allow the time-dependent Love and Shida numbers $h_\ell^V(t)$, $l_\ell^V(t)$ and $k_\ell^V(t)$ to be expressed for the chosen rheology (Equation 6.101).

Once the time-dependent Love numbers have been solved for (whether for the Maxwell model using normal mode analysis, or for the transient model using the collocation method), they can be combined with their elastic counterparts (which are agnostic to the choice of viscoelastic parameterisation), providing the complete forms $h_\ell(t)$, $l_\ell(t)$ and $k_\ell(t)$. These functions can then be convolved in space and time with a loading function $\boldsymbol{\sigma}_L$ to calculate perturbations to Earth's scalar surface topography and gravity fields. The Love number approach can be combined with a sea level equation, to calculate how meltwater contributions are redistributed over Earth's surface through time. Such spatiotemporal patterns of sea level depend principally on Earth's gravity field and the shape of the oceans, but are also affected by ice-ocean self-gravitation, shoreline migration, and adjustments to Earth's rotational state. Since sea level redistribution itself induces a load change, the solid Earth continuously evolves in response to this forcing.

Therefore, the sea level and solid Earth systems are inherently coupled, and must be treated as part of a system incorporating this coupling, to derive gravitationally self-consistent patterns of sea level change.

6.4.2 Sea Level Equation

Sea level, $S(\mathbf{r}, t)$, is a scalar field defined over all of Earth's surface as the distance between the geoid and the solid surface, i.e. (Farrell and Clark, 1976; Kendall et al., 2005)

$$S(\mathbf{r}, t) = G(\mathbf{r}, t) - R(\mathbf{r}, t). \quad (6.116)$$

Topography can also be defined with respect to the geoid, such that (Kendall et al., 2005)

$$L(\mathbf{r}, t) = -S(\mathbf{r}, t), \quad (6.117)$$

where L is the topography field. Ocean depth is defined as zero on the continents, and over the portions of ocean covered by grounded ice, but is otherwise equal to the sea level (Kendall et al., 2005). Mathematically, this is expressed as

$$H(\mathbf{r}, t) = O(\mathbf{r}, t)\beta(\mathbf{r}, t)S(\mathbf{r}, t), \quad (6.118)$$

where the ocean function is

$$O(\mathbf{r}, t) = \begin{cases} 1 & \text{if } S(\mathbf{r}, t) > 0 \\ 0 & \text{otherwise,} \end{cases} \quad (6.119)$$

and the ice function is

$$\beta(\mathbf{r}, t) = \begin{cases} 1 & \text{if } I(\mathbf{r}, t) > 0 \\ 0 & \text{otherwise,} \end{cases} \quad (6.120)$$

where $I(\mathbf{r}, t)$ is the spatial field representing ice thickness, provided by the input ice model. It will be convenient to combine the ocean and ice functions to find the ice-free ocean area, given by $O'(\mathbf{r}, t) = O(\mathbf{r}, t)\beta(\mathbf{r}, t)$. Changes in the ocean depth field, $\Delta H(\mathbf{r}, t, t_0) = H(\mathbf{r}, t) - H(\mathbf{r}, t_0)$, since the initiation of loading at t_0 are connected to changes in sea level, topography, and the time-dependent ice-free ocean function by the generalised sea level equation, given by (Kendall et al., 2005)

$$\Delta H(\mathbf{r}, t) = \Delta S(\mathbf{r}, t, t_0)O'(\mathbf{r}, t) - L(\mathbf{r}, t_0)\Delta O'(\mathbf{r}, t, t_0). \quad (6.121)$$

The generalised sea level equation captures the coupling between sea level and solid Earth mentioned earlier, since the ocean depth changes expressed on the left hand side of the equation are required to calculate the sea level and oceanic domain changes expressed on the right hand side. Therefore, it must be solved iteratively to achieve convergence (Kendall et al., 2005). Note also that in modelling GIA and sea level in response to past glaciation-deglaciation histories, one of the boundary conditions is the present-day topography L_f , which should be arrived at by the end of the simulation. This means a further iterative process is required, which involves selecting an initial topography field $L(\mathbf{r}, t_0)$, and running the whole simulation. The final topography at time t_f , given by $L(\mathbf{r}, t_f)$ must then be compared to the boundary condition L_f , and the misfit used to inform an appropriate perturbation to $L(\mathbf{r}, t_0)$ run in a successive simulation. This process must be repeated until a suitable $L(\mathbf{r}, t_0)$ is found, such that $|L(\mathbf{r}, t_f) - L_f|^2 < \epsilon$, where ϵ is a prescribed misfit tolerance. In this work, such an iterative process will not be needed, since the initial topography field will be set to present-day, according to **ETOPO2** (NOAA National Geophysical Data Center, 2006).

To solve the generalised sea level equation, the procedure laid out fully in Kendall et al. (2005) is employed, known as the pseudo-spectral approach. This approach employs spherical harmonic basis functions of degree ℓ (where theoretically $\ell = 0, 1, \dots, \infty$; in computational applications ℓ is truncated at some resolution-dependent ℓ_{\max}) and order m_ℓ (where $m_\ell =$

$-l, -l+1, \dots, 0, \dots, l-1, l$), referred to as $Y_{m_\ell}^\ell$. Globally defined fields (such as sea level), referred to generally as $X(\mathbf{r}, t)$ can be expressed in this basis using the form

$$\chi(\mathbf{r}, t) = \sum_{l=0}^{\infty} \sum_{m_\ell=-l}^l \chi_{m_\ell}^\ell(t) Y_{m_\ell}^\ell, \quad (6.122)$$

where $\chi_{m_\ell}^\ell$ are the time-dependent coefficients of each basis function. The basis functions $Y_{m_\ell}^\ell$ are orthogonal, such that

$$\int_{\partial V} Y_{m_\ell}^\ell Y_{m'_\ell}^{\dagger \ell'} d\Omega = 4\pi \delta_{\ell\ell'} \delta_{m_\ell m'_\ell}, \quad (6.123)$$

where $d\Omega = \sin \theta d\theta d\varphi$ (latitude, θ , and longitude, φ), $Y_{m_\ell}^{\dagger \ell}$ is the complex conjugate of $Y_{m_\ell}^\ell$, and δ_{ij} is the Kronecker delta. Orthogonality ensures that in the limit $l \rightarrow \infty$, χ is a complete representation of X , i.e.

$$\lim_{l \rightarrow \infty} \chi(\mathbf{r}, t) \rightarrow X(\mathbf{r}, t). \quad (6.124)$$

The spherical harmonic basis functions $Y_{m_\ell}^\ell$ are related to the Legendre polynomials used to generate viscoelastic deformation Love numbers by the following relationship

$$Y_{m_\ell}^\ell(\theta, \varphi) = N(-1)^{m_\ell} \sin^{m_\ell} \theta \exp(im_\ell \varphi) \frac{d^{m_\ell}}{d \cos^{m_\ell} \theta} P_l(\cos \theta), \quad (6.125)$$

where N is a degree- and order-dependent normalisation, given by

$$N \equiv \sqrt{(2\ell + 1) \frac{(\ell - m_\ell)!}{(\ell + m_\ell)!}}. \quad (6.126)$$

These fundamental mathematical relationships make incorporating the Green's functions associated with deformation to Earth's surface and gravity field (expressed as a function of Love numbers and Legendre polynomials, e.g. Equation 6.95), compatible with the spectral (spherical harmonic) domain fields harnessed in the sea level equation. Furthermore, solving the

generalised sea level equation involves a number of integrals which are rapid to calculate in the spectral domain, due to the orthogonality of the spherical harmonic basis functions. However, fields projected onto the ice-free oceanic domain cannot be represented using the spherical harmonic decomposition, and thus calculations involving such fields must be made in the spatial domain. Therefore, the procedure used to solve for gravitationally self-consistent sea level changes on a spherically symmetric Earth is termed pseudo-spectral. A flowchart describing the algorithmic process by which the generalised sea level equation is solved, using the pseudo-spectral approach, is provided in Figure 4 of Kendall et al. (2005).

6.4.3 Ice Loading and Earth Structure

Having established a procedure for calculating time-dependent Love numbers for both a Maxwell and transient Earth (using normal mode analysis, and the collocation method, respectively), as well as an iterative method for solving the sea level equation, there are two remaining requirements. First, a suitable ice loading history is needed. For this, a uniform ice sheet of thickness 1 km was assumed to cover all of West Antarctica in a static state for a period $3 \times t_m$, before decaying completely over a period t_m , and then remaining fully deglaciated for a further time period $6 \times t_m$, such that the total simulation time $t_f = 10 \times t_m$. A total of 99 equally spaced time steps were used. The assumed loading history is not designed to be physically realistic, but rather to allow direct and simple comparison between Maxwell and transient rheologies, in the general context of glacial collapse and warming climatic conditions. In order to test how the frequency content of a given ice loading history influences the modelled deformation response, a range of melting periods were considered:

$$t_m = [25, 50, 100, 250, 500, 1000] \text{ years.} \quad (6.127)$$

The second requirement is a model of Earth's internal steady-state viscosity and elastic shear modulus structure. In the upper mantle (0 km to 400 km), tomographic velocities derived from **ANT-20** were converted into η and M_U using the MAP set of parameters from the adapted pre-melting parameterisation laid out at the end of Section 6.3. These thermomechanically self-consistent values are applicable to both the Maxwell and transient rheological models. Since the Love number formulation requires a spherically symmetric Earth model, it is necessary to select a single η and M_U at each depth node of the GIA model. In order to assess the influence of transient rheology on the stability of the marine-grounded West Antarctic Ice Sheet, the radial structure at a longitude of 292.0° and latitude -68.0° (Marguerite Bay, Antarctic Peninsula) was selected. In this region, the lithosphere is approximately 50 km thick, as inferred using the depth to the $1200\text{ }^\circ\text{C}$ isotherm as a proxy for the LAB. Between the LAB and 400 km depth, steady-state viscosity ranges between

$$\log_{10} \eta(z = 175 \text{ km}) = 19.1 \quad (6.128)$$

and

$$\log_{10} \eta(z = 50 \text{ km}) = 22.5, \quad (6.129)$$

and is on average $\log_{10} \eta = 20.0 \pm 0.9$ (Figure 3.4). The low steady-state viscosity profile selected from the Antarctic Peninsula is similar to that estimated around the rest of the margin of the West Antarctic Ice Sheet. Therefore, the near-field topography and RSL changes produced by the GIA model using this Earth model will be representative of West Antarctica in general. On the other hand, the intermediate- and far-field topography and RSL changes will be ignored, for two main reasons. Firstly, globally averaged values of Earth's upper mantle viscosity (approximately $\log_{10} \eta = 21$), and lithospheric thickness (approximately 100 km), are significantly higher than that of the Antarctic Peninsula. Secondly, the Earth as a whole exhibits significant

lateral variation in upper mantle viscosity (approximately $19 \leq \log_{10} \eta \leq 23$) and lithospheric thickness (approximately 40 to 350 km), which affects patterns of solid Earth deformation in a way that cannot be captured by spherically symmetric GIA models (Powell et al., 2022). Since the focus of this study is the potential effect of transient rheology on near-field bedrock-ice-ocean feedbacks which occur in the near-field, spherical symmetry is an acceptable assumption in this region.

The estimated upper mantle structure was interpolated onto a set of depth slices between 0 km to 400 km for which corresponding density and bulk moduli values were available from the Preliminary Reference Earth Model (**PREM**, Dziewonski and Anderson, 1981). In the case of Maxwell rheology, the η and M_U values themselves are all that are necessary to compute the Laplace transform domain function $M(s)$ (using Equation 6.106), and combined with the assumed bulk modulus, they can be used to compute $\Lambda(s)$ (using Equation 6.105). For transient rheology, these values must be used to compute the relevant $J(\omega)$ spectrum at each depth slice, which is then used in the construction of $M(s)$ according to the method specified in Section 6.4.1. The transient form for $\Lambda(s)$ is computed using the relationship (Lau, 2023)

$$\Lambda(s) = K - \frac{2}{3}M(s), \quad (6.130)$$

where K is still assumed to be frequency-independent and taken from **PREM**, as for the Maxwell model.

6.4.4 Results

The radial and lateral displacement Love numbers calculated for the assumed Maxwell and transient rheologies are shown in Figure 6.24. Of principle interest are the radial displacement Love numbers, $h_\ell(s)$. In the infinite frequency limit, $s \rightarrow \infty$, the Maxwell and transient h_ℓ spectra converge. This is consistent with the approach towards purely elastic behaviour,

where viscous deformation is negligible. Convergence of h_ℓ between the two rheologies also occurs in the zero frequency limit, $s \rightarrow 0$, since in this regime only the steady-state viscosity controls the amplitude of radial displacements. However, close convergence does not occur until $s \leq 10^{-9}$ kyr $^{-1}$, whereas in reality the Maxwell and transient spectra should converge when $\tau \gg \tau_M$, which corresponds roughly to $s \ll 10^{-1}$ kyr $^{-1}$. This result highlights one of the drawbacks of the Love Number approach to solving the GIA problem. Namely, that when implementing an upper mantle structure with fine-scale radial layering (i.e., sub-100 km-scale variations in viscosity and shear modulus), the Laplace transform domain space for each Love and Shida number becomes structurally complex. This makes locating all of the poles (and their associated residues) challenging in the case of Maxwell rheology, and obtaining a suitable approximation of h_ℓ (as well as k_ℓ and l_ℓ) via the collocation technique challenging in the case of transient rheology. This issue is likely responsible for the lack of convergence at more realistic frequencies. Within the intermediate range of frequencies relevant to GIA (in addition to the viscous and elastic end-member limits), 10^{-1} kyr $^{-1} < s < 10^2$ kyr $^{-1}$, the magnitude of $h_\ell(s)$ is larger for the transient Earth as compared to the Maxwell Earth. The same pattern is seen for the lateral displacement Shida numbers, $l_\ell(s)$. Physically, this means that for relaxation processes triggered within this frequency band, the transient Earth will exhibit displacements of greater amplitude than the Maxwell Earth. Indeed, the same behaviour would be observed for geodynamic processes operating at different frequencies to GIA, since the transient values, $h_\ell(s)$ and $l_\ell(s)$, are of equal or greater magnitude than their Maxwell counterparts across the entire spectrum.

For each combination of rheology and ice loading history, the sea level equation was solved, resulting in global surface deformation, topography and RSL fields at each of the 99 time steps specified in the simulation, i.e. $R(\mathbf{r}, t)$, $L(\mathbf{r}, t)$ and $S(\mathbf{r}, t)$. Extracting the value of these fields

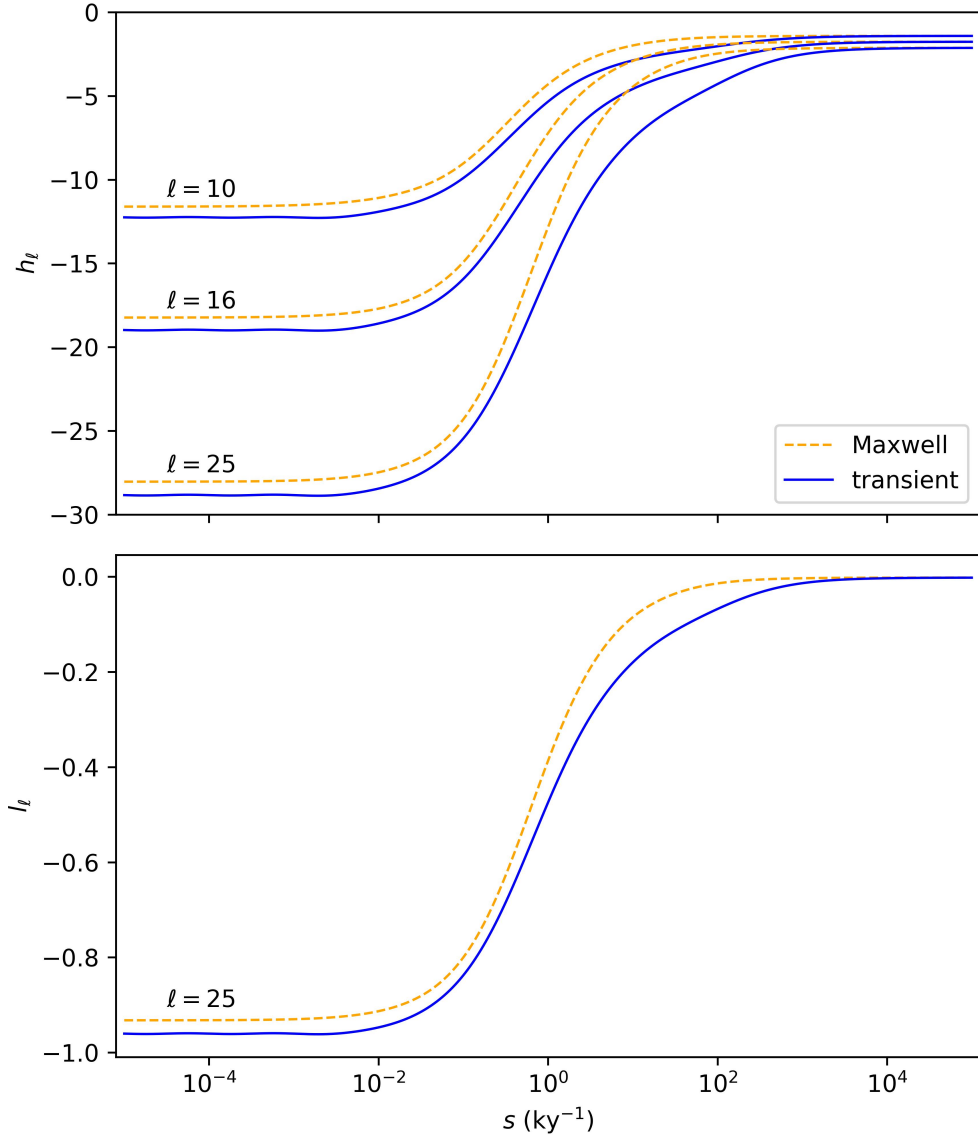


Figure 6.24: Love and Shida numbers relevant to Earth surface displacement, as a function of Laplace transform domain frequency s (for real s) on a transient viscoelastic Earth. The Love numbers $h_\ell(s)$ control Legendre polynomial degree- and frequency-dependent radial displacements to Earth's surface (shown here for $\ell = 10, 16$ and 25). The Shida numbers $l_\ell(s)$ are analogous to $h_\ell(s)$, but instead control lateral displacements. Shida numbers only shown for single degree ($\ell = 25$), due to relative insensitivity of $l_\ell(s)$ to ℓ .

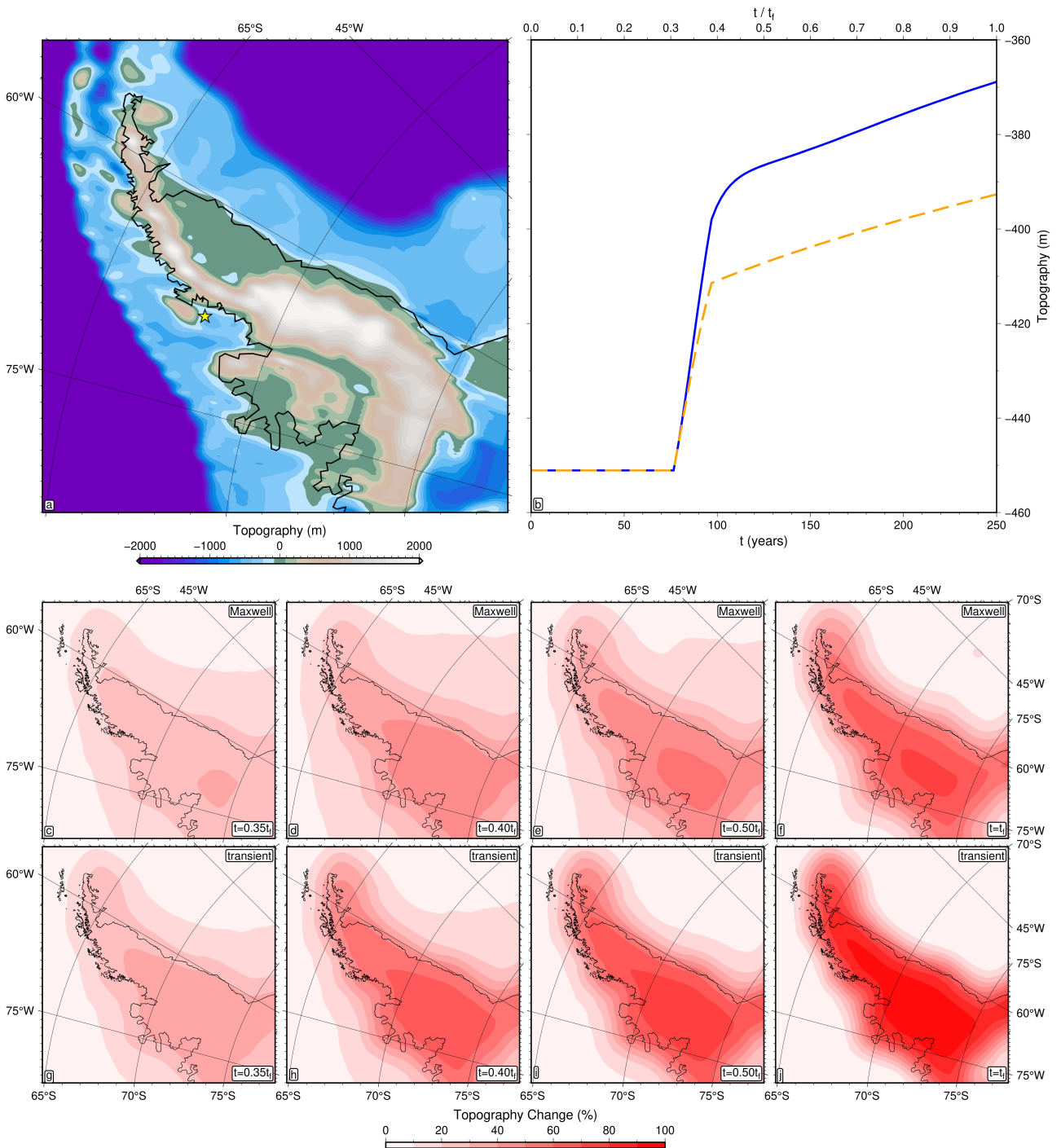


Figure 6.25: GIA induced topography change at the Antarctic Peninsula on a transient Earth. Note that topography is defined relative to the geoid (Equation 6.117). Initial topography set according to present-day, using **ETOPO2** (NOAA National Geophysical Data Center, 2006, panel a). Melting timescale $t_m = 25$ years. Topography evolution (panel b) at Marguerite Bay (292.0°E , -68.0°S , yellow star on panel a) shown for Maxwell (orange dashed line) and transient (blue solid line) viscoelastic models. Maps of topography change, $\Delta L = L(t) - L(t = 0)$, at specific time intervals ($t = [0.35, 0.40, 0.50, 1.00] t_f$, where $t_f = 10 \times t_m = 250$ years is the total simulation time) for the Maxwell (panels c-f) and transient (panels g-j) models. Topography change expressed as a percentage of the maximum Antarctic Peninsula ΔL value, which occurs in the transient GIA simulation at $t = t_f$.

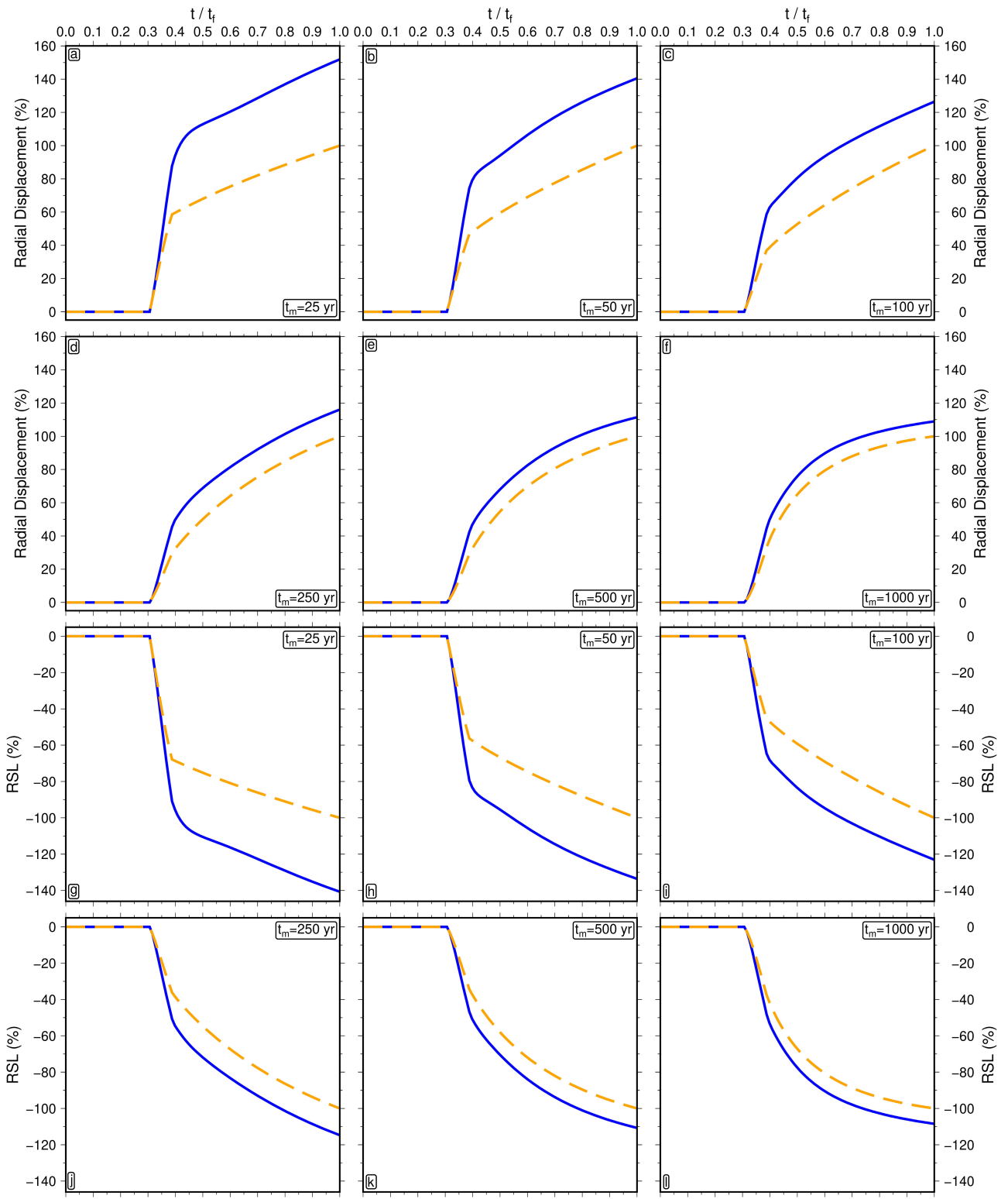


Figure 6.26: Earth surface displacement and RSL (R and S , respectively) evolution at Marguerite Bay for each ice loading history, shown for Maxwell (orange dashed lines) and transient (blue solid lines) viscoelastic models. For each ice loading history (melting time t_m shown in topography panel inset, total simulation time $t_f = 10 \times t_m$), radial displacement and RSL are shown as percentages of the (absolute) value of the Maxwell model at the end of the simulation (complete values reported in Table 6.3).

Melting Timescale t_m (years)	Rheology	ΔR (m)	\dot{R}_{\max} (m yr $^{-1}$)	ΔS (m)	\dot{S}_{\max} (m yr $^{-1}$)
25	Maxwell	46	1.45	-58	-2.17
	transient	69 (+52%)	2.17 (+50%)	-82 (+41%)	-2.84 (+31%)
50	Maxwell	60	0.75	-73	-1.1
	transient	85 (+41%)	1.26 (+69%)	-98 (+34%)	-1.6 (+45%)
100	Maxwell	84	0.40	-97	-0.58
	transient	106 (+26%)	0.69 (+72%)	-119 (+23%)	-0.87 (+50%)
250	Maxwell	129	0.20	-141	-0.27
	transient	149 (+16%)	0.32 (+58%)	-162 (+15%)	-0.39 (+44%)
500	Maxwell	164	0.14	-177	-0.16
	transient	183 (+11%)	0.20 (+44%)	-196 (+11%)	-0.23 (+44%)
1000	Maxwell	191	0.10	-203	-0.11
	transient	208 (+9%)	0.12 (+25%)	-220 (+8%)	-0.14 (+27%)

Table 6.3: Earth surface displacement and RSL change measures. Radial displacement amplitude change ($\Delta R = R(t = t_f) - R(t = 0)$), maximum rate of displacement ($\dot{R}_{\max} = \dot{R}(\ddot{R} = 0, \dot{R} < 0)$, where $\dot{R} \equiv \frac{dR}{dt}$), and the equivalent measures for RSL (ΔS and \dot{S}_{\max}) shown for each choice of rheology (Maxwell or transient), and each melting timescale t_m . Percentages reported in parentheses in each of the transient entries represent a comparison to their corresponding Maxwell value, analogously to Equation 6.135.

at a given near-field location, \mathbf{r}_{NF} , such that

$$R_{\text{NF}}(t) = R(\mathbf{r}_{\text{NF}}, t), \quad (6.131)$$

$$L_{\text{NF}}(t) = L(\mathbf{r}_{\text{NF}}, t), \quad (6.132)$$

and

$$S_{\text{NF}}(t) = S(\mathbf{r}_{\text{NF}}, t), \quad (6.133)$$

it is possible to compare the unique deformation behaviour predicted by each rheological model in response to the experienced ice loading changes. Honing in on the bedrock topography field computed over the Antarctic Peninsula, $L_{\text{NF}}(t)$, the results of the GIA simulation for which $t_m = 25$ years are shown in Figure 6.25. Bedrock in this region is situated either beneath or within close proximity to the simulation's melting ice load, leading to a general pattern of topographic uplift for both rheologies. Roughly 80% of this increase in topography is caused

by Earth's radial displacement. The remainder is caused by a reduction in local gravitational field strength, which occurs due to ice melting. However, the amplitude and rate of topography change during and after melting is significantly higher for the transient model, as compared to its Maxwell counterpart. This can be seen by looking at the total RSL change over the simulation, defined as

$$\Delta S = S(t = t_f) - S(t = 0), \quad (6.134)$$

whose amplitude is equal to the amplitude of topography change (see Equation 6.117). At Marguerite Bay (292.0°E , -68.0°S), ΔS is -82 m in the transient model, which is 41% larger than the Maxwell model (-58 m). The peak rate of RSL change, referred to as \dot{S}_{\max} , occurs during melting and equates to -2.84 m yr^{-1} in the transient model, which is 31% higher than the Maxwell model (-2.17 m yr^{-1}). The Earth surface displacement and RSL (R and S , respectively) evolution associated with each t_m is shown in Figure 6.26, and the full set of ΔR , \dot{R}_{\max} , ΔS , \dot{S}_{\max} measures corresponding to each simulation is presented in Table 6.3. When comparing the percentage difference between ΔR in the case of transient versus Maxwell Earths, i.e.

$$\frac{\Delta R_{\text{transient}} - \Delta R_{\text{Maxwell}}}{\Delta R_{\text{Maxwell}}} \quad (6.135)$$

as a function of the melting timescale t_m , the following succession is observed: +52% (25 years), +41% (50 years), +26% (100 years), +16% (250 years), +11% (500 years) and +9% (1000 years). Therefore, the extent to which more deformation occurs in the transient model diminishes as the melting timescale increases, due to the smaller contribution arising from the activation of transient relaxation processes and the increasing dominance of end-member steady-state viscous relaxation.

6.4.5 Discussion

These results have significant implications for three main areas of research related to ice sheet stability and sea level change. First, palaeo sea level and fingerprinting studies seek to understand past patterns of deglaciation. The temporal patterns of near-field surface displacement and RSL change presented in Figure 6.26 show that for rapid deglaciation events such as Meltwater Pulse 1A (MWP-1A, 14,650 years ago, duration roughly 500 years), transient rheological models cause the Earth to deform more, and more rapidly, than their reference Maxwell counterparts. This behaviour will also be reflected in the intermediate- and far-field, where canonical sea level marker locations such as Barbados and Tahiti are used to provide sensitivity to the spatiotemporal deglaciation pattern of MWP-1A. The results corroborate the findings of Lau (2023), that time-dependent variations in apparent viscosity may be critically important in determining the RSL fingerprint of a particular ice melting configuration. However, the Love and Shida numbers presented in Figure 6.24 differ significantly from those presented in Lau (2023), in which an Extended Burgers model was used. The former Love and Shida number spectra imply that the transient rheological model is more yielding than its Maxwell counterpart across all frequencies. The latter (see also Lau, 2024, in which the master curve parameterisation of McCarthy and Takei, 2011 is used) imply that there is a crossover point, s_c , such that the transient model is less yielding than its Maxwell counterpart for all $s < s_c$. It appears as if s_c is dependent on the Legendre polynomial degree ℓ , but corresponds to timescales of order 1 kyr and longer. The cause of this discrepancy has not been confidently identified, however it is possible to speculate that it could be due to the different choice of rheological model (which must affect the shape of the $h_\ell(s)$ and $l_\ell(s)$ spectra, but would not necessarily introduce the observed crossover frequency s_c), or a less obvious change in modelling assumptions.

Secondly, inversions of upper mantle structure based on present-day observations of deformation will be heavily affected by the exhibition of transient deformation. Let us assume

that an extreme event of glacial collapse occurs at Marguerite Bay, with a melting timescale of $t_m = 25$ years, and Earth deforms as a transient body. Therefore, the blue solid line in panel a of Figure 6.26 will approximate the observed pattern of deformation in response to such an event. Now, a research team take these observations, along with an accurate model of the ice melting history, and invert them for a best-fitting rheological model. If a Maxwell rheology is assumed (as is usual for studies of this sort, see e.g. Samrat et al., 2021), a much lower best-fitting viscosity will be obtained than the true steady-state value, due to the effect of transient relaxation on lowering the apparent viscosity (as shown in Section 3.3.3). Furthermore, since transient rheology not only alters the average observed strain rate, but also the time-dependent pattern of deformation, it will not be possible to fully fit the observations using a Maxwell model. This source of phenomenological error will therefore further bias the inverted viscosity. Although, this effect is likely to be of second-order importance, since the difference in deformation pattern appears to be relatively minor (compare shape of blue and orange lines, panel b of Figure 6.25) and may be smaller in scale than typical data uncertainty. Returning to the issue of inverted Maxwell viscosities, these values will only be useful in forward models of GIA in the following situation: modelling deformation on a Maxwell Earth in response to the precise ice melting history relevant to the viscosity inversion. Therefore, the results presented in Figure 6.25 and 6.26 show that integrating estimates of mantle structure derived from local studies into a larger-scale (e.g. global) model will not yield reliable results unless the local studies themselves incorporate experimentally derived parameterisations of transient rheology. This means that care is needed to avoid interpreting variations in viscosity arising due to time-dependent mechanics as due to three-dimensional variations in steady-state viscosity structure, which would ultimately lead to discrepant predictions of RSL when used in forward modelling of the GIA problem.

Finally, on the issue of forward modelling, the radial displacement and RSL changes pre-

sented herein highlight that for ice melting events operating on short timescales (i.e., 1,000 years and less, particularly 25 to 100 years), such as glacial collapse, the presence of transient behaviour significantly increases deformation rates as compared to a reference Maxwell viscoelastic model. As a result, near-field RSL falls faster, and by a greater total amplitude, in response to such an event (as shown in Figure 6.26). A correspondingly larger and more rapid rise in far-field RSL will therefore counter this near-field behaviour in the transient case, preserving the total meltwater content. More importantly, increased rebound rates at the grounding line of the retreating ice may reduce the impact, or negate the onset, of the marine ice sheet instability (MISI). MISI is a scenario which may occur when ice grounded below sea level, upon bedrock which deepens towards the ice sheet interior, experiences runaway retreat. It is caused by the thickening of the water column as the ice retreats backwards, which in-turn accelerates melting rates, leading to a positive feedback cycle. If the bedrock rebounds rapidly enough in response to ice mass loss, however, MISI may be less likely to occur in potentially vulnerable areas such as the Antarctic Peninsula, and the Amundsen Sea Embayment, due to the reduction in water column thickness caused by enhanced bedrock uplift (Gomez et al., 2010; Kingslake et al., 2018). Since the development (or lack thereof) of MISI is a critical factor determining the stability of the West Antarctic Ice Sheet, accurate modelling of these coupled interactions between ice sheets, sea level and solid Earth is required to predict future sea level. The patterns of RSL change shown in panels a-e of Figure 6.26 therefore show that incorporation of transient rheology into forward models of GIA will be critical to improving predictions of future global sea level change.

6.5 Conclusions

A theoretical basis for the application of arbitrarily complex parameterisations of viscoelasticity to finite element models of continuum mechanics has been developed. This basis involves

connecting experimentally constrained models of the complex compliance, $J(\omega)$, to Prony series representations of the relaxation modulus, $M(t)$. It was shown that the master curve parameterisation of McCarthy and Takei (2011), which obeys Maxwell timescale scaling, can be incorporated by normalising the discrete set of timescales and amplitudes associated with the Prony series expansion. This normalisation procedure allows element-to-element changes in state variables (such as temperature T , pressure, P , and composition, X) to be accounted for while using the same underlying Generalised Maxwell Model. The theoretical framework was then further developed to enable the use of a general compliance parameterisation, such as Yamauchi and Takei (2016), which does not obey Maxwell scaling. This development was made by obtaining a recursive scaling relationship between Prony series at a prescribed reference homologous temperature, Θ_r , and an arbitrary homologous temperature, Θ . The error introduced by using the approximate recursive scaling method was shown to be significantly smaller than that caused by using a Prony series of $N_M = 15$ Maxwell elements. Therefore, the theoretical basis laid out in Section 6.2 represents a key development towards utilising the most accurate parameterisations of Earth's mechanical behaviour into geodynamic simulations.

In Section 6.3, an optimised form of Yamauchi and Takei (2016) was developed, which was motivated by two main factors. First, computationally efficient access to the complex compliance spectrum, $J(\omega)$, is required to use the recursive scaling method for calculation of state-dependent relaxation moduli. In the original parameterisation, implementation of the pre-melting functions $A_P(\Theta)$, $\sigma_P(\Theta)$ and $A_\eta(\Theta)$ required computationally expensive if-else statements. By substituting their piecewise definitions with scaled hyperbolic tangent functions, such if-else statements could be replaced with efficient vectorised function calls. Second, the original parameterisation was obtained subjectively, and therefore the reported pre-melting parameters were not optimised against the experimental data. By performing a Bayesian inversion, a set of best-fitting pre-melting parameters most faithful to the original experimental

data could be obtained, as well as a set of corresponding uncertainties. Furthermore, by combining the experimental and geophysical data constraints within a joint inversion framework, the pre-melting and viscoelasticity parameter space could be simultaneously optimised. This approach enables trade-off between all model parameters to be accounted for in the conversion between V_S and thermomechanical structure (including viscosity, η). The theoretical basis developed in Section 6.2, combined with the optimised form of Yamauchi and Takei (2016), lays the groundwork for a thermomechanically self-consistent implementation of transient rheology into geodynamic models (including three-dimensional variations in mantle structure).

To reveal the importance of transient rheology in GIA modelling, the optimised form of Yamauchi and Takei (2016) was used to calculate Earth surface displacement and relative sea level change in response to a melting West Antarctic Ice Sheet. The Prony series representation demonstrated in Section 6.2 was used to express the chosen rheology in the Laplace transform domain, via $M(s)$, which represents the s -domain relaxation modulus. $M(s)$ could be incorporated into the system of equations defining the GIA problem, and solved using Love and Shida numbers. Combining the Love number approach with a pseudo-spectral method for solving the sea level equation, this framework enables calculation of radial displacement and sea level changes on a transient viscoelastic Earth. To define Earth's radial mantle structure, thermodynamically self-consistent inferences of steady-state viscosity and unrelaxed shear modulus (calculated using the joint inversion procedure developed in Section 6.3) relevant to Marguerite Bay (Antarctic Peninsula) were used. It was demonstrated that for short melting timescales, significantly more near-field deformation is induced by the transient rheological model, as compared to a reference Maxwell model. For example, when $t_m = 25$ years, a 52% larger Earth surface displacement (between $t = 0$ and the final timestep of the simulation, at $t = 10 \times t_m = 250$ years) at Marguerite Bay was observed for the transient model. The presence of decadal- and centennial-timescale transient deformation is highly significant in the

context of palaeo sea level fingerprinting studies, which typically assume elasticity over such timescales. The extent to which more deformation occurs in the transient model was shown to diminish as the melting timescale increases. This result is consistent with the increasing dominance of steady-state viscous behaviour at such timescales, and leads to timescale-dependent apparent viscosity. Thus, assuming Earth is a transient body, inversions of mantle structure based on geodetic observations will recover discrepant Maxwell viscosity values, depending on the frequency content of the loading process causing the observed deformation. Furthermore, the significant contribution of transient deformation towards grounding line rebound may contribute positively towards ice sheet stability in modern melting scenarios (Gomez et al., 2010).

Chapter 7

Conclusions

7.1 Summary

The solid Earth plays a fundamental role in governing sea level change through space and time. In response to ice volume changes, perturbations to Earth's surface, rotational state, and gravitational field cause the hydrosphere to continuously redistribute water over evolving ocean basins. Accurate GIA models are therefore required to predict near- and far-future patterns of sea level change in a warming climate. Indeed, since the seminal work of Farrell (1972), theoretical and computational advances have led to increasingly powerful numerical approaches to solving the GIA problem. Sufficient progress has been made that it is now possible to calculate sea level changes on a solid Earth exhibiting lateral variations in mantle viscosity and lithospheric thickness (Whitehouse, 2018). However, difficulties constraining Earth's interior structure have led to poor inter-model agreement, and large uncertainty in resulting estimates of solid Earth deformation and sea level change (Caron et al., 2018).

In Chapter 2, this issue is addressed, using seismic wave speed as a geophysical proxy for mantle thermal structure. By utilising an experimental parameterisation of mantle rock viscoelasticity, V_S can be converted into estimates of temperature, and temperature-dependent

variables such as viscosity. This approach circumvents a number of limitations associated with empirical V_S - T conversions. In order to calibrate the free parameters contained within the viscoelasticity parameterisation, a Bayesian inversion approach incorporating geophysical data constraints is adopted. The main constraint used is based on the thermal structure of oceanic lithosphere. The statistical framework developed in Chapter 2 entails treating viscoelasticity parameters as random variables, and enables robust characterisation of their covariance. This covariance structure can be harnessed to assess uncertainty in estimated mantle structure.

A probabilistic assessment of Antarctic mantle structure is conducted in Chapter 3, by applying the inversion framework developed in the previous chapter, in order to calculate temperature-dependent variables such as viscosity, LAB depth and GHF. Uncertainty in estimates of mantle viscosity were found to be reduced by 4 to 5 orders of magnitude at 150 km depth, as compared to an approach insensitive to viscoelasticity parameter covariance. A clear dichotomy between mantle structure in East and West Antarctica is observed, in accordance with other studies. Evidence is found for mostly thick lithosphere (> 150 km), high mantle viscosity ($> 10^{23}$ Pas at 150 km depth), and low GHF (~ 40 to 50 mW m $^{-2}$) beneath East Antarctica. In West Antarctica, the opposite is seen, with average LAB depth 63 ± 13 km, presence of multiple low viscosity anomalies (e.g., $< 10^{19.5}$ Pas beneath Marie Byrd Land at 150 km depth), and GHF between 50 and 100 mW m $^{-2}$. These outputs have important implications for GIA studies, in which lateral viscosity and LAB depth variations affect the timing and character of viscoelastic deformation. Having obtained high-resolution images of Antarctic mantle viscosity structure, the issue of transient rheology is explored. Inherent within experimental parameterisations of mantle rock viscoelasticity (e.g., the pre-melting model of Yamauchi and Takei, 2016) are time-dependent apparent viscosity variations. The effect of such variations on inversions for mantle structure based on GPS deformation data was explored. It was shown that by accounting for time-dependent apparent viscosity, seemingly disparate (by ~ 1 order

of magnitude) estimates of Antarctic mantle viscosity derived from GPS observations from the same region can be reconciled.

In Chapter 4, Antarctic GHF is revisited in order to quantify the impact of laterally variable crustal conductivity and radiogenic heat production. The supply of thermal energy to the ice sheet-solid Earth interface, as quantified by GHF, can influence basal melt and sliding, englacial rheology, and erosion. As a result, ice sheet models require reliable estimates of GHF in order to accurately capture ice dynamics (Burton-Johnson et al., 2020). This problem is of particular importance in Antarctica, where significant lateral variations in GHF are estimated, based not only on geophysical inference, but also local borehole data. Building on the V_S -derived Antarctic GHF model in Chapter 3, based on reliable inferences of upper mantle structure between 50 km to 400 km, crustal V_P data is integrated to provide constraint on crustal conductivity ($2.3 \text{ W m}^{-1} \text{ K}^{-1}$ to $2.9 \text{ W m}^{-1} \text{ K}^{-1}$) and radiogenic heat production ($0 \mu\text{W m}^{-3}$ to $6 \mu\text{W m}^{-3}$), which vary as a function of crustal composition. Since conductivity and heat production are dominant controls on the shallow geothermal gradient, their constraint allows robust estimation of Antarctic GHF (20 mW m^{-2} to 130 mW m^{-2}). Compared with previous studies (including that presented in Chapter 3), which do not account for variations in crustal composition, stronger lateral variations in Antarctic GHF are estimated. Such GHF estimates agree more closely with borehole-derived GHF inferences than previous models ($\text{RMS} = 29.2 \pm 2.6 \text{ mW m}^{-2}$). Therefore, it is important to assess the implications of such a GHF model on Antarctic sub-glacial thermal conditions, and the subsequent effect on ice sheet dynamics.

Although the main focus of this thesis is on relationships between the solid Earth and cryosphere, the methods developed to estimate mantle thermomechanical structure can be used to make advances in a wide range of contexts. In Chapter 5, the Bayesian inverse framework developed in Chapter 2 is modified to allow the use of xenolith-derived palaeogeotherms as

geophysical data constraints. By using a compiled inventory of such palaeogeotherms, maps of Australian lithospheric structure are generated. A hyperparameter is applied to each locality so that data constraints can be up- or down-weighted based on their individual reliability. This feature is particularly important in the context of inverting xenolith data, since the lithosphere may have been substantially modified since the time of emplacement in certain regions, leading to discrepancies between palaeogeotherms and present-day geotherms. A total of 28 palaeogeotherms, combined with an adiabat pertaining to asthenospheric thermal structure, are used to invert for best-fitting viscoelasticity parameters. Australian LAB depth is estimated to vary between 40 km and 270 km. A powerful relationship between the 195 km LAB depth contour and the location of sediment-hosted base metal deposits is observed. 78% of metal mass associated with such deposits is found to be located within 100 km of this LAB depth contour, and 97% within 200 km, which is roughly equivalent to the horizontal resolution of the underlying tomographic inversion. As shown by comparison with a synthetic data set in which deposit locations are generated randomly, the observed LAB depth contour-deposit location correlation is found to be statistically significant. Based on a two-sample Kolmogorov-Smirnov test, the likelihood of such a correlation occurring randomly is found to be 1 in 10^{18} .

Relationships between transient rheology, ice sheet stability, and sea level are investigated in Chapter 6. In this chapter, three main developments are made. First, a blueprint for the application of experimental parameterisations of viscoelasticity to numerical continuum mechanics models is established. This involves connecting the complex compliance, $J(\omega)$, with a finite Prony series approximation of the relaxation modulus, $M(t)$. By normalising the timescales and amplitudes associated with the Prony series, spatial variation in state variables (including temperature, pressure and composition) can be accounted for within the same reference model. These steps enable the use of cutting-edge parameterisations of mantle rheology within geodynamic simulations, while self-consistently accounting for three-dimensional variations in

mantle structure. Second, a modified form of the pre-melting model of Yamauchi and Takei (2016) is constructed. This model replaces piecewise function definitions with a scaled hyperbolic tangent, which is defined by a single expression across its entire domain. This makes implementation within computationally expensive continuum mechanics models feasible, by enabling vectorised function calls instead of inefficient if-else statements. Using geophysical and experimental data to simultaneously invert for best-fitting pre-melting function parameters, and viscoelasticity parameters, an optimised pre-melting model is obtained. This model, combined with the aforementioned Prony series approach, lays the groundwork for implementation of transient rheology into geodynamic models. Finally, the optimised pre-melting model is applied to a simple simulation of Antarctic GIA in order to probe the effect of transient deformation on near-field sea level. The Love number approach is combined with a pseudo-spectral method for solving the sea level equation to calculate radial displacement and sea level perturbations. To define Earth's radial mantle structure, self-consistently inferred viscosity and shear modulus values derived from Marguerite Bay in the Antarctic Peninsula are used. An idealised West Antarctic Ice Sheet (uniform 1 km thickness) is assumed to deglaciate over a finite melting timescale t_m , where the following values for t_m are applied: 25, 50, 100, 250, 500 and 1000 years. It is demonstrated that for short melting timescales, significantly more near-field deformation is caused by the optimised pre-melting model (which exhibits transient behaviour), as compared to a reference Maxwell model. When $t_m = 25$ years, a 52% increase in Earth surface displacement is observed for the transient model at Marguerite Bay. This discrepancy reduces monotonically with t_m , down to 8% at 1000 years, and the two models are expected to perform identically as $t_m \rightarrow \infty$. Therefore, decadal- and centennial-timescale transient deformation is highly significant in the context of palaeo sea level fingerprinting studies, which typically model the Earth as a purely elastic body. In the context of modern melting, these results imply that transient deformation promotes ice sheet stability, via accelerated

grounding line rebound (Gomez et al., 2010).

7.2 Future Work

The work completed in this thesis opens an array of potential avenues for future work. First, high-resolution maps of Antarctic mantle structure: temperature, viscosity, density and LAB depth, can be applied to generate geodynamic models that faithfully represent the true physical state and evolution of Earth’s interior. Viscosity and LAB depth structures can be used to accurately model regional GIA, or integrated into global scale Earth models to calculate near- and far-field patterns of sea level. At present, GIA uncertainty is typically investigated by combining a range of possible Earth models with a range of possible ice loading histories, without rigorous quantification of the likelihood of each model combination (e.g., van der Wal et al., 2015). This type of analysis leads to a preferred GIA model (corresponding to a given Earth structure and ice loading history), rather than a probabilistic assessment of the range of possible models. By selecting Earth structures from the posterior ensemble corresponding to certain probability percentiles, such an assessment becomes feasible. If combined with a posterior ensemble of ice loading histories, GIA trends with formally quantified uncertainty can be estimated. Rigorously calculated uncertainty is required for propagation into signals of interest, including gravimetry-derived estimates of Antarctic ice mass balance, and future sea level projections (Caron et al., 2018; Oppenheimer et al., 2019a).

Three-dimensional models of mantle temperature, density, and viscosity are also essential for driving simulations of mantle convection over geological timescales. Patterns of convection exert normal stresses on Earth’s surface, deforming it at rates of up to ~ 100 m Myr⁻¹; a process known as dynamic topography (Richards et al., 2023). By building dynamic topography models on the basis of high-resolution estimates of solid Earth structure, it will be possible to assess the impact of mantle dynamics on palaeo ice sheet stability. For example, during the

Mid-Pliocene Warm Period (3.3 Ma to 3.0 Ma), atmospheric CO₂ levels were similar to present-day at approximately 400 ppm, and global mean temperature was 1.9 °C to 3.6 °C above pre-industrial levels (Richards et al., 2023). Therefore, this period is an important climate analogue, the study of which may yield information about the sensitivity of Earth’s cryosphere to modern and projected changes in climatic conditions. However, in assessing Mid-Pliocene ice volumes, it is necessary to correct palaeo sea level markers for both GIA and dynamic topography (Austermann et al., 2015; Rovere et al., 2014). Furthermore, inferences of Antarctic ice sheet stability based on recovered ice volumes must take into account differences in bedrock elevation, between the Pliocene and present-day. This is because changes in bedrock elevation impact ice sheet vulnerability to rapid ice loss via perturbations to subglacial hydrology and drainage networks, grounding line position and gradient, GHF, and ice surface elevation (Aitken et al., 2023; Burton-Johnson et al., 2020; Gasson et al., 2015; Paxman et al., 2020).

In Chapter 4, the issue of Antarctic GHF model validation is discussed. Due to difficulties in obtaining local inferences of Antarctic GHF from borehole data, data coverage over the continent is extremely sparse. Although sophisticated geophysical methods (e.g., integrating various forms of seismic data) have been developed to remotely infer GHF on continental scales, such methods require robust validation to ensure their reliability. The framework developed to estimate Antarctic GHF in Chapter 4 is theoretically applicable to any location of interest. Therefore, a detailed validation of the combined V_S and V_P method for inferring GHF, with consideration of crustal composition, could be completed by applying this method to a region where abundant local inferences of GHF are available. In the United States, 17,885 local inferences of continental GHF are available; 35% of the entire global inventory of continental GHF values, despite the USA covering only 6% of Earth’s continental surface area (Lucazeau, 2019). Compared to data coverage in Antarctica, the density of local GHF inferences in the USA is 800 times larger, calculated on a data point per continental surface area basis. Furthermore,

a densely spaced network of broadband seismometers (\sim 70 km between stations, USArray Transportable Array) has enabled development of high resolution tomographic velocity models (e.g., Shen and Ritzwoller, 2016). As a result, the United States is a suitable testing ground for robust validation of the GHF estimation method presented in Chapter 4. Significant opportunity exists to identify potential discrepancies between geophysical and local GHF inferences, and interpret whether they derive from geophysical modelling limitations. These insights can ultimately be used to improve geophysical models of Antarctic GHF, and will thus feed into improved models of ice sheet dynamics.

Finally, in Chapter 6, a blueprint for the application of experimental viscoelasticity parameterisations to numerical continuum mechanics simulations is established. Therefore, a clear future objective is to develop a stable computational implementation of these transient viscoelastic models, e.g. using the geodynamic modelling code **ASPECT**. As a first step, a proof of concept model could be developed, using simplified approximations of the geometry of the Antarctic Ice Sheet and its melting history. By experimenting with different Prony series, the impact of spatiotemporal changes in apparent viscosity on grounding line rebound rates and sea level evolution could be explored. Such work would lay the groundwork for state-of-the-art GIA simulations to be conducted. For example, fingerprinting studies could be revisited, improving constraints on past ice volume changes. The elastically adjusted contemporary GIA signal could be recalculated, and used to revise GRACE-derived constraints on present-day ice melting rates. By pairing the geodynamic model with an array of possible future climate scenarios, near- and long-term RSL projections could be generated. Incorporating physical feedbacks between near-field RSL and ice dynamics, it may be possible to predict the fate of the Antarctic Ice Sheet.

Bibliography

- Aitken, A. R. A. et al. (2023). “Antarctic Sedimentary Basins and Their Influence on Ice-Sheet Dynamics”. In: *Reviews of Geophysics* 61.3, e2021RG000767.
- An, M. et al. (2015). “Temperature, lithosphere-asthenosphere boundary, and heat flux beneath the Antarctic Plate inferred from seismic velocities”. In: *J. Geophys. Res. Solid Earth* 120.12, pp. 8720–8742.
- Andrieu, C. and J. Thoms (2008). “A tutorial on adaptive MCMC”. In: *Statistics and Computing* 18.4, pp. 343–373.
- Artemieva, I. M. et al. (2017). “Heat production in granitic rocks: Global analysis based on a new data compilation GRANITE2017”. In: *Earth-Science Reviews* 172, pp. 1–26.
- Austermann, J. et al. (2013). “Barbados-based estimate of ice volume at Last Glacial Maximum affected by subducted plate”. In: *Nature Geoscience* 6.7, pp. 553–557.
- Austermann, J. et al. (2015). “The impact of dynamic topography change on Antarctic ice sheet stability during the mid-Pliocene warm period”. In: *Geology* 43.10, pp. 927–930.
- Austermann, J. et al. (2021). “The effect of lateral variations in Earth structure on Last Inter-glacial sea level”. In: *Geophysical Journal International* 227.3, pp. 1938–1960.
- Ball, P. W. et al. (2021). “Global influence of mantle temperature and plate thickness on intraplate volcanism”. In: *Nature Communications* 12.1, p. 2045.
- Bamber, J. L. et al. (2018). “The land ice contribution to sea level during the satellite era”. In: *Environmental Research Letters* 13.6, p. 063008.

Bamber, J. L. et al. (2019). “Ice sheet contributions to future sea-level rise from structured

expert judgment”. In: *Proceedings of the National Academy of Sciences* 116.23, pp. 11195–11200.

Barletta, V. and A. Bordoni (2013). “Effect of different implementations of the same ice history

in GIA modeling”. In: *Journal of Geodynamics* 71, pp. 65–73.

Barletta, V. R. et al. (2018). “Observed rapid bedrock uplift in Amundsen Sea Embayment

promotes ice-sheet stability”. In: *Science* 360.6395, pp. 1335–1339.

Behn, M. D. and P. B. Kelemen (2003). “Relationship between seismic P-wave velocity and the

composition of anhydrous igneous and meta-igneous rocks”. In: *Geochemistry, Geophysics,*

Geosystems 4.5.

Belousova, E. A. et al. (2001). “Two age populations of zircons from the Timber Creek kimber-

lites, Northern Territory, as determined by laser-ablation ICP-MS analysis”. In: *Australian*

Journal of Earth Sciences 48, pp. 757–765.

Biggs, J. et al. (2010). “Breaking up the hanging wall of a rift-border fault: The 2009 Karonga

earthquakes, Malawi”. In: *Geophysical Research Letters* 37.L11305.

Black, L. P., J. Ferguson, and P. T. Gray (1993). *A Jurassic U-Pb age for a South Australian*

kimberlitic rock. Tech. rep. South Australia Geological Survey, pp. 2–5.

Blank, B. et al. (2021). “Effect of Lateral and Stress-Dependent Viscosity Variations on GIA

Induced Uplift Rates in the Amundsen Sea Embayment”. In: *Geochemistry, Geophysics,*

Geosystems 22.9, e2021GC009807.

Boughanemi, A. and A. Mémin (2024). “Effects of Andrade and Burgers rheologies on glacial

isostatic adjustment modeling in Antarctica”. In: *Geodesy and Geodynamics*.

Burgos, G. et al. (2014). “Oceanic lithosphere-asthenosphere boundary from surface wave dis-

persions data”. In: *J. Geophys. Res. Solid Earth* 119.2, pp. 1079–1093.

- Burton-Johnson, A., R. Dziadek, and C. Martin (2020). “Review article: Geothermal heat flow in Antarctica: current and future directions”. In: *The Cryosphere* 14.11, pp. 3843–3873.
- Caron, L. et al. (2018). “GIA Model Statistics for GRACE Hydrology, Cryosphere, and Ocean Science”. In: *Geophysical Research Letters* 45.5, pp. 2203–2212.
- Champac, V. and J. Garcia Gervacio (2018). *Timing Performance of Nanometer Digital Circuits Under Process Variations*. 1st ed. Springer International Publishing.
- Cobden, L. et al. (2008). “Thermochemical interpretation of one-dimensional seismic reference models for the upper mantle: Evidence for bias due to heterogeneity”. In: *Geophysical Journal International* 175.2, pp. 627–648.
- Colgan, W. et al. (2021). “Topographic Correction of Geothermal Heat Flux in Greenland and Antarctica”. In: *Journal of Geophysical Research: Earth Surface* 126.2, e2020JF005598.
- Cook, A. J. and D. G. Vaughan (2010). “Overview of areal changes of the ice shelves on the Antarctic Peninsula over the past 50 years”. In: *The Cryosphere* 4.1, pp. 77–98.
- Cooper, S. A. and B. J. Morris (2012). *A review of kimberlites and related rocks in South Australia*. Tech. rep. Geological Survey of South Australia, p. 36.
- Coulon, V. et al. (2021). “Contrasting Response of West and East Antarctic Ice Sheets to Glacial Isostatic Adjustment”. In: *Journal of Geophysical Research: Earth Surface* 126.7, e2020JF006003.
- Craig, T. J. et al. (2011). “Earthquake distribution patterns in Africa: Their relationship to variations in lithospheric and geological structure, and their rheological implications”. In: *Geophysical Journal International* 185.1, pp. 403–434.
- Dahl-Jensen, D., V. I. Morgan, and A. Elcheikh (1999). “Monte Carlo inverse modelling of the Law Dome (Antarctica) temperature profile”. In: *Annals of Glaciology* 29, pp. 145–150.
- Dalton, C. A., G. Ekström, and A. M. Dziewoński (2008). “The global attenuation structure of the upper mantle”. In: *Journal of Geophysical Research: Solid Earth* 113.B9.

Dalton, C. A., C. H. Langmuir, and A. Gale (2014). “Geophysical and Geochemical Evidence for

Deep Temperature Variations Beneath Mid-Ocean Ridges”. In: *Science* 344.6179, pp. 80–83.

Davies, B. J. et al. (2014). “Modelled glacier response to centennial temperature and precipi-

tation trends on the Antarctic Peninsula”. In: *Nature Climate Change* 4.11, pp. 993–998.

Davies, D. R. et al. (2019). “Earth’s multi-scale topographic response to global mantle flow”.

In: *Nature Geoscience* 12.10, pp. 845–850.

Debayle, E., F. Dubuffet, and S. Durand (2016). “An automatically updated S-wave model of

the upper mantle and the depth extent of azimuthal anisotropy”. In: *Geophysical Research*

Letters 43, pp. 674–682.

DeConto, R. M. and D. Pollard (2016). “Contribution of Antarctica to past and future sea-level

rise”. In: *Nature* 531.7596, pp. 591–597.

DIGIS Team (2021). “GEOROC Compilation: Rift Volcanics”. In: *Goettingen Research Online*

/ Data, V6.

Downes, P. J. et al. (2023). “Perovskite geochronology and petrogenesis of the Neoproterozoic

Mad Gap Yards ultramafic lamprophyre dykes, East Kimberley region, Western Australia”.

In: *Contributions to Mineralogy and Petrology* 178, p. 21.

Dziadek, R., K. Gohl, and N. Kaul (2019). “Elevated geothermal surface heat flow in the

Amundsen Sea Embayment, West Antarctica”. In: *Earth and Planetary Science Letters*

506, pp. 530–539.

Dziadek, R. et al. (2021). “Towards Closing the Polar Gap: New Marine Heat Flow Observations

in Antarctica and the Arctic Ocean”. In: *Geosciences* 11.1.

Dziewonski, A. M. and D. L. Anderson (1981). “Preliminary reference Earth model”. In: *Physics*

of the Earth and Planetary Interiors 25.4, pp. 297–356.

Eilon, Z., K. M. Fischer, and C. A. Dalton (2018). “An adaptive Bayesian inversion for upper-

mantle structure using surface waves and scattered body waves”. In: *Geophysical Journal International* 214.1, pp. 232–253.

Engelhardt, H. (2004). “Ice temperature and high geothermal flux at Siple Dome, West Antarctica, from borehole measurements”. In: *Journal of Glaciology* 50.169, pp. 251–256.

Farrell, W. E. (1972). “Deformation of the Earth by surface loads”. In: *Reviews of Geophysics* 10.3, pp. 761–797.

Farrell, W. E. and J. A. Clark (1976). “On Postglacial Sea Level”. In: *Geophysical Journal International* 46.3, pp. 647–667.

Faul, U. H. and I. Jackson (2005). “The seismological signature of temperature and grain size variations in the upper mantle”. In: *Earth and Planetary Science Letters* 234.1, pp. 119–134.

Faul, U. H., I. Jackson, and Y. X (2007). “Diffusion creep of dry, melt-free olivine”. In: *J. Geophys. Res.* 112.B4.

Ferguson, J. and J. W. Sheraton (1982). “Petrogenesis of kimberlitic rocks and associated xenoliths of southeastern Australia”. In: *Kimberlites, diatremes, and diamonds: Their geology, petrology, and geochemistry*. Ed. by H. O. A. Meyer and F. R. Boyd. Vol. 15. American Geophysical Union, pp. 140–160.

Fielding, D. C. and A. L. Jaques (1986). “Geology, petrology and geochemistry of the Bow Hill lamprophyre dykes, Western Australia”. In: *Proceedings of the 4th International Kimberlite Conference*. Perth, pp. 24–26.

Fiorentini, M. L. et al. (2020). “Bushveld superplume drove Proterozoic magmatism and met-allogenesis in Australia”. In: *Scientific Reports* 10, p. 19729.

Fisher, A. T. et al. (2015). “High geothermal heat flux measured below the West Antarctic Ice Sheet”. In: *Science Advances* 1.6.

- Fishwick, S. and N. Rawlinson (2012). “3-D structure of the Australian lithosphere from evolving seismic datasets”. In: *Australian Journal of Earth Sciences* 59, pp. 809–826.
- Fretwell, P. et al. (2013). “Bedmap2: improved ice bed, surface and thickness datasets for Antarctica”. In: *The Cryosphere* 7.1, pp. 375–393.
- Fukuda, J. and K. M. Johnson (2010). “Mixed linear–non-linear inversion of crustal deformation data: Bayesian inference of model, weighting and regularization parameters”. In: *Geophysical Journal International* 181.3, pp. 1441–1458.
- Gallagher, K. et al. (2009). “Markov chain Monte Carlo (MCMC) sampling methods to determine optimal models, model resolution and model choice for Earth Science problems”. In: *Marine and Petroleum Geology* 26.4. Thematic Set on Basin Modeling Perspectives, pp. 525–535.
- Gasson, E., R. DeConto, and D. Pollard (2015). “Antarctic bedrock topography uncertainty and ice sheet stability”. In: *Geophysical Research Letters* 42.13, pp. 5372–5377.
- Gaul, O. F., S. Y. O'Reilly, and W. L. Griffin (2003). “Lithosphere structure and evolution in southeastern Australia”. In: *Geological Society of Australia Special Publications* 372, pp. 185–202.
- Gelman, A., W. R. Gilks, and G. O. Roberts (1997). “Weak convergence and optimal scaling of random walk Metropolis algorithms”. In: *The Annals of Applied Probability* 7.1, pp. 110–120.
- Gibson, G. et al. (2016). “Basin architecture and evolution in the Mount Isa mineral province, northern Australia: Constraints from deep seismic reflection profiling and implications for ore genesis”. In: *Ore Geology Reviews* 76, pp. 414–441.
- Gleadow, A. J. W. and A. C. Edwards (1978). “Mineralogical note: Fission-track age of a basic inclusion from the Kayrunnera kimberlitic breccia pipe”. In: *Journal of the Geological Society of Australia* 25, p. 359.

Goes, S. et al. (2020). “Continental lithospheric temperatures: A review”. In: *Physics of the*

Earth and Planetary Interiors 306, p. 106509.

Gomez, N., K. Latychev, and D. Pollard (2018). “A Coupled Ice Sheet–Sea Level Model Incorporating 3D Earth Structure: Variations in Antarctica during the Last Deglacial Retreat”.

In: *Journal of Climate* 31.10, pp. 4041–4054.

Gomez, N. et al. (2010). “Sea level as a stabilizing factor for marine-ice-sheet grounding lines”.

In: *Nature Geoscience* 3.12, pp. 850–853.

Goodge, J. W. and J. P. Severinghaus (2016). “Rapid Access Ice Drill: a new tool for exploration

of the deep Antarctic ice sheets and subglacial geology”. In: *Journal of Glaciology* 62.236,

pp. 1049–1064.

Griffin, T. J. and I. McDougall (1975). “Geochronology of the Cainozoic McBride volcanic

province, northern Queensland”. In: *Journal of the Geological Society of Australia* 22,

pp. 387–396.

Griffin, W. L. and S. Y. O'Reilly (1986). “Mantle-derived sapphirine”. In: *Mineralogical Mag-*

azine 50, pp. 635–640.

Griffin, W. L., S. Y. O'Reilly, and A. Stabel (1988). “Mantle metasomatism beneath west-

ern Victoria, Australia: II. Isotopic geochemistry of Cr-diopside lherzolites and Al-augite

pyroxenites”. In: *Geochimica et Cosmochimica Acta* 52, pp. 449–459.

Griffin, W. L., F. L. Sutherland, and J. D. Hollis (1987). “Geothermal profile and crust-mantle

transition beneath east-central Queensland: Volcanology, xenolith petrology and seismic

data”. In: *Journal of Volcanology and Geothermal Research* 31, pp. 177–203.

Griffin, W. L., S. Wass, and J. D. Hollis (1984). “Ultramafic xenoliths from Bullenmerri and

Gnotuk Maars, Victoria, Australia: Petrology of a sub-continental crust-mantle transition”.

In: *Journal of Petrology* 25, pp. 53–87.

- Griffin, W. L. et al. (1999). “Harzburgite to lherzolite and back again: Metasomatic processes in ultramafic xenoliths from the Wesselton kimberlite, Kimberley, South Africa”. In: *Contrib Mineral Petrol* 134, pp. 232–250.
- Grose, C. J. and J. C. Afonso (2013). “Comprehensive plate models for the thermal evolution of oceanic lithosphere”. In: *Geochemistry, Geophysics, Geosystems* 14.9, pp. 3751–3778.
- Haario, H., E. Saksman, and J. Tamminen (2001). “An Adaptive Metropolis Algorithm”. In: *Bernoulli* 7.2, pp. 223–242.
- Haeger, C., A. G. Petrunin, and M. K. Kaban (2022). “Geothermal Heat Flow and Thermal Structure of the Antarctic Lithosphere”. In: *Geochemistry, Geophysics, Geosystems* 23.10, e2022GC010501.
- Hasterok, D. and D. S. Chapman (2011). “Heat production and geotherms for the continental lithosphere”. In: *Earth and Planetary Science Letters* 307.1, pp. 59–70.
- Hazzard, J. A. N. and F. D. Richards (2024a). “Antarctic Geothermal Heat Flow, Crustal Conductivity and Heat Production Inferred From Seismological Data”. In: *OSF Online Repository*. Dataset.
- (2024b). “Antarctic Geothermal Heat Flow, Crustal Conductivity and Heat Production Inferred From Seismological Data”. In: *Geophysical Research Letters* 51.7, e2023GL106274.
- Hazzard, J. A. N. et al. (2023). “Probabilistic Assessment of Antarctic Thermomechanical Structure: Impacts on Ice Sheet Stability”. In: *Journal of Geophysical Research: Solid Earth* 128.5, e2023JB026653.
- Hell, A. et al. (2003). “The geology, age, near surface features and mineralogy of the Merlin kimberlites, Northern Territory, Australia”. In: *Proceedings of the 8th International Kimberlite Conference*, p. 5.
- Hinkel, J. et al. (2014). “Coastal flood damage and adaptation costs under 21st century sea-level rise”. In: *Proceedings of the National Academy of Sciences* 111.9, pp. 3292–3297.

Hirth, G. and D. Kohlstedt (2004). “Rheology of the Upper Mantle and the Mantle Wedge: A View from the Experimentalists”. In: *Inside the Subduction Factory*. American Geophysical Union (AGU), pp. 83–105.

Hoggard, M. J. et al. (2020). “Global distribution of sediment-hosted metals controlled by craton edge stability”. In: *Nature Geoscience* 13.7, pp. 504–510.

Hondoh, T. et al. (2002). “Depth–age and temperature prediction at Dome Fuji station, East Antarctica”. In: *Annals of Glaciology* 35, pp. 384–390.

Huston, D. L. et al. (2016). “Tectono-metallogenic systems — The place of mineral systems within tectonic evolution, with an emphasis on Australian examples”. In: *Ore Geology Reviews* 76, pp. 168–210.

Hutchison, M. T. (2011). *Northern Territory diamond exploration database*. Tech. rep. Northern Territory Geological Survey.

Hutchison, M. T. (2018). “Diamond exploration and regional prospectivity of Western Australia”. In: *Mineralogy and Petrology* 112, pp. 737–753.

Irving, A. J. (1974). “Geochemical and high pressure experimental studies of garnet pyroxenite and pyroxene granulite xenoliths from the Delegate basaltic pipes, Australia”. In: *Journal of Petrology* 15.1, pp. 1–40.

Ivins, E. R. et al. (2020). “A linear viscoelasticity for decadal to centennial time scale mantle deformation”. In: *Reports on Progress in Physics* 83.10, p. 106801.

Ivins, E. R. et al. (2021). “Antarctic upper mantle rheology”. In: *Geological Society, London, Memoirs* 56.

Ivins, E. R. et al. (2011). “On-land ice loss and glacial isostatic adjustment at the Drake Passage: 2003–2009”. In: *Journal of Geophysical Research: Solid Earth* 116.B2.

Jackson, I. (2019). “Viscoelastic Behaviour from Complementary Forced-Oscillation and Microcreep Tests”. In: *Minerals* 9.12.

Jackson, I. and U. H. Faul (2010). “Grainsize-sensitive viscoelastic relaxation in olivine: Towards

a robust laboratory-based model for seismological application”. In: *Physics of the Earth and Planetary Interiors* 183.1-2, pp. 151–163.

Jackson, I., U. H. Faul, and R. Skelton (2014). “Elastically accommodated grain-boundary

sliding: New insights from experiment and modeling”. In: *Physics of the Earth and Planetary Interiors* 228. High-Pressure Research in Earth Science: Crust, Mantle, and Core, pp. 203–210.

Jain, C., J. Korenaga, and S.-i. Karato (2019). “Global Analysis of Experimental Data on the

Rheology of Olivine Aggregates”. In: *Journal of Geophysical Research: Solid Earth* 124.1, pp. 310–334.

Jaques, A. L. and S. F. Foley (2018). “Insights into the petrogenesis of the West Kimberley lamproites from trace elements in olivine”. In: *Mineralogy and Petrology* 112, pp. 519–537.

Jaques, A. L., J. D. Lewis, and C. B. Smith (1986). *The Kimberlites and Lamproites of Western Australia*. Tech. rep. Perth: Geological Survey of West Australia, p. 357.

Jaques, A. L. and P. R. Milligan (2004). “Patterns and controls on the distribution of diamondiferous intrusions in Australia”. In: *Lithos* 77, pp. 783–802.

Jaques, A. L. et al. (1984). “The diamond-bearing ultrapotassic (lamproitic) rocks of the West Kimberley region, Western Australia”. In: *Developments in Petrology* 11.A, pp. 225–254.

Jaques, A. L. et al. (1989a). “Composition of crystalline inclusions and C-isotopic composition of Argyle and Ellendale diamonds”. In: *Geological Society of Australia Special Publication* 14, pp. 966–989.

Jaques, A. L. et al. (1989b). “Mineralogy and petrology of the Argyle (AK1) lamproite pipe, Western Australia”. In: *Geological Society of Australia Special Publications* 14, pp. 153–188.

Jaques, A. L. et al. (1990). "Diamondiferous peridotite xenoliths from the Argyle (AK1) lam-

proite pipe, Western Australia". In: *Contributions to Mineralogy and Petrology* 104, pp. 255–276.

Jaques, A. L. et al. (1994). "Peridotitic planar octahedral diamonds from the Ellendale lam-

proite pipes, Western Australia". In: *Proceedings of the 5th International Kimberlite Conference*, pp. 69–77.

Jennings, S., D. Hasterok, and J. Payne (2019). "A new compositionally based thermal con-

ductivity model for plutonic rocks". In: *Geophysical Journal International* 219.2, pp. 1377–1394.

Karato, S. and H. Jung (1998). "Water, partial melting and the origin of the seismic low velocity

and high attenuation zone in the upper mantle". In: *Earth and Planetary Science Letters* 157.3, pp. 193–207.

Kay, S. M. and R. W. Kay (1983). "Thermal history of the deep crust inferred from granulite

xenoliths, Queensland, Australia". In: *American Journal of Science* 283-A, pp. 486–513.

Kendall, R. A., J. X. Mitrovica, and G. A. Milne (2005). "On post-glacial sea level – II. Numer-

ical formulation and comparative results on spherically symmetric models". In: *Geophysical Journal International* 161.3, pp. 679–706.

Kennett, B. L. N. et al. (2011). "AusMoho: the variation of Moho depth in Australia". In:

Geophysical Journal International 187.2, pp. 946–958.

King, M. A. et al. (2012). "Lower satellite-gravimetry estimates of Antarctic sea-level contri-

bution". In: *Nature* 491.7425, pp. 586–589.

Kingslake, J. et al. (2018). "Extensive retreat and re-advance of the West Antarctic Ice Sheet

during the Holocene". In: *Nature* 558.7710, pp. 430–434.

- Klein, E. et al. (2016). “Afterslip and viscoelastic relaxation model inferred from the large-scale post-seismic deformation following the 2010 Mw 8.8 Maule earthquake (Chile)”. In: *Geophysical Journal International* 205.3, pp. 1455–1472.
- Klöcking, M. et al. (2020). “A tale of two domes: Neogene to recent volcanism and dynamic uplift of northeast Brazil and southwest Africa”. In: *Earth and Planetary Science Letters* 547, p. 116464.
- Kolff, L. (2010). *Timber Creek ERL 25981 – Final diamond recovery and mineral chemical data*. Tech. rep. Tawana Resources, CR2010–0065.
- Korenaga, T. and J. Korenaga (2016). “Evolution of young oceanic lithosphere and the meaning of seafloor subsidence rate”. In: *Journal of Geophysical Research: Solid Earth* 121.9, pp. 6315–6332.
- Larour, E. et al. (2012). “Ice flow sensitivity to geothermal heat flux of Pine Island Glacier, Antarctica”. In: *Journal of Geophysical Research: Earth Surface* 117.F4.
- Lau, H. C. P. (2024). “Surface loading on a self-gravitating, linear viscoelastic Earth: moving beyond Maxwell”. In: *Geophysical Journal International* 237.3, pp. 1842–1857.
- Lau, H. C. P. et al. (2021). “Frequency Dependent Mantle Viscoelasticity via the Complex Viscosity: Cases From Antarctica”. In: *J Geophys Res Solid Earth* 126.11, e2021JB022622.
- Lau, H. C. P. and B. K. Holtzman (2019). ““Measures of Dissipation in Viscoelastic Media” Extended: Toward Continuous Characterization Across Very Broad Geophysical Time Scales”. In: *Geophysical Research Letters* 46.16, pp. 9544–9553.
- Lau, H. C. P. et al. (2016). “Inferences of mantle viscosity based on ice age data sets: Radial structure”. In: *Journal of Geophysical Research: Solid Earth* 121.10, pp. 6991–7012.
- Lau, H. C. (2023). “Transient rheology in sea level change: Implications for Meltwater Pulse 1A”. In: *Earth and Planetary Science Letters* 609, p. 118106.

- Lee, C. (2003). “Compositional variation of density and seismic velocities in natural peridotites at STP conditions: Implications for seismic imaging of compositional heterogeneities in the upper mantle”. In: *Journal of Geophysical Research: Solid Earth* 108.B9.
- Lee, D. C. et al. (1997). “The Merlin kimberlites, Northern Territory, Australia”. In: *Russian Geology and Geophysics* 38, pp. 82–96.
- LeMasurier, W. E. (2008). “Neogene extension and basin deepening in the West Antarctic rift inferred from comparisons with the East African rift and other analogs”. In: *Geology* 36.3, pp. 247–250.
- Lin, Y. et al. (2021). “A reconciled solution of Meltwater Pulse 1A sources using sea-level fingerprinting”. In: *Nature Communications* 12.1, p. 2015.
- Lloyd, A. J. et al. (2020). “Seismic Structure of the Antarctic Upper Mantle Imaged with Adjoint Tomography”. In: *Journal of Geophysical Research: Solid Earth* 125.3.
- Lösing, M., J. Ebbing, and W. Szwilus (2020). “Geothermal Heat Flux in Antarctica: Assessing Models and Observations by Bayesian Inversion”. In: *Frontiers in Earth Science* 8.
- Love, A. E. H. (1909). “The yielding of the earth to disturbing forces”. In: *Proceedings of the Royal Society of London. Series A, Containing Papers of a Mathematical and Physical Character* 82.551, pp. 73–88.
- Lovering, J. F. and J. R. Richards (1964). “Potassium-argon age study of possible lower-crust and upper-mantle inclusions in deep-seated intrusions”. In: *Journal of Geophysical Research* 69, pp. 4895–4901.
- Lovering, J. F. and A. J. R. White (1969). “Granulitic and eclogitic inclusions from basic pipes at Delegate, Australia”. In: *Contributions to Mineralogy and Petrology* 21, pp. 9–52.
- Lu, J. et al. (2018). “Tracking deep lithospheric events with garnet-websterite xenoliths from southeastern Australia”. In: *Journal of Petrology* 59, pp. 901–930.

- Lu, J. et al. (2020). "Lithospheric memory of subduction in mantle pyroxenite xenoliths from rift-related basalts". In: *Earth and Planetary Science Letters* 544, p. 116365.
- Lucas, E. M. et al. (2021). "Seismicity and Pn Velocity Structure of Central West Antarctica". In: *Geochemistry, Geophysics, Geosystems* 22.2, e2020GC009471.
- Lucazeau, F. (2019). "Analysis and Mapping of an Updated Terrestrial Heat Flow Data Set". In: *Geochemistry, Geophysics, Geosystems* 20.8, pp. 4001–4024.
- Luguet, A. et al. (2009). "An integrated petrological, geochemical and Re-Os isotope study of peridotite xenoliths from the Argyle lamproite, Western Australia and implications for cratonic diamond occurrences". In: *Lithos* 112, pp. 1096–1108.
- Martos, Y. M. et al. (2017). "Heat Flux Distribution of Antarctica Unveiled". In: *Geophysical Research Letters* 44.22, pp. 11, 417–11, 426.
- Mather, K. A. et al. (2011). "Constraints on the depth and thermal history of cratonic lithosphere from peridotite xenoliths, xenocrysts and seismology". In: *Lithos* 125, pp. 729–742.
- Maule, C. F. et al. (2005). "Heat Flux Anomalies in Antarctica Revealed by Satellite Magnetic Data". In: *Science* 309.5733, pp. 464–467.
- McCarthy, C. and Y. Takei (2011). "Anelasticity and viscosity of partially molten rock analogue: Toward seismic detection of small quantities of melt". In: *Geophys. Res. Lett.* 38.18.
- McKenzie, D. (2000). "Constraints on melt generation and transport from U-series activity ratios". In: *Chemical Geology* 162.2, pp. 81–94.
- McKenzie, D., J. Jackson, and K. Priestley (2005). "Thermal structure of oceanic and continental lithosphere". In: *Earth and Planetary Science Letters* 233.3, pp. 337–349.
- Metropolis, N. et al. (1953). "Equation of State Calculations by Fast Computing Machines". In: *J. Chem. Phys.* 21.6, pp. 1087–1092.

Milne, G., M. Yousefi, and K. Latychev (2021). “Quantifying the influence of glacial isostatic ad-

justment on current and future sea-level change using 3-D Earth models”. In: *EGU General Assembly 2021, online, 19-30 Apr 2021, EGU21-13813*.

Milne, G. A. et al. (2018). “The influence of lateral Earth structure on glacial isostatic adjustment in Greenland”. In: *Geophysical Journal International* 214.2, pp. 1252–1266.

Mitrovica, J. X., J. L. Davis, and I. I. Shapiro (1994). “A spectral formalism for computing three-dimensional deformations due to surface loads: 1. Theory”. In: *Journal of Geophysical Research: Solid Earth* 99.B4, pp. 7057–7073.

Mitrovica, J. X. and W. R. Peltier (1992). “A comparison of methods for the inversion of viscoelastic relaxation spectra”. In: *Geophysical Journal International* 108.2, pp. 410–414.

Mitrovica, J. and G. Milne (2002). “On the origin of late Holocene sea-level highstands within equatorial ocean basins”. In: *Quaternary Science Reviews* 21.20, pp. 2179–2190.

Mitrovica, J. et al. (2020). “Dynamic Topography and Ice Age Paleoclimate”. In: *Annual Review of Earth and Planetary Sciences* 48.1, pp. 585–621.

Morlighem, M. et al. (2017). “BedMachine v3: Complete Bed Topography and Ocean Bathymetry Mapping of Greenland From Multibeam Echo Sounding Combined With Mass Conservation”. In: *Geophysical Research Letters* 44.21, pp. 11, 051–11, 061.

Morlighem, M. et al. (2020). “Deep glacial troughs and stabilizing ridges unveiled beneath the margins of the Antarctic ice sheet”. In: *Nature Geoscience* 13.2, pp. 132–137.

Nicholls, R. J. and A. Cazenave (2010). “Sea-Level Rise and Its Impact on Coastal Zones”. In: *Science* 328.5985, pp. 1517–1520.

Nicholls, R. J. et al. (2011). “Sea-level rise and its possible impacts given a ‘beyond 4°C world’ in the twenty-first century”. In: *Philosophical Transactions of the Royal Society A: Mathematical, Physical and Engineering Sciences* 369.1934, pp. 161–181.

- Nickel, K. G. and D. H. Green (1985). “Empirical geothermobarometry for garnet peridotites and implications for the nature of the lithosphere, kimberlites and diamonds”. In: *Earth and Planetary Science Letters* 73, pp. 158–170.
- Nield, G. A. et al. (2014). “Rapid bedrock uplift in the Antarctic Peninsula explained by viscoelastic response to recent ice unloading”. In: *Earth and Planetary Science Letters* 397, pp. 32–41.
- Nield, G. A. et al. (2023). “Postseismic Deformation in the Northern Antarctic Peninsula Following the 2003 and 2013 Scotia Sea Earthquakes”. In: *Journal of Geophysical Research: Solid Earth* 128.10. e2023JB026685 2023JB026685, e2023JB026685.
- Nimis, P. and H. Grüter (2010). “Internally consistent geothermometers for garnet peridotites and pyroxenites”. In: *Contributions to Mineralogy and Petrology* 159, pp. 411–427.
- Nimis, P. and W. R. Taylor (2000). “Single clinopyroxene thermobarometry for garnet peridotites. Part I. Calibration and testing of a Cr-in-Cpx barometer and an enstatite-in-Cpx thermometer”. In: *Contributions to Mineralogy and Petrology* 139, pp. 541–554.
- NOAA National Geophysical Data Center (2006). *2-minute Gridded Global Relief Data (ETOPO2)* v2. Ed. by NOAA National Centers for Environmental Information.
- Noble, T. L. et al. (2020). “The Sensitivity of the Antarctic Ice Sheet to a Changing Climate: Past, Present, and Future”. In: *Reviews of Geophysics* 58.4, e2019RG000663.
- Nowick, A. S. and B. S. Berry (1972). *Anelastic Relaxation in Crystalline Solids*. Academic Press.
- O'Reilly, S. Y. and W. L. Griffin (1985). “A xenolith-derived geotherm for southeastern Australia and its geophysical implications”. In: *Tectonophysics* 111, pp. 41–63.
- Olierook, H. K. H. et al. (2023). “Emplacement of the Argyle diamond deposit into an ancient rift zone triggered by supercontinent breakup”. In: *Nature Communications* 14, p. 5274.

- Oppenheimer, M. et al. (2019a). *IPCC Special Report on the Ocean and Cryosphere in a Changing Climate. Sea Level Rise and Implications for Low-Lying Islands, Coasts and Communities*.
- (2019b). “Sea Level Rise and Implications for Low-Lying Islands, Coasts and Communities”. In: *IPCC Special Report on the Ocean and Cryosphere in a Changing Climate*.
- Pappa, F. et al. (2019). “Modeling Satellite Gravity Gradient Data to Derive Density, Temperature, and Viscosity Structure of the Antarctic Lithosphere”. In: *J. Geophys. Res. Solid Earth* 124.11, pp. 12053–12076.
- Paxman, G. J. G. et al. (2020). “Long-Term Increase in Antarctic Ice Sheet Vulnerability Driven by Bed Topography Evolution”. In: *Geophysical Research Letters* 47.20, e2020GL090003.
- Peltier, W. R. (1974). “The impulse response of a Maxwell Earth”. In: *Reviews of Geophysics* 12.4, pp. 649–669.
- (1976). “Glacial-Isostatic Adjustment—II. The Inverse Problem”. In: *Geophysical Journal International* 46.3, pp. 669–705.
- (1985). “The LAGEOS constraint on deep mantle viscosity: Results from a new normal mode method for the inversion of viscoelastic relaxation spectra”. In: *Journal of Geophysical Research: Solid Earth* 90.B11, pp. 9411–9421.
- Phillips, D., L. F. Fourie, and G. B. Kiviet (1997). *⁴⁰Ar/³⁹Ar laser probe analysis of groundmass phlogopite grains from the Jewill kimberlite, Yilgarn Craton, Western Australia*. Tech. rep. Anglo American Research Laboratories.
- Phillips, D., W. Clarke, and A. L. Jaques (2022). “Age and origin of the West Kimberley lamproites, Western Australia”. In: *Lithos* 432-433, p. 106913.
- Pidgeon, R. T., C. B. Smith, and C. M. Fanning (1989). “Kimberlite and lamproite emplacement ages in Western Australia”. In: *Geological Society of Australia Special Publication* 14, pp. 369–381.

- Powell, E. et al. (2022). “The robustness of geodetically derived 1-D Antarctic viscosity models in the presence of complex 3-D viscoelastic Earth structure”. In: *Geophysical Journal International* 231.1, pp. 118–128.
- Press, W. H. et al. (2007). *Numerical Recipes: The Art of Scientific Computing*. Third edition. Cambridge University Press.
- Price, P. B. et al. (2002). “Temperature profile for glacial ice at the South Pole: Implications for life in a nearby subglacial lake”. In: *Proceedings of the National Academy of Sciences* 99.12, pp. 7844–7847.
- Priestley, K. and D. McKenzie (2006). “The thermal structure of the lithosphere from shear wave velocities”. In: *Earth and Planetary Science Letters* 244.1, pp. 285–301.
- (2013). “The relationship between shear wave velocity, temperature, attenuation and viscosity in the shallow part of the mantle”. In: *Earth and Planetary Science Letters* 381, pp. 78–91.
- Priestley, K., D. McKenzie, and T. Ho (2018). “A Lithosphere–Asthenosphere Boundary—a Global Model Derived from Multimode Surface-Wave Tomography and Petrology”. In: *Lithospheric Discontinuities*. American Geophysical Union (AGU). Chap. 6, pp. 111–123.
- Priestley, K. et al. (2024). “The thermal and anisotropic structure of the top 300 km of the mantle”. In: *Earth and Planetary Science Letters* 626, p. 118525.
- Qu, T., I. Jackson, and U. H. Faul (2021). “Low-Frequency Seismic Properties of Olivine-Orthopyroxene Mixtures”. In: *Journal of Geophysical Research: Solid Earth* 126.10, e2021JB022504.
- Qu, T. et al. (2024). “The onset of anelastic behavior in fine-grained synthetic dunite”. In: *Physics of the Earth and Planetary Interiors* 350, p. 107160.
- Ramsay, R. R. (1992). “Geochemistry of diamond indicator minerals”. PhD. University of Western Australia.

Richards, F. D. et al. (2018). “Reassessing the Thermal Structure of Oceanic Lithosphere With Revised Global Inventories of Basement Depths and Heat Flow Measurements”. In: *Journal of Geophysical Research: Solid Earth* 123.10, pp. 9136–9161.

Richards, F. D. et al. (2020a). “Quantifying the Relationship Between Short-Wavelength Dynamic Topography and Thermomechanical Structure of the Upper Mantle Using Calibrated Parameterization of Anelasticity”. In: *Journal of Geophysical Research: Solid Earth* 125.9, e2019JB019062.

Richards, F. D. et al. (2020b). “Structure and dynamics of the oceanic lithosphere-asthenosphere system”. In: *Physics of the Earth and Planetary Interiors* 309, p. 106559.

Richards, F. D. et al. (2023). “Geodynamically corrected Pliocene shoreline elevations in Australia consistent with midrange projections of Antarctic ice loss”. In: *Science Advances* 9.46, eadg3035.

Roach, I. C. (2004). “Mineralogy, textures and P-T relationships of a suite of xenoliths from the Monaro volcanic province, New South Wales, Australia”. In: *Journal of Petrology* 45, pp. 739–758.

Robertson, A. D., F. L. Sutherland, and J. D. Hollis (1985). “Upper mantle xenoliths and megacrysts and the origin of the Brigooda basalt and breccia, near Proston, Queensland”. In: *Papers of the Department of Geology, University of Queensland* 11.3, pp. 58–71.

Rovere, A. et al. (2014). “The Mid-Pliocene sea-level conundrum: Glacial isostasy, eustasy and dynamic topography”. In: *Earth and Planetary Science Letters* 387, pp. 27–33.

Roy, V. (2020). “Convergence Diagnostics for Markov Chain Monte Carlo”. In: *Annual Review of Statistics and Its Application* 7.1, pp. 387–412.

Salamatin, A. N. et al. (1998). “Ice core age dating and paleothermometer calibration based on isotope and temperature profiles from deep boreholes at Vostok Station (East Antarctica)”. In: *Journal of Geophysical Research: Atmospheres* 103.D8, pp. 8963–8977.

Sammon, L. G., W. F. McDonough, and W. D. Mooney (2022). “Compositional Attributes of

the Deep Continental Crust Inferred From Geochemical and Geophysical Data”. In: *Journal of Geophysical Research: Solid Earth* 127.8, e2022JB024041.

Samrat, N. H. et al. (2021). “Upper Mantle Viscosity Underneath Northern Marguerite Bay, Antarctic Peninsula Constrained by Bedrock Uplift and Ice Mass Variability”. In: *Geophysical Research Letters* 48.24, e2021GL097065.

Sas, Z. A. (1997). *Brigooda diamond project*. Tech. rep. Australian Kimberley Diamonds, p. 13.

Sauli, C. et al. (2021). “Neogene development of the terror rift, Western Ross Sea, Antarctica”. In: *Geochemistry, Geophysics, Geosystems* 22.3, e2020GC009076.

Schaeffer, A. J. and S. Lebedev (2013). “Global shear speed structure of the upper mantle and transition zone”. In: *Geophysical Journal International* 194.1, pp. 417–449.

Scott Smith, B. H. et al. (1984). “Kimberlites near Orroroo, South Australia”. In: *Proceedings of the 3rd International Kimberlite Conference*. Ed. by J. Kornbrobst. Vol. 1. Elsevier, pp. 121–142.

Seroussi, H. et al. (2017). “Influence of a West Antarctic mantle plume on ice sheet basal conditions”. In: *Journal of Geophysical Research: Solid Earth* 122.9, pp. 7127–7155.

Shapiro, N. M. and M. H. Ritzwoller (2004). “Inferring surface heat flux distributions guided by a global seismic model: particular application to Antarctica”. In: *Earth and Planetary Science Letters* 223.1, pp. 213–224.

Shen, Q. et al. (2018a). “Recent high-resolution Antarctic ice velocity maps reveal increased mass loss in Wilkes Land, East Antarctica”. In: *Scientific Reports* 8.1, p. 4477.

Shen, W. and M. H. Ritzwoller (2016). “Crustal and uppermost mantle structure beneath the United States”. In: *Journal of Geophysical Research: Solid Earth* 121.6, pp. 4306–4342.

Shen, W. et al. (2018b). “The Crust and Upper Mantle Structure of Central and West Antarctica From Bayesian Inversion of Rayleigh Wave and Receiver Functions”. In: *Journal of Geophysical Research: Solid Earth* 123.9, pp. 7824–7849.

Shen, W. et al. (2020). “A Geothermal Heat Flux Map of Antarctica Empirically Constrained by Seismic Structure”. In: *Geophysical Research Letters* 47.14, e2020GL086955.

Shepherd, A., H. A. Fricker, and S. L. Farrell (2018a). “Trends and connections across the Antarctic cryosphere”. In: *Nature* 558.7709, pp. 223–232.

Shepherd, A. et al. (2018b). “Mass balance of the Antarctic Ice Sheet from 1992 to 2017”. In: *Nature* 558.7709, pp. 219–222.

Shepherd, A. et al. (2020). “Mass balance of the Greenland Ice Sheet from 1992 to 2018”. In: *Nature* 579.7798, pp. 233–239.

Shida, T. (1912). “On the elasticity of the Earth and the Earth’s crust”. In: *Memoirs of the College of Science and Engineering, Kyoto Imperial University* 4, pp. 1–286.

Slangen, A. B. A. et al. (2017). “A Review of Recent Updates of Sea-Level Projections at Global and Regional Scales”. In: *Surveys in Geophysics* 38.1, pp. 385–406.

Sloan, R. A. et al. (2011). “Earthquake depth distributions in central Asia, and their relations with lithosphere thickness, shortening and extension”. In: *Geophysical Journal International* 185.1, pp. 1–29.

Sobolev, N. V. et al. (1989). “A comparative study of the morphology, inclusions and carbon isotopic composition of diamonds from alluvials of the King George River and Argyle lamproite mine (Western Australia), and of cube microdiamonds from northern Australia”. In: *Soviet Geology and Geophysics* 12, pp. 3–19.

Spencer, S. E. (2021). “Accelerating adaptation in the adaptive Metropolis–Hastings random walk algorithm”. In: *Australian & New Zealand Journal of Statistics* 63.3, pp. 468–484.

- Stachel, T. et al. (2018). “Argyle diamonds: How subduction along the Kimberley Craton edge generated the world’s biggest diamond deposit”. In: *Society of Economic Geologists Special Publication* 20, pp. 145–167.
- Steinberger, B. et al. (2019). “On the amplitude of dynamic topography at spherical harmonic degree two”. In: *Tectonophysics* 760. Linking Plate Tectonics and Volcanism to Deep Earth Dynamics – a tribute to Trond H. Torsvik, pp. 221–228.
- Stephenson, S. N., P. W. Ball, and F. D. Richards (2023). “Destruction and regrowth of lithospheric mantle beneath large igneous provinces”. In: *Science Advances* 9.36, eadf6216.
- Stixrude, L. and C. Lithgow-Bertelloni (2011). “Thermodynamics of mantle minerals - II. Phase equilibria”. In: *Geophysical Journal International* 184.3, pp. 1180–1213.
- Stolz, A. J. (1987). “Fluid activity in the lower crust and upper mantle: Mineralogical evidence bearing on the origin of amphibole and scapolite in ultramafic and mafic granulite xenoliths”. In: *Mineralogical Magazine* 51, pp. 719–732.
- Sudholz, Z. J. et al. (2021). “Experimental recalibration of the Cr-in-clinopyroxene geobarometer: Improved precision and reliability above 4.5 GPa”. In: *Contributions to Mineralogy and Petrology* 176.11.
- Sudholz, Z. J. et al. (2022). “Multi-stage evolution of the South Australian Craton: Petrological constraints on the architecture, lithology, and geochemistry of the lithospheric mantle”. In: *Geochemistry, Geophysics, Geosystems* 23, e2022GC010558.
- Sudholz, Z. J. et al. (2023a). “Mapping the structure and metasomatic enrichment of the lithospheric mantle beneath the Kimberley Craton, Western Australia”. In: *Geochemistry, Geophysics, Geosystems* 24, e2023GC011040.
- Sudholz, Z. J. et al. (2023b). “Petrology, age, and rift origin of ultramafic lamprophyres (Ailikites) at Mount Webb, a new alkaline province in central Australia”. In: *Geochemistry, Geophysics, Geosystems* 24, e2023GC011120.

Sutherland, F. L. (1996). “Alkaline rocks and gemstones, Australia: A review and synthesis”. In: *Australian Journal of Earth Sciences* 43, pp. 323–343.

Sutherland, F. L., J. D. Hollis, and L. M. Barron (1984). “Garnet lherzolite and other inclusions from a basalt flow, Bow Hill, Tasmania”. In: *Developments in Petrology* 11, pp. 145–160.

Sutherland, F. L. and P. Wellman (1986). “Potassium-argon ages of Tertiary volcanic rocks, Tasmania”. In: *Papers and Proceedings of the Royal Society of Tasmania* 120, pp. 77–86.

Takei, Y. (2017). “Effects of Partial Melting on Seismic Velocity and Attenuation: A New Insight from Experiments”. In: *Annual Review of Earth and Planetary Sciences* 45.1, pp. 447–470.

Tappert, R. et al. (2011). “Garnet peridotite xenoliths and xenocrysts from the Monk Hill kimberlite, South Australia: Insights into the lithospheric mantle beneath the Adelaide Fold Belt”. In: *Journal of Petrology* 52, pp. 1965–1986.

Tappert, R. et al. (2019). “The petrology of kimberlites from South Australia: Linking olivine macrocrystic and micaceous kimberlites”. In: *Journal of Volcanology and Geothermal Research* 373, pp. 68–96.

Taylor, G. et al. (1990). “Early Tertiary palaeogeography, landform evolution, and palaeoclimates of the Southern Monaro, N.S.W., Australia”. In: *Palaeogeography, Palaeoclimatology, Palaeoecology* 78, pp. 109–134.

Taylor, W. R. (1998). “An experimental test of some geothermometer and geobarometer formulations for upper mantle peridotites with application to the thermobarometry of fertile lherzolite and garnet websterite”. In: *Neues Jahrbuch für Mineralogie - Abhandlungen* 172, pp. 381–408.

The Economist (2019). “Ore bodies, it has been discovered, are not randomly distributed”. In: *The Economist (Science and technology)*.

Thomas, I. D. et al. (2011). “Widespread low rates of Antarctic glacial isostatic adjustment revealed by GPS observations”. In: *Geophysical Research Letters* 38.22.

Tozer, B. et al. (2019). “Global bathymetry and topography at 15 arc sec: SRTM15+”. In:

Earth and Space Science 6.10, pp. 1847–1864.

Twinn, G. et al. (2022). “Thermal history of the southern Antarctic Peninsula during Cenozoic oblique subduction”. In: *Journal of the Geological Society* 179.6.

van der Wal, W., P. L. Whitehouse, and E. J. Schrama (2015). “Effect of GIA models with 3D composite mantle viscosity on GRACE mass balance estimates for Antarctica”. In: *Earth and Planetary Science Letters* 414, pp. 134–143.

Vaughan, D. et al. (2013). “Observations: Cryosphere”. In: *Climate Change 2013: The Physical Science Basis. Contribution of Working Group I to the Fifth Assessment Report of the Intergovernmental Panel on Climate Change*. Ed. by T. Stocker et al.

Wass, S. Y. and J. D. Hollis (1983). “Crustal growth in south-eastern Australia –Evidence from lower crustal eclogitic and granulitic xenoliths”. In: *Journal of Metamorphic Geology* 1, pp. 25–45.

Watts, A., S. Zhong, and J. Hunter (2013). “The Behavior of the Lithosphere on Seismic to Geologic Timescales”. In: *Annual Review of Earth and Planetary Sciences* 41. Volume 41, 2013, pp. 443–468.

Whitehouse, P. L. (2018). “Glacial isostatic adjustment modelling: historical perspectives, recent advances, and future directions”. In: *Earth Surface Dynamics* 6.2, pp. 401–429.

Whittington, A. G., A. M. Hofmeister, and P. I. Nabelek (2009). “Temperature-dependent thermal diffusivity of the Earth’s crust and implications for magmatism”. In: *Nature* 458.7236, pp. 319–321.

Wolstencroft, M. et al. (2015). “Uplift rates from a new high-density GPS network in Palmer Land indicate significant late Holocene ice loss in the southwestern Weddell Sea”. In: *Geophysical Journal International* 203.1, pp. 737–754.

- Yabe, K. and T. Hiraga (2020). “Grain-Boundary Diffusion Creep of Olivine: 2. Solidus Effects and Consequences for the Viscosity of the Oceanic Upper Mantle”. In: *Journal of Geophysical Research: Solid Earth* 125.8.
- Yamauchi, H. and Y. Takei (2016). “Polycrystal anelasticity at near-solidus temperatures”. In: *Journal of Geophysical Research: Solid Earth* 121.11, pp. 7790–7820.
- Ziberna, L. et al. (2016). “Error sources in single-clinopyroxene thermobarometry and a mantle geotherm for the Novinka kimberlite, Yakutia”. In: *American Mineralogist* 101, pp. 2222–2232.
- Zwally, H. J. and M. B. Giovinetto (2011). “Overview and Assessment of Antarctic Ice-Sheet Mass Balance Estimates: 1992-2009”. In: *Surveys in Geophysics* 32.4, pp. 351–376.
- Zwally, J. H. et al. (2012). *Antarctic and Greenland Drainage Systems*. GSFC Cryospheric Sciences Laboratory.

Appendix A

BANCAL22: An Open-Source

Algorithm for Bayesian Anelasticity

Model Calibration

The Bayesian inverse modelling framework developed in Chapter 2, and extended to incorporate xenolith-derived palaeogeotherm data in Chapter 5, enables self-consistent mapping of Earth’s thermomechanical structure. Due to the flexibility of the modelling framework, it can be used to generate images of lithospheric and asthenospheric structure anywhere where V_S data of sufficient resolution and quality is available, using any combination of five core geophysical data constraints: palaeogeotherms, oceanic plate temperatures, adiabatic average asthenosphere temperatures, shear-wave attenuation, and viscosity. It can also be adapted to use other data types as needed. Furthermore, while applications of the Bayesian inverse model have been restricted to the anelasticity parameterisation of Yamauchi and Takei (2016) in this thesis, any such parameterisation can be included by simply adding a Python script. To encourage its use by the wider geophysics community, I have made the modelling framework **BANCAL22** available via GitHub, using the following URL: <https://github.com/JamesHazzard/BANCAL22>. This

section provides a brief overview of the software, and how it can be used.

A.1 Installation

To install **BANCAL22**, the simplest option is to clone the repository by running the following line of code.

```
git clone https://github.com/JamesHazzard/BANCAL22
```

If you wish to contribute to the development of the code, it is best to fork the repository following the instructions available at this [link](#).

A.2 Performing Inversions Using **BANCAL22**

The modular structure of **BANCAL22** makes it flexible and easily extensible. Several different built-in options are already available when running inversions with the code, including the ability to specify the combination of input data sets, Bayesian sampling algorithm, and viscoelasticity parameterisation that is implemented. These selections can be made by changing the files in the `options` subdirectory of the root directory. Once the desired options have been selected, running the inversion itself is straightforward.

A.3 Data, Algorithm and Anelastic Parameterisation Selection

The `data_selection.txt` file allows you to specify which independent observational constraints you want to fit in the inversion (i.e., xenolith V_S and T data, age-dependent oceanic V_S and T , adiabatic V_S and T , sublithospheric Q_S^{-1} and V_S and/or average sublithospheric η and V_S). Setting a 1 in a given column indicates that you wish to fit that data set; a

0 will exclude it from the inversion. Note that data files need to be saved in the relevant `data/[xenolith|plate|adiabat|attenuation|viscosity]` subdirectories of the root directory. These files must be formatted as follows:

`data/xenolith/nodule_obs_all.zTVslln` — xenolith-based geotherm data with the following column arrangement: depth (in km); temperature (in °C); V_S (in km s^{-1}); longitude of xenolith eruption site (decimal degrees); latitude of site (decimal degrees); numerical index of site (0–N).

`data/plate/plate.VseTz` — age-dependent oceanic V_S and T data: V_S (in km s^{-1}); $1\sigma V_S$ uncertainty (in km s^{-1}); depth (in km); temperature (in °C).

`data/adiabat/adiabat.VseTz` — adiabatic V_S and T data: V_S (in km s^{-1}); $1\sigma V_S$ uncertainty (in km s^{-1}); depth (in km); temperature (in °C).

`data/attenuation/attenuation.QeVsZ` — sublithospheric attenuation (Q_S^{-1}) data: Q_S^{-1} , $1\sigma Q_S^{-1}$ uncertainty, V_S (in km s^{-1}), depth (in km).

`data/viscosity/viscosity.neVsZ` — sublithospheric viscosity (η) data: η (Pa s), $1\sigma \eta$ uncertainty (Pa s), V_S (in km s^{-1}), depth (in km).

An additional subdirectory called `data/potential_temperature` can be used to make note of the potential temperature associated with the relevant observational constraints, and set the preferred solidus temperature at 50 km depth, set as default to 1333°C and 1326°C, respectively.

The `algorithm_selection.txt` file allows you to specify which Bayesian sampling algorithm you would like to employ in the inversion. There are currently two options to select from: **GASWAM** (*Global Adaptive Scaling Within Adaptive Metropolis*; Andrieu and Thoms, [2008](#)) or **ASASM** (*Accelerated Shaping Accelerated Scaling Metropolis*; Spencer, [2021](#)). GASWAM is the default option and described in detail in Chapter 2. ASASM adopts a similar approach and also uses the history of samples to iteratively update the covariance matrix that is used to propose new samples (see Spencer, [2021](#)). However, unlike GASWAM, it systematically ‘forgets’

a certain number of previous samples as the inversion progresses. This strategy is based on the observation that earlier samples are less likely to accurately characterise the true model covariance and so should be preferentially ignored when generating new proposals. It should be emphasised that neither GASWAM nor ASASM is necessarily ‘better’, indeed the algorithm that performs best will likely depend on the nature of the input data and parameterisation choices. I tested both algorithms using the data and parameterisation choices described in Chapter 2, and found no notable differences in runtime or end result.

The `parameterisation_selection.txt` file currently only has YT16 as an option, i.e., the premelting model of Yamauchi and Takei (2016), and therefore cannot be adapted for now. However, any other choice of parameterisation (e.g., the Extended Burgers model of Jackson and Faul, 2010) can easily be implemented locally. Other users can also contribute their implementation of a given model to the code repository via a pull request.

A.4 Running an Inversion

Once the various options have been set following the guidelines outlined in the previous section, the inversion can be run by first entering

```
python3 setup.py
```

on the command line in the root directory. This command prepares the correct viscoelasticity parameter and hyperparameter prior distributions based on the choice of parameterisation and data, respectively. It also imports the relevant modules associated with the chosen inversion algorithm and parameterisation. The inversion itself can then be run using

```
python3 main.py
```

whereupon “Beginning inversion at [YYYY-MM-DD_HH-mm-ss]” should be the first output. The inversion will continue, printing summary statistics every 100 samples, until it reaches the

maximum number of samples set in `main.py` using the `n_trials` variable (400,000 by default).

At the end of a successful inversion “Inversion completed in [runtime] seconds” will appear, while outputs are saved to a subdirectory with the path `output/[YYYY-MM-DD_HH-mm-ss]`.

The data and inversion options used are also stored in `output/[YYYY-MM-DD_HH-mm-ss]`, for clarity.